UNIVERSITÉ DE GENÈVE
Département de Physique Nucléaire et Corpusculaire

FACULTÉ DES SCIENCES
Professeur Xin Wu
Docteur Merlin Kole

Development of the Next Generation Space-based Compton Polarimeter and Energy Resolved Polarization Analysis of Gamma-Ray Bursts Prompt Emission

THÈSE

Présentée à la Faculté des sciences de l'Université de Genève
Pour obtenir le grade de Docteur ès sciences, mention physique

Par

Nicolas De Angelis

de

Cluses (France)

Thèse N°5785

Genève

Atelier d'impression ReproMail

2023

UNIVERSITÉ DE GENÈVE

FACULTÉ DES SCIENCES

DOCTORAT ÈS SCIENCES, MENTION PHYSIQUE

Thèse de Monsieur Nicolas DE ANGELIS

intitulée :

«Development of the Next Generation Space-based Compton Polarimeter and Energy Resolved Polarization Analysis of Gamma-Ray Bursts Prompt Emission»

La Faculté des sciences, sur le préavis de Monsieur X. WU, professeur ordinaire et directeur de thèse (Département de Physique Nucléaire et Corpusculaire), Monsieur M. R. KOLE, docteur et codirecteur de thèse (Département de Physique Nucléaire et Corpusculaire), Monsieur M. HELLER, docteur (Département de Physique Nucléaire et Corpusculaire) et Monsieur V. BHALERAO, professeur (Department of Physics, Indian Institute of Technology Bombay, Bombay, India), autorise l'impression de la présente thèse, sans exprimer d'opinion sur les propositions qui y sont énoncées.

Genève, le 13 décembre 2023

Thèse - 5785 -

Le Décanat

N.B. - La thèse doit porter la déclaration précédente et remplir les conditions énumérées dans les "Informations relatives aux thèses de doctorat à l'Université de Genève".

"Il viaggio scombussola le nostre certezze,
mostra quanto poco sappiamo e quanto abbiamo da imparare."

— Beppe Severgnini

"L'Homme a toujours eu besoin de se confronter à des choses qui le dépassent.
C'est en sortant de sa zone de confort qu'on apprend."

— Thomas Pesquet

ABSTRACT

As the most powerful events since the Big Bang, Gamma-Ray Bursts (GRBs) typically emit in a few seconds the amount of energy that the Sun would deliver in its entire life. These transient events are of extragalactic origin and consist of a prompt γ-ray emission followed by an afterglow emission spanning the entire electromagnetic spectrum. GRBs can be classified into two distinct populations based on the duration of their prompt emission. Bursts lasting for less than 2 seconds, called short GRBs, are originated by the merger of binary neutron stars. Long GRBs, whose prompt emission can last up to tens of minutes, are associated with very powerful supernovae. Although these extreme events have been discovered half a century ago, with several decades of extensive spectral, temporal, and localization studies, a lot remains to be understood about GRBs. The composition and dynamics of the outflow and whether it is highly magnetized or dominated by kinetic energy, is one of the mystery that needs to be answered. The place where the energy dissipation takes place in the source, as well as the configuration of the magnetic fields and the structure of the ultrarelativistic jets are also not known at the moment. Furthermore, the emission mechanism responsible for the tremendous observed amount of energy is currently still an open question. Measuring the polarization of the prompt emission is thought to be able to answer all the remaining major points to be addressed on the physics of GRBs.

Photons consist of orthogonal magnetic and electric fields propagating in space and time. A source is highly polarized when a large fraction of the photons emitted have their electric field aligned in a given direction. Photons interact via three processes with matter. At low energy, the photoelectric effect is dominant. In this effect, a photon is absorbed by an electron, transferring its original energy into kinetic energy of the recoil electron. At intermediate energies, a photon will undergo Compton scattering, transferring part of its energy to an electron without being entirely absorbed. At high energy, a photon can produce a pair of electron-positron. In all three cases, the angular distribution of the daughter particles is related to the polarization of the original photon source. The secondary products of the interaction are preferentially produced in a plane orthogonal to the polarization vector of the incoming photon. The polarization of a source can therefore be determined by measuring the angular distribution of these secondary products. This principle is at the basis of all detection techniques of high-energy polarimetry. Many high-energy polarimeters based on different concepts have been proposed or operated in space over the last decades. The increasing sensitivity of such instruments opens up new possibilities in astrophysical high-energy polarimetry.

One of the first missions dedicated to measuring the polarization of the prompt emission of GRBs was POLAR. Launched in September 2016 for about 6 months of operation on the Tiangong-2 space lab, it consisted of a segmented

array of elongated plastic scintillators read out by multi-anode photo-multiplier tubes. Thanks to a wide field of view, POLAR was able to detect 55 GRBs as well as several pulsars and solar flares. Out of the 55 GRBs, 14 had enough statistics for proper polarization analysis. A low polarization degree was reported for all of these GRBs. However, time-resolved analysis of the three brightest observed GRBs showed, for the two single pulse bursts, a hint of time-evolving polarization angle with moderate polarization degree. The evolution of the polarization angle washes out the polarization degree on time-integrated analysis. The main conclusion of the POLAR mission is that more statistics are needed in order to provide precise time and energy-resolved polarization results of GRBs and disentangle between the existing emission models.

An interesting input to theoretical models that was not exploited until now with the POLAR data is the energy dependence of polarization. The existing analysis software used for the integrated analysis was therefore modified in order to perform energy resolved polarization analysis. The polarization degree was first fitted versus energy for 13 GRBs using a Heaviside and a linear function. The polarization angle was also fitted with a linear expression. No significant energy dependence of any of these two parameters was found, although no stringent limits could be established due to the limited statistics, not discarding any existing energy dependent polarization model.

The POLAR mission delivered very exciting science outcome, but the limited statistics did not allow for time and energy resolved polarization analysis of many GRBs. A successor mission to POLAR, POLAR-2, was therefore proposed. Accepted for a launch to the China Space Station, POLAR-2 will contain 4 times more channels than POLAR with technological upgrades improving its sensitivity. This improved sensitivity, especially at low energies, is partly due to the use of silicon photomultipliers instead of multi-anode photomultiplier tubes. As a space based instrument, POLAR-2 needs to undergo many space qualification tests, such as irradiation, vibration and shock tests, and thermal vacuum cycling.

The use of silicon photomultipliers as many advantages over the previously employed photomultiplier tubes like mechanical robustness, compactness, lower bias voltages, or higher detection efficiency. The main drawback of theses devices in the presence of dark noise, increasing not only with temperature but also after being exposed to radiation. A cooling system was developed to operate the sensors as cold as possible, but their performances still degrade after some time in the space radiation environment. A thermal annealing strategy consisting of heating up the sensors for a few days after a year of operation would allow to recover part of the original performances of the sensors. Multiple sensors with difference microcell sizes were therefore irradiated to a dose equivalent to 1.7 years in space for the POLAR-2 orbit. These sensors were then placed at different temperatures for several months, monitoring their dark current as a function of time. The annealing of the dark current was then characterized as a function of temperature. Annealing strategies applicable to any space-based

instrument employing silicon photomultipliers were proposed.

Finally, the polarimeter modules of POLAR-2 are a crucial piece of the instrument as they are responsible for converting the deposited γ-ray energy into optical photons and later into an electronic signal. The modules are therefore optical systems, were all components have to be optimized to maximize the light collection and therefore the sensitivity of the polarimeter. Many optical components, such as the reflective foils, optical coupling pads, scintillators, or mechanical alignment grids, were therefore characterized. An optical simulation of the polarimeter module was implemented in Geant4 in order to fully understand and model its optical behavior. The module simulated performances were then compared to the actual performances using calibration setups based on radioactive sources or polarized X-ray beam.

This thesis starts with an introduction on the current knowledge on gamma-ray bursts as well as what can be learned from polarization measurements of their prompt emission. An overview of the current state of the art of high energy polarimetry is then given. The work performed in the frame of this thesis is then divided into two parts. The first part presents the POLAR instrument and its past achievements, followed by an energy resolved polarization analysis of the POLAR GRB catalog. The second part describes the design and development work for the successor mission of POLAR, called POLAR-2. Starting with a detailed description of the POLAR-2 design and qualification, this part then discusses the annealing study performed to characterize the recovery from radiation damage of silicon photomultipliers. Lastly, the optical characterization and simulation of the POLAR-2 polarimeter module are described.

RÉSUMÉ

En tant qu'événements les plus puissants depuis le Big-Bang, les sursauts gamma (GRBs) émettent typiquement en quelques secondes la quantité d'énergie que le Soleil délivrerait pendant toute sa vie. Ces événements transitoires sont d'origine extragalactique et consistent en une émission rapide de rayons gamma suivie d'une émission rémanente couvrant l'ensemble du spectre électromagnétique. Les GRBs peuvent être classés en deux populations distinctes en fonction de la durée de leur émission rapide. Les sursauts d'une durée inférieure à 2 secondes, appelés sursauts courts, proviennent de la fusion d'un système binaire d'étoiles à neutrons. Les GRBs longs, dont l'émission rapide peut durer jusqu'à quelques dizaines de minutes, sont associés à des supernovae très puissantes. Bien que ces événements extrêmes aient été découverts il y a un demi-siècle, avec plusieurs décennies d'études spectrales, temporelles et de localisation approfondies, il reste encore beaucoup à comprendre sur les GRBs. La composition et la dynamique du flux sortant et la question de savoir s'il est fortement magnétisé ou s'il est dominé par l'énergie cinétique est l'un des mystères auxquels il faut répondre. L'endroit où la dissipation de l'énergie a lieu dans la source, ainsi que la configuration des champs magnétiques et la structure des jets ultrarelativistes ne sont pas non plus connus à l'heure actuelle. De plus, le mécanisme d'émission responsable de l'énorme quantité d'énergie observée reste une question ouverte. La mesure de la polarisation de l'émission rapide devrait permettre de répondre à tous les points importants qui restent à traiter concernant la physique des GRBs.

Les photons sont constitués de champs magnétiques et électriques orthogonaux se propageant dans l'espace et le temps. Une source est fortement polarisée lorsqu'une grande partie des photons émis ont leur champ électrique aligné dans une direction donnée. Les photons interagissent avec la matière par le biais de trois processus.À basse énergie, l'effet photoélectrique est dominant. Dans cet effet, un photon est absorbé par un électron, transférant son énergie d'origine en énergie cinétique de l'électron de recul. À des énergies intermédiaires, un photon subit une diffusion Compton, transférant une partie de son énergie à un électron sans être entièrement absorbé. À haute énergie, un photon peut produire une paire électron-positron. Dans les trois cas, la distribution angulaire des particules filles est liée à la polarisation de la source originale de photons. Les produits secondaires de l'interaction sont préférentiellement produits dans un plan orthogonal au vecteur de polarisation du photon entrant. La polarisation d'une source peut donc être déterminée en mesurant la distribution angulaire de ces produits secondaires. Ce principe est à la base de toutes les techniques de détection de la polarimétrie de haute énergie. De nombreux polarimètres à haute énergie basés sur différents concepts ont été proposés ou exploités dans l'espace au cours des dernières décennies. La sensibilité croissante de ces instruments ouvre de nouvelles possibilités dans le domaine de la polarimétrie astrophysique

à haute énergie.

L'une des premières missions dédiées à la mesure de la polarisation de l'émission rapide des GRBs a été POLAR. Lancée en septembre 2016 pour une durée d'opération d'environ six mois sur le laboratoire spatial Tiangong-2, elle consistait en un réseau segmenté de scintillateurs plastiques allongés lus par des tubes photomultiplicateurs à anodes multiples. Grâce à son large champ de vision, POLAR a pu détecter 55 GRBs ainsi que plusieurs pulsars et éruptions solaires. Sur les 55 GRBs, 14 avaient suffisamment de statistiques pour permettre une analyse correcte de la polarisation. Un faible degré de polarisation a été rapporté pour tous ces GRBs. Cependant, l'analyse résolue en temps des trois GRB les plus brillants observés a montré, pour les deux sursauts à impulsion unique, une potentielle évolution temporelle de l'angle de polarisation avec un degré de polarisation modéré. L'évolution de l'angle de polarisation efface le degré de polarisation sur l'analyse intégrée dans le temps. La principale conclusion de la mission POLAR est que davantage de statistiques sont nécessaires pour fournir des résultats précis sur la polarisation des GRBs, résolus en temps et en énergie, et pour démêler les modèles d'émission existants.

La dépendance en énergie de la polarisation est une donnée intéressante pour les modèles théoriques qui n'a pas été exploitée jusqu'à présent avec les données de POLAR. Le logiciel d'analyse existant utilisé pour l'analyse intégrée a donc été modifié afin d'effectuer une analyse de la polarisation résolue en énergie. Une régression du degré de polarisation a d'abord été effectuée en fonction de l'énergie pour 13 GRBs en utilisant une fonction Heaviside et une fonction linéaire. Une régression linéaire de l'angle de polarisation en fonction de l'énergie à aussi été faite. Aucune dépendance significative à l'énergie de l'un de ces deux paramètres n'a été trouvée, bien qu'aucune limite stricte n'ait pu être établie en raison des statistiques limitées, ce qui n'exclut aucun modèle existant de polarisation dépendant de l'énergie.

La mission POLAR a donné des résultats scientifiques très intéressants, mais les statistiques limitées n'ont pas permis d'analyser la polarisation résolue en temps et en énergie de nombreux GRBs. Une mission succédant à POLAR, POLAR-2, a donc été proposée. Accepté pour un lancement vers la station spatiale chinoise, POLAR-2 contiendra quatre fois plus de canaux que POLAR et bénéficiera de mises à jour technologiques améliorant sa sensibilité. Cette amélioration de la sensibilité, en particulier aux basses énergies, est en partie due à l'utilisation de photomultiplicateurs en silicium au lieu de tubes photomultiplicateurs multi-anodes. En tant qu'instrument spatial, POLAR-2 doit subir de nombreux tests de qualification dans l'espace, tels que des tests d'irradiation, de vibration et de choc, ainsi que des cycles thermiques sous vide.

L'utilisation de photomultiplicateurs en silicium présente de nombreux avantages par rapport aux tubes photomultiplicateurs précédemment utilisés, tels que la robustesse mécanique, la compacité, des tensions d'alimentation plus faibles ou une efficacité de détection plus élevée. Le principal inconvénient de ces dispositifs est la présence d'un bruit d'obscurité, qui augmente non seule-

ment avec la température, mais aussi après avoir été exposé à des radiations. Un système de refroidissement a été mis au point pour que les capteurs soient aussi froids que possible, mais leurs performances continuent de se dégrader après un certain temps dans l'environnement des radiations spatiales. Une stratégie de recuit thermique consistant à chauffer les capteurs pendant quelques jours après une année de fonctionnement permettrait de récupérer une partie des performances initiales des capteurs. Plusieurs capteurs avec des tailles de micro-cellules différentes ont donc été irradiés à une dose équivalente à 1,7 année dans l'espace pour l'orbite de POLAR-2. Ces capteurs ont ensuite été placés à différentes températures pendant plusieurs mois, en surveillant leur courant d'obscurité en fonction du temps. Le recuit du courant d'obscurité a ensuite été caractérisé en fonction de la température. Des stratégies de recuit applicables à tout instrument spatial employant des photomultiplicateurs en silicium ont été proposées.

Enfin, les modules polarimétriques de POLAR-2 sont un élément crucial de l'instrument car ils sont responsables de la conversion de l'énergie déposée par les rayons gamma en photons optiques et, plus tard, en un signal électronique. Les modules sont donc des systèmes optiques dont tous les composants doivent être optimisés pour maximiser la collecte de lumière et donc la sensibilité du polarimètre. De nombreux composants optiques, tels que les feuilles réfléchissantes, les joints de couplage optique, les scintillateurs ou les grilles d'alignement mécanique, ont donc été caractérisés. Une simulation optique d'un module de polarimètre a été mise en œuvre dans Geant4 afin de comprendre et de modéliser pleinement son comportement optique. Les performances simulées du module ont ensuite été comparées aux performances réelles à l'aide de calibrations basées sur des sources radioactives ou un faisceau de rayons X polarisés.

Cette thèse commence par une introduction sur les connaissances actuelles sur les sursauts gamma ainsi que sur ce que l'on peut apprendre des mesures de polarisation de leur émission rapide. Une vue d'ensemble de l'état actuel de l'art de la polarimétrie à haute énergie est ensuite donnée. Le travail effectué dans le cadre de cette thèse est ensuite divisé en deux parties. La première partie présente l'instrument POLAR et ses réalisations passées, suivie d'une analyse de polarisation résolue en énergie du catalogue de GRB de POLAR. La seconde partie décrit les travaux de conception et de développement de la mission qui succédera à POLAR, appelée POLAR-2. En commençant par une description détaillée de la conception et de la qualification de POLAR-2, cette partie aborde ensuite l'étude de recuit réalisée pour caractériser la récupération des photomultiplicateurs en silicium endommagés par les radiations. Enfin, la caractérisation optique et la simulation d'un module du polarimètre de POLAR-2 sont décrites.

ACKNOWLEDGMENTS

The work presented in this thesis has been made possible thanks to the help and support of many people. I wish to express my gratitude to all of these people in the following paragraphs.

To start with, I would like to thank Xin Wu for welcoming me in his group at DPNC, University of Geneva. I also want to express my deep recognition to my supervisor, Merlin Kole, for all his support and advices all along my thesis. I could not have hoped of a having better supervisor.

I would like to thank Nicolas Produit for making research fun by continually sharing interesting discussion topics, as well as his inventive ideas and impressive knowledge on a wide variety of topics. I would also like to thank Hancheng Li for introducing me to the POLAR analysis tools and for all the good time spent in Geneva and abroad during many conference and vacation trips. I would also like to thank Hancheng and Dongmei for all the lunch breaks spent on the Badminton court as well as for preparing amazingly delicious Chinese food to the group. I would also like to thank my office mate, Johannes Hulsman, for all the fun discussions and experiences we shared during all these years.

I am very grateful to Slawomir Mianowski and Dominik Rybka from NCBJ, Jianchao Sun from IHEP, J. Michael Burgess and Jochen Greiner from MPE, and more broadly to all my colleagues from the POLAR and POLAR-2 collaborations for their warm welcome in their respective research group and for all the enjoyable moments we shared. It was a real pleasure to work with all of you.

Warm acknowledgements are extended to the mechanics and electronics groups of DPNC for their amazing work and commitment to the different projects I have been involved in during my PhD. Many of the achievements described in this thesis could not have been made possible without the precious help of Franck Cadoux, Coralie Husi, Gabriel Pelleriti, Yannick Favre, Javier Mesa, Jérôme Stauffer, Stéphane Debieux, Daniel La Marra, and Adrien Stil. I am also very thankful to all the interns and students that worked in our groups during these past years for their contribution to the POLAR-2 project, that is Clara, Corentin, Fiona, Camille, Arnas, Gilles, Eren, and Rim.

I would also like to thank the members of my thesis committee, Prof. Varun Bhalerao and Dr. Matthieu Heller, for having taken time to carefully evaluate my work and for improving this thesis through there comments and suggestions. I furthermore gratefully acknowledge the support of the Swiss National Science Foundation for funding my PhD research.

Additionally, I wish to thank Sébastien Clément and his team from the CERN Polymer Laboratory for helpful exchanges about the design of the scintillator

alignment grids; Thomas Schneider from the CERN Thin Film & Glass service for welcoming us in his lab and bringing his precious knowledge for optical characterization of many polarimeter module components; Kurt Dittrich from MPE for helping us with the POLAR-2 space qualification, especially with thermal vacuum tests and the vibration and shock campaign; Alessandro La Rosa and his team from the CERN QART lab for his help with the eXTP LAD module thermal qualification test; Jérémie Teyssier from LTA and Marc Jobin from HEPIA for their help with the measurement of plastic scintillator surface roughness; and Jan Swakon and his team in IFJ for welcoming us many times in Krakow and helping us with the irradiation of many POLAR-2 items.

I am also very thankful to all my other colleagues from DPNC for all the journal clubs, coffee breaks and many other activities we shared. In particular, I wish to thank Matthieu Heller and Teresa Montaruli for having supervised me during my Master's thesis and for all the helpful discussions we had during my PhD. I also want to thank Philip Azzarello for teaching me how to use the DPNC probe stations that I have extensively been using for POLAR-2.

Moreover, I wish to express my sincere gratitude to all my teaching colleagues, too numerous to mention them all here, with a special thank to Sandro D'Aleo and Vicenzo Fontana for their very precious help. Teaching with all of you in parallel to my research activities was really a great experience. I should also thank Nathalie Chaduiron, Liliane Nagy, Catherine Blanchard, and Yann Meunier for their help on administrative and IT related matters.

I would like to thank all my colleagues from the eXTP and LEAP collaborations, as well as from the SMILE project. I wish to thank in particular Yulia Akisheva with whom it has always been a great pleasure to work and exchange. More broadly, I am very thankful to all the people I have been discussing with during conferences, workshops, seminars, etc. for many interesting exchanges of ideas that helped me to improve my research.

Last but not least, I want to extend my warm gratitude to all my friends, Laura, Bastien, Anthony, David, Rebecka, Julien, Guillaume, Enzo, Yannick, Alexandre et al., as well as my family, for always supporting me all along the 9 years I spent studying at the University of Geneva.

PUBLICATIONS

Some ideas and figures discussed in this thesis have previously been or will be published in the following works:

This compact list of publications is just given for the reader's convenience. These papers will be directly cited from the Bibliography section when the ideas discussed have already been published. All the figures are re-used from these works with permission from the respective journals.

[1] Nicolas De Angelis et al. "Energy-resolved polarization analysis of Gamma-Ray Bursts' prompt emission with the POLAR and POLAR-2 instruments." *In preparation*. 2024.

[2] Nicolas De Angelis et al. "Optical design, simulations, and characterization of a POLAR-2 polarimeter module." *In preparation*. 2024.

[3] N. De Angelis et al. "Temperature dependence of radiation damage annealing of Silicon Photomultipliers." In: *Nuclear Instruments and Methods in Physics Research Section A: Accelerators, Spectrometers, Detectors and Associated Equipment* 1048 (2023), p. 167934. DOI: https://doi.org/10.1016/j.nima.2022.167934.

[4] Nicolas De Angelis et al. "Development and science perspectives of the POLAR-2 instrument: a large scale GRB polarimeter." In: *PoS* ICRC2021 (2021), p. 580. DOI: 10.22323/1.395.0580.

[5] Nicolas De Angelis et al. "Energy-dependent polarization of Gamma-Ray Bursts' prompt emission with the POLAR and POLAR-2 instruments." In: *PoS* ICRC2023 (2023), p. 619. DOI: 10.22323/1.444.0619.

[6] Johannes Hulsman, Nicolas De Angelis, Slawmoir Mianowski, et al. "Space Radiation Qualification of POLAR-2 Electronics." *In preparation*. 2024.

[7] Slawomir Mianowski et al. "Proton irradiation of SiPM arrays for POLAR-2." In: *Experimental Astronomy* 55.2 (2023), pp. 343–371. DOI: 10.1007/s10686-022-09873-6.

[8] Slawomir Mianowski et al. "Proton irradiation of plastic scintillator bars for POLAR-2." In: *Experimental Astronomy* (2023). DOI: 10.1007/s10686-023-09906-8.

CONFERENCES & WORKSHOPS

Part of the work and ideas described in this thesis have been presented and discussed at the following conferences and workshops:

- **Analysis Workshop** *Bringing Theory into the Data Space, Nendaz, Switzerland* (9-13 October 2023) https://indico.cern.ch/event/1288612/
- **Energy-dependent polarization of Gamma-Ray Bursts' prompt emission with the POLAR and POLAR-2 instruments** *38th International Cosmic Ray Conference, ICRC2023, Nagoya, Japan* (26 July-3 August 2023) https://www.icrc2023.org
- **Energy-dependent polarization of Gamma-Ray Bursts' prompt emission with the POLAR and POLAR-2 instruments** *European Astronomical Society Annual Meeting EAS2023, Krakow, Poland* (10-14 July 2023) https://eas.unige.ch/
- **Measuring Gamma-Ray Burst Polarization with the POLAR-2 mission** *Young researchers' day, Geneva, Switzerland September 16th* (16 September 2022) https://partphys-indico.unige.ch/event/703/
- **Measuring Gamma-Ray Transients Polarization with the POLAR-2 Compton Polarimeter** *Astrophysical Polarimetry in the Time-Domain Era, Lecco, Italy* (28 August-1 September 2022) https://indico.ict.inaf.it/event/982/
- **Gamma-Ray Polarization Measurements with the POLAR-2 mission** *COSPAR 2022, 44th Scientific Assembly, Athens, Greece* (16-24 July 2022) https://www.cosparathens2022.org/
- **Gamma-Ray Burst Polarization Measurements with the POLAR-2 mission** *1st Mondragone Frontiers of Astronomy Series, Frascati, Italy* (18-20 May 2022) https://astrodragon.web.roma2.infn.it/
- **Annealing Characterization of Hamamatsu S13360-60xx SiPMs for Space Applications** *SiPM Radiation: Quantifying Light for Nuclear, Space and Medical Instruments under Harsh Radiation Conditions, CERN, Geneva* (25-29 April 2022) https://indico.cern.ch/event/1093102/
- **Development and science perspectives of the POLAR-2 instrument: a large scale GRB polarimeter** *INTEGRAL: towards the third decade of X and Gamma ray observations, Santa Margherita di Pula, Italy* (11-15 October 2021) https://indico.ict.inaf.it/event/1001/
- **Development and science perspectives of the POLAR-2 instrument: a large scale GRB polarimeter** *37th International Cosmic Ray Conference, ICRC2021, Berlin, Germany* (12-23 July 2021 – Online) https://icrc2021.desy.de/

- **POLAR-2: Development of a Large Scale Gamma-ray Polarimeter** *IAU Symposium 360, ASTROPOL 2020, Hiroshima, Japan* (22-26 March 2021 – Online) https://astropol2020-iau.jp/

CONTENTS

LIST OF FIGURES

LIST OF TABLES

ACRONYMS

AGN Active Galactic Nuclei

APD Avalanche PhotoDiode

BAT The Burst Alert Telescope on-board the Swift Observatory

BATSE Burst And Transient Source Experiment

BEE Back-End Electronics

BSD Broad energy-band Spectrum Detector

BNS Binary Neutron Star

CERN European Organization for Nuclear Research

CFRP Carbon Fiber Reinforced Polymer
CGRO Compton Gamma-Ray Observatory
CNES Centre National d'Etudes Spatiales
CSS China Space Station
DA Detector Assembly of the LAD
DCR Dark Count Rate
EBL Extragalactic Background Light
ESR Enhanced Specular Reflector
ESRF European Synchrotron Radiation Facility
eXTP enhanced X-ray Timing and Polarimetry mission
FEB Front-End Board
FEE Front-End Electronics
FET Field Effective Transistor
FoV Field-of-View
FRED Fast-Rising Exponential Decay
GAP Gamma-ray Burst Polarimeter
GCN Gamma-ray Coordinates Network
GJ Gaussian Jet
GPD Gas Pixel Detector
GW Gravitational Waves
HPGe High Purity Germanium detector
HVPS High Voltage Power Supply
ICMART Internal Collision induced MAgnetic Reconnection and Turbulence
IFJ-PAN Institute of Nuclear Physics of the Polish Academy of Science
IOM Interference Optical Microscope
ISS International Space Station
IXPE Imaging X-ray Polarimetry Explorer
KED Kinetic Energy Dominated
LAD Large Area Detector of the eXTP mission
LEAP LargE Area Burst Polarimeter
LEO Low Earth Orbit
LOS Line Of Sight
lGRB long Gamma-Ray Burst
LHAASO Large High Altitude Air Shower Observatory
LIV Lorentz Invariance Violation
LOFT Large Observatory For X-ray Timing
LPD Low-energy Polarization Detector

LVDS Low Voltage Differential Signaling
LVPS Low Voltage Power Supply
LY Light Yield
MA-PMT Multi-Anode PhotoMultiplier Tube
MDP Minimum Detectable Polarization
MHD Magneto-Hydro-Dynamic
MLI Multi Layer Insulation
NTC Negative Temperature Coefficient
p.e. photo-electron
PA Polarization Angle
PCB Printed Circuit Board
PDE Photo Detection Efficiency
PEEK PolyEther Ether Ketone
PFA Polarimetry Focusing Array of the eXTP mission
PFD Poynting Flux Dominated
PLJ Power-Law Jet
PMT PhotoMultiplier Tube
PWM Pulse-Width Modulation
QE Quantum Efficiency
RadFET Radiation sensitive Field Effective Transistors
RTV Room Temperature Vulcanizing
SAA South Atlantic Anomaly
SDD Silicon Drift Detector
SED Spectral Energy Distribution
SFA Spectroscopic Focusing Array of the eXTP mission
SFL Solar Flare
sGRB short Gamma-Ray Burst
SiPM Silicon PhotoMultiplier
SNR Signal-to-Noise Ratio
TG-2 Tiangong-2
THJ Top-Hat Jet
TPC Time Projection Chamber
TVT Thermal Vacuum Test
UVOT The Ultra-violet Optical Telescope on-board the Swift Observatory
WFM Wide Field Monitor of the eXTP mission
XRT The X-Ray Telescope on-board the Swift Observatory
XTP X-ray Timing and Polarimetry mission

Part I

INTRODUCTION

Gamma-Ray Bursts (GRBs) are among the major mysteries of modern astrophysics. As the most powerful events in the universe since the Big-Bang, GRBs are a probe to fundamental physics phenomena like Lorentz invariance violation or Einstein's equivalence principle. These powerful transient events could further be used to probe the intergalactic medium or bring important pieces of information about the history of the Universe. But despite more than half a century of temporal, spectral, and localization studies, these events remain poorly understood. Polarization measurements have been theorized as a key to solve the biggest questions on GRBs, including the emission mechanisms at play in the sources and their jet and magnetic field structure. The first instruments dedicated to GRB prompt emission polarization measurements have been launched in the previous decade, bringing interesting information for modelling the sources and unveiling the need for more sensitive instruments to fully resolve GRB features. This introductory part aims to summarize the current state of the art of GRB polarimetry, by first covering our knowledge on the sources and later discussing the physics of high energy polarimeters as well as the current instrumental technologies available to probe GRB polarization.

1

THE GAMMA-RAY BURST PARADIGM

Discovered over half a century ago [125], Gamma-Ray Bursts (GRBs) are among the most energetic events in the Universe. They consist of transient bursts in the γ band lasting from fractions of seconds to tens of minutes, followed by an emission in all wavelengths from radio to TeV energies that can last several weeks or months. Two populations of GRB can be distinguished based on the duration of their prompt γ-ray emission. Short GRBs, whose prompt emission is typically less than 2 seconds, were proved to be related to Binary Neutron-star Merger (BNS) [4], while long GRBs are associated with explosions of very massive stars [100].

Even though a general picture of GRBs is well established and despite several decades of spectral, localization, and temporal studies, a lot of questions remain unanswered about these sources. The physical mechanisms at the origin of the emission and the structure of the magnetic field and jets are part of the poorly understood features of GRBs. Spectral and temporal measurements alone are not sufficient to disentangle between the proposed models to explain the physics of GRBs [84]. Measuring the polarization of the prompt emission would bring a more complete picture and is thought to be a powerful way of addressing fundamental questions on GRBs [83]. Because of the extreme nature of GRBs, understanding them goes far beyond GRB physics and is a way of probing many other aspects of astrophysics and fundamental physics.

Different levels of polarization are expected depending on whether the emission has a synchrotron or photospheric origin. Measuring the polarization of the prompt emission of GRBs could therefore help to explain the radiation mechanism causing the observed spectra. Polarization can as well vary depending on the magnetic field, a higher polarization degree being expected in the case of an ordered magnetic field compared to a random one. The composition and structure of the outflowing jets can also be better understood thanks to the polarization information.

Starting with an historical introduction on the discovery of gamma-ray burst, we will then move to a review of their main observational features. The way polarization can be used to answer important questions on GRB physics as well as the main theoretical predictions of the expected polarization from different models will then be detailed.

1.1 DISCOVERY OF GAMMA-RAY BURSTS AND HISTORICAL MILESTONES

In November 1st 1952, the United States of America exploded their first Hydrogen device in the Pacific ocean, entirely vaporizing an island. The Soviet Union followed 10 months later by detonating a 400 kilotons of TNT equivalent hydrogen engine at the Semipalatinsk test site in Kazakhstan. A lot of other thermonuclear tests followed during that decade, rising the concern about the danger of radioactive fallout. Discussions for an international agreement ending the nuclear tests started at the UN Disarmament Commission in May 1955 between the US, the UK, Canada, France, and USSR. An agreement was finally reached several years later with the Test Ban Treaty, that entered into force in October 10, 1963. The treaty, originally signed by the US, the UK, and Soviet Union, bans nuclear weapon tests in the atmosphere, in outer space, and under water. It is in this context that the US Air Force started the Project Vela to monitor compliance to the treaty by the Soviet Union. Multiple satellites were launched by pairs to detect possible detonation of nuclear bombs.

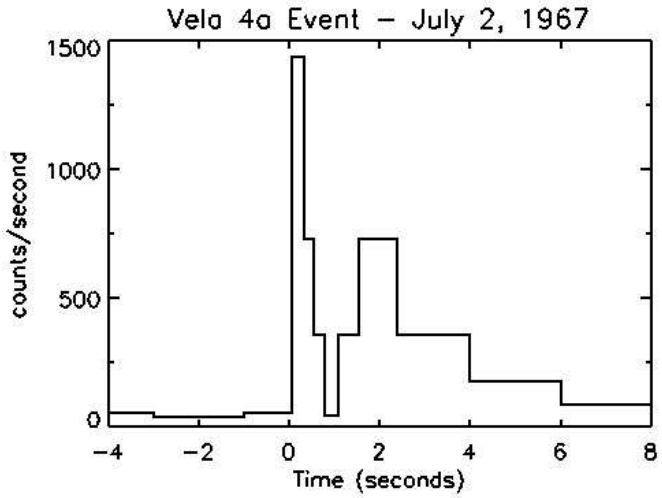

Figure 1.1: Light curve of the first ever detected Gamma-Ray Burst, GRB670702, measured by the Vela IVa satellite (Credit: R. Klebesadel, I. Strong & R. Olson (LANL), Vela Project).

In July 2, 1967, an unexpected burst of γ-ray was measured by the Vela IVa satellite [125]. With a duration of about 10 seconds and a light curve with two separate pulses, the measured burst was very different from what could be expected from a nuclear explosion in space. We would indeed expect a hard X-ray flash of the order of milliseconds with a single peak light curve[1]. This burst of γ-ray was indeed not originated from a nuclear explosion, but from what we nowadays call a gamma-ray burst. The light curve of this first ever measured GRB is shown in Figure 1.1. In the following years, similar bursts were measured by the IMP-6 [37] and Cosmos 461 [160] missions. This marked

1 The X-ray light curve of a nuclear explosion in the atmosphere indeed has a double peak structure. However, the second peak is caused by the shock wave of the explosion that compresses the surrounding air and heats it up until it releases emission. We would therefore only expect a single peak for a nuclear test in space, i.e. in vacuum

the birth of GRB astrophysics, although the poor timing and spectral resolution of the detectors at the time did not allow for very advanced studies.

1.2 OBSERVATIONAL PROPERTIES OF GRBS

Fifty years after the publication of the first detected GRB, many scientific breakthrough allowed to improve our understanding on GRBs. In this section we focus on the current knowledge on GRBs based on observations while the next section will discuss the existing GRB models and how polarization can help having a deeper understanding of these sources.

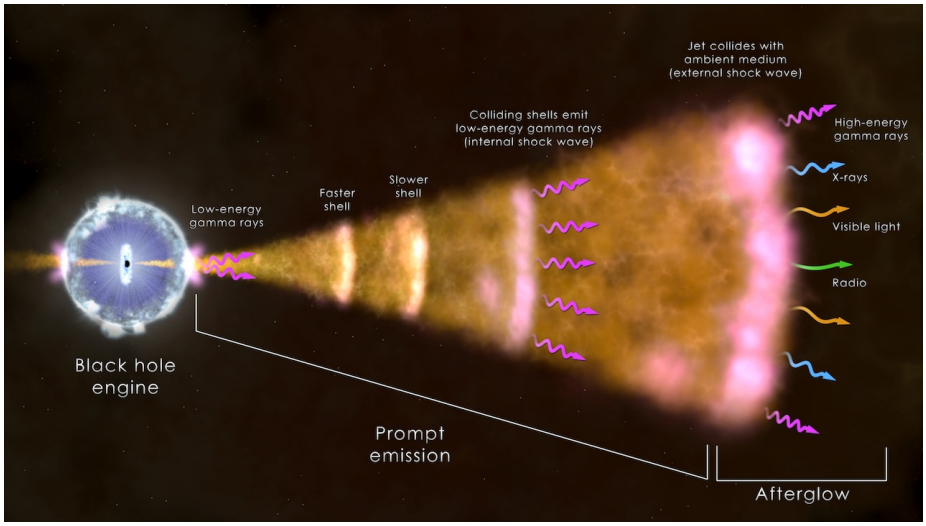

Figure 1.2: Schematic view showing the current understanding of GRB emission (Credit: NASA's Goddard Space Flight Center). The central engine emits jets of γ-ray accelerated through internal shocks, causing the prompt γ-ray emission. This is later followed by an external shock of the jet in the surrounding medium, causing the afterglow emission in the entire electromagnetic spectrum.

Gamma-Ray Bursts are transient events consisting of an initial burst of γ-rays, called prompt emission, followed by an afterglow emission spanning the entire electromagnetic spectrum. The prompt emission phase can last for fraction of seconds to minutes. Two populations of GRBs have been identified based on the duration of the prompt emission [135]: short ones (sGRB), with a duration of typically less than 2 seconds and originated from Binary Neutron Star (BNS) mergers; and long ones (lGRB), caused by the death of very massive stars. A simplified view of the current understanding of the GRB emission timeline is depicted in Figure 1.2. The central engine is emitting relativistic jets, in which γ-rays are emitted through internal shocks in the outflow, causing the prompt γ-ray emission. The leading process through which the γ-rays are emitted from the internal energy dissipation are namely the optically-thin synchrotron emission and the dissipative photospheric emission. These models and the polarization we expect in different configurations are discussed in the next section. The jet is later colliding with the ambient medium (external shock), causing the afterglow emission. These long-lived shocks are also called forward shock, in opposition to the short-lived reverse shock [77] propagating into the jet that can emit short optical or infrared flashes as well as radio flares. These very bright and energetic events are uniformly distributed in the sky and of extragalactic origin. They are so extreme that their typical luminosity is of the order of $10^{51} - 10^{53}$ erg s^{-1},

Internal shocks are occurring when a shell in the outflow takes over another slower shell.

and they release an energy equivalent to that released by the Sun in its entire lifetime in less than a second. The main observational features of GRBs are detailed below.

1.2.1 *Prompt Emission Temporal Properties*

An important parameter to describe the duration of the prompt phase of a GRB is the duration parameter T_{90}. It is defined as the time interval during which the burst is emitting from 5 to 95% of its total fluence. Many instruments use the total measured counts to compute the T_{90} instead of fluence, in which case the definition is energy and sensitivity dependent, implying that slightly different duration can be reported by different instruments for a given GRB depending on their sensitivity and energy band. One should note that by definition, the T_{90} can over-estimate the actual duration of the emission in the case of multi-pulse prompt emission. By measuring the duration parameter of many GRBs, the Konus/Venera experiment reported an evidence for two separated populations of GRBs [159]. This was strongly confirmed with the GRB catalog of the Burst And Transient Source Experiment (BATSE) experiment on-board the Compton Gamma-Ray Observatory (CGRO), as plotted in Figure 1.3. Two clear categories both following a log-normal distribution can be distinguished from the duration histogram: short GRBs peaking at 0.3 s, and long GRBs peaking at 40 s; with a conventional separation between them of 2 s. Short GRBs have typically harder spectra than long ones, as will be discussed in Section 1.2.2. The conventional 2 s limit for classifying a GRB as short or long does not always work, as there seems to be an overlap between short and long GRBs in the duration distribution. Some apparently short GRBs detected by Swift-BAT have been found to be more consistent with the properties of long GRBs [87, 141], and inversely [79, 235].

Swift-BAT is the Burst Alert Telescope of the Neil Gehrels Swift Observatory.

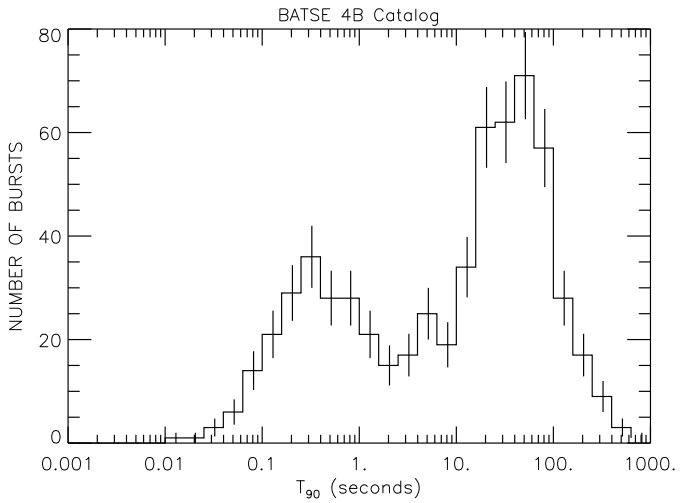

Figure 1.3: Histogram of the burst duration T_{90} of all the GRBs measured by BATSE (Credit: BATSE 4B Catalog, Robert S. Mallozzi). Two populations can be distinguished.

A wide variety of light curves can be measured from GRBs. The irregular nature of GRB prompt pulses can be observed in the sample of light curves

plotted in Figure 1.4. GRB light curves can be smooth or very variable with fluctuations as short as a few milliseconds [218]. The prompt emission can consist of a single pulse or several pulses sometimes separated by long gaps. The temporal separation between pulses follows a log-normal distribution [147, 161, 182], while the duration of individual pulses is energy dependent (following a power-law [186]) with a tendency for shorter pulses at high energy. Individual bright pulses can usually be described by a Fast-Rising Exponential Decay (FRED) function, which consists of a fast rising exponential part followed by a slower exponential decay described by equation (1.1) [187].

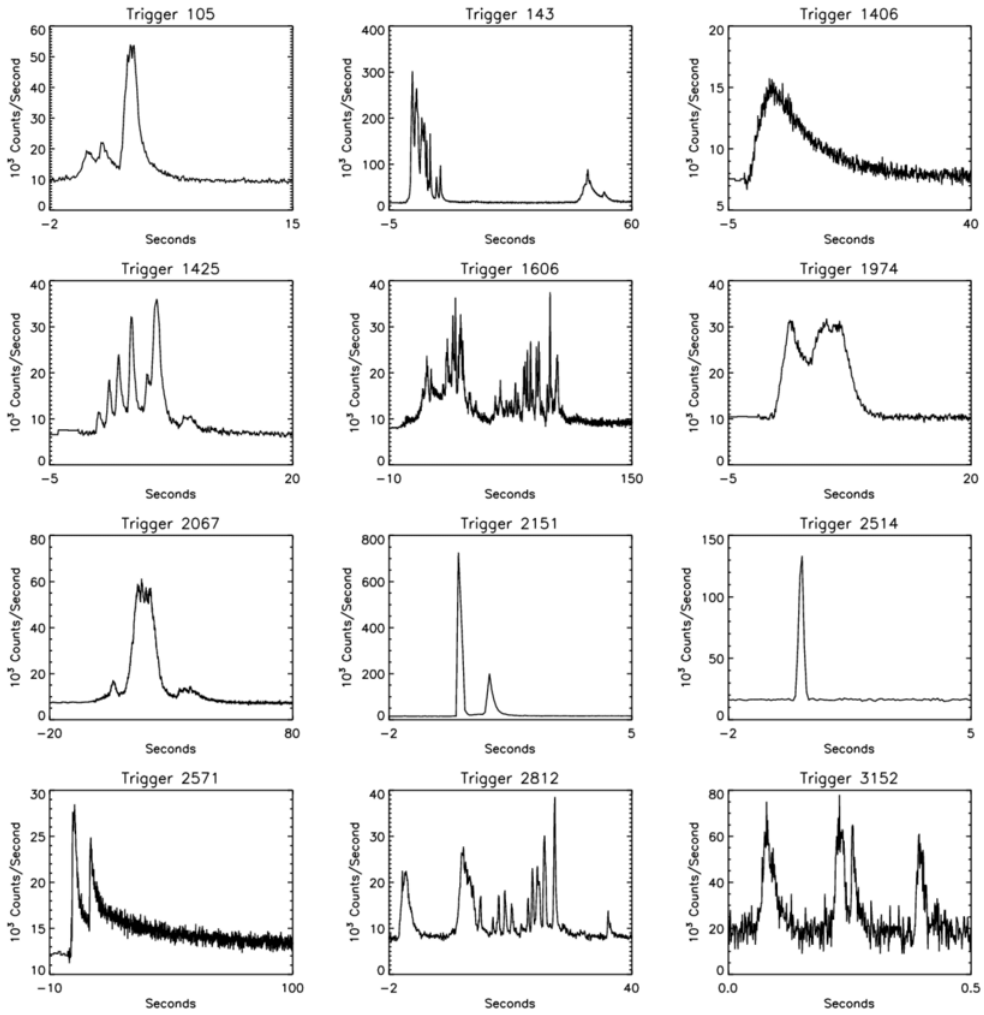

Figure 1.4: Samples of GRB measured light curves showing the rich variety of pulses (Credit: J.T. Bonnell (NASA/GSFC)).

$$I(t) = \begin{cases} A \exp\left[-\left(\frac{|t-t_{max}|}{\sigma_r}\right)^{\nu}\right] & \text{if } t < t_{max}; \\ A \exp\left[-\left(\frac{|t-t_{max}|}{\sigma_d}\right)^{\nu}\right] & \text{if } t > t_{max}. \end{cases} \tag{1.1}$$

where:

t_{max}	time of the pulse's maximum intensity
σ_r	rise time constant
σ_d	decay time constant
ν	pulse sharpness (low value corresponds to a more peaked pulse).

Finally, it should be mentioned that a *precursor* emission occurring tens to hundreds of seconds before the main prompt phase was reported for a small fraction of GRBs. The precursor signal is typically weaker and softer than the prompt emission. The fraction of GRBs showing this feature is dependent on the criteria used for determining the presence of a precursor and can vary from 3 to 20% [28, 41, 134].

1.2.2 *Prompt Emission Spectral Properties*

Most of the GRBs are described by a non-thermal spectrum which can be parameterized using for example a *Band* function [13]:

$$N_E(E) = \begin{cases} A\left(\frac{E}{100\ keV}\right)^{\alpha} e^{-E/E_0} & \text{if } (\alpha-\beta)E_0 \geq E; \\ A\left(\frac{(\alpha-\beta)E_0}{100\ keV}\right)^{\alpha-\beta} e^{\beta-\alpha}\left(\frac{E}{100\ keV}\right)^{\beta} & \text{if } (\alpha-\beta)E_0 \leq E. \end{cases} \tag{1.2}$$

where:

A	amplitude in photons $s^{-1}\ cm^{-2}\ keV^{-1}$
$E_{peak} = (2+\alpha)E_0$	peak energy in keV
α	spectral index at low energy
β	spectral index at high energy
100 keV	pivot energy

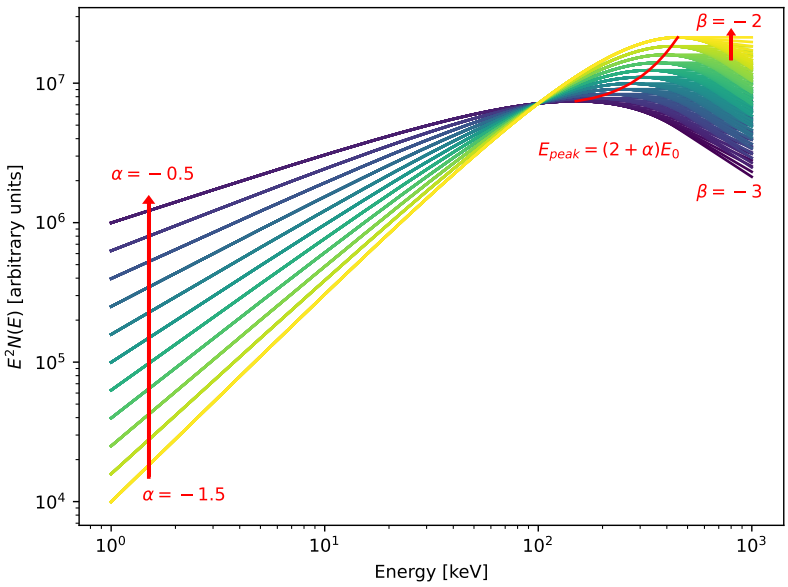

Figure 1.5: Band function plotted for different values of α and β, with $E_0 = 300\ keV$.

A widely used parameter is the energy E_{peak} at which the Spectral Energy Distribution (SED) $E^2N(E)$ is maximal. The SED of the Band function is plotted in Figure 1.5 for various values of α and β. The spectral indices reported by BASTE, Fermi, and Integral are in the interval $\alpha = -1 \pm 1$ and $\beta = -2^{+1}_{-2}$ [25, 183, 198, 232]. Depending on the GRB and on the width of the energy band of the instrument, the β parameter is not always well constrained and some bursts can be better described by a cutoff power-law (CPL) spectrum, as described in equation (4.1).

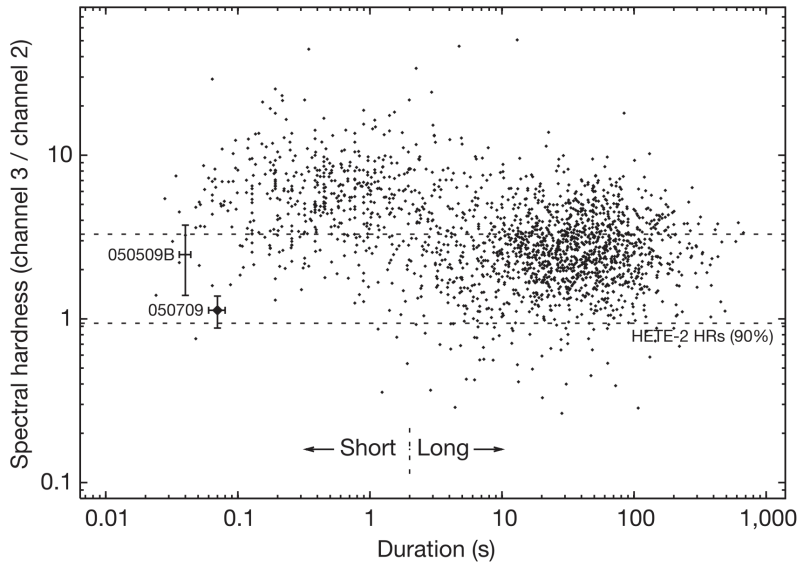

Figure 1.6: Spectral hardness versus burst duration from the BATSE catalog (taken from [102], with permission). Two clusters are clearly distinguishable: short hard GRBs and long soft GRBs.

As observed in the BATSE catalog (see Figure 1.6), short GRBs tend to have a harder spectrum than long bursts. The GRB spectrum is also time-dependent, with either a softening of the spectra during the entire prompt emission [188] or a hardening in the rising phase of the pulses and a softening in the decaying phases [85].

1.2.3 *GRB Distribution and Afterglow*

GRBs are uniformly distributed in the sky, as shown by the BATSE catalog skymap in Figure 1.7. The isotropic distribution of the GRBs from the BATSE catalog brought a hint that these sources are of extragalactic origin. But no precise measurement of the GRB distance was available at the time and the extragalactic nature of GRBs was not widely accepted at the time of the BATSE experiment.

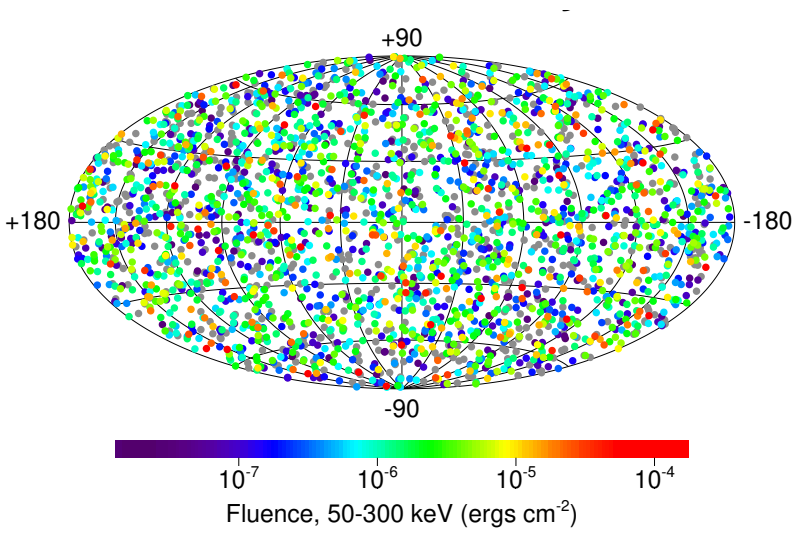

Figure 1.7: Skymap of the 2704 GRBs measured by BATSE (Credit: BATSE 4B Catalog, Michael S. Briggs). An isotropic distribution is clearly observed.

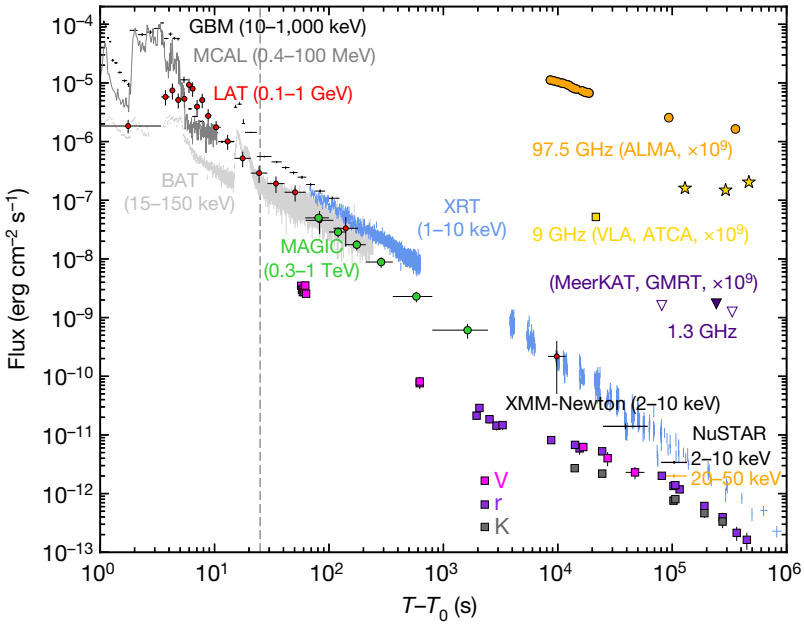

Figure 1.8: Light curve measured for GRB190114C by many instruments (taken from [5], with permission). The vertical dashed line indicates the separation between the prompt γ-ray emission and the afterglow observed in many bands.

Low-energy counterparts were difficult to find since even the strongest bursts measured by BATSE had an angular error of about 0.2°, which contains a lot of astronomical objects. It is only in 1997, thanks to the BeppoSAX instrument and its more precise localization capabilities, that an X-ray counterpart, the afterglow, was discovered for two GRBs [46]. This discovery also allowed us to find the optical and radio afterglow [71, 193]. The better localization accuracy of optical and radio instruments helped to identify the host galaxies of GRBs, definitely proving their extragalactic origin with the first GRB redshift measurement of $z = 0.835$ for GRB970508 [170]. The discovery of the afterglow of GRBs also

opened the field of GRB astrophysics to multi-wavelength observations, as shown for instance in the GRB190114C light curve plotted in Figure 1.8. The prompt emission of this long GRB is measured from 10 keV up to 1 GeV by several instruments among which Fermi-GBM/LAT and Swift-BAT. This is followed by the afterglow measured in very high energy γ-rays up to 1 TeV, as well as in X-ray, optical, and radio bands. These light curves show a good example of how different energy bands can be exploited to study different phases of the GRB emission. The creation of the Gamma-ray Coordinates Network (GCN), nowadays known as the General Coordinates Network, allows for rapid search of low-energy counterpart as soon as a GRB is detected by a γ-ray instrument and an alert is distributed.

1.2.4 *Progenitors*

Short and long GRBs are originated from different astrophysical sources. Long GRBs are associated with the death of very massive stars (supernovae, SN), while short GRBs are produced by neutron star-neutron star mergers and possibly neutron star-black hole mergers.

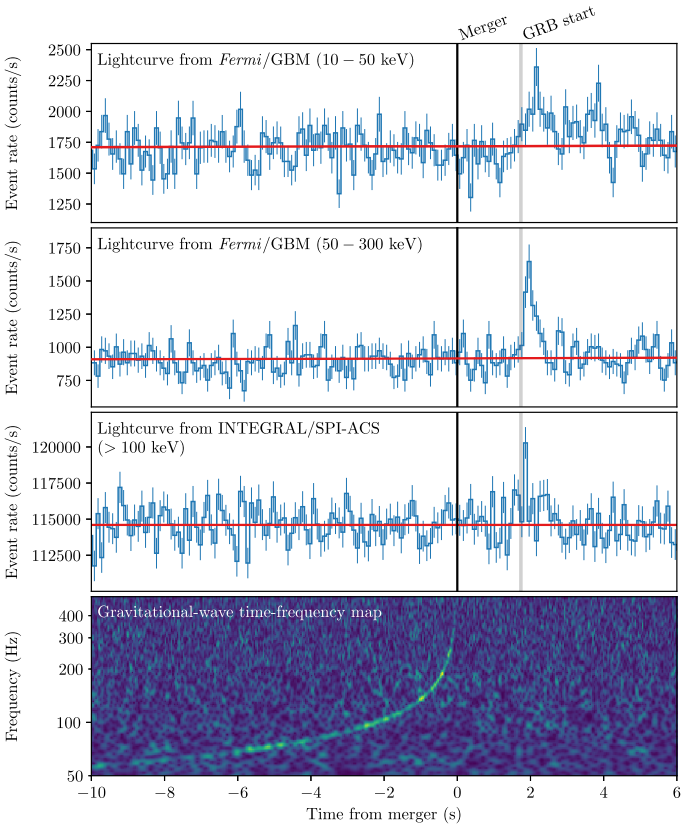

Figure 1.9: Multi-messenger detection of GW170817 by LIGO and GRB170817A by Fermi-GBM and INTEGRAL-SPI (taken from [4], with permission).

The association of long GRBs with supernovae was first hinted by the detection of GRB980425 by BeppoSAX within the angular error of a TypeIc supernova, SN1998bw [75, 138]. This was later confirmed by HETE-2 with the

GRB030329/SN2003dh association [101, 208]. A study has later shown that long GRBs are associated with the explosion of the most extremely massive stars by studying the location of over 40 lGRBs in their host galaxies [73].

Locating short GRBs within their host galaxy by measuring their afterglow was made possible by the Swift telescope and its γ-ray (BAT), X-ray (XRT), and optical/UV (UVOT) instruments. They were found to be located in different regions of their host galaxy compared to lGRBs, giving a clue that sGRBs are originated from different objects [14, 22, 80]. The origin of short GRBs was confirmed by the detection of GRB170817A as the electromagnetic counterpart of a gravitational wave (GW) event GW170817 [3, 4], showing the association of sGRBs with BNS. The joint detection of this GRB with a GW event, shown in Figure 1.9, opened the window on a new messenger to study GRBs.

1.2.5 *GRBs as a Probe to Fundamental Physics*

Gamma-ray bursts share interconnections with many fields of modern astrophysics. For instance, understanding the physics of the jets is not only important in the GRB field but also for other extreme phenomena such as blazars and Active Galactic Nuclei (AGNs). GRBs have links to stellar physics, compact objects, galactic astrophysics, or cosmology. GRBs are an ideal candidate to probe fundamental physics in so extreme conditions that they cannot be reproduced in the lab. Very high energy photons detected from GRBs, such as the up to 18 TeV γ-rays detected by the Large High Altitude Air Shower Observatory (LHAASO) from GRB221009A [105] (nicknamed the BOAT, for Brightest Of All Time), bring not only constraints on GRB physics but can also be a way to probe fundamental physics such as Lorentz Invariance Violation (LIV) [146], or to study Extragalactic Background Light (EBL). A discussion on the connections between GRB astrophysics and the other fields of astrophysics as well as the connection with physics in general is provided in [233]. A review of the links between GRBs and fundamental physics is given in [196].

1.2.6 *Polarization of the Prompt Emission*

Half a century after the publication of the first measured GRB, Gamma-Ray Burst astrophysics has become one of the hot topics of modern astrophysics. Even though the field of GRBs has seen a lot of important discoveries, many questions remain unanswered about these very powerful bursts. In particular, the emission mechanisms at play in these extreme sources are still poorly understood. Measuring the polarization of the prompt emission is thought to be a way to resolve the physics at the origin of GRB emissions. Although several missions measured the prompt polarization in the γ-ray band in the last two decades, as described in Section 3.1, these measurements are not enough to give a clear picture on the polarization of GRBs. The next section aims to summarize the key questions that measuring the polarization could solve, as well as the expected polarization in the main theoretical emission models.

1.3 THE ROLE OF PROMPT EMISSION POLARIZATION IN UNDERSTANDING GAMMA-RAY BURSTS

We discuss here how measuring the polarization of the GRB prompt emission can help answering key questions about their nature and composition. The composition and dynamics of the outflow are first addressed, followed by a discussion on the different energy dissipation scenarios and their related polarization levels. The expected polarization from the different existing emission models are then covered. Finally, the current scenarios for the angular structure of the relativistic outflow are explained. A review of the existing emission mechanisms and their corresponding linear polarization is given in [83], while [84] discusses both the polarization in the different models and how polarization can help solving the biggest open questions on GRBs. Figure 1.10 summarizes the expected ranges of polarization degree from different emission mechanisms, magnetic field configurations, and jet structure. Each of the configurations shown in this figure is discussed below.

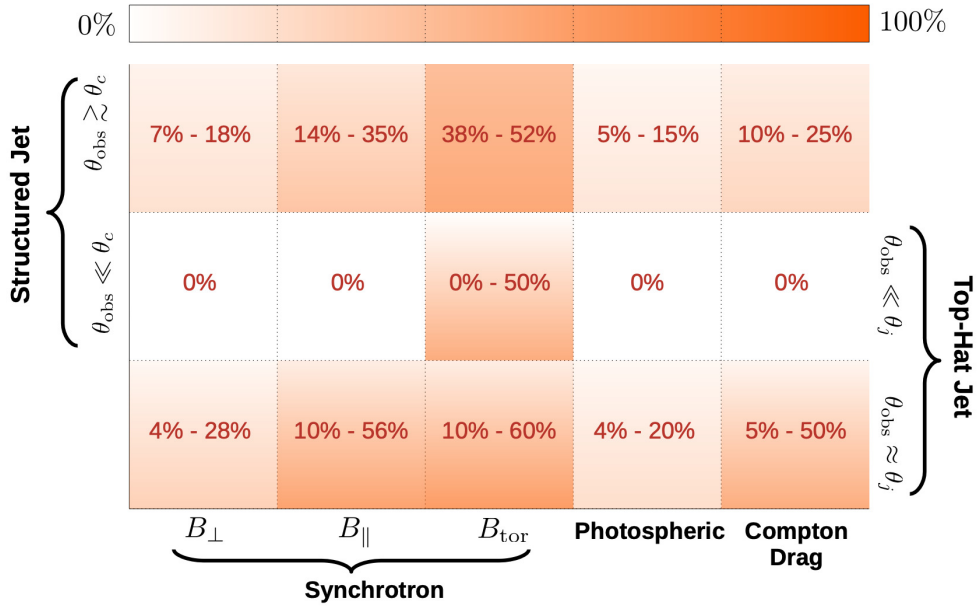

Figure 1.10: Expected polarization degree from different jet structures and emission models (taken from [84], with permission).

1.3.1 *Outflow Composition and Dynamics*

The composition of the relativistic[2] outflow is decisive as to the radiation and energy dissipation mechanisms. The leading theoretical configurations are that the outflow is either Kinetic Energy Dominated (KED) or Poynting Flux Dominated (PFD). In a KED scenario, the thermal energy is transferred to the cold baryons in the medium in the form of kinetic energy. In a PFD scenario, the acceleration and expansion of the outflow are dominated by the possibly ordered

2 The outflow needs to be relativistic in order to solve the *compactness problem* and explain how γ-rays can escape from the optically thick medium and reach us. [197]

magnetic field. The structure of the magnetic field has an impact on the polarization levels for both scenarios in the case of a synchrotron emission mechanism. Polarization measurements can therefore bring valuable information on the outflow composition. In order to quantify the contribution of the kinetic and magnetic field energies to the outflow composition, one can use the ratio of the magnetic field and matter enthalpy densities in the comoving frame, called *magnetization* and expressed as [83]:

$$\sigma \equiv \frac{w'_B}{w'_m} = \frac{B'^2}{4\pi\left(\rho' c^2 + \frac{\hat{\gamma}}{\hat{\gamma}-1}P'\right)} \tag{1.3}$$

where:

- B' magnetic field strength
- ρ' matter rest density
- c speed of light in vacuum
- $\hat{\gamma}$ adiabatic index: $4/3$ for a relativistic fluid, $5/3$ in the cold baryons limit
- P' pressure, negligible in front of the particle inertia in the cold baryon limit

All primed quantities are expressed in the comoving frame. For a KED outflow, we have $\sigma < 1$ and the magnetic fields are weak (with short coherence scale and random orientation) if not non-existing and do not play an important role in the dynamics of the outflow. For a PFD outflow, $\sigma > 1$ and the acceleration of the outflow is driven by the more ordered magnetic field.

A widespread example of KED outflow is the *fireball* model [86, 192], where the energy is contained near the central engine in a limited space. The outflow is optical thick with very high temperatures ($> MeV$) producing many electrons and positrons ($\gamma\gamma \rightarrow e^- e^+$) thereby intensifying the optical thickness. The radiation-dominated outflow is expanding because of tremendous radiation pressure, converting the thermal energy into kinetic energy. The outflow is cooling down as the adiabatic acceleration goes, with a temperature inversely proportional to the radius and a bulk Lorentz factor Γ increasing with the radial coordinate.

In PFD outflows, the magnetic field is propagating from the central engine with an angular coherence of $\theta_B > 1/\Gamma$, which also corresponds to the angle in which the radiation is beamed. No standard model exists for PFD outflows and many idealized Magneto-Hydro-Dynamic (MHD) models have been proposed [151, 156, 220].

1.3.2 *Energy Dissipation*

The energy dissipation mode is highly impacted by the composition of the outflow. The radial location at which the energy is dissipated rules the shape of the spectrum, together with the emission mechanism. The spectrum can have two components: a quasi-thermal and a non-thermal part. The non-thermal

component is generated by energy dissipation which happens in the optically thin parts of the outflow, while the quasi-thermal component comes from energy dissipation in the photosphere. The quasi-thermal component does not perfectly follow a black body spectrum because different parts of the jet are observed with different Doppler boosts.

In the case of a uniform outflow, with no significant variations within angular region $\lesssim 1/\Gamma$ (in the plane perpendicular to the outflow), the quasi-thermal component will have no significant polarization. On the other hand, outflow with angular structure can give moderate polarization levels ($\Pi \lesssim 20\%$) for the quasi-thermal part. The non-thermal component polarization is dependent on the radiation mechanism, the subject of the next section.

In the case of a KED outflow, the bulk Lorentz factor Γ is saturating after the rapid expansion of the fireball to values $\sim 10^2 - 10^3$ at a radius of $R_s \sim 10^9 - 10^{10}$ cm. Outside this radius ($R > R_s$), the kinetic energy is dissipated via internal shocks between shells catching up each other. The shells collision generates a forward shock going in the flow direction and accelerating the slower shells, while a reverse shock is also produced towards the faster shells, decelerating them. Part of the electrons are heated up by the shocks, keeping a fraction of the energy behind the shock. Another fraction of the internal energy density behind the shock is transferred to magnetic fields (of typical strength $B' \sim 10^2 - 10^3$ G) generated by the shock. The coherence length of these magnetic fields is much smaller than the angular size in which the radiation is beamed ($\theta_B \ll 1/\Gamma$), giving rise to limited polarization $\Pi \lesssim 30\%$. Furthermore, turbulence can be caused by interaction of the shocks with inhomogeneities in the density, amplifying an upstream magnetic field divided in multiple incoherent patches of highly ordered field. The polarization is averaging out over the patches to levels as low as $\Pi \lesssim 2\%$.

Alternatively, in PFD outflows, the energy dissipation occurs either via MHD instabilities or magnetic reconnection. Electrons are accelerated by magnetic field energy dissipation that occurs when field lines of opposite polarities reconnect. The electrons are then cooling down either by emitting synchrotron radiation or via inverse Compton scattering. The polarization can be energy dependent depending on the way particles are accelerated when the magnetic field energy is dissipated as the outflow becomes optically thin. Polarization as high as $\Pi \lesssim 60\%$ can be reached if the synchrotron process is dominating with a magnetic field coherence length $\theta_B \gtrsim 1/\Gamma$ (neaer the line of sight). Lastly, a common example of PFD model is the Internal Collision induced MAgnetic Reconnection and Turbulence (ICMART) model [234], where the central engine is ejecting highly magnetized shells which dissipate their magnetic energy via magnetic reconnection and turbulence induced by collisions between different magnetic shells. Three-dimensional MHD simulations of this model have shown a 90° rotation of the polarization angle between the first part and second part of the prompt light curve, with a trend for increasing polarization degree [59].

1.3.3 *Outflow Angular Structure*

The polarization of the prompt GRB emission is highly dependent on the angular structure of the outflow. The outflow in GRBs is beamed into bipolar jets. The rudimentary *top-hat* model, which consists of a uniform conical jet, can be parameterized as a function of the half jet opening angle θ_j [84]:

$$\frac{L'_{\nu'}(\theta)}{L'_{\nu',0}} = \frac{\Gamma(\theta)}{\Gamma_0} = \begin{cases} 1 & \text{if } \theta \leq \theta_j; \\ 0 & \text{if } \theta > \theta_j. \end{cases} \tag{1.4}$$

The comoving spectral luminosity $L'_{\nu'}$ is described by a Heaviside function, mimicking the sharp edges of the jets with a uniform luminosity inside the outflow and a null luminosity outside. A useful parameter to characterize the line of sight of the observer with respect to the edge of the beam is $q \equiv \theta_{obs}/\theta_j$, which is null when the beam is aligned with the Line Of Sight (LOS) of the observer (on-axis) and equal to 1 when the observer is looking toward the edge of the jet. The quantities indexed with a 0 are therefore on-axis quantities ($q = 0$), namely the on-axis comoving spectral luminosity $L'_{\nu',0}$ and the on-axis bulk Lorentz factor Γ_0.

θ_{obs} is the angle at which the observer is placed, or viewing angle.

Top-hat jets (THJs) are of course very idealized and a more complex jet parametrization with smoother edges seems more realistic. As a first correction, the core of the jet is kept to have a uniform brightness, but with smoothly decaying *wings* [83]. Two types of decays are commonly considered: *exponential wings* described in equation (1.5), and power-law rings described in equation (1.6).

$$\frac{L'_{\nu'}}{L'_{\nu',0}} = \begin{cases} 1 & \text{if } \xi \leq \xi_j; \\ \exp\left[\left(\sqrt{\xi_j} - \sqrt{\xi}\right)/\Delta\right] & \text{if } \xi > \xi_j. \end{cases} \tag{1.5}$$

$$\frac{L'_{\nu'}}{L'_{\nu',0}} = \begin{cases} 1 & \text{if } \xi \leq \xi_j; \\ \left(\frac{\xi}{\xi_j}\right)^{-\delta/2} & \text{if } \xi > \xi_j. \end{cases} \tag{1.6}$$

In these two cases, the emission either drops exponentially or as a power law outside the uniform core of the jet, and even though the spectral luminosity is allowed to vary with θ ($\xi_j \equiv (\Gamma\theta_j)^2$) the dynamics of the jet does not ($\Gamma(\theta) = \Gamma_0$).

The cases considered above were not truly structured jets, but uniform jets with smoother edges. The dynamics of the jet and therefore the bulk Lorentz factor must also be angle-dependent in structured jets. The radial dependence of both the comoving spectral luminosity and the bulk Lorentz factor can typically be described by either a Gaussian or a Power-Law [83]. Such jets are respectively called *Gaussian Jets* (GJs) and *Power-Law Jets* (PLJs), expressed in equations (1.7) and (1.8).

$$\frac{L'_{\nu'}(\theta)}{L'_{\nu',0}} = \frac{\Gamma(\theta) - 1}{\Gamma_c - 1} \propto \exp\left(-\frac{\theta^2}{2\theta_c^2}\right) \tag{1.7}$$

$$\frac{L'_{\nu'}(\theta)}{L'_{\nu',0}} = \Theta^{-a}\,, \quad \frac{\Gamma(\theta)-1}{\Gamma_c - 1} = \Theta^{-b}\,, \quad \Theta \equiv \sqrt{1+\left(\frac{\theta}{\theta_c}\right)^2} \tag{1.8}$$

Quantities indexed with a "c" correspond to the compact core of the jet: θ_c is the core angle and Γ_c is the bulk Lorentz factor in the core of the jet. In the case of a truly structured jet, we conveniently define q as $q \equiv \theta_{obs}/\theta_c$. Depending on the emission mechanisms, uniform or structured jets can imply different levels of polarization, as will be discussed in the next section.

1.3.4 *Radiation Mechanism*

We discuss here the two main radiation mechanisms proposed for explaining the GRB emissions, namely the synchrotron and photospheric models. Other models, such as the Compton drag model [140], self-synchrotron Compton (SSC), or jitter radiation are also proposed in the literature. A review can be found in [84].

1.3.4.1 *Synchrotron Emission Models*

One of the leading radiation mechanism scenario for GRBs is synchrotron emission, happening when relativistic electrons are gyrating in a magnetic field and emit synchrotron photons to cool down. As GRBs are point sources, the polarization measured on Earth is integrated over the entire source image and cannot be spatially resolved. The observed polarization can therefore be affected by the LOS of the observer with respect to the axis of the jet, but also by the geometry of the jet and the configuration of the magnetic field. Four magnetic field configurations are typically considered in the literature [83]:

- Ordered magnetic field $\mathbf{B_{ord}}$ with an angular coherence length bigger than the beaming cone but very small in front of the jet aperture ($1/\Gamma \lesssim \theta_B \ll \theta_j$).
- Random ($\theta_B \ll 1/\Gamma$) magnetic field $\mathbf{B}_\perp$ oriented in a plane orthogonal to the local velocity of the flow.
- Ordered magnetic field $\mathbf{B}_\parallel$ aligned with the local velocity of the flow, opposite scenario to $B_\perp$.
- Globally ordered toroidal[3] magnetic field $\mathbf{B_{tor}}$ with a symmetry around the jet symmetry axis. This configuration implies a high magnetization.

GRBs are distant point sources and their image cannot be resolved in the γ band with current technologies. Furthermore, the emission being relativistic, the observed polarization is seen integrated over the beamed $1/\Gamma$ part of the jet. By integrating over the observed GRB image, a non-axisymmetric jet, i.e. not

3 There is also a poloidal component to the magnetic field, B_{pol}, whose flux decreases with the radial distance squared. The contribution of the poloidal field is negligible at large distances as the toroidal flux only decreases linearly with the distance.

symmetric around the viewing axis, would naturally lead to a finite polarization level. Non-axisymmetric jets composed of many mini-jets or patches have recently been proposed [81] to explain observations of continuously evolving polarization angle (PA), while axisymmetric jets can only generate a switch of 90° in the PA. In the case of symmetry around the axis, a possible break of symmetry that would result in a net polarization is when the LOS is near the edge of the jet. We now discuss the expected polarization from synchrotron emission with the different magnetic field configurations described earlier. Assuming a power-law distribution of the electrons generating the synchrotron photons, the maximum local polarization for a locally ordered magnetic field depends on the local spectral index $\alpha(\nu) = -d\log F_\nu / d\log\nu$:

$$\Pi_{max} = \frac{\alpha + 1}{\alpha + 5/3} \tag{1.9}$$

The effective power-law index of the electron distribution can be expressed as $p_{eff} = 2\alpha + 1$. For optically-thin synchrotron emission, $\alpha \geq -1/3$, which implies that the maximum local polarization cannot be lower than 50%. The maximum local polarization is constrained to $\Pi_{max} \lesssim 75\%$ from shock-acceleration theory. In the case of a tangled magnetic field on small angular scales ($\ll \Gamma$), the local degree of polarization (on a given point of the ultrarelativistic thin shell) obtained when averaging over the random directions of the magnetic field with the assumption $\alpha = 1$ is given by:

$$\frac{\bar{\Pi}_{rnd}}{\Pi_{max}} = \frac{(b-1)\sin^2\tilde{\theta}'}{2 + (b-1)\sin^2\tilde{\theta}'} = \begin{cases} \frac{-\sin^2\tilde{\theta}'}{1+\cos^2\tilde{\theta}'} & \text{if } b = 0 \ (B \to B_\perp); \\ 1 & \text{if } b \to \inf \ (B \to B_\parallel). \end{cases} \tag{1.10}$$

where $\tilde{\theta}'$ is the polar angle in the comoving frame measured from the LOS, and $b = 2\langle B_\parallel^2\rangle / \langle B_\perp^2\rangle$ is a parameterization of the level of anisotropy of the magnetic field expressed as the ratio of magnetic field average energy density in the $\parallel$ and $\perp$ directions.

Polarization maps showing the polarized intensity (black double arrows) and polarization levels (color map) over the jet surface in the case of a uniform (top-hat) jet are plotted in Figure 1.11 for the four magnetic field configurations discussed earlier. The measured polarization information is contained in the red circled area, which corresponds to the beaming cone towards the LOS of the observer. The maps are centered around the axis of symmetry of the jet. For axisymmetric jets, the polarization maps show a symmetry around the axis linking the LOS and the symmetry axis of the jet. Either this direction or the direction orthogonal to it (the plotted maps use the latter convention) can therefore naturally be chosen to define an origin for the local polarization angle $\bar{\theta}_p$. The base for polarization is therefore vertical/horizontal, which implies that the Stokes parameter $U \propto \sin(2\bar{\theta}_p)$ is null and that the polarization intensity is fully given by the Stokes parameter $Q \propto \cos(2\bar{\theta}_p)$. Depending on the B-field

Stokes parameters are used to describe polarization, as later discussed in Chapter 2.

configuration, the local polarization angle in the ultrarelativistic limit $\Gamma \ll 1$ can be expressed as [83]:

$$\bar{\theta}_p = \begin{cases} \varphi_B + \arctan\left[\left(\frac{1-\tilde{\zeta}}{1+\tilde{\zeta}}\right)\cot\varphi_B\right] & \text{for } B_{ord}; \\ \tilde{\varphi} & \text{for } B_{\perp}; \\ \begin{cases} 0 & \text{if } \bar{\Pi} > 0 \\ \pi/2 & \text{if } \bar{\Pi} < 0 \end{cases} & \text{for } B_{\parallel}; \\ \tilde{\varphi} - \arctan\left[\left(\frac{1-\tilde{\zeta}}{1+\tilde{\zeta}}\right)\frac{\sin\tilde{\varphi}}{\tilde{\theta}/\theta_{obs}+\cos\tilde{\varphi}}\right] & \text{for } B_{tor}. \end{cases} \tag{1.11}$$

where $\tilde{\varphi}$ and $\tilde{\theta}$ are respectively the azimuthal and polar angles measured with respect to the LOS, and φ_B is the azimuthal angle of the globally ordered magnetic field in the case of B_{ord}.

The different magnetic structures lead to very different polarization maps with regions contributing either along the line that links the jet's axis of symmetry to the LOS (with local polarization $\bar{\Pi} < 0$, orange on the color maps), or in the transverse direction (with $\bar{\Pi} > 0$, white color on the maps). As mentioned before, one can notice that when averaging over the GRB image for axisymmetric jets, two directions of polarization are possible, only allowing for discrete 90° changes in polarization angle.

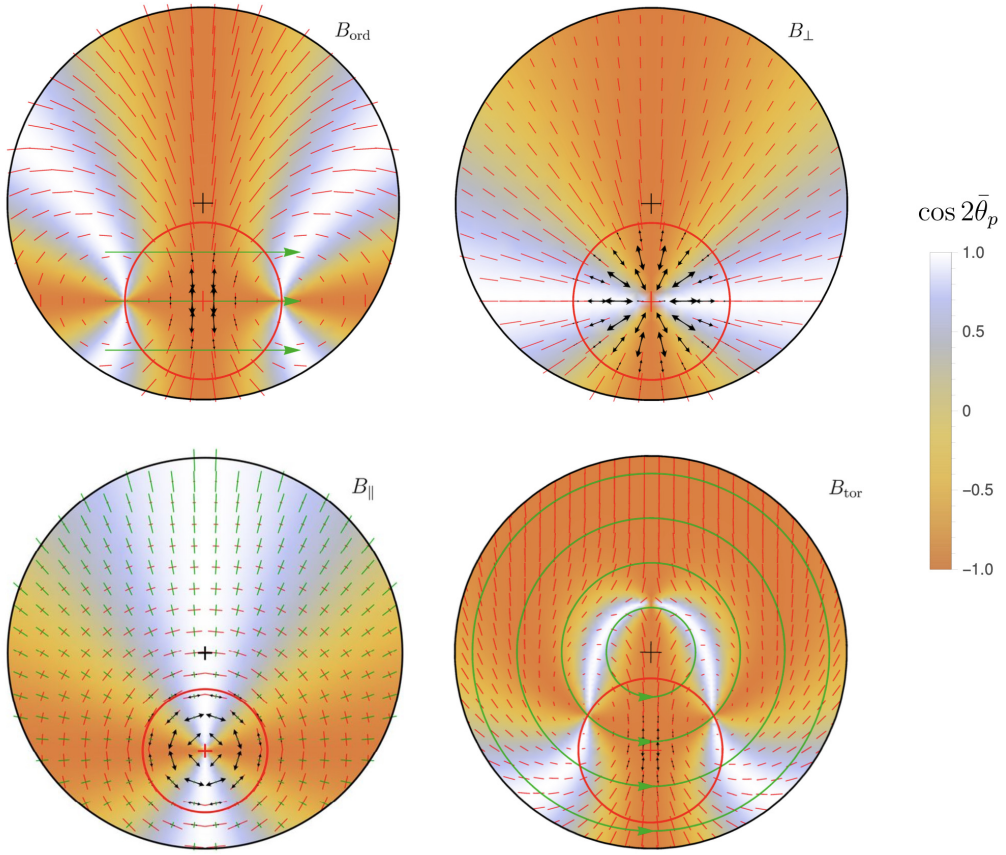

Figure 1.11: Polarization maps for different magnetic field configurations (taken from [84], with permission). The black + symbol shows the axis of symmetry of the jet, while the red one (+) is the LOS. The red circle is the beaming cone, and the polarized intensity is shown with the black double arrows. The red segments show the polarized intensity without the relativistic beaming effects. The green lines are the direction of the magnetic field lines for the locally ordered B_{ord} and B_{tor} fields.

The symmetry around the LOS in the polarization maps of Figure 1.11 is dictating the level of polarization obtained when averaging on the image of the GRB in the sky. In the case of $B_{\parallel}$ and $B_{\perp}$, the beamed image is symmetric around the LOS, leading to a null averaged net polarization $\Pi = 0$. This symmetry is broken when the magnetic field is locally ordered and the polarization vectors align transverse to it, implying a finite net polarization $|\Pi| > 0$. If part of the beaming cone is outside the jet surface, that is the LOS is near the edge of the jet, the symmetry can also be broken yielding a net finite polarization as well. The sign of the polarization Π is dictated by whether the polarized intensity is horizontally or vertically aligned. A vertical alignment implies a negative Π (-Q), corresponding to the orange part of the polarization maps. On the other hand, a horizontal alignment implies $\Pi > 0$ (+Q), corresponding to the white part of the maps.

See Chapter 2 for discussion on Stokes parameters $\pm Q$.

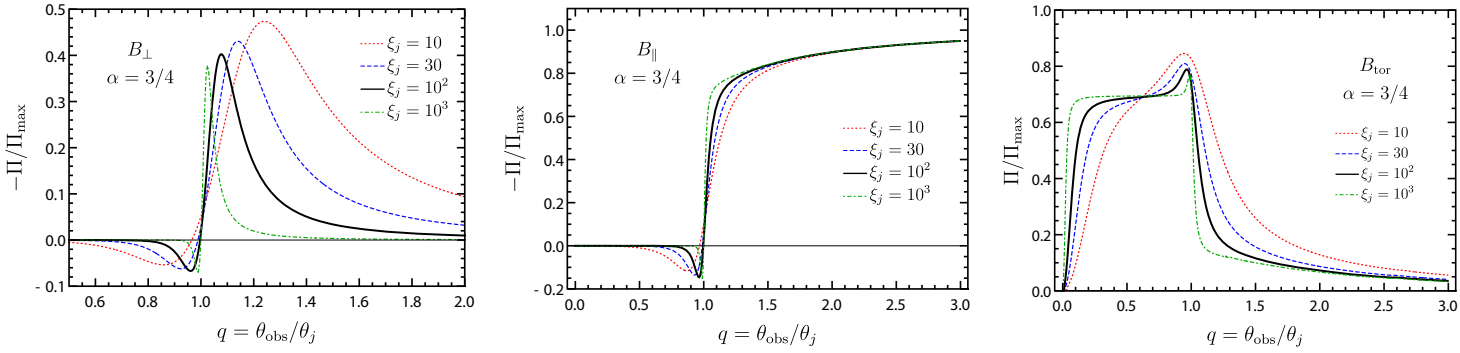

Figure 1.12: Polarization obtained for synchrotron emission as a function of q for different cone aperture ξ_j of a top-hat jet. The curves are plotted for a spectral index of $\alpha = 3/4$ (polarization increases with α) and for different magnetic field configurations, namely $B_\perp$ (**left**), $B_\parallel$ (**center**), and B_{tor} (**right**) (taken from [84], with permission).

Figure 1.12 gives the polarization as a function of q for the $B_\perp$, $B_\parallel$, and B_{tor} configurations and for a top-hat jet. The curves are plotted for different cone aperture to beaming aperture ratios (ξ_j) and for a spectral index $\alpha = 3/4$ (the net polarization is increasing with the spectral index, as shown in [83]). When the LOS is aligned with the jet axis (q=0), the net polarization is null in all cases. It then grows slowly for $B_\perp$ and $B_\parallel$, and rapidly for B_{tor}. The polarization reaches a local maximum when the LOS is near the edge of the jet, and then declines sharply only for $B_\perp$ and B_{tor}. The polarization keeps increasing when going off-axis from the jet for $B_\parallel$, which is less likely to observe since the luminosity sharply drops after the edge for the top-hat case. At the edge of the jet (for $q = 1$), the net polarization is null and a 90° flip in the PA occurs. As for a uniform jet GRBs can only be observed for $q < 1$, the field configuration for which the highest polarization degree can be expected is B_{tor} with $50\% \lesssim \Pi \lesssim 65\%$, while most of the GRBs would show low levels of polarization for the $B_\perp$ and $B_\parallel$ configurations.

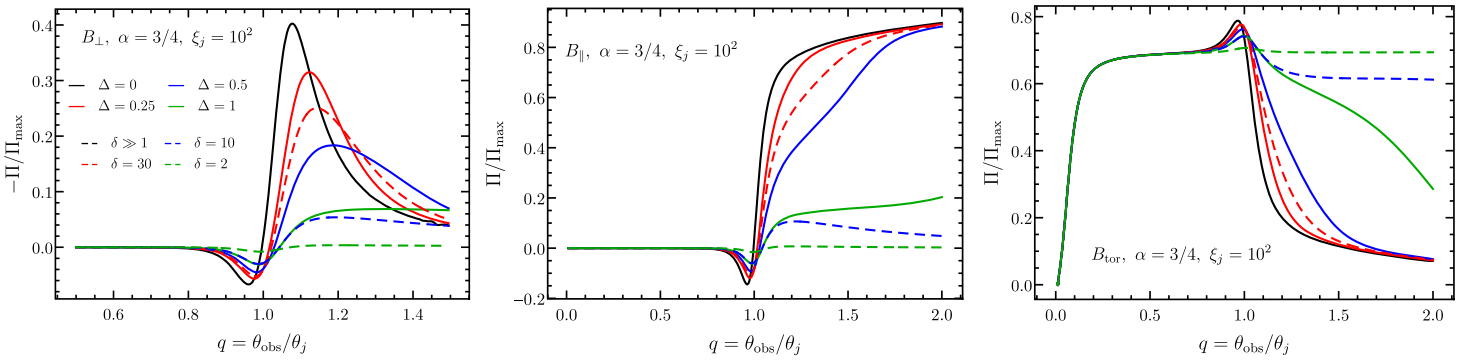

Figure 1.13: Polarization obtained for synchrotron emission as a function of q for a top-hat jet with exponential (solid lines) or power-law (dashed lines) wings. The curves are plotted for a spectral index of $\alpha = 3/4$, a relative cone aperture $\xi_j = 10^2$, and for different magnetic field configurations, namely $B_\perp$ (**left**), $B_\parallel$ (**center**), and B_{tor} (**right**) (taken from [84], with permission).

Figure 1.13 shows the polarization as a function of q for the $B_\perp$, $B_\parallel$, and B_{tor} configurations and for a smoothed top-hat jets with exponential and power-law wings (see equations (1.5), (1.6)). A similar behavior is observed for all B-field configurations when the LOS lies inside the jet ($q < 1$). Nevertheless, the fluence does not drop as sharply anymore when going out of the jet, which makes the polarization at $q > 1$ detectable as GRBs seen off-axis can now be detected. For $B_\perp$ and $B_\parallel$, which showed a symmetric beam image for $q < 1$, the polarization outside the jet decreases as the jets are made smoother. For B_{tor}, the opposite behavior is observed, with a polarization level outside the jet increasing with the smoothness of the edge of the jet. This implies similar observable polarization than for the standard top-hat jet, that is a low level of polarization for $B_\perp$ and $B_\parallel$ and a higher level for B_{tor}, the only difference being now that off-axis GRBs can be observed with smoother jet edges.

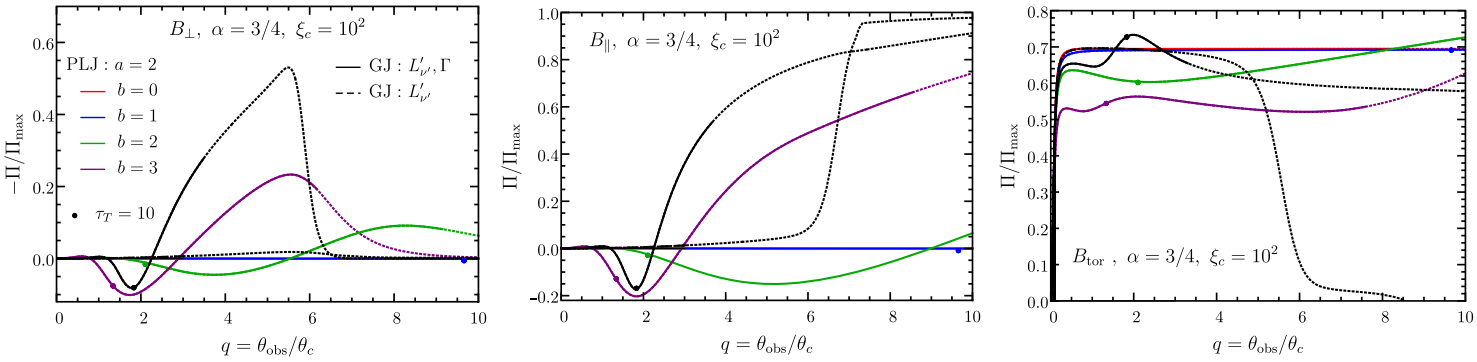

Figure 1.14: Polarization obtained for synchrotron emission as a function of q for a structured jet, namely gaussian jet (black lines) and power-law jet (colored lines). The curves are plotted for a spectral index of $\alpha = 3/4$, a relative cone aperture $\xi_j = 10^2$, and for the $B_\perp$ (**left**), $B_\parallel$ (**center**), and B_{tor} (**right**) magnetic field configurations (taken from [84], with permission). A dot • shows the angular position at which the Thomson optical depth is $\tau_T = 10$.

Finally, the polarization level for a structured jet are shown in Figure 1.14 as a function of q and for the same three field configurations as before. The overall shape of the polarization curves are similar to the top-hat and smooth top-hat curves, except that the curves are now expanding toward much higher viewing angles. Polarization can thus be reasonably measured also for far off-axis LOS as the drop in fluence is not as dramatic as for the previous cases. The polarization curves of Figure 1.14 change from solid line to dashed lines when the fluence measured off-axis drops below 1% of that measured on-axis, making the polarization barely measurable. Other limitations exist on the detectability of off-axis jets because of compactness [83], depicted by the dot • on the polarization curves which shows the q at which the Thomson optical depth of electron positron pairs produced by $\gamma\gamma$ interactions becomes greater than 10. For $\tau_T > 10$, the opacity starts to be a problem and the γ-ray emission is not longer possible. This limits observations to jets for which the LOS is not too dramatically outside the bright core, i.e. $q \lesssim 2$. Polarization is consequently limited to $\Pi \lesssim 20\%$ for $B_\perp$ and $B_\parallel$, while it is expected to be much higher for B_{tor}.

1.3.4.2 *Photospheric Emission Model*

If we consider an optically thick flow (because of high $e^{\pm}$ pairs production) adiabatically expanding under its own pressure. The radiation comoving energy density is dominant over the magnetic field energy density, that is $3L_\gamma/16\pi R^2\Gamma^2 c \gg B'^2/8\pi$, such that relativistic electrons and positrons mainly cool down through *inverse-Compton scattering*. The soft seed photons gain energy by getting upscattered by the electrons. The resulting energy of the upgoing photons can be expressed as $E' = (4/3)\gamma_e^2 E'_s$, where E'_s is the initial energy of the seed photons and γ_e is the Lorentz factor of the incoming electrons/positrons. The seed photons undergo multiple scatterings until the Thomson optical depth becomes $\tau_T < 1$ and radiation decouples with matter at the *photosphere*. The bulk factor increases linearly as the fireball expands $\Gamma(r) \propto r$ until all the initial energy is transferred to baryon kinetic energy. The bulk LF is then constant and the medium becomes optically thin at the photospheric radius r_{ph}. This process is known as *Comptonization* and is at the origin of a class of proposed models called *photospheric emission* models.

If a fireball passively expands without any energy dissipation, it would lead to a quasi-thermal spectrum which disagrees with observations. Instead, sub-photospheric dissipation is thought to play a crucial role to explain the low energy part of the observed spectra. But dissipation above the photosphere through inverse-Compton scattering is also needed in order to explain the non-thermal nature of the high energy part of the spectra. A Comptonized spectrum for a uniform outflow would lead to negligible polarization levels because of the random orientations of the polarization vectors, while an angular structure in the jet would lead to moderate polarization levels of $\Pi \lesssim 20\%$ [83, 154].

Compared to synchrotron models, Comptonization has the potential of explaining a wider range of low energy spectral slope and can yield narrower spectral peaks than synchrotron more consistent with observations [84]. This is however still debated as proper synchrotron spectra fitting accounting for electron cooling seems to be able to reproduce the observed time resolved spectra of most of the GRBs [27].

When energy is dissipated below the photosphere, the spectral peak is dominated by photospheric emission. At the photosphere the radiation is decoupled from matter and travels to the observer. If the outflow is matter dominated, that is if the baryon rest mast energy density dominates ($\rho' c^2 \gg 3L_\gamma/16\pi R^2\Gamma^2 c$), the radiation at the photosphere is highly anisotropic, yielding finite local polarization that vanishes when averaging over the source image. A net polarization can be obtained if the flow shows non-homogeneous structures with gradients in the bulk LF, as discuss later. If the outflow is radiation dominated ($\rho' c^2 \ll 3L_\gamma/16\pi R^2\Gamma^2 c$), the isotropic radiation field in the optically thick part of the outflow stays isotropic after the decoupling as scattering as no effect on the isotropy of the field. The local polarization therefore stays negligible before and after radiation decouples from matter.

Having a structured jet can yield to higher polarization levels. This has been shown in [83] by radially integrating the radiation transfer equations for a jet with angular structure in the bulk LF and comoving emissivity. The resulting polarization levels as a function of q are given in Figure 1.15 where polarization levels of $\Pi \lesssim 15\%$ are achieved for steep gradients in Γ. Monte Carlo simulations of the photospheric emissions were also performed for axisymmetric relativistic outflows [115, 154]. These works have shown that for steep gradients of Γ, polarization levels of $\Pi \lesssim 10\%$ can be expected outside the core of the flow with $\Gamma\theta_c \approx 10$. Higher levels of polarization $\Pi \lesssim 40\%$ can be obtained for (less realistic) narrower jets with $\Gamma\theta_c \approx 1$. More complex two dimensional hydrodynamic simulations have also been carried out [194], showing low levels of polarization $\Pi \lesssim 2.5 - 5\%$ with either steady or time evolving PA depending on the cases.

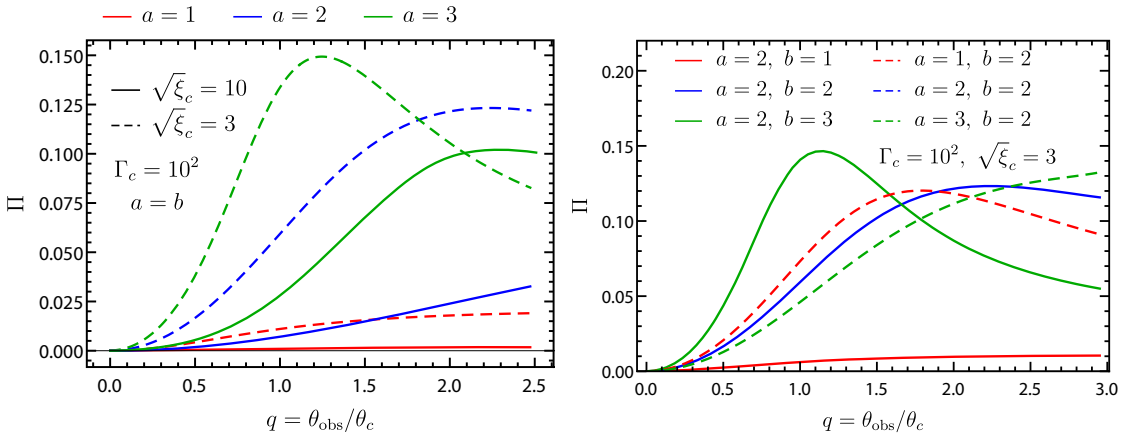

Figure 1.15: **Left:** Polarization obtained for photospheric emission as a function of q for a structured power-law jet compared for narrow ($\sqrt{\xi_c} = 3$) and wide ($\sqrt{\xi_c} = 10$) jets (taken from [83], with permission). **Right:** Polarization obtained for photospheric emission as a function of q for a narrow structured jet for different power-law jet parameters (taken from [83], with permission).

1.3.5 *Time and Energy Dependence of Polarization*

As discussed in the previous sections, measuring the polarization of the prompt emission of GRBs can bring information about the emission mechanisms as well as the jet and magnetic field structure of the bursts. The polarization measured from a GRB is integrated over the entire image of the source in the sky, but can vary with time and with energy. While the time and energy integrated polarization was discussed until now, we detail here how polarization can change in time and with energy and what additional understanding temporally and spectrally resolved polarization measurements can provide.

Because of the statistically demanding nature of polarimetric measurements, past experiments were already limited by the acquired statistics for energy and time integrated measurements. But with the upcoming polarimetric missions in the γ-ray band with great improvements in sensitivity, time and energy resolved polarization measurements start to become realistically possible. Time

and energy dependent polarization models have therefore recently started to be developed. Such energy and time resolved theoretical models do not yet exist for all the emission mechanism models.

Time resolved synchrotron models of the prompt emission polarization for different jet structures, magnetic field configurations, and outflow dynamics, are presented in [82]. A wide variety of polarization temporal evolution profiles can be expected from different jets and B-fields, also depending on the light curve structure (single or multiple pulses). The radiation is considered to be emitted in the radial range $R_0 \leq R \leq R_f \equiv R_0 + \Delta R$. In a top-hat jet for $q \equiv \theta_{obs}/\theta_j < 1$, as for the time integrated case the ordered B_{tor} field is expected to provide the highest polarization degree (as high as $\Pi \lesssim 75\%$), all along the pulse duration. For the $B_\perp$ and $B_\parallel$ fields, the polarization is initially null until the observer reaches the nearest edge of the jet, time at which the polarization starts increasing to $\Pi \lesssim 15\%$. The polarization levels continue to grow in the tail of the pulses, where the statistics is likely too poor for measuring the polarization of the source. Only 90° flips in the PA are observed during the pulses for axisymmetric jets, for some B-field configurations (B_{tor}) even several times during the emission. This change in the PA only occurs in the tail of the pulse, making the detection of such a change highly challenging. Non-axisymmetric jets are needed to explain gradual changes in the PA [81]. Going off-axis ($q > 1$), high polarization levels can be measured from the start of the emission, but the low fluence at these viewing angles makes the detection difficult. Very different polarization levels can be obtained with time resolved (single or multiple pulse) models than the levels obtained with the time integrated models.

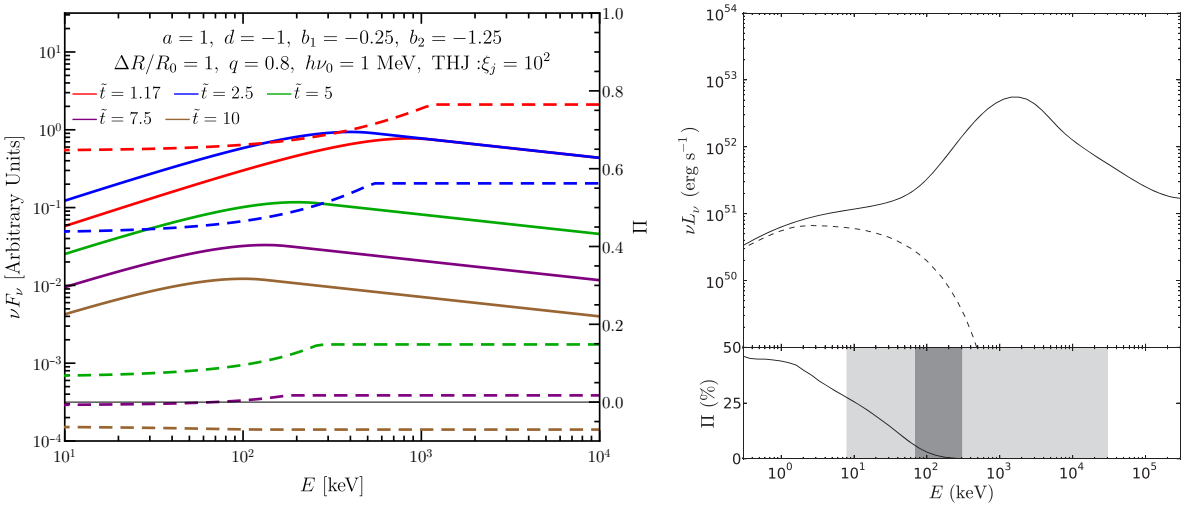

Figure 1.16: **Left:** Temporal evolution of the Band-like spectrum (solid lines) and its corresponding polarization (dashed lines) for a top-hat jet with B_{tor} synchrotron emission (taken from [83], with permission). **Right:** Multi-component spectrum and its corresponding polarization degree as a function of energy simulated for GRB990123 (taken from [155], with permission). The shaded area corresponds to the energy ranges of the Fermi-GBM and GAP instruments.

If optically thin synchrotron is the main emission mechanism responsible for the GRB prompt emission, the local polarization degree is obviously energy dependent from equation (1.9). The energy-dependent spectro-polarimetric evolution for synchrotron emission is shown on the left of Figure 1.16. The polarization increases at the peak energy, where the spectral index changes when expressed as a typical Band spectrum. As the spectrum (and the polarization as discussed earlier) evolves with time, the temporal evolution and energy dependence of the prompt emission polarization are linked to the temporal evolution of the spectrum.

If the local polarization degree does not directly depend on energy, for instance in the case of the Compton drag model [84, 140], the energy-independent polarization would still depend on the spectral index. Different spectral indices would weight differently the regions of the GRB image. These regions would be Doppler boosted such that they have different comoving energies although their observed energy is the same.

Finally, a hybrid spectrum with contributions from different radiation mechanisms would lead to different polarization levels in different energy bands. This is the case for the photospheric model presented in [155], where the spectral peak region is dominated by a quasi-thermal photospheric component while the low and high energy parts are non-thermal and can be generated by synchrotron emission. In this such a case, as shown on the right plot of Figure 1.16, the polarization would vanish near the spectral peak.

1.4 SUMMARY AND OUTLOOK

As one of the most, if not the most, energetic electromagnetic phenomenon in the Universe since the Big Bang, gamma-ray bursts are a very interesting case for studying physics in extreme environments. Discovered half a century ago, GRBs are still a hot topic of modern astrophysics as many mysteries remain on the mechanisms responsible for these powerful emissions. Despite many groundbreaking discoveries about their timing, spectral, and localization properties, a lot of questions still remain to be answered as for the jet composition, magnetic field structure, and emission mechanisms at play in GRBs.

GRBs are extragalactic transient sources emitting a prompt γ-ray emission followed by a multi-wavelength afterglow, from radio up to TeV energies. The bursts can be classified into two categories based on whether their prompt emission lasts longer or shorter than 2 seconds. Short GRBs, originated by binary neutron star mergers, tend to have a harder spectrum than long ones, associated with the death of very massive stars.

Half a century after the first publications about GRBs, a lot has been learned about these events thanks to many studies in temporal, localization, and spectral studies, as well as multi-wavelength detections. Nevertheless, a lot of questions remain unanswered about the structure and physical origin of these very powerful emissions. Polarization of the prompt γ-ray emission has been theorized as a very powerful tool to solve many of the remaining points on GRBs.

Polarization measurements can not only bring information on the dynamics, composition, and angular structure of the outflow, but they can also help to disentangle between the existing emission models and bring information about the sites and mode of energy dissipation in the bursts. The two main processes proposed to explain the observed spectral and polarization properties of the GRB prompt emissions are the synchrotron process and inverse-Compton scattering. In the former, electrons gyrating in magnetic fields will emit high-energy photons, the polarization levels of the emission being highly dependent on the configuration of the magnetic field. In the latter, relativistic $e^{\pm}$ are transferring part of their kinetic energy to seed photons from the medium through inverse Compton scattering, which in turn undergo multiple Compton scatterings until the expanding outflow becomes optically thin, at the photosphere. The decoupled photons can then freely travel towards the observer. Typically, higher polarization levels are expected from synchrotron emission than from photospheric emission. Time and energy evolution of the polarization are also very powerful tools for understanding GRBs, but theoretical work on this has only been recently started.

Polarization measurements are very challenging due to the high statistics required to determine such a quantity, the low statistics usually available at high energies, and the low efficiency of polarimeters. Advanced detection techniques have therefore been developed in the past decades in order to assess the polar-

ization of high-energy photons. The formalism of polarization as well as the state of the art of high energy polarimetry are introduced in the next Chapter.

2

HIGH ENERGY POLARIMETRY

The study of the universe naturally started with the observation of optical light, directly observable by the human eye. It is only over the last century that observations were extended to other wavelengths (Infra Red, Ultra Violet, Radio Waves, X/γ-rays) and messengers (Cosmic Rays, Neutrinos, Gravitational Waves), opening new fields of research in astrophysics. High energy astrophysics, focusing on X and γ-rays, is one of them and saw a rapid expansion in the last decades thanks to the development of new types of instrumentation and the possibility of sending scientific payloads into space in order to directly measure X and γ-rays of cosmic origin. Observing the sky through several bands brings a more complete picture and allows to better understand the physical behavior of cosmic sources and of the Universe as a whole. The observation of the Universe at high energies is particularly interesting in order to resolve the processes at play in extreme sources, of which GRBs are an example.

In usual spectral and timing measurements, the amount of photons per unit of energy and per sky bin as well are their arrival time are studied. But there is an additional information, other than the arrival direction and time of the photon, that is not exploited in typical spectral, timing, imaging, and localization analyses. Indeed, the orientation of the electric field of each high energy photon, or polarization, is propagated from the source to the observer. Polarization is a powerful parameter to probe the physical mechanism and structure of cosmic sources beyond the knowledge brought by spectral and timing studies, and opens a new window of possibilities in high energy astrophysics. Indeed, as discussed in the previous chapter, polarization is a direct probe to the magnetic fields configuration, the jet structure, the energy dissipation, and the emission mechanism. Many instruments making use of the polarization dependence of the photon interaction with matter were therefore developed in the last decades in order to measure the polarization of X and γ-rays in space.

The concept of polarization is first introduced, followed by the major interactions of high energy photons with matter and their link to polarization. A summary of the state of the art of polarization instrumentation in high energy astrophysics is then given.

2.1 PHOTON POLARIZATION

Electromagnetic radiation behave both as individual particles and as a wave [58]. Gamma-rays, and photons in general, can be described by a transverse wave composed of two fields orthogonal to each other. These two fields are the electric (**E**) and magnetic (**B**) fields and are sketched in Figure 2.1 in the case of a linearly polarized wave. As the **E** and **B** fields are always orthogonal to each other, the convention is to use the electric field vector as the polarization direction.

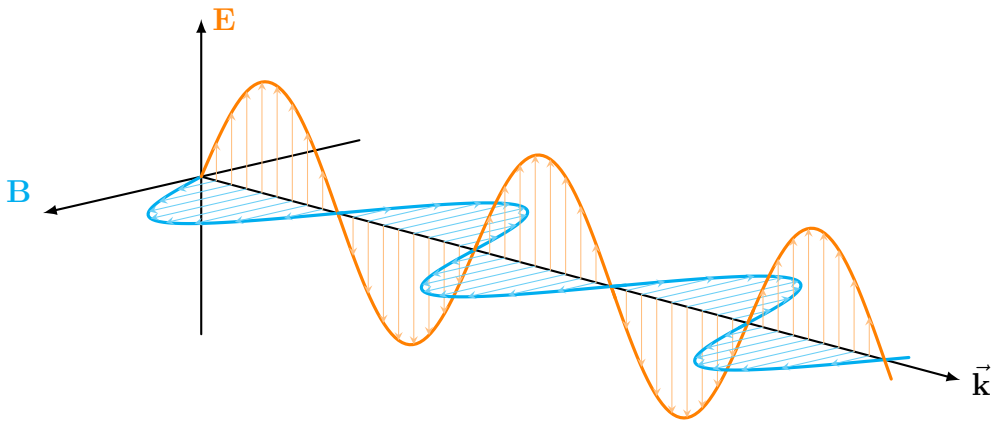

Figure 2.1: Illustration of an electromagnetic wave with the evolution of the electric and magnetic fields along the wave propagation direction.

The polarization vector, or electric field, can precess in the (**E**, **B**) plane during the photon propagation as shown in Figure 2.2. Such variation is called circular polarization, as opposed to the linear polarization depicted in Figure 2.1. Only linear polarization is studied in the case of gamma-ray bursts since no model predicts emission of circularly polarized waves, and no instrumentation is currently capable of measuring circular polarization of γ-rays.

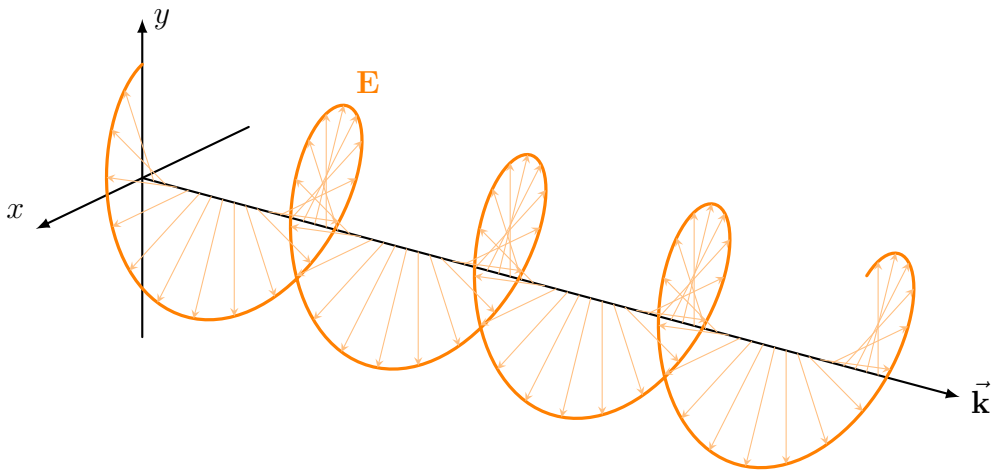

Figure 2.2: Evolution of the electric field along the wave vector for a circularly polarized wave.

Polarization can be parameterized using a polarization ellipse, mathematically expressed in the form of four Stokes parameters [39, 174, 209, 216]:

$$\vec{\mathbf{S}} = \begin{cases} S_0 \equiv I = \langle E_x^2 \rangle + \langle E_y^2 \rangle = \langle E_{45^\circ}^2 \rangle + \langle E_{-45^\circ}^2 \rangle = \langle E_R^2 \rangle + \langle E_L^2 \rangle \\ S_1 \equiv Q = \langle E_x^2 \rangle - \langle E_y^2 \rangle = I \cos 2\chi \cos 2\psi \\ S_2 \equiv U = \langle E_{45^\circ}^2 \rangle - \langle E_{-45^\circ}^2 \rangle = I \cos 2\chi \sin 2\psi \\ S_3 \equiv V = \langle E_R^2 \rangle - \langle E_L^2 \rangle = I \sin 2\chi \end{cases} \tag{2.1}$$

where ψ and χ are respectively the orientation and eccentricity angles of the ellipse. I is the total intensity of the electromagnetic wave, Q gives the fraction of horizontal and vertical polarization, U is the diagonal polarization, and V the circular polarization (left and right handed base). In the case of a fully polarized wave, made of several photons whose electric field are all aligned in the same direction, the four Stokes parameters are linked through the relation $I^2 = Q^2 + U^2 + V^2$. In the more physical case of partial polarization, this relation broadens to $I^2 \geq Q^2 + U^2 + V^2$. Figure 2.3 illustrates the cases of pure polarization in the Q, U, and V bases.

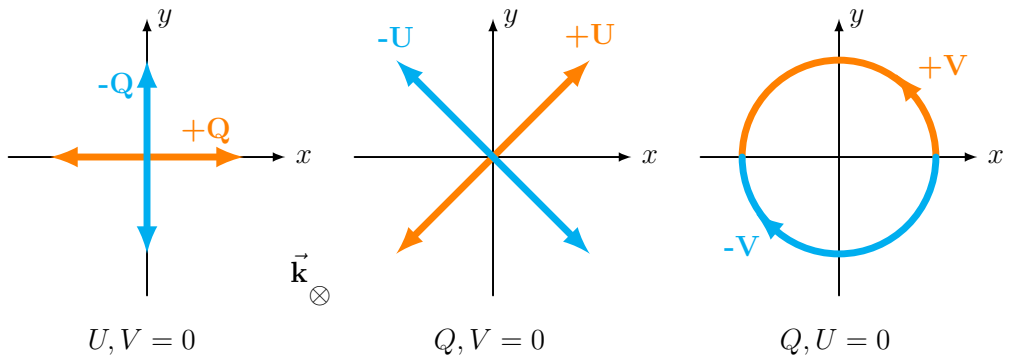

$U, V = 0$ $\quad$ $Q, V = 0$ $\quad$ $Q, U = 0$

Figure 2.3: Illustration of the polarization for specific values of Stokes parameters, namely in the case of a vertically/horizontally (**left**), diagonally (**center**), and circularly (**right**) polarized wave.

The $0 \leq \psi \leq \pi$ and $-\frac{\pi}{4} \leq \chi \leq \frac{\pi}{4}$ angles can be expressed as a function of the Stokes parameters, and the polarization degree p can be defined:

$$\chi = \frac{1}{2} \arcsin \frac{V}{I} \; ; \qquad \psi = \frac{1}{2} \arctan \frac{U}{Q} \; ; \qquad p = \frac{\sqrt{Q^2 + U^2 + V^2}}{I} \tag{2.2}$$

V and χ express the circular component of polarization, and are therefore null in the case of linearly polarized waves.

2.2 PHOTON INTERACTION WITH MATTER AND POLARIZATION

The three interactions used to detect photons are the photo-electric effect, the Compton scattering, and the pair production. Depicted in Figure 2.4, these three processes have in common the partial or entire transfer of the incoming photon energy to an electron. Each individual process has an angular behavior correlated with the photon polarization. The photo-electric effect is dominant at low energies, while pair production is the more probable process at high energies. Compton scattering is dominant at intermediate energies. The dominance of a process over another at a given energy is also dependent on the atomic number Z of the material in which the interaction is happening, as shown in Figure 2.5. We will now discuss how these mechanisms can be used for polarization measurements.

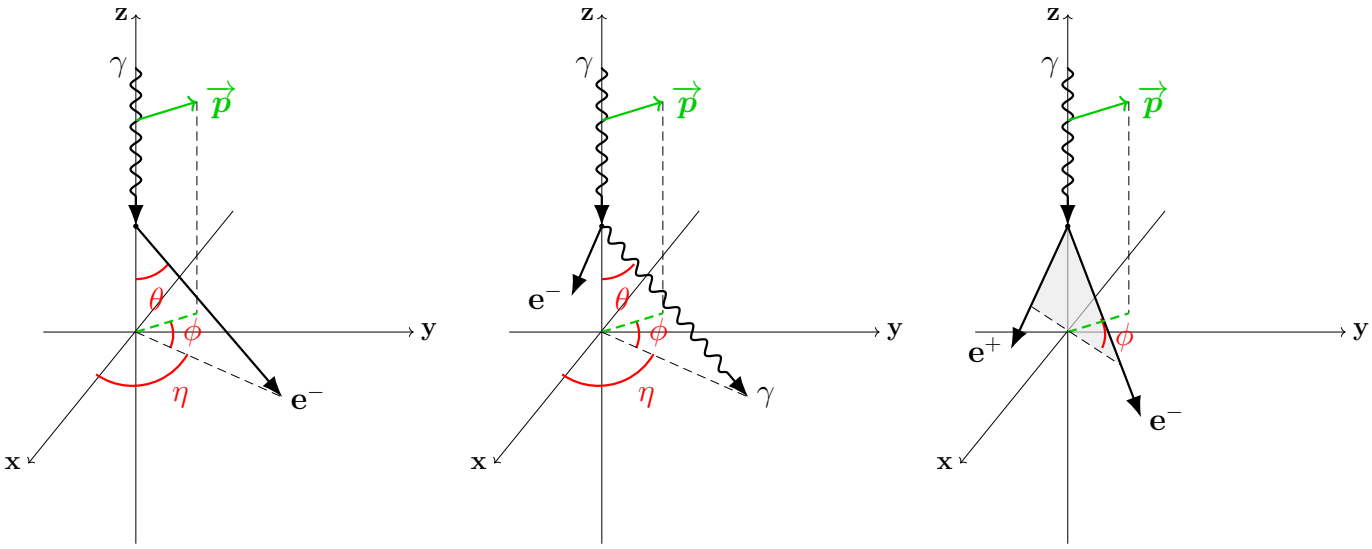

Figure 2.4: Representations of the main gamma-ray interaction processes. **Left:** Photo-electric effect. **Middle:** Compton scattering. **Right:** Pair production.

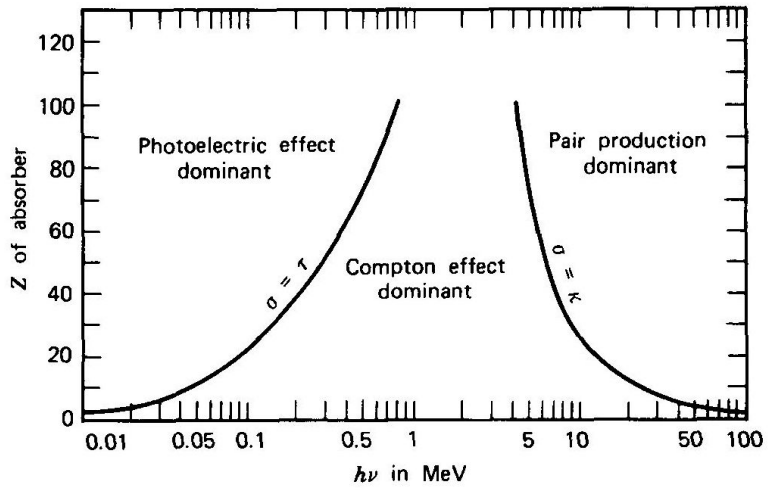

Figure 2.5: Plot showing the dominant effect based on the cross section as a function of energy and absorber density (taken from [127], with permission).

2.2.1 *Photoelectric Effect*

First proposed by Albert Einstein in 1905 [62], the photoelectric is the dominant mode of interaction for low energy photons. It consists of an absorption process, where the incoming photon interacts with an atom of an absorber. The energy of the photon is fully transferred to an electron in one of the bound shells of an atom, typically the K-shell. The electron is ejected from the atom with an energy corresponding to the incoming photon energy minus the binding energy of the shell:

$$E_{e^-} = h\nu - E_b \tag{2.3}$$

We call the electron expelled from the atomic shell a photoelectron. This effect is not only dominant for low energy X-rays, but also down to optical photons. The photoelectric effect is at the center of optical light detection and is the process at play in optical sensors, such as a smartphone camera or the human eye. After the electron is ejected from an atomic shell, the vacant location is either filled via capture of a free electron in the media or de-excitation of an electron in an outer shell. The difference in energy is compensated by either the emission of fluorescence X-ray photons or in some cases by the emission of an Auger electron [9, 168]. These secondary X-rays or electrons are typically re-absorbed near their emission point, but can sometimes escape from the absorber, influencing the response in the case of a detector. As shown in Figure 2.5, the photoelectric absorption is dominant up to even higher energies for a high-Z material, explaining the high density of typical γ-ray shields. This is also the reason why low-Z materials are typically preferred for Compton polarimeters in order to enhance the sensitivity to polarization down to lower energies. The photoelectric effect can be used for polarimetery as the angular distribution of the photoelectrons is dependent on the polar (θ) and azimuthal (ϕ) scattering angles [40, 174]:

$$\frac{d\sigma}{d\Omega} \propto \frac{\sin^2(\theta)\cos^2(\phi)}{(1-\beta cos(\theta))^4} \tag{2.4}$$

where β is the reduced velocity of the photoelectron. As can be observed from the $\cos^2$ dependency of the cross section, the photon will preferentially scatter 90° from its original polarization vector. In the case of a polarized source, a $\cos^2$ modulation will therefore be observed in the azimuthal scattering angle distribution, also known as *modulation curve*. On one hand, the amplitude of the modulation ca be used to determine the PD, i.e. the fraction of incoming photons that have their polarization vector oriented in the same direction. On the other hand, the phase of the modulation corresponds to the polarization angle PA, or the direction in which a fraction of the incoming photons have their polarization vector aligned. In the case of an unpolarized source, the polarization vector of each incoming photon will be isotropically distributed and the modulation will vanish, giving a flat scattering angle distribution. This is depicted in Figure 2.6.

2.2.2 *Compton Scattering*

Going to higher energies, that is in the 10 keV to 10 MeV band, the incoming photon is energetic enough to not be fully absorbed by the material. It will instead only transfer a portion of its energy to the *recoil* electron through Compton scattering. The outgoing photon will be deviated by a polar angle θ (see Figure 2.4) from its original direction, and its remaining energy can be expressed as:

$$E' = \frac{E}{1 + (\frac{E}{m_e c^2})(1 - \cos\theta)} \tag{2.5}$$

where $m_e c^2 = 511$ keV is the electron mass. It can be noted that a larger deflection will lead to a bigger energy loss.

The Compton scattering cross-section is described by the Klein-Nishina equation [126], expressed in Formula (2.6) for a linearly polarized photon. Once again, the $\cos^2$ dependency of the cross section implies that the photon will preferentially scatter 90° from its original polarization vector. The scattering angle distribution obtained for a polarized source would therefore have a sinusoidal shape, where the relative amplitude corresponds to the PD and the phase to the PA, as plotted in Figure 2.6.

$$\frac{\mathrm{d}\sigma}{\mathrm{d}\Omega} = \frac{r_e^2}{2}\left(\frac{E'}{E}\right)^2\left[\frac{E'}{E} + \frac{E}{E'} - 2\sin^2(\theta)\cos^2(\phi)\right] \tag{2.6}$$

where:

$r_e \approx 2.8 \cdot 10^{-15}$ m	classical radius of the electron
E	energy of the incoming photon
E′	energy of the scattered photon
θ	polar scattering angle
ϕ	angle between the initial polarization vector and the scattering direction.

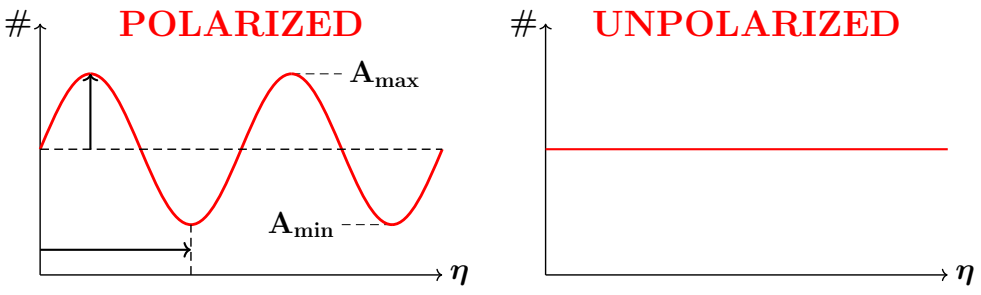

Figure 2.6: Theoretical structure of the azimuthal scattering angle distribution in the case of a polarized (**left**) and an unpolarized (**right**) source. In the case of a polarized source, a $\cos^2$ modulation, whose amplitude and phase are related to the polarization degree and angle, is observed.

2.2.3 *Pair Production*

For photons more energetic than 1.022 MeV, that is twice the mass of an electron, the pair production process starts to be possible. The photon is converted into an electron-positron pair, and the extra energy of the incoming photon (above the 1.022 MeV) is transferred to the electron and positron in the form of kinetic energy. The positron is usually annihilating with another electron in the media, creating a secondary pair of γs, affecting the response in the case of a detector. The probability of such interaction goes with the square of the atomic number of the material, and the effect typically becomes dominant above $\sim$10 MeV. The azimuthal direction of the plane in which the pair is created is once again linked to the polarization of the incoming photon. An asymmetry of the azimuthal distribution can be observed in the case of a polarized source.

2.2.4 *Quantifying the sensitivity to polarization*

The azimuthal angular dependency of the three main photon interactions (namely the photoelectric effect, Compton scattering, and pair production) allows to extract the polarization parameters from the measured scattering azimuthal angle distribution. For a polarized source, this distribution follows a sinusoidal modulation as depicted in Figure 2.6, also known as a *modulation curve*. As explained previously, the phase and relative amplitude of the modulation are respectively linked to the PA and the PD of the source. A figure of merit to represent the resolution to polarization of an instrument is the relative amplitude of the modulation for a fully polarized source, called the modulation factor and defined as [12]:

$$\mu_{100} = \frac{A_{max} - A_{min}}{A_{max} + A_{min}} \tag{2.7}$$

where A_{min} and A_{max} are the minimum and maximum of the modulation. The polarization degree of a source can be expressed as the ratio between the measured modulation amplitude and the modulation factor: $PD = \frac{\mu}{\mu_{100}}$. For typical γ-ray polarimeters, the μ_{100} is in the range 10-50%.

Measuring the polarization of γ-ray sources is statistically highly challenging because of the limited number of photons available and the statistically hungry nature of such measurement. Indeed, only the polarized fraction of the photons contribute to the signal. Resolving the polarization of a source with a PD of 1% with a 99% confidence level typically requires about 10^6 counts [222]. On the basis of this consideration, another figure of merit for the efficiency of γ-ray polarimeters is the Minimum Detectable Polarization (MDP), defined as a function of the confidence level as [222]:

$$\mathrm{MDP}_{99\%} = \frac{2\sqrt{-\ln(1 - CL)}}{\mu_{100} R_S} \sqrt{\frac{R_S + R_B}{T}} \tag{2.8}$$

where R_S and R_B are the signal and background count rates and T is the duration of the signal. The MDP is usually given for a 99% confidence level,

where $2\sqrt{-\ln(1-CL)} = 4.29$ in equation (2.8). Similarly, the MDP can be expressed for 3 and 5 σ confidence levels, for which this factor is 4.86 and 7.58, respectively.

2.3 STATE OF THE ART OF HIGH ENERGY POLARIMETRY INSTRUMENTATION

Ideally all three processes described in the previous section can be employed to measured the polarization of a X/γ-ray source. However, most of the astronomical polarimeters are based on either the photoelectric effect or Compton scattering, and no polarimeter based on pair production has been launched to space yet. The former is convenient for measuring the polarization of X-rays and soft γ-rays, while the latter is relevant for γ-ray polarimetry above 10 keV. Pair production being predominant at high energies, it can be exploited for polarization measurements above tens of MeV. We describe here the main technologies and instruments currently used in order to assess the polarization of astrophysical sources at high energy using these three interactions.

2.3.1 *Photoelectric Polarimeters*

The main technology based on the photoelectric effect in high energy polarimetery are Gas Pixel Detectors (GPDs) [47]. It consists of a gas detector in which the incoming photon is absorbed through the photoelectric effect, extracting an electron which will ionize the gas along its path. The electron-hole pairs produce by this ionization will drift the track towards the Gas Electron Multiplier (GEM) thanks to an electric field. The GEM consists of a very thin polyimide foil perforated with tiny holes, in which a high electric field is amplifying the charge. The charge is finally collected by a pixelated detector able to precisely reconstruct the track of the photoelectron. A schematic view of such detector is shown in Figure 2.7. By analyzing many photoelectron tracks from an astrophysical source, one can extract a distribution of the initial direction of the photoelectrons. This allows to extract information on the polarization of the incoming X-rays. Choosing the gas material in which the photoelectric absorption happens is highly challenging. On one hand, the medium should not be too dense for the electron to travel enough to be able reconstruct its track. On the other hand, the gas should still be dense enough to stop the incoming X-ray photon.

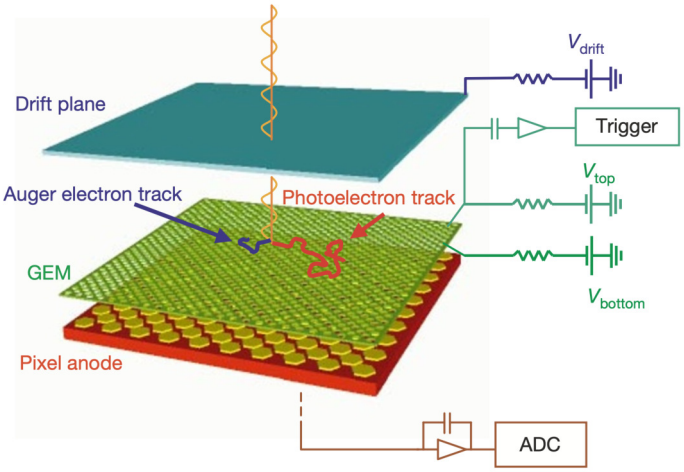

Figure 2.7: Working principle of a Gas Pixel Detector (taken from [47], with permission). The initial direction of the photoelectron is linked to the incoming X-ray polarization. The first part of the photoelectron track has a more precise direction, while the end of the track has more charge deposition. The full track is therefore used to determine the polarization of the incoming photons. The Auger electron does not provide any information on polarization.

Such technology was first demonstrated in space by the PolarLight 1U CubeSat [67] launched in October 2018. It was then followed by the very successful Imaging X-ray Polarimetry Explorer (IXPE) [223], launched in December 2021. GPDs will also be used in the future Low-energy Polarization Detector (LPD) [68] in order to enhance the POLAR-2 polarimetry capabilities at low energies. A CubeSat demonstrator of the LPD was launched in June 2023[1]. They will also constitute one of the four payloads of the enhanced X-ray Timing and Polarimetry mission (eXTP) mission ([239], appendix C), scheduled for a launch in 2028.

Another technology used for photoelectric polarimetry, also based on gas detectors, are Time Projection Chambers (TPCs) [21, 124]. The detection principle is the same, except that the GEM is usually read out using strips. This is the case of the Gravity and Extreme Magnetism Small Explorer (GEMS) project [65].

2.3.2 *Compton Polarimeters*

A widespread design for Compton polarimeters is to have an array of elongated scintillator bars individually read out by photomultipliers. The deposited γ-ray energy is converted into optical photon through the scintillation process. Depending on the mission, either Avalanche PhotoDiodes (APDs), Multi-Anode PhotoMultiplier Tubes (MA-PMTs), or Silicon PhotoMultipliers (SiPMs) are employed to optically read out the scintillators. Using a segmented detector allows to resolve the Compton scattering direction. We distinguish two types of instruments: single and dual phase Compton polarimeters.

1 https://english.gxu.edu.cn/info/1085/1281.htm

On one hand, single phase polarimeters simply consist of an array of scintillators all made of the same material, usually plastic to optimize the Compton cross section with a low-Z material. In this case the incoming photon will Compton scatter in a scintillator bar and deposit part or all of its remaining energy to another bar. The relative location of the two triggered bar can be used to deduce the azimuthal scattering angle, useful to determine the polarization of the source. This is the case of POLAR ([199], Chapter 3), POLAR-2 ([56, 200], Chapter 5), or PoGOLite/PoGO+ [35].

On the other hand, dual phase polarimeters employ two types of scintillator bars, as illustrated in Figure 2.8. As for single phase polarimeters, plastic bars are used for the γ-ray to Compton scatter. However, denser inorganic scintillators (e.g. Cesium Iodide - CsI) are used in order to fully absorb the photon afterwards and better measure the incoming energy. This is the case of TSUBAME [139], GRAPE [23], LEAP ([162, 164, 169], Appendix D), and CUSP [66].

Scintillators can also be arranged in other modes for Compton polarimetery. The Gamma-ray Burst Polarimeter (GAP) [230] was made of a dodecagon plastic scintillator with the 12 faces surrounded by CsI plates. All the scintillators of this dual phase polarimeters were read out using PMTs. Denser scintillators such as CsI(Na) can also be used in single phase polarimeters Compton polarimetry, as it is the case in the APT instruments and its demonstrator ADAPT [104]. Tiled CsI(Na) scintillators are used for measuring the Compton scattering interaction of the incoming γ-ray. The tiles are read out on both sides by perpendicular arrays of optical fibers coupled to SiPMs. Although primarily designed for GRB localization, the detected Compton scattering events can be used for polarimetery.

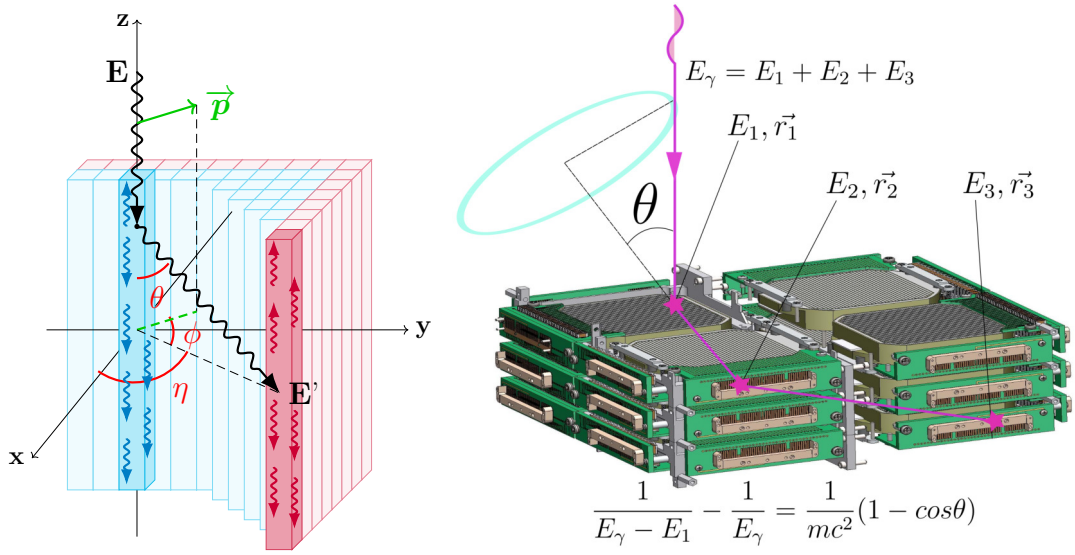

Figure 2.8: **Left:** Illustration of the Compton scattering in a dual phase Compton polarimeter. The photon is Compton scattering in a first segment of the detector made of plastic (blue) and later fully absorbed in a segment made of a denser scintillator (red). **Right:** Illustration of a Compton event in the COSI detector (taken from [153], with permission).

High energy polarimetery can also be made with segmented semiconductor detectors, in which the deposited γ-ray energy is directly converted into an electrical signal.

Cadmium Zinc Telluride (CdZnTe) segmented detectors, such as the CZT Imager (CZTI) on the AstroSat satellite [17, 217] or the future Daksha mission [11, 18] can be used for polarimetry. The high density of the material composing the single phase segmented detector and the geometry of the instrument implies an energy threshold of about 100 keV for Compton polarimetry. Polarimetry is also performed using CZT detectors in the focal plane of X-ray optics, for instance with X-Calibur [2] and XL-Calibur [116].

Germanium strip detectors can be employed in Compton telescopes such as COSI (super pressure balloon [123] and satellite/SMEX mission [30, 153, 213, 214]). Even though the primary goal of COSI is spectroscopy and imaging in the MeV band, poorly covered until now, the detection technique allows for polarization measurement in the 0.2-5 MeV range. As illustrated in Figure 2.8, the instrument is measuring for each incoming γ-ray a sequence of Compton scatterings happening in the sensitive volume of the detector. Determining the temporal order of each scattering as well as the scattering angle of the first interaction allows to constrain the photon arrival location into an annulus. Measuring several photons, the localization of the source can be obtained with the intersection of the annuli. The polarization information comes as a by-product of the measurement from the angle of the first Compton scattering.

Double sided strip detectors based on Silicon are also considered for future Compton telescopes such as AMEGO/AMEGO-X [32, 70, 165] and e-ASTROGAM [49, 50]. As for COSI, polarization measurements are not part of the primary science goal but comes as an additional possibility thanks to the measurement technique. These next generation instruments will be sensitive from hundreds of keV up to energies as high as a few GeV.

2.3.3 *Pair Production Polarimeters*

Compared to photoelectric or Compton polarimetry, not many detectors have been proposed for measuring the polarization using the pair production asymmetry. In order to assess the polarization of a source through pair production, a detector should be able to precisely measure the track of the electron and positron produce by the incoming γ-ray. Two main technologies have been thought to achieve such a measurement: Time Projection Chambers (TPCs) and emulsion films. On one end, gas TPCs could be used to collect the track of the electron-positron pairs and produce a distribution of the azimuthal orientation of the plane in which the pair is produced. This technology was demonstrated for polarization measurement with the HARPO TPC [15] using a γ-ray beam in the lab. The AdEPT mission [111] plans to operate TPCs in space for pair production polarimetry in the 5-200 MeV range. On the other end, the use of stacked emulsion film for polarization measurements with pair production

have been demonstrated with the GRAINE balloon experiment [181, 190, 210]. The emulsion films are optically scanned after the measurement campaign and the tracks are reconstructed via software. For instruments with silicon trackers in space like Fermi-LAT, AMS-02 and DAMPE, these measurements are in principle possible, however, low efficiencies and multiple scattering make such measurements highly challenging or impossible [16].

2.4 SUMMARY

Electromagnetic waves consist of an electric and a magnetic fields orthogonal to each other and propagating along a third direction orthogonal to the two fields. The electromagnetic wave is unpolarized if the electric field vectors of all the photons, or polarization vector, are uniformly distributed. If a source of photons is polarized a given fraction of these photons, called the polarization degree, will have their polarization vector in a certain direction given by the polarization angle. In the context of astrophysics, polarization is an important property of light that can bring additional information about the properties of a cosmic source.

High energy photons are detected using three main interactions: the photoelectric effect, the Compton scattering, and the pair creation. In the photoelectric effect, the incoming photon is fully absorbed, transferring its energy to an electron that gets ejected from the material composing the detector. For Compton scattering, only part of the energy of the incoming photon is transferred to a recoil electron, while the photon is deflected from its original direction. Finally, pair production is the annihilation of the photon and creation of an electron-positron pair. Each of these three processes are dominant in different energy ranges, with the photoelectric effect at sub-keV energies, the Compton scattering up to tens of MeV, and the pair production at higher energies. All three interactions have in common the angular dependency of the secondary products with the polarization of the incoming photon. Measuring the angular distribution of secondary particles produced by γ-rays from a given source is therefore a way to measure polarization.

The azimuthal distribution of the secondaries, commonly called modulation curve, shows a sinusoidal shape in the case of a polarized source. The amplitude of the measured modulation is linked to the polarization degree of the source, while its phase is related to the polarization angle. Two important figures of merit to assess the sensitivity to polarization of an instrument are the modulation factor μ_{100} and the minimum detectable polarization for a given confidence level $\mathrm{MDP}_{\mathrm{CL}}$. The modulation factor is defined as the amplitude of the modulation measured for a fully polarized source and gives an idea of the resolution on the polarization degree. It can be obtained for different incoming energies and directions through simulations. The minimum detectable polarization corresponds to the minimum polarization degree a source would need to have to be disentangled from a non-polarized source with a given confidence level. This last parameter is meaningful since as polarization is measured using the amplitude of a sinusoidal modulation, it is a positive definite measurement. It is therefore easier to artificially measure a high than a low polarization level.

With the advent of more and more sensitive X/γ-ray detectors, polarization measurements of astrophysical sources at high energies have been made possible. Polarimetry in the keV band is mainly accomplished with Gas Pixel Detectors, in which the track direction of the photoelectron produced through the photoelectric effect is measured. The distribution of the azimuthal direction of the

scattering is then used to determine the polarization of the source. Above 10 keV, segmented detectors can be used for Compton-based polarimetry. Measurement of the Compton scattering direction can either be made with single phase or dual phase instruments. Dual phase polarimeters employs two types of material: a low-Z material for the Compton interaction which gives the information on polarization, and a denser material to fully absorb the scattered photon. Single phase polarimeters use the same material for all the segments of the instrument. Many polarimeters are based on plastic scintillators for the Compton scattering detection, optimized for such interaction down to lower energies thanks to their low density. The absorber material is a denser scintillator, such as CsI. The scintillators are optically read out using either PhotoMultiplier Tubes, Avalanche PhotoDiodes, or Silicon PhotoMultipliers. Segmented semiconductor detectors for instance base on Cadmium Zinc Telluride, Germanium, or Silicon, can also be employed to for polarimetry at slightly higher energies, i.e. in the MeV region and even up to GeV energies. Finally, the possibility of measuring polarization with the pair production interaction was also shown to be possible with both Time Projection Chambers and segmented detectors based on emulsion films.

Part II

ENERGY RESOLVED POLARIZATION WITH THE POLAR INSTRUMENT

As one of the first instruments dedicated to the measurement of GRB prompt emission, POLAR brought very important results to the scientific community to take another step toward understanding these very powerful transient emissions. Launched in September 2016 together with the Tiangong-2 Chinese space laboratory, POLAR acquired science data for about 6 months, detected 55 GRBs as well as several pulsars and solar flares. Analyzing the GRB data of the POLAR mission brought a new picture to the field, showing lowly polarized prompt emissions for 14 bursts. An interesting hint of temporal evolution of the polarization angle was also observed for two of the brightest GRBs, washing out the moderate polarization degree down to lower levels in time-integrated analysis. After studying integrated and time-resolved polarization of the GRB prompt emission with POLAR data, a last interesting question to answer is whether the burst polarization is energy dependent. An energy resolved polarization analysis was therefore carried out on the POLAR GRB catalog, preparing as well the analysis pipeline for such study with future generation instruments.

3

THE POLAR INSTRUMENT AND PAST RESULTS

As already discussed in Chapter 1, measuring the polarization of Gamma-Ray Bursts is crucial in order to better understand the origin of these transient events. Since their discovery more than half a century ago [37, 125], many X/γ-ray instruments have been used to measure the temporal and spectral properties of GRBs as well as their distribution in the sky. But even though attempts to measure polarization with standard telescopes had already been carried out, no dedicated γ-ray polarization instrument had been operated before the last decade. The first dedicated instrument for such measurements was launched in 2010 by a Japanese collaboration [230]. Called GAP, for GAmma-ray burst Polarimeter, this satellite detected a few GRBs as it small size only allowed it to detect very bright GRBs.

As the second experiment designed for GRB polarization measurements, POLAR brought a considerable sample of polarization measurements. Making use of the fact that a γ-ray would preferentially Compton scatter 90° to its polarization vector, the polarimeter consisted of an array of 40×40 elongated plastic scintillators read out by Multi-Anode PhotoMultiplier Tubes (MA-PMTs). Operated for 6 months starting September 2016 on the Tiangong-2 Chinese space laboratory, POLAR detected 55 GRBs [228]. Only 14 GRBs among the 55 detected were bright enough to collect the statistics required to analyse their polarization. Time resolved polarization has also been studied on the few brighter GRBs of the POLAR catalog, showing interesting behavior [26, 128]. Finally, POLAR was able to detect several Solar Flares (SFLs) [149, 238] as well as to provide spectral and polarization properties of the Crab [142–145] matching with most of the existing measurements, showing a good understanding of the detector calibration and performance.

After discussing the pre-POLAR GRB polarization results, the POLAR instrumental design and calibration method will be shown, followed by a summary of the POLAR results prior to the work performed in this thesis. Conclusions will then be presented on the overall outcome of the POLAR mission.

3.1 GRB POLARIZATION MEASUREMENTS BEFORE THE POLAR ERA

Before the operation of the POLAR instrument, several polarization measurements of the prompt emission of GRBs were carried out. These are summarized in Table 3.1 and described in [163]. As can be observed in this table, most of the results are not very constraining on the polarization degree. Some of them are even inconsistent with other results. This is the case of GRB041219A, which was measured by two instruments on-board the INTEGRAL telescope, SPI and IBIS, and gave two very different results [92, 119, 166]. This might show a limited

understanding of the detectors or a problem in the analysis procedure, limiting the confidence that one can have in these results. Some polarization results have been shown to be wrong, such as the first RHESSI results for GRB021206 reporting a very high degree of polarization [38]. The later studies on the same GRBs have shown that the PD is fully unconstrained [204, 225].

GRB	INSTRUMENT	ENERGY (KEV)	PD (%)	REF.
021206	RHESSI	150-2000	80±20%	[38]
021206	RHESSI	150-2000	<100%	[204]
021206	RHESSI	150-2000	41^{+57}_{-44}%	[225]
930131	CGRO/BATSE	20-1000	35-100%*	[226]
960924	CGRO/BATSE	20-1000	50-100%*	[226]
041219A	INTEGRAL/SPI	100-350	98±33%	[119]
041219A	INTEGRAL/SPI	100-350	96±40%	[166]
041219A	INTEGRAL/IBIS	200-800	43±25%†	[92]
061122	INTEGRAL/SPI	100-1000	$< 60\%$	[167]
100826A	IKAROS/GAP	70-300	27±11%‡	[229]
110301A	IKAROS/GAP	70-300	70±22%	[231]
110721A	IKAROS/GAP	70-300	80±22%	[231]
061122	INTEGRAL/IBIS	250-800	$> 60\%$	[90]
140206A	INTEGRAL/IBIS	200-800	$> 48\%$	[91]
151006A	Astrosat/CZTI	100-300	-	[202]
160530A	COSI	200-5000	$< 46\%$	[152]

Table 3.1: Summary of the published GRB polarization measurements in the pre-POLAR era. Special notes: *Albedo polarimetry. †Variable PD. ‡Variable position angle. (adapted from [163])

In the case of the GAP detector, three GRB polarization measurements were published [229, 231]. One with a low polarization degree, and two with very high PDs. But four GRBs were also not published by the GAP collaboration for which 90% upper limits were obtained. These are GRB100715, GRB101014, GRB110625, and GRB110825, for which respective upper limits of 83%, 71%, 56%, and 47% for the PD were reported [76]. The latest polarization measurement before POLAR's launch was provided by the COSI balloon flight mission. The measured value for the PD was below the Minimum Detectable Polarization (MDP) and a 90%

confidence upper limit of 46% could be extracted.

Overall the GRB polarization measurements until 2016 did not provide a constraining picture on the polarization fraction of GRBs' prompt emission. A lot of inconsistencies and poorly constraining results were reported, partly due to the fact that most of the instruments were not designed for polarimetry. It is in this ambiguous landscape that the POLAR detector was launched.

3.2 THE POLAR GRB POLARIMETER

3.2.1 *POLAR instrument design and calibration*

The sensitive part of the POLAR instrument [199] was divided into 25 polarimeter modules. A polarimeter module consisted of a target, in which the γ-rays undergo Compton scattering, made of 64 plastic scintillators arranged in an 8×8 array layout. The scintillators are separated by Enhanced Specular Reflector (ESR) films in order to prevent the optical light to escape from a bar to its neighbours. A low-Z material, the EJ-248M plastic from Eljen [64], was used for the scintillating material in order to optimize the Compton cross-section at low energy and therefore lower the energy threshold for polarization measurements. The $5.8\times5.8\times176$ mm^3 bars are truncated at both extremities in order to reduce the optical crosstalk, and to fit a mechanical grid that holds the target in place and ensures good alignment between the different scintillators. A PolyEther Ether Ketone (PEEK) plate with Sorbothane damping pads is placed on top of the target in order to dampen the vibrations and shocks during the rocket launch. This is especially relevant since the target is read out by a 64 channel Multi-Anode PhotoMultiplier Tube (MA-PMT) (HAMAMATSU R10551-00-M64) which contains a fragile Borosilicate entrance glass window. A good optical coupling between the scintillators and the MA-PMT is ensured thanks to a Room Temperature Vulcanizing (RTV) silicone optical pad (QS1123 from MAP space coating [89, 157]). The MA-PMT is mounted on the Front-End Electronics (FEE), responsible for pre-processing the signal and applying the local triggering logic (internal to the module). The assembly of the optical targets with dampers and photomultipliers is housed in a 1-mm thick Carbon Fiber Reinforced Polymer (CFRP) socket in order to shield the scintillators from low energy electrons.

Compton scattering is dominant down to lower energies in low-Z than in high-Z materials, see Figure 2.5.

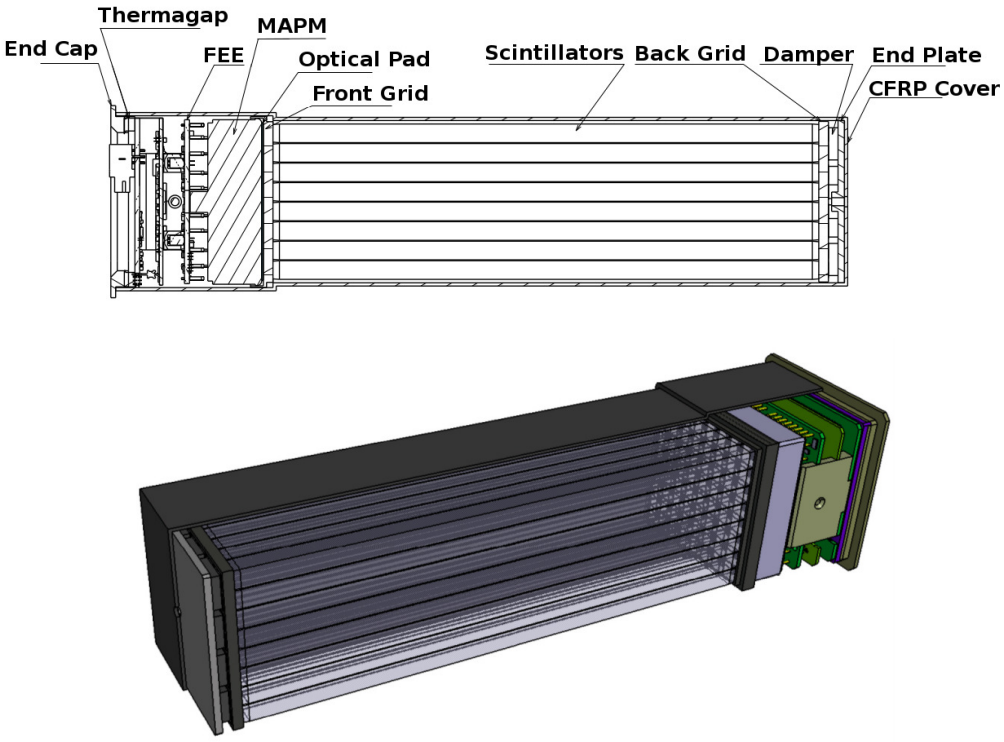

Figure 3.1: Sketch and CAD model of the POLAR module design. The target is made of 64 plastic scintillators of dimensions $5.8 \times 5.8 \times 176$ mm^2, truncated on both sides for mechanical reasons. The truncated extremities are inserted into a plastic grid, The scintillators are placed in a 8×8 configuration and are separated by highly reflective foils. The top of the module is also covered with a highly reflective foil as well as with dampers placed on a support plate for vibrations dampening. The other side of the target is coupled to the Multi-Anode PMT using a silicone based optical pad. The PMT is mounted on the Front-End Electronics and the assembly is encapsulated into a carbon fiber housing thanks to an end cap. (Credit: Franck Cadoux)

The POLAR instrument was composed of 25 polarimeter modules placed in an Aluminum 7075T7351 mechanical grid. A 1 mm thick CFRP top cover is housing the 5×5 modules to provide light tightness and shielding to low energy electrons. A Multi Layer Insulation (MLI) foil is covering the polarimeter, providing quasi-perfect thermal insulation with outer space and shielding from micro-meteorites. The aluminum frame is painted using a special white coating (GS121FD from MAP [157]) with an emissivity of 0.8 in order to passively cool down the instrument and protect the aluminum from atomic oxygen. The Back-End Electronics (BEE), placed at the bottom of the modules, is responsible for collecting the data and trigger signals from the modules and applying trigger logic on the overall instrument. A High Voltage Power Supply (HVPS) is providing a voltage in the 600-1200 V range to the MA-PMTs, and a Low Voltage Power Supply (LVPS) is providing +3.3, +2, and -2.5 V voltages to each FEE. Kapton heaters are placed next to the BEE in order to heat up the instrument in case of extremely cold conditions that could damage the payload. The polarimeter together with the BEE, LVPS, and HVPS, whose assembly is called OBOX, are placed on the outside of the space lab. A second part of the

This specific Aluminum alloy is chosen for its mechanical rigidity due to its high Zinc content, but also for its low Manganese content. This last point is important because Manganese can be activated by radiation, which would cause an additional background once the instrument is exposed to the space radiation environment.

payload, called IBOX, is placed on the inside of the space lab and is responsible for converting the provided 100 V to 28 V for the LVPS as well as for data management and communication with the platform.

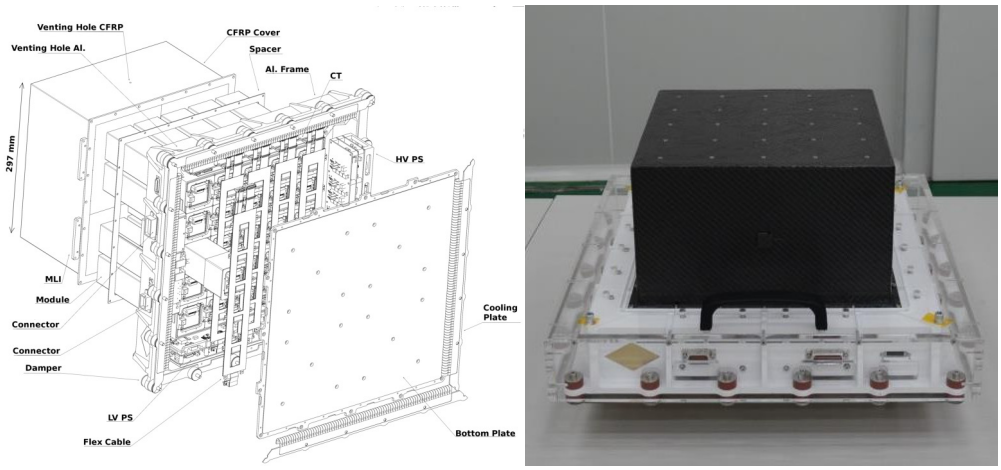

Figure 3.2: **Left:** Sketch of the POLAR overall instrument design (taken from [199], with permission). **Right:** Picture of the assembled POLAR instrument (Credit: POLAR collaboration).

Calibration of the instrument was performed both on-ground [129] and during the flight [150]. A calibration campaign at European Synchrotron Radiation Facility (ESRF) in Grenoble, France was carried out using a polarized beam with energies ranging from 60 to 140 keV. This allowed to calibrate both the spectral and polarization responses of the instrument. A Monte-Carlo model based on Geant4 [6] has also been built in order to reproduce the behavior of the instrument. In order to allow in-orbit calibration, 4 ^{22}Na sources have been placed in the instrument. The sodium source emits two back-to-back 511 keV photons from a positronium state. A 200 μm Copper housing was shielding the source in order to prevent positrons to escape and to get a clean photon source. The 340 keV Compton edge of the 511 keV photon is used for energy calibration [227].

3.2.2 *The POLAR mission*

POLAR was launched in space together with the Tiangong-2 (TG-2) Chinese space lab on a Long March 2F rocket on September 15 2016 at 14:04 UTC, as shown in Figure 3.3. Placed at an averaged altitude of about 375 km with an orbit inclination of 42.79°, the space lab re-entered the atmosphere for a controlled decommissioning on July 19, 2019. But POLAR saw the end of its data taking early April 2017, due to a malfunctioning of the HVPS board.

Figure 3.3: **Left:** POLAR mounted on the TG-2 space lab. **Right:** Picture of the TG-2 launch in Jiuquan, China. (Credit: China Manned Space Agency (CMSA))

The data acquisition was also stopped in October 2016 due to the presence of two taikonauts on the station. During about 6 months of operation, POLAR detected 55 GRBs [228] as well as several Solar Flare (SFL) and pulsars. The science output of the POLAR mission is described in the next section.

3.3 POLAR GRB ANALYSIS PRIOR TO THIS WORK

3.3.1 *Initial analysis of 5 bright GRBs and time*

The initial GRB analysis was performed on 5 of the brightest GRBs that were detected by POLAR, for which good spectral measurement and location were provided by other instruments. The selected bursts had fluences higher than $5 \cdot 10^{-6}$ erg·cm^{-2} in the 10-1000 keV and were not more than 45° off-axis in POLAR's FoV, as described in [240].

Only GRBs within 45° of the POLAR zenith are selected here to ensure no contamination from materials around POLAR that could alter the polarization.

A set of 61 simulated modulation curves were produced using the POLAR Monte Carlo code described in [129] for each GRB. The spectral parameters were fixed based on the spectrum provided by other instruments (e.g. Fermi-GBM). Sixty distributions were simulated for a 100% polarized source for different PA with a resolution of 3°, and one distribution was produced for the unpolarized case, for which the PA has no relevance. A weighted average of the unpolarized and fully polarized distributions was used to generate modulations with intermediate polarization fractions, resulting into 6060 simulated modulation curves in the PD-PA space with a 1% resolution on the PD and 3° on the PA. A modulation curve is produced with the background time intervals which is subtracted from the measured modulation during the source interval in order to get rid of any background induced modulation. The subtracted modulation curve for a given GRB is then fitted with the set of the 6060 simulated distributions using a chi-square method. Finding the modulation curve for which the chi-square is minimal, the polarization degree and angle of the GRB are extracted.

For the 5 GRBs, the polarization degree chi-square is minimal between 4% and 11%, implying that the most probable PD values are very low. Upper limits

between 28% and 45% were also reported for those GRBs with a 99% confidence level. Time evolution of the polarization parameters was studied for four of the GRBs by splitting the pulse into 2 or 3 equal time bins. Only GRB170114A showed a hint for some temporal evolution, for which a dedicated analysis was carried out later, as described in Section 3.3.3.

GRB170127C having too low statistics, no constraining results could be obtained for the polarization angle variability in time.

3.3.2 *POLAR GRB catalog analysis*

Some improvement were brought to the analysis to extract the polarization parameters of the GRBs detected by POLAR. The main changes in the analysis method are the use of forward folding and the way of dealing with background.

As mentioned in Section 3.3.1, the spectral information of the GRB in the previous analysis were fixed using information from other instruments. The polarization fit was therefore performed independently of the spectral fit, not allowing to propagate the spectral errors to the polarization degree and angle. The effects of spectral errors were only studied for one GRB by running 10'000 times the analysis, slightly variating the input spectrum every time within the reported spectral error bars. The estimated systematic errors on the polarization parameters induced by the spectral component were assumed to be representative for the 5 analyzed GRBs. This method was considered satisfactory, but the error propagation is not strictly correct, and running 10'000 times the analysis per GRB is not a very efficient technique. The main improvement in the catalog analysis method is therefore the use of a forward folding method. Polarization responses are produced for 150 energy bins ranging from 5 to 750 keV, allowing to subsequently produce responses for any possible spectrum by weighting correctly the bins of the polarization response. The polarization fit is performed in parallel to the spectral one, not only allowing a correct spectral error propagation to the polarization parameters, but also enabling the use of the POLAR data to improve the spectral fit. This last point allows to independently analyze a GRB that has not been detected by any other instrument, which was a selection criterion in the previous analysis.

Subtracting the background from the modulation curve, as was done in the previous analysis, is not the proper way of propagating Poisson errors. For the catalog analysis [128], the background was therefore modeled by selecting background time intervals before and after the prompt pulse. No subtraction is therefore occurring in this process, since the measured spectrum and modulation curve are compared to their respective simulated curves that contained both background and source contributions.

Out of the 55 GRBs detected by POLAR, 14 were analyzed for polarization, the others having too little counts for providing an accurate polarization result. The analysis was based on the Multi-Mission Maximum Likelihood framework (threeML) [219] that allows to jointly fit spectral data of several instruments. A feature was added to the framework in order to be able to perform both spectral and polarization fit in parallel. The `polarpy` plugin [26, 245] was built to adapt

As mentioned earlier, fitting both spectral and polarization components in parallel allows to independently analyze bursts that have only been observed by POLAR, increasing the number of analyzed GRBs from 5 to 14.

the POLAR data to the threeML framework, similar plugins can be built for other instruments for joint analysis. Most of the 14 GRBs reported in the POLAR catalog paper [128] were also observed by Fermi-GBM or Swift-BAT, for which a joint fit for the spectral component was performed often using the Band function [13], or sometimes using a cutoff powerlaw function.

The polarization results for these 14 GRBs were mostly consistent with a lowly polarized or unpolarized source, disfavouring models based on synchrotron emission with highly ordered magnetic fields, for which we expect high levels of polarization. However, the PDs measured by POLAR are not tightly constrained. It is therefore required to build more sensitive instruments, like POLAR-2 [56] or LEAP [162, 164], to bring high precision measurements of GRB polarization.

The analysis work performed in this thesis on energy resolved polarization is using an analysis method based on that used for the catalog analysis. More details on the forward folding method are therefore provided in Chapter 4.

3.3.3 *Time resolved analysis of GRBs' prompt emission*

Using the threeML Bayesian framework [219], a detailed time resolved polarization analysis was performed on GRB170114A [26]. The GRB pulse was divided into 9 time bins optimized via Bayesian blocks [205]. The method used for the time integrated analysis, described in section 3.3.2, was employed for each time bin, providing a polarization angle and degree for each of the bins. Even though the polarization parameters were not strongly constrained, a hint for a higher polarization degree than in the time integrated result was reported. This higher PD was accompanied by a time evolving PA, washing out the PD in time integrated analysis and explaining the lower integrated PD observed. Due to the lack of statistics in other GRBs observed by POLAR, only GRB170101A and GRB170207A underwent the time resolved analysis. The former, which as GRB170114A has a FRED like light curve, also shown a hint for a temporal evolution of polarization, while the latter did not show any interesting time variation of the PD/PA [128].

3.3.4 *Non-GRB POLAR science outcome*

PSR B0531+21, also known as the Crab pulsar, was observed by POLAR. POLAR not being designed for persistent sources and having a wide FoV, a very complex analysis was used in order to significantly see the pulsations of the Crab. The arrival time of each photon observed by POLAR was corrected to the Solar System Barycentric frame and a phase folding was applied on the data since the Crab period is well known. The phase of the pulsar was divided into 40 bins and the spectrum was fitted for each of these bins using a power law function [143, 144]. The phase resolved power law index obtained by POLAR was shown to be consistent with that reported by other instruments in the past, showing a good understanding of the POLAR instrument and its spectral response. The polarization of the Crab was also studied for the full

phase interval as well as for the two individual peaks [142, 145]. The results were also consistent with most of the Crab polarization measured by other instruments in the past. Analyzing the Crab pulsar spectrum and polarization with POLAR-2, the successor of POLAR (see 5), will also be a good way to check the understanding of the instrument behavior and give more confidence into the GRB results. Another pulsar, PSR B1509-58 was also seen by POLAR [145]. Due to its lower brightness, not enough statistics was accumulated to get a phase profile with enough statistics for proper spectral and polarization analysis.

Furthermore, numerous Solar Flare (SFL) were detected by POLAR [149, 238]. Due to the duration of such events, typically of the order of 10's of minutes, the background is very complex to model. But the main limitation for SFLs is that they are too soft, with most of the emission below 50 keV, where POLAR is not sensitive enough to polarization. Only spectral analysis of these SFLs is therefore possible with POLAR. This will be improved for POLAR-2 which will be sensitive to polarization down to 30 keV.

Finally, a SGR-like event has been found while doing blind search of transient events in the archive POLAR data, as reported in [136]. The burst happened the 18th of January 2017 at 16:16:25.5 UTC, and has a duration of $T_{90} = 0.32 \pm 0.02$ s and a fluence of $(5.09 \pm 1.33) \cdot 10^{-6}$ erg·cm^{-2} in the 50-500 keV range.

3.4 CONCLUSION AND THE NEED FOR A MORE SENSITIVE/BIGGER INSTRUMENT

Before the launch of the POLAR mission, the GRB polarization measurements, mostly carried out by non-dedicated instruments, did not give a clear and consistent picture. Furthermore, some results with low polarization levels were not published, biasing the overall picture of GRB polarization. Indeed, a low polarization degree is sometimes perceived as a less exciting result. Polarization being a positive definite measurement, a low measured value is also very physically interesting since it provides a powerful insight to probe the emission mechanism.

During its 6 months of operation on board the TG-2 space lab, POLAR detected 55 GRBs, 14 of which were bright enough to provide sufficient statistics for polarization analysis. A low polarization degree was reported for most of these GRBs, disfavouring synchrotron emission models with ordered magnetic fields. A time resolved polarization analysis was also carried out on the brightest GRBs, showing for two of them a hint for a time evolving polarization angle washing out the time integrated polarization fraction. Nevertheless, the low polarization fractions were originally not consistent with the picture provided by the ASTROSAT-CZTI instrument, that reported high polarization levels for several GRBs [34]. The effective area of this instrument for polarization measurements is very low compared to that of POLAR, and the initially reported high polarization levels have later been updated by a second publication providing mostly upper limits for the polarization degree [33]. A joint analysis work with POLAR and ASTROSAT data is currently ongoing on commonly observed GRBs.

POLAR provided exciting results, but polarization being a very statistically demanding measurement, a more sensitive instrument is needed to provide very constraining polarization measurements of GRB's prompt emission. This is the reason why based on the legacy of POLAR a 10 times more sensitive instrument is currently under development. Called POLAR-2, this instrument is the subject of Part iii of this work.

Meanwhile, the POLAR data can be still used to perform interesting analysis. The time evolution of the polarization parameters has already been studied for the brightest GRBs seen by POLAR. The time evolution of the GRB spectrum was also reported. But another interesting feature of the GRB polarization is its energy dependence. The tools used for the integrated catalog analysis were therefore modified in order to perform energy resolved analysis. Although limited by statistics, the POLAR data contains a good set of GRBs to perform energy resolved polarization analysis as well as to prepare the pipeline for such analysis for the future missions. This work is described in the next chapter.

4

ENERGY RESOLVED POLARIZATION ANALYSIS WITH THE POLAR GRB CATALOG

With about 6 months of operation, POLAR was able to detect 55 GRBs and provide polarization results for a 14 of them. The polarization results reported by POLAR brought a consistent picture to the GRB polarization field, with emissions consistent with a lowly polarized or unpolarized flux [128]. However, a time resolved analysis performed on the three brightest GRBs detected by POLAR revealed an interesting feature for two of them [26, 128], which were both FRED-like. It indeed showed a hint for a time evolving polarization angle with a moderate polarization degree. The low PD obtained in the time integrated analysis could therefore be explained by the fast temporal change in the PA, washing out the integrated polarization level.

FRED, for fast-rising exponential decay, is a type of bright single pulse GRB that can be described by an asymmetric exponential rise and decay, as discussed in Chapter 1

Although this hint for polarization temporal evolution is very exciting, no strong conclusions could be made on this temporal evolution due to limited statistics. For this reason, a next generation polarimeter (POLAR-2) based on the legacy of the POLAR mission and with a sensitivity improved by an order of magnitude is currently under development, and is the subject of Part iii of this thesis. In the mean time, the polarization can be studied as a function of energy. Energy resolved polarization analysis on the POLAR data could allow to bring an additional piece of information in order to disentangle between the different existing emission models. For instance, it might tell us whether the polarization degree is higher at low energies, as predicted by [155], or if it increases at the spectral peak, which would be a sign of a synchrotron emission process [84, 212]. The goal of this work is therefore to look for energy dependence of polarization in the POLAR data, but also to prepare the pipeline for future energy resolved analysis with POLAR-2, LEAP [162, 164], and Daksha [18].

We first present here the analysis methodology used for energy resolved analysis of GRB prompt emission with the POLAR data, based on the method used for the energy integrated catalog analysis. We then present the energy integrated analysis of GRB170114A, already published in the past [128], to give a precise idea of the steps of the analysis. The energy resolved analysis on the POLAR GRB catalog is then presented for several energy dependent functions. Finally, a summary of the energy resolved analysis and future prospects with the POLAR-2 mission are given.

4.1 ANALYSIS METHOD

The polarization analysis is based on the Multi-Mission Maximum Likelihood framework (`threeML`) [1, 219] and the `astromodels` package [246]. The `polarpy` plugin [245] was built for the past analysis [26] in order to format the data and instrument responses to be compatible with `threeML`.

As explained in Section 3.3.2, past analysis [34, 229, 240] were based on fitting the data to responses produced for a specific spectrum. This type of techniques prevents to perform spectral and polarization fits in parallel. As a result, the systematic errors from the spectral components are not properly propagated to the polarization parameters. A novel polarization analysis technique based on forward folding was therefore developed for the integrated and time-resolved POLAR analyses [26, 128]. This technique is used for the energy resolved polarization analysis and is therefore detailed below.

As for the past catalog analysis, detected GRBs are selected for polarization analysis based on two criteria: their brightness - the fluence in the 10-1000 keV range should be higher than 5×10^{-6}erg/cm^2; and their location in the sky - the burst should occur within 90° of the polarimeter Zenith direction to be in POLAR's FoV. The fluence is measured using the POLAR data, and the best available GRB localization is used in order to simulate the POLAR instrument response as the uncertainty on location leads to systematic effects in the polarization results [221].

A schematic representation of the Bayesian analysis steps is shown in Figure 4.1. A spectrum and scattering angle distribution are first produced from the POLAR data. Spectral parameters are picked from either a Band or cutoff powerlaw prior (see next Section for the definition of the functions), and are used to produce a simulated spectrum using the spectral response. The simulated and measured spectrum are then used to determine a likelihood. In parallel of this process, both spectral and polarization parameters are combined with the polarization response in order to produce a simulated modulation. A likelihood for the polarization part is then computed using the measured histogram. Repeating this process many times while picking the spectral and polarization parameters from the respective priors in order to minimize the likelihood, a posterior distribution is obtained for each of the parameters.

It should be mentioned that not only POLAR data are used for fitting the spectrum. The spectral part is indeed jointly fitted with other's instrument data when available, namely data from the Gamma-ray Burst Monitor on-board the Fermi Gamma-ray Space Telescope, from hereon referred as Fermi-GBM, and the Burst Alert Telescope on-board the Neil Gehrels Swift Observatory, from hereon referred as Swift-BAT. Some of the GRBs observed by POLAR were also detected by the Konus-Wind instrument, but as there is no 3ML-compatible data publicly available such data could not be used in the analysis. Additional normalization parameters are used in the fit when data from several mission are

jointly analyzed to correct for potential errors in the effective area determination of one of the instruments.

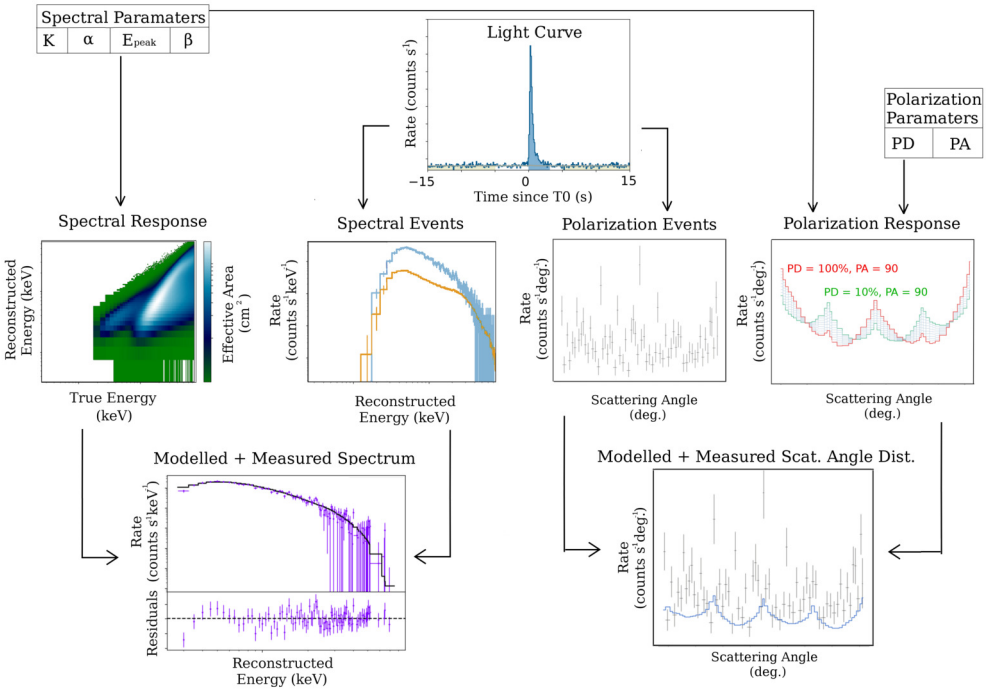

Figure 4.1: Forward folding analysis flow chart for POLAR spectral-polarization analysis (taken from [128], with permission). A set of spectral parameters is used to produce a spectral response as well as a polarization response with the addition of the polarization parameters PD and PA. A spectrum and a scattering angle distribution are produced from the observed data and compared to their respective responses in order to determine the most likely set of spectral and polarization parameters.

With the polarization response already being produced for 150 5 keV energy bins, the energy dependent fit can directly be implemented in the existing analysis tool with some adaptations. The main changes implemented in the analysis tools are the following:

- **`astromodels/core/model_parser.py` -** Implementation of the additional polarization parameter(s) for the energy dependence in the function `_parse_polarization`.
- **`astromodels/core/polarization.py` -** Implementation of the additional polarization parameter(s) for the energy dependence in the class `LinearPolarization`.
- **`polarpy/polar_like.py` -** Implementation of the additional polarization parameter(s) for the energy dependence in the function `set_model` and in the `eval_points` array of the `_get_model_rate` function.
- **`polarpy/polar_response.py` -** Computing the interpolated polarization response matrix for the new set of parameters. Each additional polarization parameter adds a new dimension to the response matrix, which can make complex energy-dependent models very computationally heavy.

- **`analysis_script.py` -** Defining prior distributions for the new polarization parameters and initialize them.

The energy response matrix for GRB170114A is shown in Figure 4.2. In most of the cases, the reconstructed energy is lower than the actual incoming γ-ray energy. The spectral response is therefore not diagonal, and suffers from energy dispersion as for any γ-ray instrument. The dispersion is enhanced by the use of plastic scintillators, which have a poor energy resolution. That is, there is no bijective function between the true and reconstructed energy. This dispersion is enhanced by the use of plastic scintillators. Being a low-Z material, plastic is good for polarization measurements since it maximizes the Compton cross-section at low energies, but is however not optimal for precise energy measurement. This energy dispersion is anyway accounted for in the spectral response and accordingly in the forward folding analysis process. It will therefore not lead to any mistake in determining the energy in the energy resolved polarization analysis, but will just lead to bigger systematic errors that will be propagated to the final result. Past analyses have been directly using the reconstructed energy for studying the polarization energy dependence. This is obviously not the correct method as the instrument response would not be accounted for.

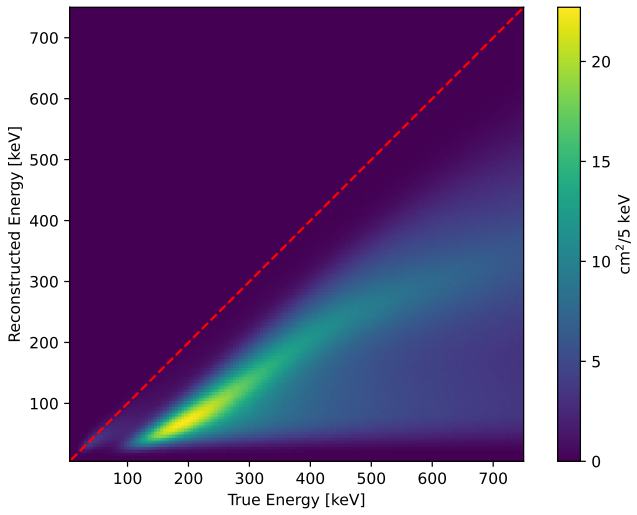

Figure 4.2: POLAR spectral response for GRB170114A. The energy response matrix is giving the measured energy as a function of the true incoming energy. A diagonal red dashed line is given as reference. The energy dispersion, enhanced by the use of plastic scintillating material, can be observed.

4.2 ENERGY INTEGRATED POLARIZATION ANALYSIS OF GRB170114A

We show here the energy integrated result of one of the brightest GRB observed by POLAR, GRB170114A. This results were already published in the past [128], but are a good way to show the important steps of the analysis.

The first step, as shown on the left plot of Figure 4.3, is to select source and background time intervals. As for all the GRBs jointly detected by Fermi-GBM,

the time interval are not only selected for the POLAR data but also for the three NaI (Sodium Iodide) and one BGO (Bismuth Germanate) GBM detectors with the highest significance. The starting time of the burst T_0 is, as reported by Fermi-GBM [191], January 14, 2017 at 22:01:09.50 (UT). The duration of the burst measured with the POLAR light curve is $T_{90} = (10.48 \pm 0.16)$ s.

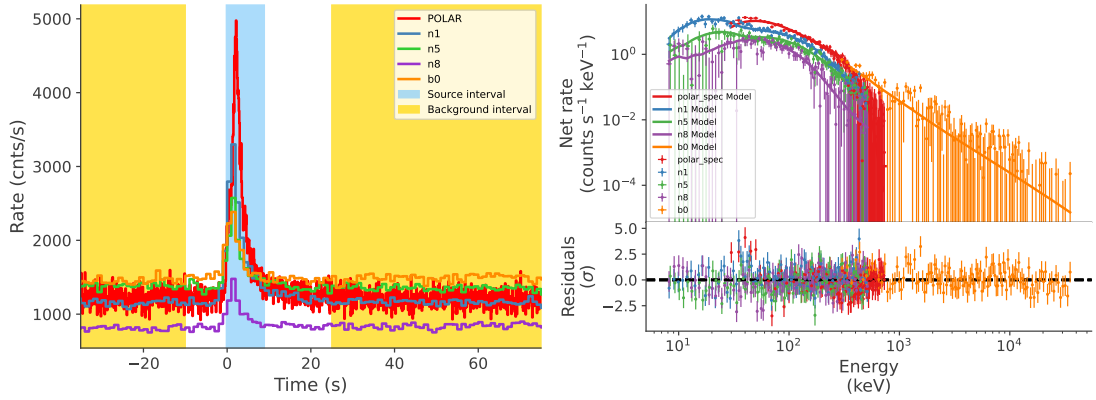

Figure 4.3: **Left:** GRB170114A light curve measured by POLAR and several NaI/BGO detectors of Fermi-GBM. The yellow region shows the background interval selections, while the cyan region correspond to the source selection. **Right:** GRB170114A spectrum (in data space) measured by POLAR and Fermi-GBM, fitted with a Band function [13].

The spectra are jointly fitted for all the selected detectors using a Band function [13], whose expression is shown in equation (1.2). The measured spectra and their respective fits are shown in the right plot of Figure 4.3, where a good agreement between the data and the Band model can be noticed. In parallel to the spectral fitting, scattering angle distributions are produced for different polarization angle and degree as a function of energy. The measured modulation curve can then be fitted against the polarization response. This can be done accounting for the spectral component by weighting the energy bins of the polarization response according to the spectral fit. The measured and fitted modulations are shown in the left plot of Figure 4.4, while the right plot is showing the corresponding polarization degree and angle plotted against each other.

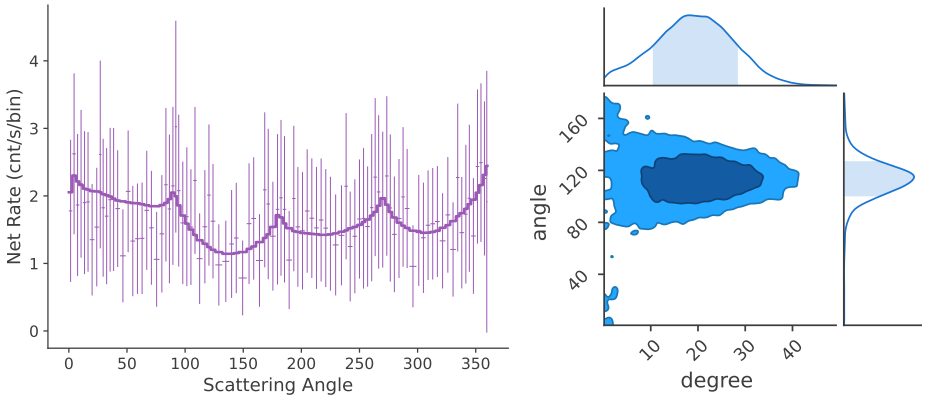

Figure 4.4: **Left:** Azimuthal scattering angle distribution measured by POLAR for GRB170114A and its best PD/PA modelling. **Right:** Corner plot showing the obtained polarization angle and polarization degree as a function of each other, as well as their respective posterior distributions.

It can be noticed that the measured scattering angle distribution does not follow a perfect squared cosine modulation as predicted by the Klein-Nishina cross-section described in equation (2.6). The reason for this more complex structure is explained by instrumental effects. A 90° spurious modulation is present due to the square geometry of the POLAR instrument. An additional 360° modulation is also produced by the fact that photons back scattering to the incoming direction have a greater chance of escaping the sensitive volume of the instrument. Furthermore, more complex effects exist due to non-uniformity of the MA-PMT efficiency. It is therefore crucial to have a complete knowledge of the instrument to be able to produce accurate spectral and polarization responses.

The same analysis is used for other GRBs observed by POLAR. Some of them are also jointly observed by Fermi-GBM, or even Swift-BAT and Konus-Wind, while some GRBs are only observed by POLAR. Most of the GRBs in the POLAR catalog are fitted using a Band function, except GRB170101A and GRB170127C, for which a cutoff powerlaw (CPL) function is used to describe the spectrum:

A deviance information criterion [207] was used on spectral-only analysis in order to determine the function that best described the spectrum of each GRB (Band or CPL).

$$N_E(E) = K\left(\frac{E}{100\ keV}\right)^{-\alpha} e^{-E/E_c} \tag{4.1}$$

with K the normalization constant in cnts $s^{-1}cm^{-2}keV^{-1}$, E the energy in keV, α the powerlaw index, and E_c the cutoff energy in keV.

The posterior distribution of the polarization degree obtained for the energy integrated analysis are shown in Figure 4.5 for 13 GRBs[1]. The distributions obtained for the polarization angle are also shown in the same figure, although not necessarily relevant for very low polarization levels. As discussed earlier in Chapter 3, the results are compatible with lowly polarized or even unpolarized

1 For the final GRB in the catalog, GRB161218B, an issue with the analysis software was encountered which did not allow to perform the analysis on this very weak GRB.

emissions. The light curves, spectra, and fluences of all these GRBs are provided in the POLAR catalog [128].

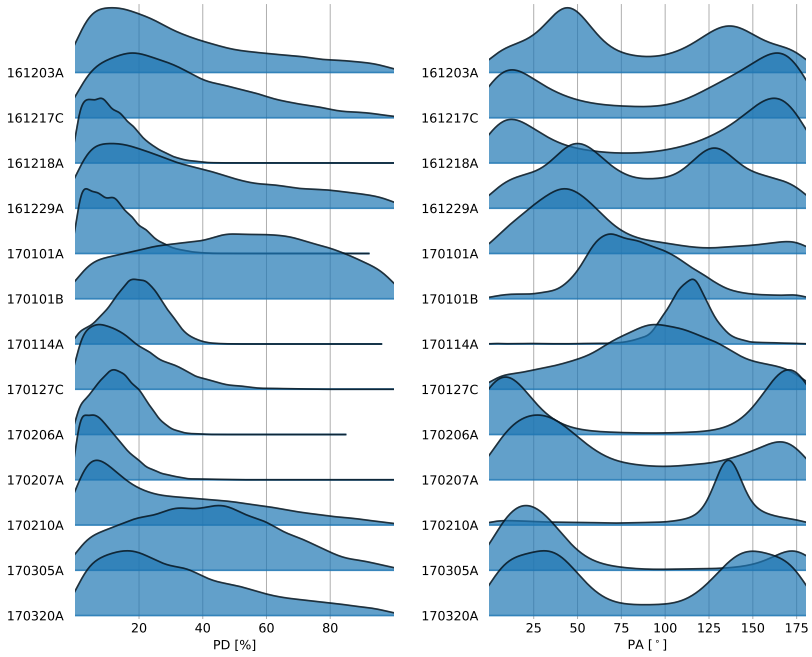

Figure 4.5: Posterior distributions of the polarization degree and angle obtained for the energy integrated analysis for the 13 brightest GRBs observed by POLAR.

4.3 ENERGY RESOLVED POLARIZATION ANALYSIS

4.3.1 *Heaviside fit of the PD versus energy*

We first investigate the energy dependence of the polarization degree. The simplest function to parameterize the PD as a function of energy is a Heaviside distribution:

$$PD = \begin{cases} PD_{low} & if\ E < E_{break} \\ PD_{high} & if\ E > E_{break} \end{cases} \qquad PA = cst. \tag{4.2}$$

This parametrization uses three parameters: the PD at low energies PD_{low}, the PD at high energies PD_{high}, and the energy break which separates the two energy bins E_{break}. Such parametrization is used for its simplicity, in order to check if the polarization degree is different at low and high energy. The polarization angle is kept constant, like in the case of the energy integrated analysis. The resulting corner plot showing the polarization parameters posterior results against each other is shown on the left of Figure 4.6.

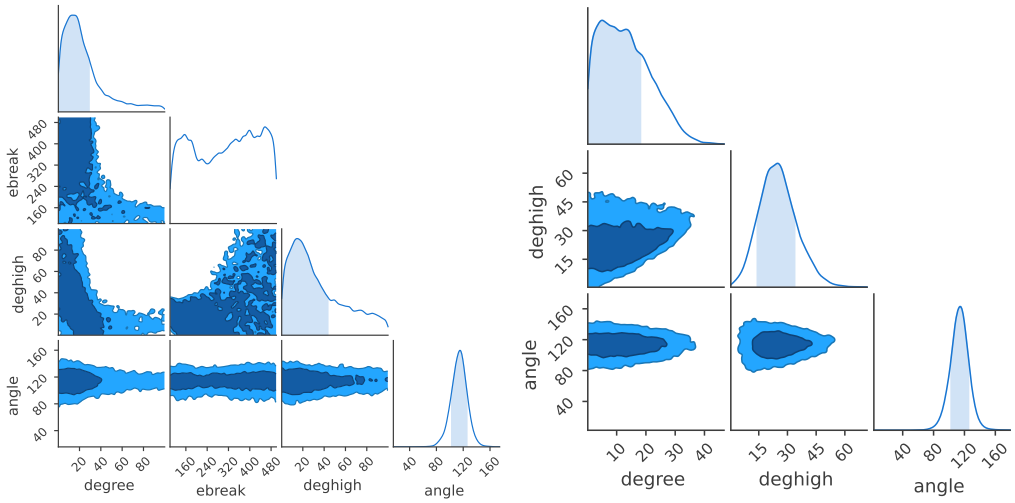

Figure 4.6: Corner plot showing the obtained polarization parameters as a function of each other and their respective posterior distributions when fitting the PD with a Heaviside function. **Left:** Heaviside fit on the polarization degree with a free break. The parameters are the PD at low and high energies, respectively called "degree" and "deghigh", the energy break "ebreak" and the polarization angle. **Right:** Heaviside fit on the polarization degree with an energy break fixed to 150 keV. The fit parameters are the same than in the previous case, except for "ebreak" that is now fixed.

The PD at low energy and the PA are obtained with the Heaviside fit are compatible with the energy integrated result. The posterior distribution of the PD for high energies is peaking at a slightly higher value, with a slower decaying tail towards high PD values compared to the PD distribution for low energies. However, the PD values obtained for the low and high energy bins are within one sigma of each other. No significant energy dependence is therefore found for GRB170114A using a Heaviside fit of the PD. Finally, it can be noticed that the energy break is not constrained at all. We therefore try to fix the energy break to 150 keV based on [155] to fit the PD as a function of energy:

$$PD = \begin{cases} PD_{low} & if\ E < 150\ keV \\ PD_{high} & if\ E > 150\ keV \end{cases} \qquad PA = cst. \tag{4.3}$$

The resulting parameters are shown on the right plot of Figure 4.6. The polarization angle is once again compatible with the energy integrated result. By looking at the distributions of the polarization degrees in the two energy bins, a hint can be observed for a slightly higher PD at high energies. But the two PD values being within 1 σ of each other, no significant energy dependence can be reported. A summary of the polarization parameters values obtained with the two fits compared to the energy integrated result are given in Table 4.1. The same exercise has been repeated by fixing the energy break to other values. The PDs at low and high energies as a function of the break are shown in Figure 4.7. The PD at high energies shows a tendency for higher values than the one at low energies, but no significant difference is observed between the two PDs.

	Energy integrated	$PD_{Heaviside}$ with a free break	$PD_{Heaviside}$ for E_{break}=150keV
PD [%]	$22.8^{+45.5}_{-12.3}$	-	-
PD_{low} [%]	-	$5.71^{+35.69}_{-1.20}$	$19.6^{+2.7}_{-15.5}$
PD_{high} [%]	-	$79.6^{+14.4}_{-70.0}$	$19.5^{+15.3}_{-4.0}$
PA [°]	117^{+9}_{-16}	115^{+10}_{-12}	109^{+15}_{-7}
E_{break} [keV]	-	334^{+111}_{-172}	150

Table 4.1: Mean and standard deviation of the polarization parameters for different fits (energy integrated, Heaviside polarization degree with a free or fixed energy break) extracted from the posterior distributions shown in Figures 4.4 and 4.6 [57].

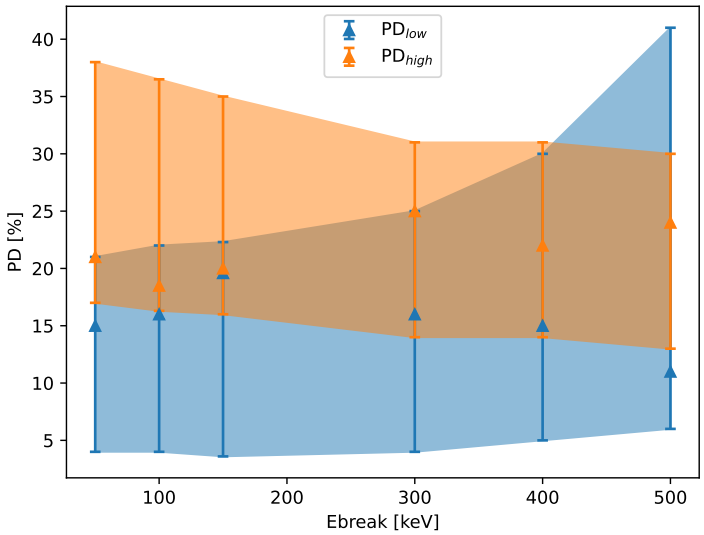

Figure 4.7: Polarization degree at low and high energies for a Heaviside fit with a fixed break, as a function of the energy break. The error bars and shadow region correspond to a 1 σ confidence level.

The Heaviside fit on the PD has been repeated on 13 GRBs of the POLAR catalog, for both cases discussed earlier, i.e. with a free energy break and fixing the break to 150 keV. The posterior distribution of the PA and the two PDs for each GRBs are compared to the energy integrated results in Figures 4.8 and 4.9. In the former case, the distribution obtained for the energy break is also shown, while it is no longer a fit parameter in the latter case since the value is being fixed.

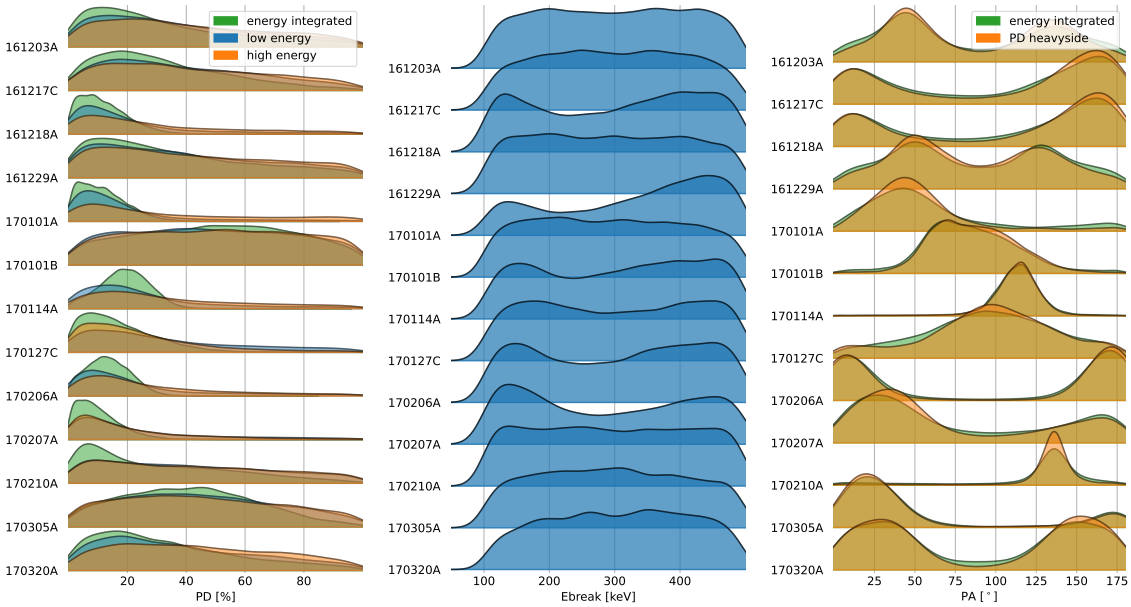

Figure 4.8: Resulting posterior distributions for the different parameters when fitting the polarization degree with a Heaviside function. The results are shown for the 13 brightest GRBs observed by POLAR. **Left:** Polarization degree at low and high energies compared to the energy integrated result. **Middle:** Energy break for the Heaviside fit. **Right:** Polarization angle obtained with the Heaviside fit compared to that obtained with the energy integrated analysis.

The PA is compatible with the energy integrated results for all GRBs and for both fit functions. In the case of a free energy break, no important difference can be observed between the energy integrated PD and the two PDs fitted with the Heaviside function, as depicted in Figure 4.8. The distributions for the last two PDs are just wider due to bigger errors since less statistics is used per energy bin compared to the energy integrated case. Furthermore, no strong constraint could be made on the energy break which shows a flat distribution, except at very low energies (below 100 keV) where the break is highly suppressed.

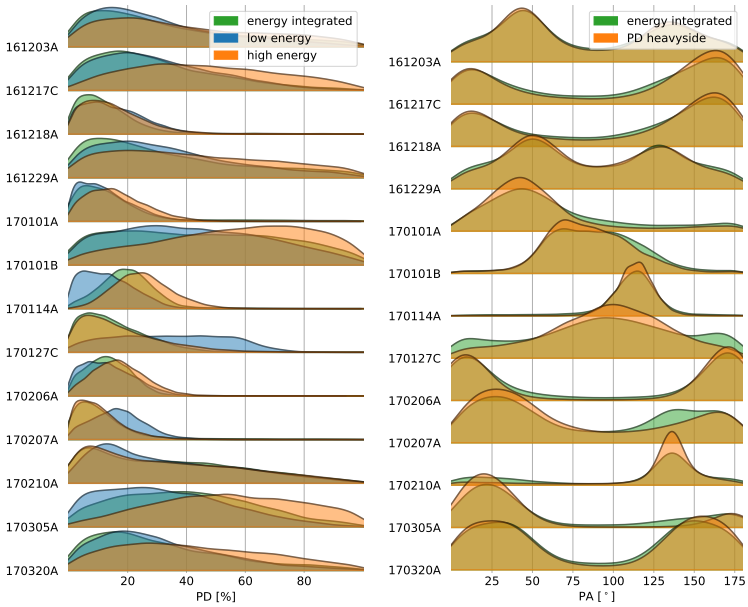

Figure 4.9: Resulting posterior distributions for the different parameters when fitting the polarization degree with a Heaviside function with a fixed energy break at 150 keV. **Left:** Polarization degree at low and high energies compared to the energy integrated result. **Right:** Polarization angle obtained with the Heaviside fit compared to that obtained with the energy integrated analysis.

In the case of a fixed 150 keV break, the PD at high energies tends to go towards higher values than the one at low energies for several GRBs, as observed for 170114A, but the difference between the two PDs is not significant enough to draw any conclusion.

4.3.2 *Linear fit of the PD versus energy*

Another simple function that is being used to look for potential energy dependence of the polarization degree is a linear function:

$$PD = PD_{intercept} + PD_{slope} \times \frac{E}{E_{max}} \; ; \quad E_{max} = 750 \; keV \; ; \quad PA = cst. \tag{4.4}$$

where $PD_{intercept}$ can be seen as the PD value extrapolated to 0 keV, PD_{slope} is the change in PD from null to maximum energy (750 keV), and E is the energy in keV. The polarization angle is kept constant versus energy, just like in the energy integrated standard analysis.

The resulting corner plot of the linear PD fit is shown in Figure 4.10 for GRB170114A. The polarization angle is compatible with the one obtained for the energy integrated analysis. The polarization degree intercept is also consistent with the polarization degree from the energy integrated result. The slope of the polarization degree is not constrained at all and is linearly correlated with the intercept, indicating that no significant linear dependence is found.

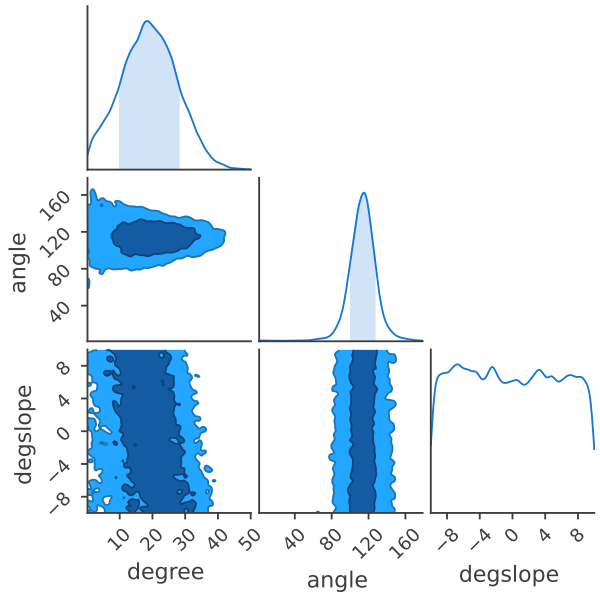

Figure 4.10: Corner plots of the polarization parameters for a linear fit of the PD versus energy. The fit parameters are the polarization angle, the polarization degree intercept (extrapolation of the PD at null energy), and the polarization degree slope in units of %/750 keV (due to the energy normalization in the linear function). These parameters are respectively called "angle", "degree", and "degslope" in the plot.

Similar behavior is observed for the 13 GRBs shown in Figure 4.11. The PD intercept and PA are respectively compatible with the energy integrated PD and PA, while the posterior distribution of the slope of the polarization degree is flat over the entire probed range. No significant linear energy dependence of the PD is therefore observed for any of the analyzed bursts.

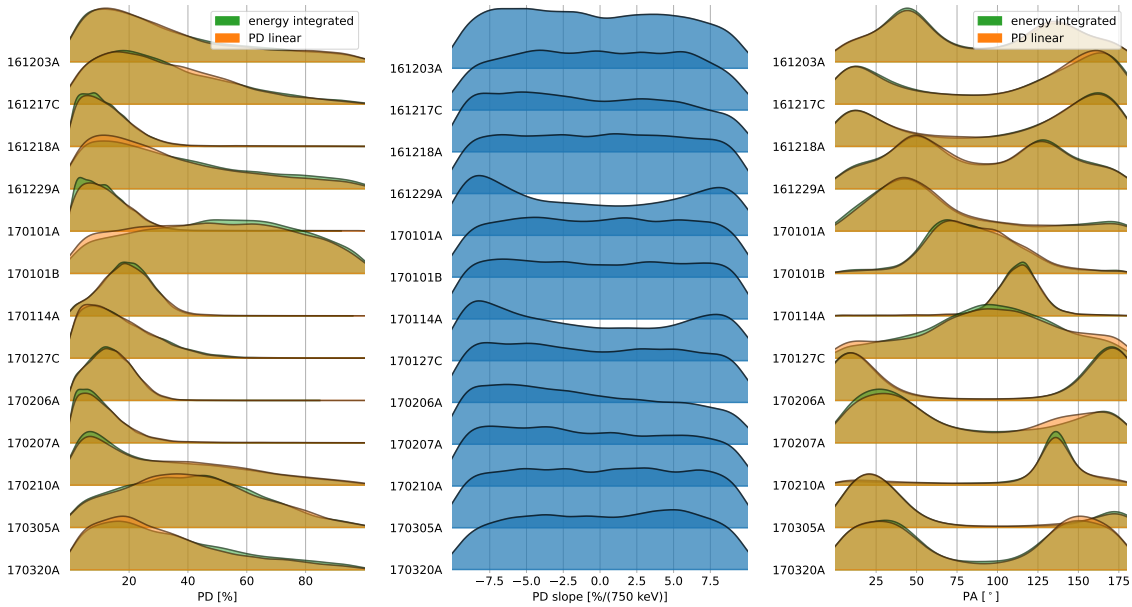

Figure 4.11: Resulting posterior distributions for the different parameters when fitting the polarization degree with a linear function. The results are shown for the 13 brightest GRBs observed by POLAR. **Left:** Polarization degree intercept (extrapolation of the PD at null energy) compared to the energy integrated result. **Middle:** Polarization degree slope in units of %/750 keV (due to the energy normalization in the linear function). **Right:** Polarization angle obtained with the linear fit on the PD compared to that obtained with the energy integrated analysis.

4.3.3 *Linear fit of the PA versus energy*

A linear function has also been used to search for energy dependence of the polarization angle:

$$PA = PA_{intercept} + PA_{slope} \times \frac{E}{E_{max}} \; ; \quad E_{max} = 750 \; keV \; ; \quad PD = cst. \tag{4.5}$$

where $PA_{intercept}$ can be seen as the PA value extrapolated to null energy, PA_{slope} is the change in PA from null to maximum energy (750 keV), and E is the energy in keV. This time the polarization degree is kept constant versus energy.

The posterior results of the linear PA fit are shown in the form of a corner plot in Figure 4.12 for GRB170114A. The result is similar to what was observed when linearly fitting the PD as a function of energy, but with th role of PD and PA inverted. That is, the PD and PA intercept are respectively compatible with the energy integrated result, while the slope of the PA is not constrained and is linearly correlated with the PA intercept. Once again, as shown in Figure 4.13, similar results are found for the 13 analyzed GRBs. No significant linear energy dependence of the PA is observed.

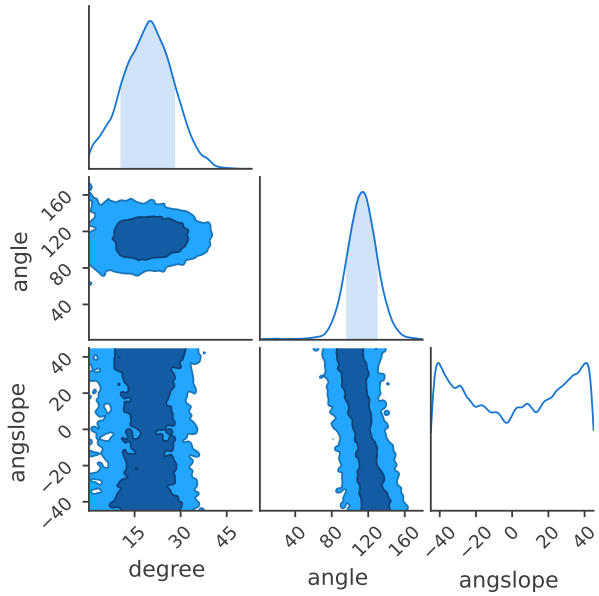

Figure 4.12: Corner plots of the polarization parameters for a linear fit of the PA versus energy. The fit parameters are the polarization degree, the polarization angle intercept (extrapolation of the PA at null energy), and the polarization angle slope in units of °/750 keV (due to the energy normalization in the linear function).

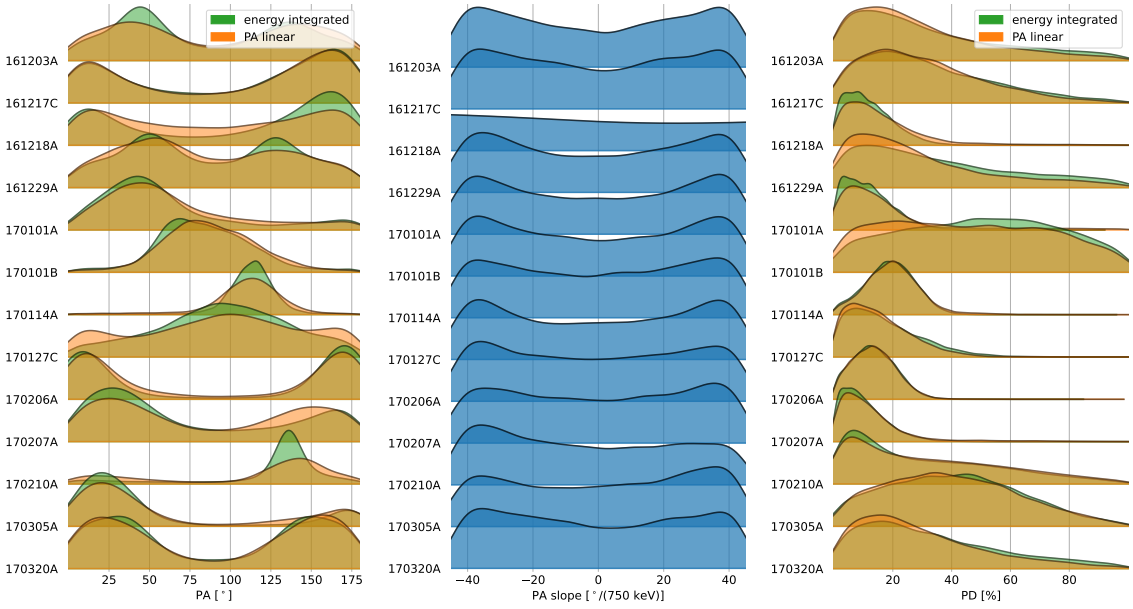

Figure 4.13: Resulting posterior distributions for the different parameters when fitting the polarization angle with a linear function. The results are shown for the 13 brightest GRBs observed by POLAR. **Left:** Polarization angle intercept (extrapolation of the PA at null energy) compared to the energy integrated result. **Middle:** Polarization angle slope in units of °/750 keV (due to the energy normalization in the linear function). **Right:** Polarization degree obtained with the linear fit on the PA compared to that obtained with the energy integrated analysis.

4.4 CONCLUSIONS AND FUTURE PROSPECTS

After having studied energy and time integrated and time-resolved polarization of the brightest GRBs detected by POLAR, the energy dependence of polarization had to be studied as it can bring important information to disentangle between the existing emission models. Energy-dependent fitting of the polarization parameters has therefore been implemented in the existing Bayesian framework, `threeML`, as well as in the `astromodels` package and `polarpy` plugin also used in the analysis process. Even though the energy dispersion and restricted statistics are limiting factors for studying energy dependence of polarization, the analysis has been performed on the POLAR data, and the analysis pipeline is ready for future missions such as POLAR-2.

The detected GRB, 170114A, has first been used to perform the energy resolved analysis, followed by 12 other GRBs from the POLAR catalog. On one hand, the polarization degree has been fitted using both a Heaviside and a linear function. The linear fit did not show any energy dependence, while the PDs obtained at low and high energies for the Heaviside fit were not strongly constrained. In order to reduce the number of parameters, the energy break, which was not constrained at all in the previous Heaviside fit, has been fixed to 150 keV. For GRB170114A, the PD at low energy is compatible with that obtained for the energy integrated result, while the PD at high energy appears to be slightly higher. But no strong conclusion could be made since the PDs at low and high energies are about 1 σ away from each other, even when changing the fixed value of the energy break. This was also observed for several other GRBs. The polarization angle has also been fitted versus energy using a linear function. No significant energy dependence could be observed for any of the analyzed GRBs. However, the results are not constraining enough to rule out any theoretical models either from photospheric [155] or synchrotron [84] emission.

Other energy dependent models could be tried, for instance fitting both PD and PA in parallel with a Heaviside or linear function. This would add new fitting parameters, which would make the analysis script very computationally demanding. But such fits could be implemented for the POLAR-2 mission as it will be able to gather more statistics, especially below 50 keV. Using the POLAR-2 effective area and polarization sensitivity μ_{100} as a function of energy, predictions on its sensitivity to energy dependence of polarization compared to POLAR can be made. Such comparison can be produced by artificially generating several GRBs with different properties and a fake energy dependent polarization, and see how well this energy dependence can be resolved using the POLAR and POLAR-2 responses. This work would be interesting in the frame of a future publication on this energy resolved study [8].

It should finally be noted that due to the positive definite nature of the polarization degree, one should limit the number of attempts to fit for energy dependent polarization. It could indeed be tempting to try many energy dependent fittings until finding the more significant energy dependence. However,

this is statistically wrong as the significance goes down with the number of attempts and the results should be corrected for that.

Part III

DESIGN AND DEVELOPMENT OF POLAR-2, THE NEXT GENERATION GRB DEDICATED POLARIMETER

Even though it operated for a shorter period than originally planned, the POLAR mission was very fruitful it terms of science outcome. It detected 55 GRBs during its 6 months of operation, 14 of which could be analyzed for polarization. The prompt emissions of these GRBs have been found to be compatible with a lowly polarized or unpolarized flux. Time-resolved analysis shown, for two of the brightest detected GRBs, an interesting time evolution of the polarization angle with a higher polarization degree, washed out in time-integrated analyses. Energy resolved polarization analysis was also carried out in the frame of this thesis, and no significant energy dependence of the polarization parameters could be observed. In addition to the exciting science output of POLAR, the main conclusion on GRB polarization is that more statistics is needed in order to provide detailed time and energy resolved polarization results. A more sensitive instrument, based on the POLAR legacy, is therefore under development. Called POLAR-2, it is composed of 4 times more polarimeter channels and have seen some technological upgrades to further improve its sensitivity, especially at low energies. Scheduled for a launch in 2025 to the China Space Station, it aims to operate for at least two years in low Earth orbit and bring detailed polarization measurements of about 50 GRBs per year. The design and development of the instrument is described in this part, as well as all the characterization, simulation, and qualification work that was accomplished within the scope of this thesis.

5

POLAR-2 DESIGN AND DEVELOPMENT

After the premature end of the POLAR mission and thanks to its scientific success, a more sensitive successor instrument, creatively named POLAR-2, has been proposed. In June 2019, the POLAR-2 mission has been accepted for a launch to the China Space Station (CSS), currently scheduled for 2026. It consists of a Compton polarimeter 4 times bigger than POLAR, with an improved sensitivity by one order of magnitude thanks to several technological upgrades and design optimization. With a nominal life-time of 2 years, the aim of the POLAR-2 mission is to provide measurements of about 50 GRBs every year with quality equal or better than those provided by POLAR. The overall instrumental design is first discussed, followed by a detailed description of the polarimeter module. The installation of the polarimeter on the CSS as a scientific payload and its preliminary science performance are then presented. Finally, the space qualification through irradiation, vibration and shock, and thermal vacuum tests is described.

5.1 POLAR-2 INSTRUMENT DESIGN

An exploded view showing the main parts of the POLAR-2 instrument is provided in Figure 5.1. The polarimeter modules, individually housed in a 0.75 mm thick Carbon Fiber Reinforced Polymer (CFRP) socket, are mechanically assembled in a 10×10 configuration with a 57 mm pitch. Each module, whose design is described in Section 5.2, consists of a 8×8 array of scintillators. The sensitive part of the modules, that is the top part containing the scintillators, stick out of the polarimeter Aluminum 7075 (or similar) grid. A carbon fiber top cover is placed on top of the 10×10 array of the polarimeter modules, with a thickness of 2.25 mm on the top and 3.25 mm on the sides in order to shield the scintillators from low energy electrons. Under the polarimeter grid are mounted the Low Voltage Power Supply (LVPS) and Back-End Electronics (BEE) grids. The BEE grid, located at the bottom of the instrument, is hosting the primary electronics responsible for sending orders to the individual Front-End Electronics (FEE), applying the trigger logic on the instrument level, and collecting the data. The same grid also contains the communication system used to exchange information with the space station, as well as the first stage of the LVPS responsible for receiving 100 V from the CSS and converting them into 28 V inputs for the LVPS Hub. Five LVPS Hubs are mounted on the middle LVPS grid. Each of these Hub is collecting the data from 20 polarimeter modules, and powering them with 3.8 V converted from the 28 V voltage provided by the LVPS first stage. The instrument dimensions are within a $500\times600\times600$ mm^2 envelope in order for the payload to fit through the doors inside the CSS during the installation. The total mass of the instrument is 101.5 kg without accounting for the different adapters needed for the installation (see Section 5.3).

The top cover thickness is not the same on the sides and on the top in order to have a cumulated carbon fiber thickness of 4 mm on all sides when accounting for the modules' socket and mechanics. The 4 mm of carbon fiber gives the same shielding than that of POLAR, which was shown to be sufficient during data analysis.

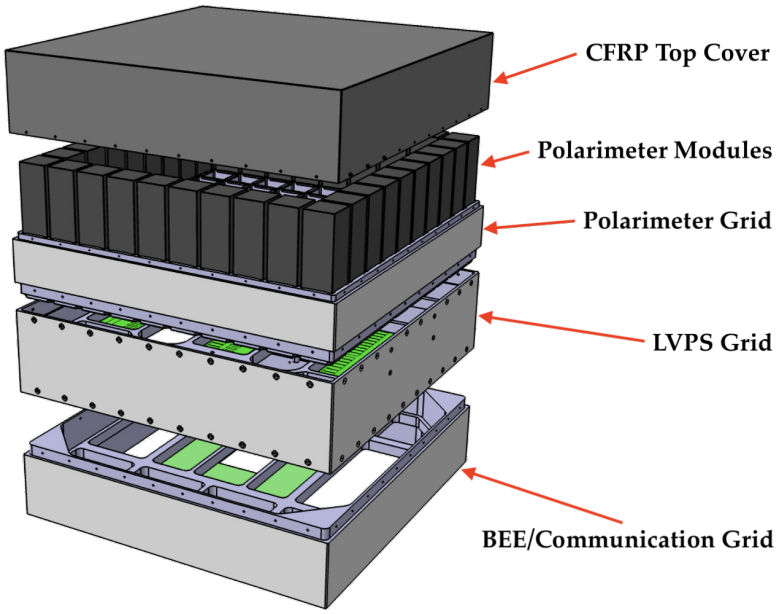

Figure 5.1: Exploded view of the POLAR-2 instrument.

The trigger logic for polarization events, which have at least 2 bars (or channels) triggering, is based on the two thresholds of the CITIROC ASIC [29]: the charge threshold and the time threshold. Figure 5.2 shows a state machine diagram of the POLAR-2 trigger logic. If at least a single channel goes above one of these two thresholds, the peak sensing is started for acquisition. The 64 trigger lines of the two ASICs are read out by the FPGA, which applies the local module triggering logic. If the time multiplicity (i.e. the number of channels that went over the time threshold) $trig_t$ is greater than a fixed number of channels N, the event is discarded in order to get rid of cosmic-ray induced events. In the case of a 2-bars event within a single module, that is $1 < trig_t < N$, the ADC readout is directly started. The ADC is also started if any channel is triggering on the charge threshold : $trig_c > 0$. If at least one channel is triggering the time threshold, $trig_t \geq 1$, the FEE will ask the BEE if another module has at least one channel above threshold in a set time interval of 100 ns. For $trig_t = 1$, the BEE will send back a positive answer and start the acquisition only if another module has at least a bar triggering. If the BEE sends back a positive answer, the event will be read out. This is the case if an event is triggering 2 bars in 2 different polarimeter modules. An additional type of event is the pedestal events, for which the BEE is forcing an FEE to acquire pedestal levels of all 64 channels. Physical events have priority over pedestal events, the latter can not be taken if the peak sensing is activated. Another special kind of event is pre-scaled events, which are high multiplicity events being stored despite the $trig_t < N$ condition mentioned earlier every M occurrence of such events.

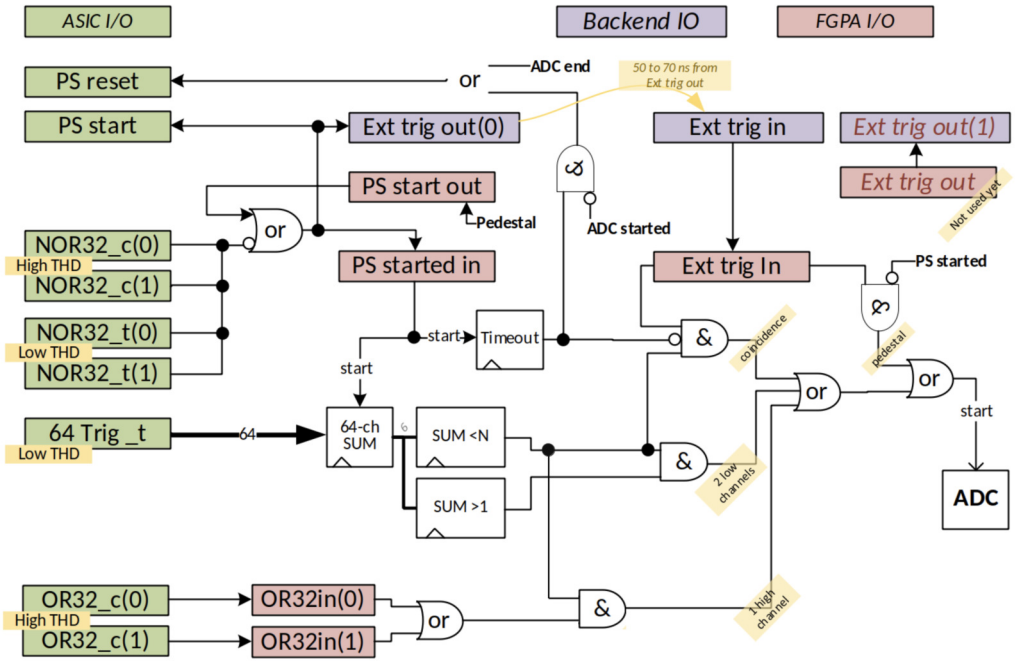

Figure 5.2: State machine diagram of the trigger logic foreseen to be employed in POLAR-2 (taken from [132], with permission).

5.2 POLARIMETER MODULE DESIGN

The polarimeter module is a central part of the POLAR-2 detector. It consists of 8×8 plastic scintillator bars, wrapped in reflective foils, and read out by Silicon PhotoMultiplier (SiPM) arrays. It also contains the FEE, responsible to pre-processing the signal of the sensors and to send it to the central electronics. The FEE is mounted on a mechanical frame, optimized for thermal cooling of the sensors. An exploded view of the CAD model of the polarimeter module can be seen in Figure 5.3, while the individual parts of the module are described here.

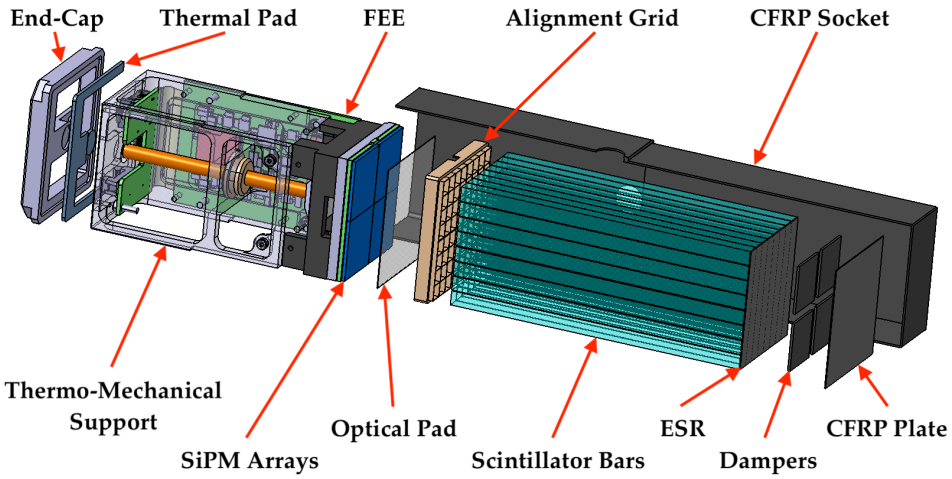

Figure 5.3: Exploded view of a POLAR-2 polarimeter module.

5.2.1 *Polarimeter Targets*

Making the scintillators wider by 0.1 mm increases the effective area by 3.5%.

The target is composed of 64 scintillator bars of dimension 5.9×5.9×125 mm^3. The dimensions of the scintillators have been changed compared to the 5.8×5.8×176 mm^3 in POLAR. The width of the bar has been increased by 0.1 mm, minimizing the dead space in the polarimeter, since the pitch between channels is now 6.2 mm instead of 6.08 mm. The length of the bar has been optimized for improving the Signal-to-Noise Ratio (SNR) based on simulations [131]. It has been found that since the background scales with the volume of the detector and the signal scales with its surface, shortening the bars leads to an improvement of SNR. A compromise between SNR and statistics was found by choosing a scintillator length of 125 mm.

While in POLAR Vikuiti reflective sheets were placed between rows of 8 bars, in between which strips or Vikuiti were inserted in the perpendicular direction, the POLAR-2 scintillator bars are wrapped individually, as shown in Figure 5.4. As better described in Sections 5.2.4 and 7.9, the bars are wrapped with two types of reflective foils: 4 Vikuiti strips surrounded by a Claryl foil folded around the bar. The POLAR-2 target is therefore much more dense since 4 layers of reflector are now separating each bars, instead of a single layer in POLAR. These distance between two scintillator surfaces is 300 μm, gap in which two

8 μm Claryl layers and two 65 μm Vikuiti layers are placed, without forgetting the 0.1 mm thick Kapton tape used on one side to close the wrapping.

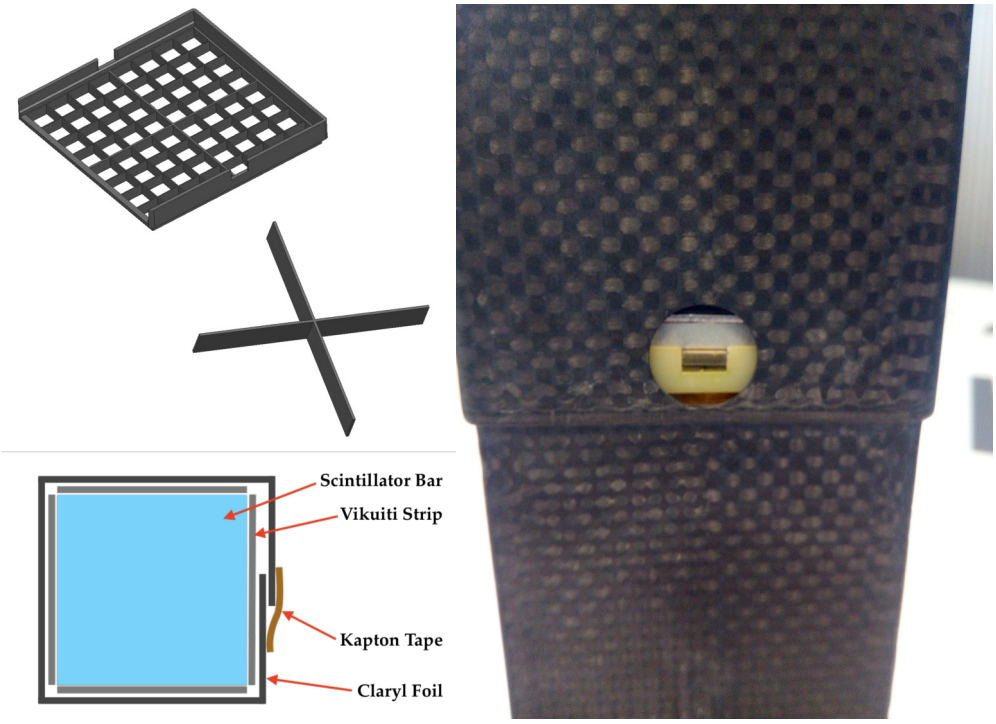

Figure 5.4: **Top Left:** CAD design of the plastic alignment grid and cross. **Bottom Left:** Schematic view of the disposition of the different wrapping layers around a scintillator bar. **Right:** Assembled module with an aperture on the side of the carbon socket to observe the stacking of the different elements and the proper insertion of the PCB into the alignment grid.

The FEE, which will be presented in the next Section, contains 4 SiPM arrays, each of dimensions 25×25 mm^2. An array is composed of 4×4 channels, of 6×6 mm^2 each, separated by a 200 μm of passive Silicon dioxide (SiO_2). The four arrays are soldered next to each other on the Printed Circuit Board (PCB), with a 0.1 mm gap in between the 2 × 2 arrays. While the dead space between two channels of the same array is 200 μm, the dead space between two adjacent channels of different arrays is therefore 2 × 200 μm + 0.1 mm = 500 μm. This is the case between the 4th and 5th lines and between the 4th and 5th columns in the 8×8 matrix. A middle cross, whose design is shown on the left image of Figure 5.4, is therefore placed at the top of the target instead of an alignment grid to act as a spacer between the four quarters of the module.

Thanks to the possibility of printing very thin mechanical pieces at the European Organization for Nuclear Research (CERN) polymer lab, the plastic alignment grid used to align the 64 bars on the sensor side has also been redesigned with much thinner elements than in POLAR. The thickness of the separation between channels of the same array is 0.2 mm, while the thickness of the central separation is 0.5 mm like for the middle cross. The reason for the bigger central separation is purely mechanical, as it is due to the use of 4 separated SiPM arrays. Having very thin mechanics for this alignment grid

The material used to 3D-print the plastic grids is the so called Accura25 *plastic resin.*

allowed to remove the truncation at the extremity of the bar (see Section 3.2.1), not needed anymore for mechanical robustness, greatly improving the contact surface between the scintillator and the sensor. While the POLAR bars were reduced from a 5.8×5.8 mm^2 surface down to 5.0×5.0 mm^2 with the truncation, the POLAR-2 bars have a 5.9×5.9 mm^2 section up to the extremity. This implies an increase of the contact surface of 39.24%, important for enhancing the optical sensitivity of the module. The CAD model of the alignment grid is shown on the left side of Figure 5.4. The outside frame is only composed of three sides, the fourth one being opened for flex part of the FEE (see next section). Two notches can be noticed on the sides of the grid's outside frame. Their purpose is to properly align the FEE during the assembly process, the PCB having two protuberances just fitting the notches. A picture of an assembled module with an opening on the carbon socket showing the insertion of the PCB in the alignment grid is displayed on the right of Figure 5.4.

The target development and its detailed optical characterization and simulation are described in Chapter 7.

5.2.2 *Front-End Electronics Development*

The POLAR-2 Front-End Electronics (FEE), shown in Figure 5.5, is composed of three rigid parts separated by two flexes. The aim of the flex parts is to fold the FEE around its thermo-mechanical support in order to extract the heat from the SiPMs, as described in Section 5.2.3. The use of SiPMs is one of the main technological upgrades of the polarimeter modules compared to POLAR, which employed MA-PMTs. Advantages of using this more recent technology is the higher detection efficiency (see Chapters 6 and 7), the compactness, and the mechanical robustness, important for surviving extreme launch condition (as discussed in Section 5.7). The main drawback of using SiPMs is the dark noise which is reduced by operating the sensors as cold as possible (see Section 5.2.3), and the increase of dark noise with radiation damage, as discussed in Chapter 6.

The first rigid part is hosting the SiPMs, the middle one the main electronics (ASICs, FPGA, ADCs, etc.), and the third rigid part hosts the connectors (for power, signal, and FPGA programming) and drivers for cooling and heating system. The FEE contains 10 layers of electronic tracks and a total of about 800 electronic components.

RC filters are the bias capacitor and resistor coupled to the SiPM cathod.

The SiPM rigid part has dimensions of 50.8×50.8 mm^2. The four SiPM arrays are mounted on one side of the PCB. The other side is hosting RC filters for each SiPM channel as well as 8 power resistors and 3 Negative Temperature Coefficient (NTC) thermistors. The role of the 8 power resistors is to heat up the SiPMs for radiation damage annealing, as discussed in Chapter 6. The NTCs are used to monitor the temperature of the SiPMs and apply a live correction to their bias voltage, since the breakdown voltage of the SiPMs is temperature dependent. Based on the readout of the NTCs, the FPGA will tune the bias voltage in order to keep the over-voltage constant with time in case of temperature variations.

An 8-bit DAC, called *inputDAC*, is also used in the CITIROC to tune the bias voltage of each channel, to wash out variations of breakdown voltage among the 64 SiPM channels of a module. The square shape of this PCB part has two small protuberances on the sides for mechanical alignment in the notches of the plastic grid, as discussed in the previous section.

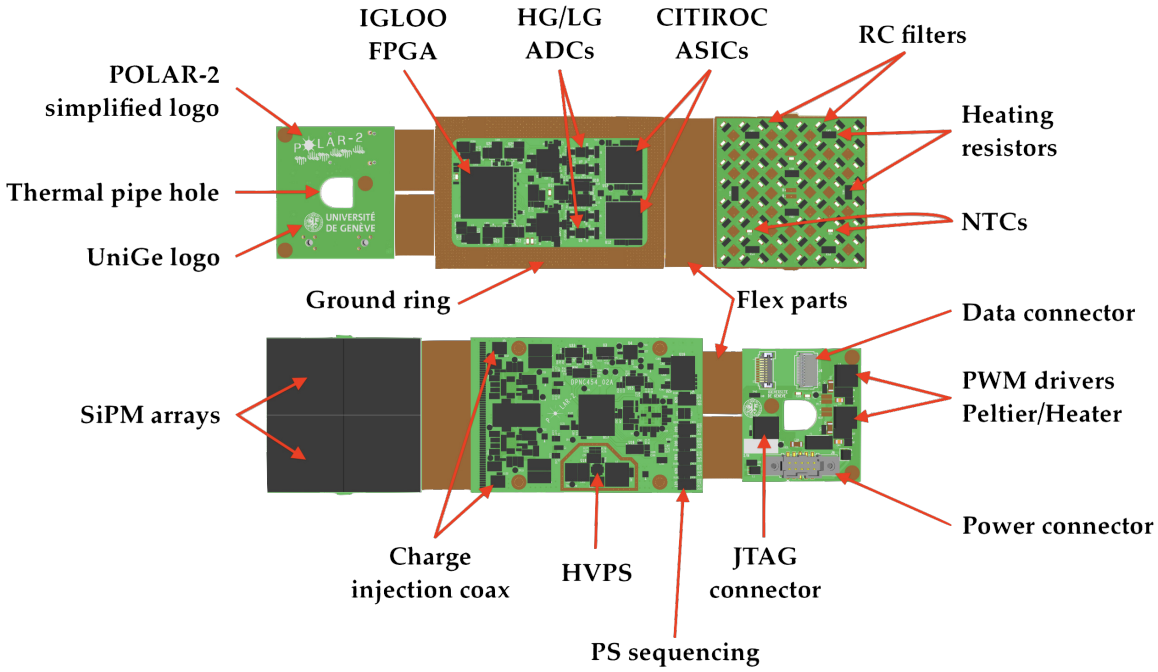

Figure 5.5: Last version of the POLAR-2 front-end electronics and its main components.

The main rigid part of the PCB has dimensions of 50.8×76 mm^2. Components are mounted on both sides of the PCB. One side is facing the inner part of the module for thermal cooling as discussed in the next section. It hosts the two CITIROC ASICs, the IGLOOv2 FPGA, and a lot more components surrounded by a ground ring for thermal and grounding connection to the mechanical support. An NTC is placed next to the FPGA to monitor the temperature of the hottest region of the FEE. The diagram shown in Figure 5.6 gives an idea of the architecture of the POLAR-2 FEE. The other side of the PCB is hosting an LT3482 DC/DC converter to bias the SiPMs, micro-coax connectors for artificial charge injection during testing, and many other electronic components. A Peltier element is used to cool down the SiPMs in order to operate them with the lowest possible temperature and reduce its dark count rate. This thermo-electric cooling unit is directly mechanically placed at the back of the SiPM arrays. The two cables of the Peltier element are soldered on two pads on the edge of the PCB in order to provide the necessary power to cool down the sensors.

The final rigid part has dimensions of 43.6×38.9 mm^2 with a hole in the center for heat extraction (see Section 5.2.3). It is hosting three connectors and two Pulse-Width Modulation (PWM) drivers for the heating resistors and Peltier element. The three connectors are a JTAG conector for flashing the FPGA, a T2M-105-01-L-D-SM-DS connector from Samtec for powering the module (3.8 V),

and a firefly connector from Samtec for the signal Low Voltage Differential Signaling (LVDS) pairs. The power and signal connectors are respectively connected to the LVPS Hub through a Teflon cable and a firefly cable from Samtec.

Early stage development of the polarimeter modules was done using a simple FEE only containing SiPMs and RC filters with a micro-coax connector per channel. Each channel was then connected to an adapter board to be used with Front-End Board (FEB) developed in Geneva for the Baby MIND experiment [185], also based on the CITIROC ASIC. This allowed for early data acquisition in parallel to the design of the complex POLAR-2 FEE.

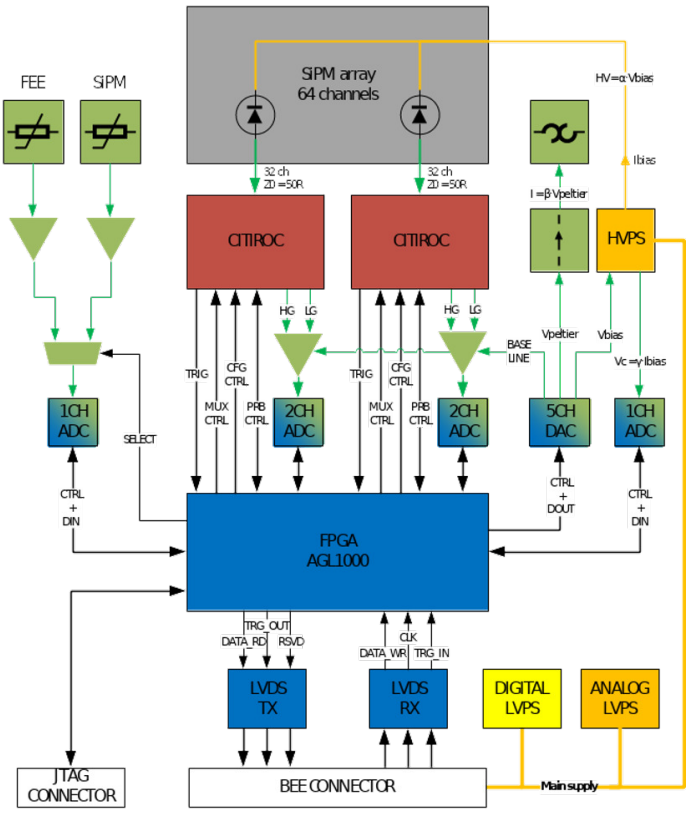

Figure 5.6: Diagram of the POLAR-2 front-end electronics. [132]

5.2.3 *Thermo-Mechanical Frame*

As previously mentioned, one of the main drawback of employing SiPMs over MA-PMTs for the scintillator readout is their dark noise. This dark noise is caused by microcells that are triggered via thermal excitation, and is therefore proportional to the operating temperature. The SiPMs should therefore be operated at temperatures as low as possible. A Peltier element is therefore placed directly on the back of the SiPMs to cool them down. The heat produced on the other side of the Peltier is then extracted with a copper bar directly connected to the back of the module. The end-cap, in which the other extremity of the copper bar is encapsulated, is thermally connected to the main polarimeter aluminum frame using a thermal pad. The FEE is folded on 3 faces of its aluminum support,

by which the copper bar is held using plastic rings. The aluminum support is mounted on a polyether ether ketone (PEEK) base in order to avoid thermal conduction between the back of the module and the SiPMs, which would re-inject heat into the sensors. The hottest part of the FEE, namely the ASICs and FPGA, are irradiating their heat directly onto the aluminum support. The design of the module thermo-mechanical support is shown in Figure 5.7. The heat is propagating to the main payload structure. Two sides of the payload facing deep space are painted with a special white paint to irradiate the heat out. The other two sides, which face neighbor payload with unknown thermal behavior, as well as the top of the instrument, facing deep space, are covered with a Multi-Layer Insulation (MLI). ANSYS thermal simulations together with thermal vacuum tests (see Section 5.8) are used to model and optimize the thermal behavior of the instrument.

The FPGA has a power consumption of 1 W and each ASIC of 350 mW.

The white paint, CovaTherm from Covalba, has been space qualified by the collaboration for Atomic Oxygen, UV-C [122], and outgassing.

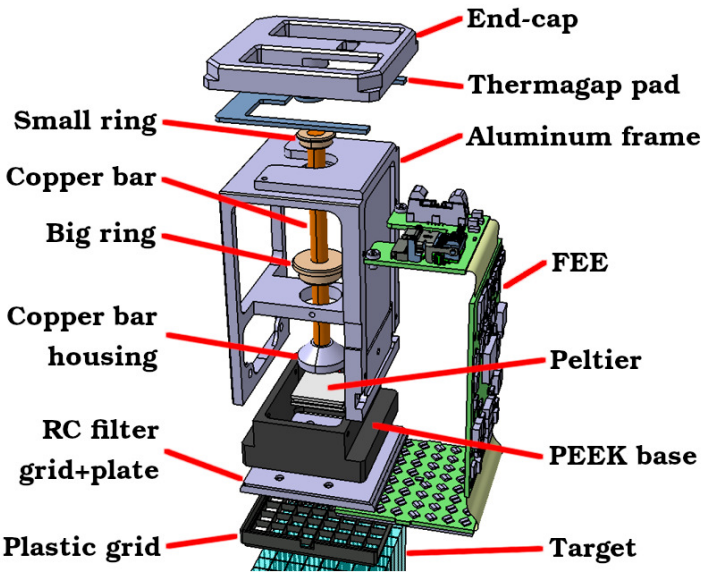

Figure 5.7: Thermo-Mechanical design at the the module level. [53]

5.2.4 *Module assembly*

A detailed procedure for assembling the POLAR-2 polarimeter modules has been developed and optimized along the years [53], since a great mechanical precision is needed to properly mount the targets. The 64 scintillator bars first have to be individually wrapped with 4 strips of Vikuiti surrounded by a foil of Claryl reflector using a specially developed mechanical jig. The final step of the highly complex wrapping process, which consists of closing the reflecting foils around the scintillator bar using 3 strips of Kapton tape, is shown on the left of Figure 5.8. Details and optical characterization of these reflective foils are presented in Section 7.1.1.

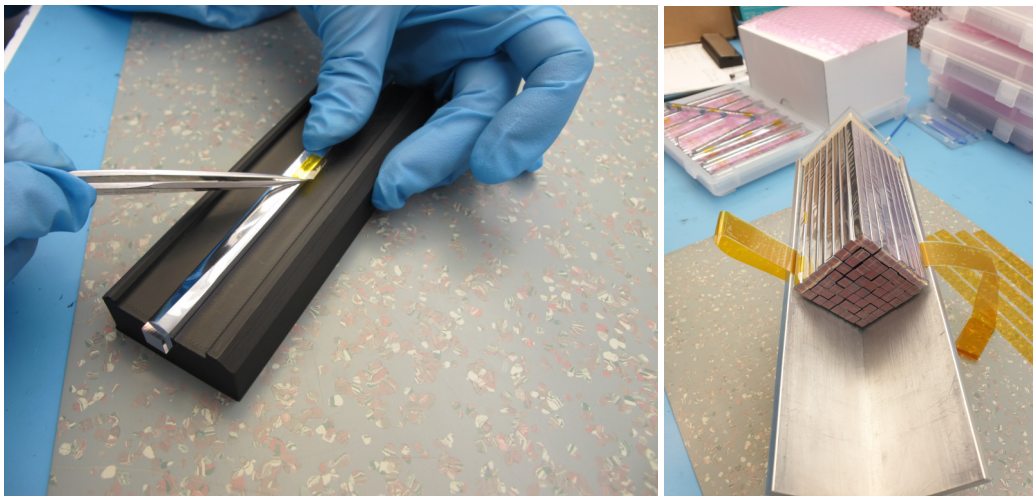

Figure 5.8: **Left:** Wrapping of a POLAR-2 scintillator bar [53]. **Right:** Fully wrapped target being assembled in the plastic alignment grid [53].

An L-shaped support hosting the plastic alignment grid is used to insert the 64 wrapped bars individually. The middle plastic cross is placed at the top extremity of the module when a quarter of the scintillators are inserted, as can be seen in Figure 7.1. Once the 64 bars are inserted (see right picture of Figure 5.8), the target is held together with 4 rigid Vetronite thin plates attached with Kapton tape. A 50×50 mm Vikuiti sheet is placed on the top of the target together with 4 Sorbothane damping pads placed in between two 0.5 mm thick carbon fiber plated with the same dimensions than the Vikuiti piece. The role of these Sorbothane pads is to dampen the vibration at which the module is exposed during the extreme conditions of the rocket launch. The assembled target is then inserted into a carbon fibre socket.

In parallel to the target assembly, a 150 μm thick optical pad based on the MAPSIL QS1123 RTV silicone is directly molded on the four SiPM arrays [113], as depicted in Figure 7.17. The FEE is then assembled to its thermo-mechanical frame described in Section 5.2.3. The assembly is subsequently inserted on top of the target in the carbon socket using a guiding carbon fibre plate until the PCB fits in the notches of the plastic alignment grid. The module can then be inserted in the polarimeter grid and closed using the end-cap and its thermal pad. The role of the thermal pad is not only to ensure a good thermal contact between the FEE and the main instrument frame, but also to apply pressure on the module so that a good optical coupling between the FEE and the target is guaranteed. In order to characterize the mechanical behavior of this thermal pad and to ensure that the compression effect is persistent, a sample of the thermal pad was compressed and the compression force due to the elasticity of the material was monitored with time. A measurement of the force temporal evolution from a compressed sample of thermal pad due to the material elasticity is shown in Figure 5.9.

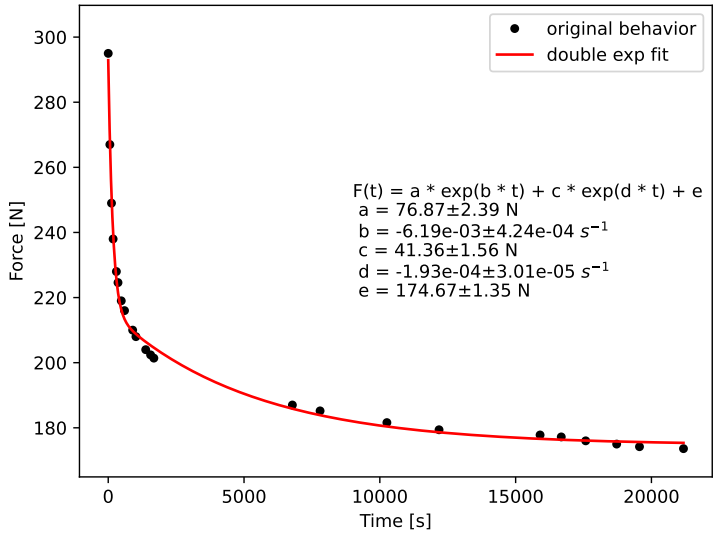

Figure 5.9: Time evolution of the force exercised by a compressed sample of thermal pad due to a 20% compression.

5.2.5 *Module calibration setup*

A calibration setup has been developed at CERN in order to be able to scan the polarimeter channel by channel with a polarized source. The X-Y scanning system is based on motorized x-y axes from OPENBUILDS mounted on a mechanical frame made of aluminum profiled bars [122]. The polarimeter grid can be directly mounted on the table, on top of which the X-Y axes will scan the instrument. A 365 MBq ^{241}Am source is used for polarization calibration. In order to get a polarized source of 59.5 keV photons from the Americium source, a special lead block was designed to scatter the photons 90° from the incoming direction and get a highly polarized source. The design of the lead block as well as a picture of the X-Y table setup at CERN are shown in Figure 5.10. Other sources such as ^{137}Cs or ^{90}Sr are also available for measurements at higher energies.

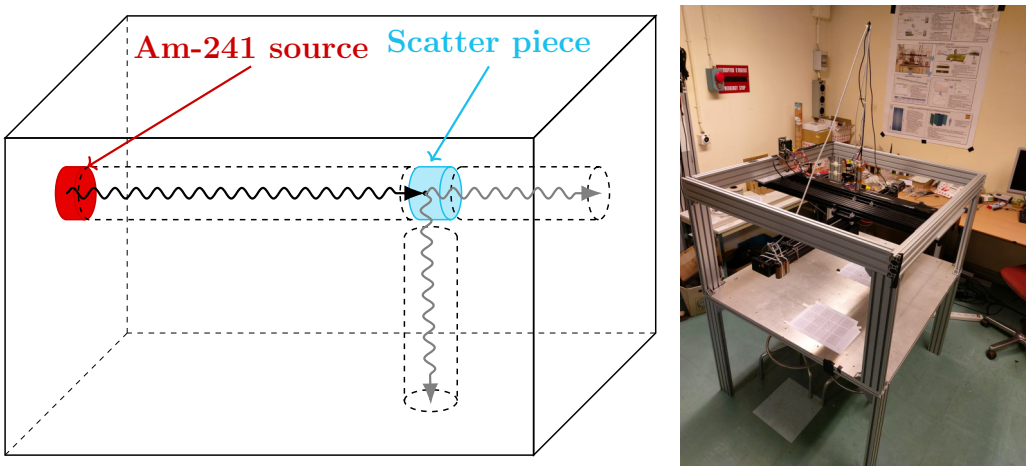

Figure 5.10: **Left:** Design of the lead block used to shield and polarize the Americium source. **Right:** Motorized X-Y scanning table developed at CERN to scan the polarimeter module channels with the polarized source [122]

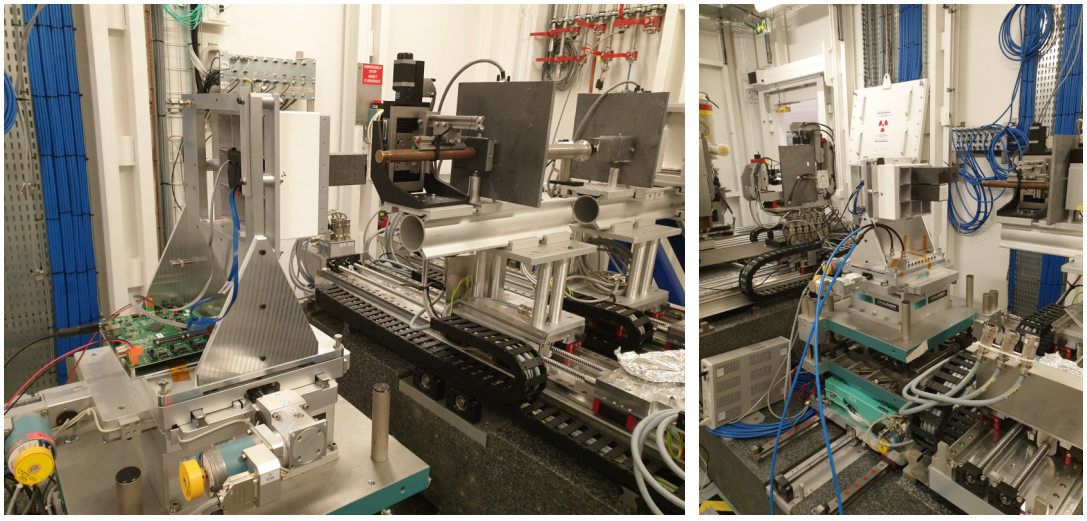

Figure 5.11: Experimental room used at ESRF used to calibrate POLAR-2 modules with a polarized X-ray synchrotron beam.

An X-ray polarized beam is also available at the European Synchrotron Radiation Facility (ESRF) in Grenoble, not far from Geneva. Calibration campaigns of about 1 week can therefore often be organized. Pictures of the setup from the calibration campaign that took place in April 2023 are shown in Figure 5.11. Three polarimeter targets as well as a monolithic 10 mm thick $CeBr_3$ [201] crystal and a segmented 5 mm thick GaGG [243] crystal were tested during this campaign. More details on the polarimeter module calibration will be provided in Chapter 7.

5.3 POLAR-2 INSTALLATION ON THE CSS

The POLAR-2 instrument will be launched to the China Space Station (CSS) with a Long March 5B rocket (or CZ-5B) from the Wenchang Space Launch Site on the Hainan Chinese island. The current schedule is to launch the instrument at the end of 2025 or in 2026 for at least 2 years of operation. Once inside the space station, the payload will be equipped with a adapter plate for an easy connection to the outside platform. As shown on the left image of Figure 5.12, a robotic arm adapter will also be mounted on one side of the payload in order for the robotic arm to transport POLAR-2 to its final location. A tungsten plate will be interfacing the aluminum robotic arm adapter to the payload. The former being in the field of view of the latter, the tungsten will act as a shield against photons scattered in the adapter back to the polarimeter. As such scattering in the aluminum adapter would change the polarization of the photons, it is important to prevent this photons from reaching the polarimeter as it would induce an artificial polarization arduous to model.

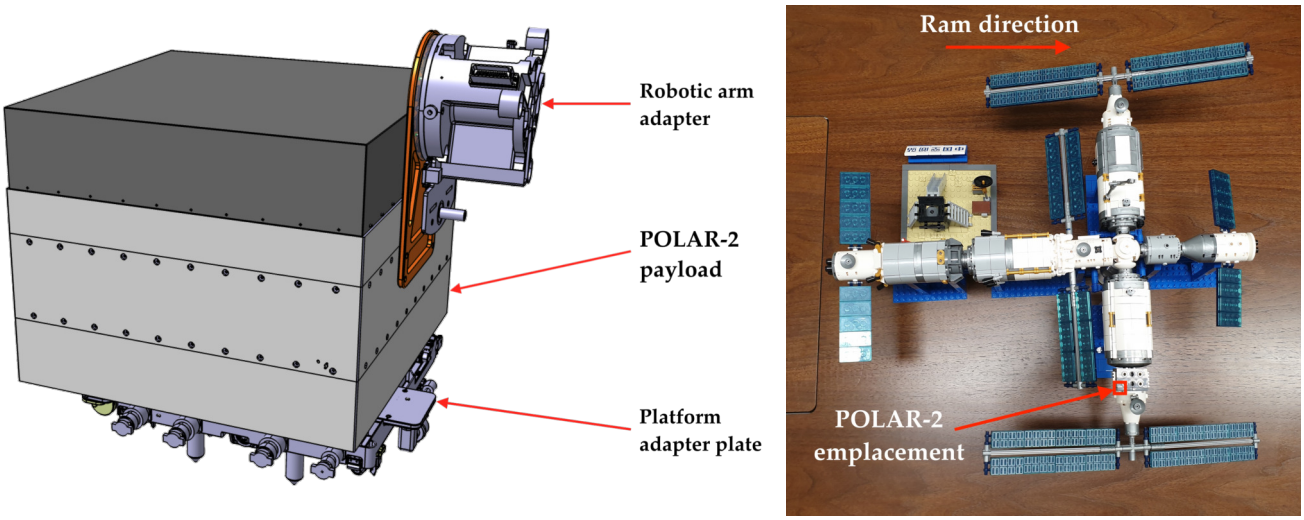

Figure 5.12: **Left:** CAD model of POLAR-2 equipped with the robotic arm adapter and plate adapter used for installing the payload on the space station. **Right:** Outreach block model of the CSS showing the installation emplacement of POLAR-2.

Once equipped with its different adapters, the payload will be placed in the decompression airlock and grabbed by the robotic arm adapter to be placed on the experimental platform facing deep space on the Experimental Module I (EM-I). The platform on which POLAR-2 will be mounted, whose location is shown on the right picture of Figure 5.12, will host 9 scientific payload in a 3×3 configuration. POLAR-2 is placed on the anti-ram direction, meaning that it will be protected by other payloads from space debris and have a much lower Atomic Oxygen flux. The orbit of the CSS has an inclination of 42° and an average altitude of 383 km.

5.4 POLAR-2 COLLABORATION

The POLAR-2 collaboration is led by the Department of High Energy Physics, or in French *Département de Physique Nucléaire et Corpusculaire* (DPNC), of the University of Geneva in Switzerland. The POLAR-2 collaboration is composed of four other institutes: the Department of Astronomy (DA) of the University of Geneva in Versoix, Switzerland; the National Centre for Nuclear Research (NCBJ) in Otwock, Poland; the Max Planck Institute for Extraterrestrial Physics (MPE) in Garching, Germany; and the Institute of High Energy Physics (IHEP) of the Chinese Academy of Sciences (CAS) in Beijing, China. The work packages for the POLAR-2 missions as well as the institutes involved in each of them are listed in Table 5.1. The POLAR-2 mission logo, as well as the simplified logo for the electronics, were both designed in the frame of this thesis and are presented in Appendix B. The logos of the institutes are shown in Figure 5.13.

WP #	WP name	Institutes
0	Management (MGT)	DPNC
1	Detector Module (DM)	DPNC
2	Front-End Electronics (FEE)	DPNC
3	Back-End Electronics (BEE)	NCBJ
4	Low Voltage Power Supply (LVPS)	NCBJ
5	Payload Thermal-Mechanical Structure (PTMS)	DPNC
6	Qualification and Verification (QV)	MPE
7	Flight Model Acceptance (FMA)	IHEP
8	POLAR-2 Onboard Software System (POSS)	DA
9	Spectrometer (SPEC)	IHEP, MPE
10	GRB Science (SCI)	DPNC, MPE, NCBJ

Table 5.1: List of POLAR-2 work packages and institutes involved in each of them.

Figure 5.13: Logos of the institutes member of the POLAR-2 collaboration.

5.5 PRELIMINARY POLAR-2 SCIENCE PERFORMANCES

The effective area of POLAR-2 for polarization events is compared to that of POLAR as a function of energy on the left plot of Figure 5.14. The curves are generated through Geant4 simulations using a $\theta = 22°$ incoming angle with respect to the instrument zenith, corresponding to one of the GRBs detected by POLAR. A third curve corresponding to a 100 modules instrument based on the POLAR module is also plotted for reference, as POLAR-2 contains 4 times more channels then POLAR. The benefits of the POLAR-2 technological and design upgrades, such as the use of SiPMs and the new scintillator shape, are clearly visible when comparing the *POLAR-2* and *POLAR×4* curves. An impressive improvement in effective area can be noticed at low energies, i.e. below 200 keV, thanks to the use of more efficient light sensors and to the increased contact surface between the scintillator bars and SiPMs. These improvements lead to a higher light yield, which increases the sensitivity at low energies (where fewer photons are produced through the scintillation process). While the number of channels has been multiplied by 4 in POLAR-2, the energy integrated effective area when combined with a typical GRB spectrum has increased by an order of magnitude.

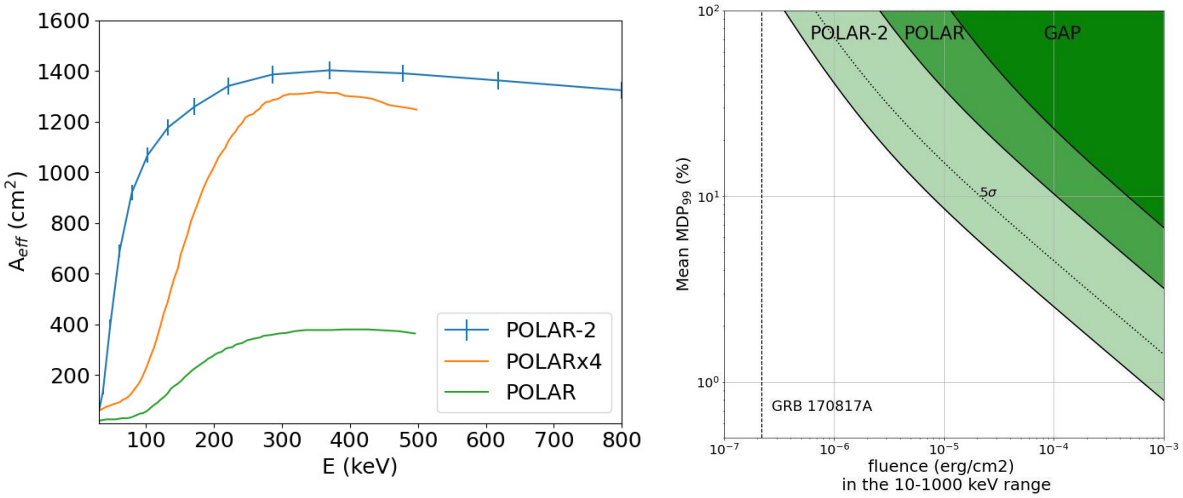

Figure 5.14: **Left:** Effective area of the POLAR-2 instrument versus energy, compared to that of POLAR. The POLAR effective area curve is also multiplied by 4 as a reference, as POLAR-2 contains 4 times more polarimeter modules than POLAR. This shows the impact of the module technological upgrade on the effective area, with a major improvement at low energies thanks to a 5 times bigger optical efficiency (see Chapter 7). **Right:** Minimum detectable polarization (at 99% C.L., averaged over the polarization angle) for a 1 s GRB for GAP, POLAR, and POLAR-2 as a function of the fluence in the 10-1000 keV energy range (taken from [84], with permission). The 5σ MDP is also given by the dashed curve for POLAR-2. The fluence of the weakest ever detected GRB, 170817A, is given as reference.

Figure 5.14 also gives the 99% Minimum Detectable Polarization (MDP), as defined in Chapter 2, averaged over the PA of POLAR-2 for 1 s GRBs. The MDP is plotted as a function of the GRB fluence in the 10-1000 keV range and is

compared to that of GAP and POLAR. As shown by the mean MDP plot, the sensitivity to polarization from POLAR to POLAR-2 was clearly improved. A similar amelioration is observed for long GRBs [84]. For a GRB with a fluence of 10^{-5} erg/cm^2 in the 10-1000 keV range, the MDP went from 39% in POLAR to 8.5% for POLAR-2. This means that for POLAR, a GRB with this fluence and a polarization degree below 39% could not be disentangled from a non-polarized source with a confidence level of at least 99%. Instead with POLAR-2, the needed minimal polarization degree for a GRB of this fluence to be distinguished from an unpolarized source with a 99% confidence level is 8.5%. This improvement will allow to probe for models predicting low polarization levels from the prompt emission of GRBs.

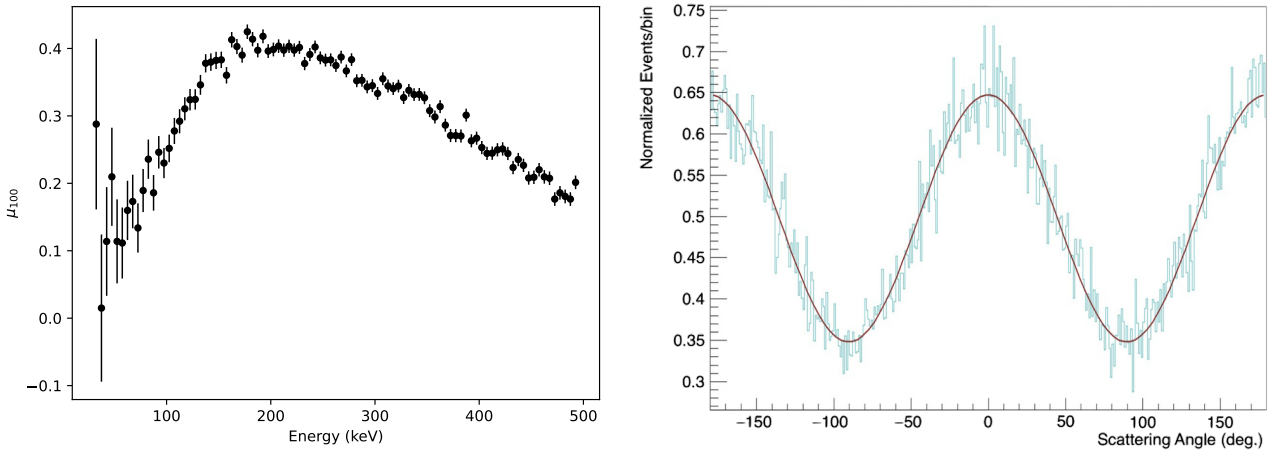

Figure 5.15: **Left:** Sensitivity to polarization (μ_{100}) as a function of energy for POLAR. **Right:** Preliminary modulation curve measured at 100 keV at ESRF in April 2023 with a single prototype module (from Merlin Kole). The corresponding μ_{100} is about 30%.

Another figure of merit that should be compared with POLAR is the modulation factor μ_{100}, i.e. the relative modulation amplitude for a fully polarized source. This quantity is important to assess the sensitivity to polarization of an instrument. The modulation factor as a function of energy is given for POLAR in the left plot of Figure 5.15. The same figure also shows a modulation curve measured for a single POLAR-2 module during a calibration beam test at ESRF in April 2023 [10]. This distribution is measured for a 100 keV polarized beam and is corrected for spurious modulation by dividing the unpolarized contribution. A modulation factor of about 30% is observed at 100 keV. The same measurement was done at 40 and 60 keV, which gives a modulation factor of 15 and 20%, respectively. These result are preliminary and will be presented in detail in a future work [133]. By comparing these 3 values to the POLAR curve given in Figure 5.15, we can see an improvement of the modulation factor at low energy already with a single POLAR-2 module. The POLAR-2 instrument is expected to give even better sensitivity to polarization thanks to its higher number of channels, allowing for a better resolution in scattering angle.

5.6 SPACE QUALIFICATION: COMPONENT IRRADIATION

For an instrument to survive the radiation environment present in Low Earth Orbit (LEO), radiation hard components should be used. Many items should therefore first be tested on ground under similar radiation exposure than what is expected in orbit. A wide list of electronics components and detector elements were therefore irradiated with neutrons or protons to certify that they can withstand the expected radiation conditions. The space environment was modeled using existing database like SPENVIS [48] and knowing the CSS orbit, as described in [171, 172], in order to determine the yearly expected dose for given components with Geant4 simulations. We here describe the neutron and proton irradiation campaigns and their main outcome for the POLAR-2 project. It should be noted that SiPMs are not covered in this Section but an entire Chapter (6) is dedicated to their behavior during and after irradiation.

5.6.1 *Neutron irradiation at NCBJ*

An irradiation campaign based on neutrons has been carried out at the National Centre for Nuclear Physics (NCBJ) in Otwock, Poland. A Plutonium Beryllium (PuBe) neutron source housed in a stainless steel cylinder of 21 mm diameter and 25 mm height is used for irradiating components of the POLAR-2 modules. The proportions of the Plutonium (Pu) and Americium (Am) isotopes present in the Beryllium absorber are given in Table 5.2. The neutron average energy from the PuBe source is 4.5 MeV, and γ-rays up to 10 MeV are emitted. At the time of the irradiation, the source flux was $7.5 \cdot 10^5$ neutrons/s on 4π steradians. The PuBe source also emits a significant amount of γs (more than 10^3 photons per neutron) with energies up to 10MeV.

Pu-237	Pu-238	Pu-239	Pu-240	Pu-241	Pu-242	Am-241
0%	1.03%	74.9%	19.1%	0.7%	1.57%	2.7%

Table 5.2: Plutonium and Americium isotopes content injected into the Beryllium absorber [96, 110].

5.6.1.1 *Peltier element activation study*

One of the components that has been irradiated with neutrons is the Peltier element used to cool down the SiPMs. The goal of this irradiation is not to assess the radiation hardness of such device, but is primarily of determining the activation of the Bismuth Telluride (Bi_2Te_3) used in the pn-junctions of the Peltier under exposure to radiation. Characterizing the activation of the thermoelectric cooling unit is all the more important knowing that it is placed just at the back of the SiPMs, which are subject to radiation damage and constitute a key component of the polarimeter.

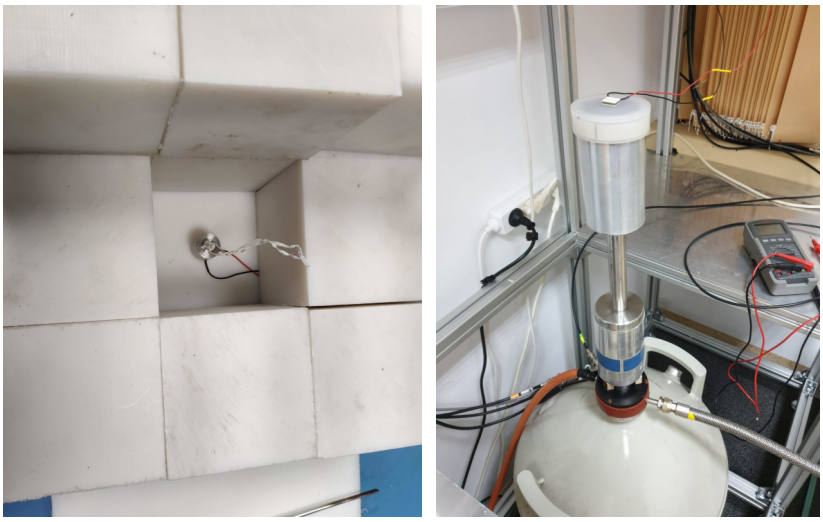

Figure 5.16: **Left:** PuBe source placed directly on top of the Peltier element, surrounded by 10x10x10 cm^3 boronated cubes of polyethylene for neutron shielding. **Right:** Peltier element placed on a HPGe detector for activation measurement.

The irradiation and measurement setup are shown in Figure 5.16. The Peltier is first placed on a High Purity Germanium detector (HPGe) for background measurement and then moved to the irradiation setup. During irradiation [110], the PuBe source is directly placed on the Peltier device, the whole being positioned between $10\times10\times10$ cm^3 boronated plastic cubes in order to reflect back neutrons into the setup. Right after the 17 hours of irradiation, the Peltier element is placed back on the HPGe detector. The emission spectrum of the Peltier element is therefore measured before and after the irradiation. These spectrum are presented on the left plot of Figure 5.18.

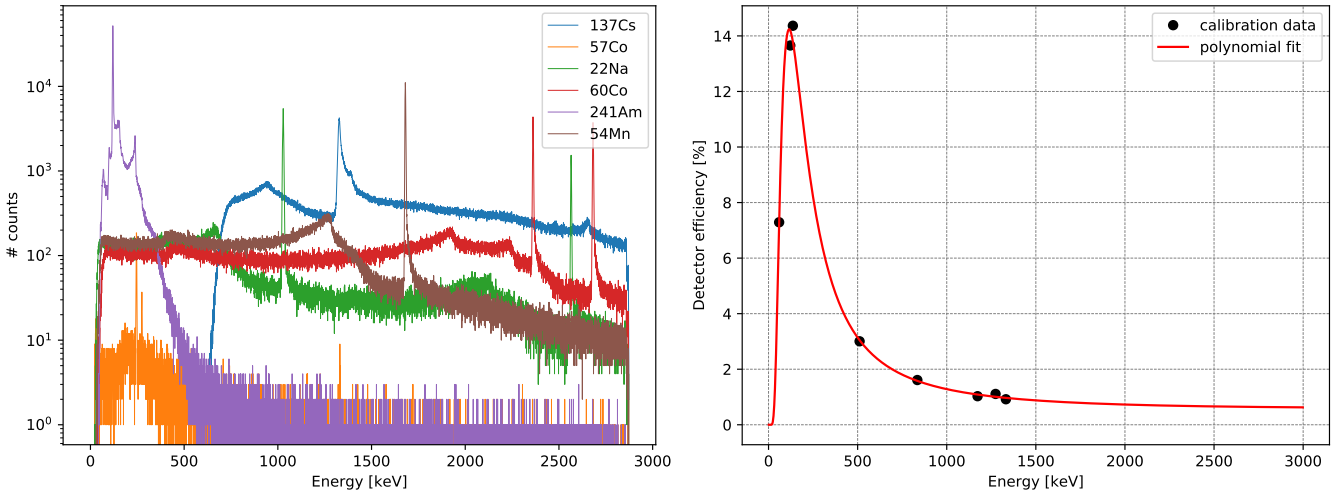

Figure 5.17: **Left:** Spectra measured with the HPGe detector for several calibration sources. **Right:** HPGe detector efficiency versus energy computed from the measured calibration sources spectra, details of the calculation are shown in Table 5.3

The measured spectra before and after irradiation are given in units of detected counts per second. The typical sensitivity of a Germanium detector being highly energy dependent, a calibration of the HPGe detector is needed. As shown on the left plot of Figure 5.17, six radioactive sources with typical peaks at known energies were placed on the detector in order to measure its efficiency at different energies. The activity of each source at the time of the measurement is calculated from the original activity and the half life time. The expected count rate is then computed using the current activity and the branching ratio of the given peak. The efficiency for each energy is then computed as the ratio of the measured and expected count rate. The numbers used in this calculation are given in Table 5.3 and the efficiency of the HPGe detector as a function of energy fitted with a polynomial function is presented on the right of Figure 5.17.

	Energy [keV]	Branching	Peak counts/s	Beginning activity [kBq]	$T_{1/2}$ [y]
Mn54	835	1	2400	1072	0.855
Co57	122.1	0.856	31.9	488	0.744
	136.5	0.107	4.195		
Co60	1173	0.9985	1020	434.2	5.27
	1332	0.9993	911.7		
Am241	59.5	0.359	10000	389	432.7
Na22	511	1.81	1716.67	625	2.602
	1274	0.9994	350		

	Energy [keV]	Source age [y]	Activity Today [kBq]	Counts/s from line	Efficiency
Mn54	835	2.43	149.020	149020	1.61052
Co57	122.1	8.04	0.272916	233.616	13.6549
	136.5			29.2020	14.3654
Co60	1173	11.21	99.3382	99189.2	1.02834
	1332			99268.7	0.918416
Am241	59.5	11.21	382.076	137165	7.29047
Na22	511	11.21	31.5587	57121.2	3.00531
	1274			31539.7	1.10971

Table 5.3: Calculation of the Germanium detector efficiency for each source characteristic peaks

The measured spectra shown on the left of Figure 5.18 can now be normalized by the detector efficiency. The spectrum measured before the irradiation is then subtracted from the one measured after the irradiation. The result is given on the right plot of Figure 5.18 where activation peaks can be observed. Most of the activation peaks are below 10^{-2} counts per second, and the most prominent peaks still have a rate smaller than 10^{-1} counts per second. Simulations have been performed in order to estimate the dose that the decay products from activation would deposit in the SiPMs [110]. The maximum dose obtained for the activation products was of the order of tens of nGy per year, negligible in comparison to the expected 67 mGy/yr in the SiPMs due to the radiation environment in space [171]. Furthermore, the 17 hours of irradiation applied to the Peltier element is equivalent to the dose the SiPMs would receive in 450 years of operation. An exaggerated dose was on purpose used to irradiate the Peltier in order to be very conservative on its activation products. The activation of the Peltier element used to cool down the sensors is therefore not worrying for the operation of POLAR-2.

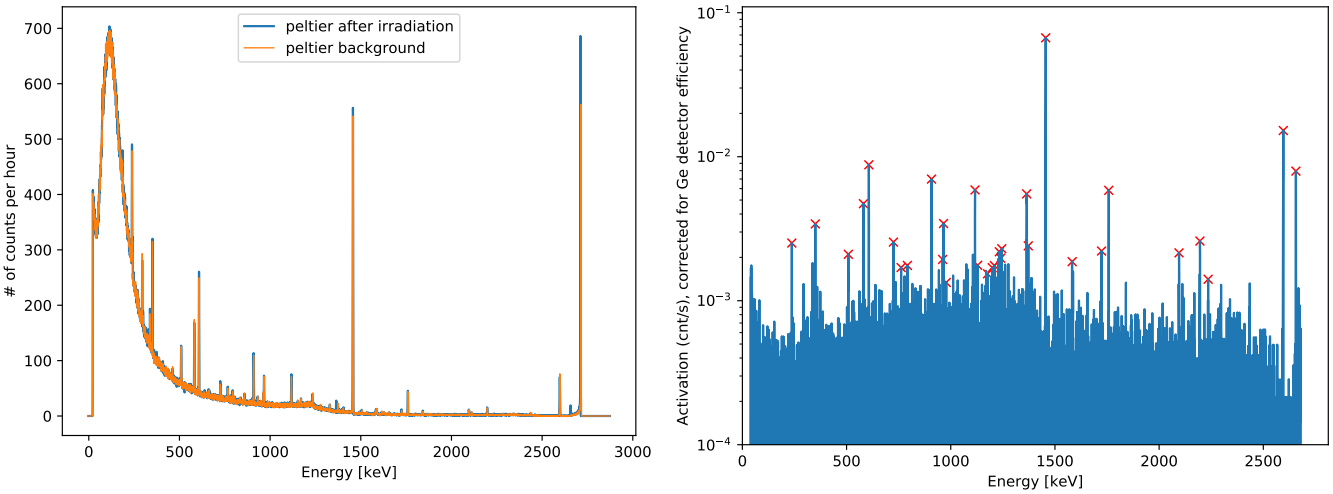

Figure 5.18: **Left:** Uncalibrated spectrum measured with the HPGe detector for the Peltier element before and after irradiation. **Right:** Efficiency corrected and background subtracted activation spectrum of the Peltier element.

5.6.1.2 *Electronic components irradiation*

Several electronics components were also irradiated using the neutron source at NCBJ. Among them, the LT3482 DC/DC converter from Linear Technology used to power the SiPMs was irradiated by steps of 15 minutes up to 5.6 hours [52]. The current and voltage provided by the chip was monitored at each step of irradiation and has shown very reliable behavior, with voltage and current variations not significant enough to be measured. The GW1N-LV4 FPGA from Gowin Semiconductor was also irradiated with higher doses than expected in orbit and was shown to be fully functional after irradiation [106, 108]. As described in Section 5.2.2, an IGLOO FPGA from MicroSemi is used in the POLAR-2 FEE, but this Gowin chip was a potential candidate FPGA at the beginning of the project.

The precision of the readout was 10 mV for the voltage and 0.1 µA for the current.

5.6.2 *Proton irradiation at IFJ-PAN*

Irradiation of many POLAR-2 items were performed with a 58 MeV proton beam used for eye therapy [173] at the Institute of Nuclear Physics of the Polish Academy of Science (IFJ-PAN) in Krakow, Poland. The irradiation setup is also used for assessing SiPM performances in space radiation environment, and is therefore described in Section 6.2.1. We discuss here the irradiation of scintillators, electronics, and radiation monitoring Field Effective Transistor (FET). Since many aspects of the SiPMs' behavior in radiation environments were studied in this thesis, the irradiation of SiPMs is discussed in a dedicated Chapter (6).

5.6.2.1 *Scintillator irradiation*

As the part of the detector responsible for detecting the γ-rays, the scintillators are located at the top of the polarimeter, facing deep space with only little shielding. The scintillators are therefore the first sensitive element of the instrument being exposed to background radiation. Assessing the behavior of the scintillators when exposed to radiation is therefore crucial to understand the evolution of the detector's behavior with time when placed in orbit. The expected dose rate in the scintillators for each module is shown in Figure 5.19.

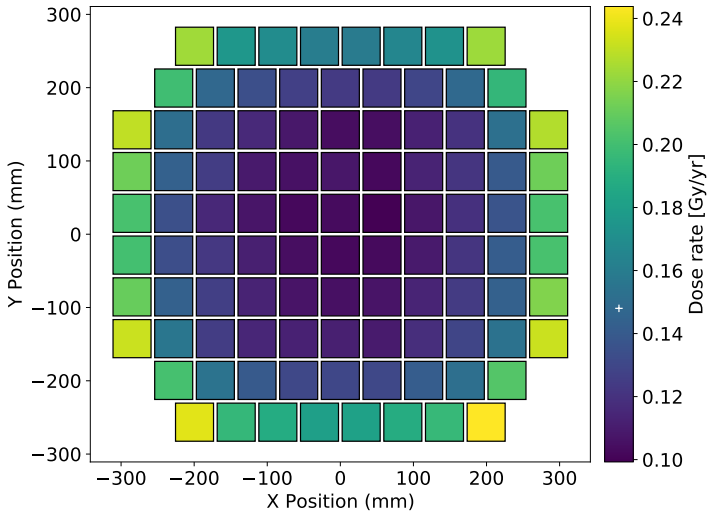

Figure 5.19: Map of the expected dose rate in the scintillators. The module configuration is not in a 10×10 configuration but in a more complex layout, which was the baseline design of the polarimeter at the time (taken from [172], with permission).

Both EJ-200 and EJ-248M scintillator bars were therefore irradiated with 58 MeV protons. Four bars of each type of plastic were exposed to doses ranging from 1.89 to 18.7 Gy [172], or 12.8 to 126 years in space for POLAR-2. The scintillation emission spectrum was measured using both a UV Xenon lamp and through radioluminescence using an X-ray source. As can be seen in Figure 5.20, the emission spectrum of the scintillator is not impacted by the irradiation.

The samples for both types of plastic are numbered from 1 to 4 with increasing dose, whose value are respectively 1.89, 5.66, 11.2, and 18.7 Gy.

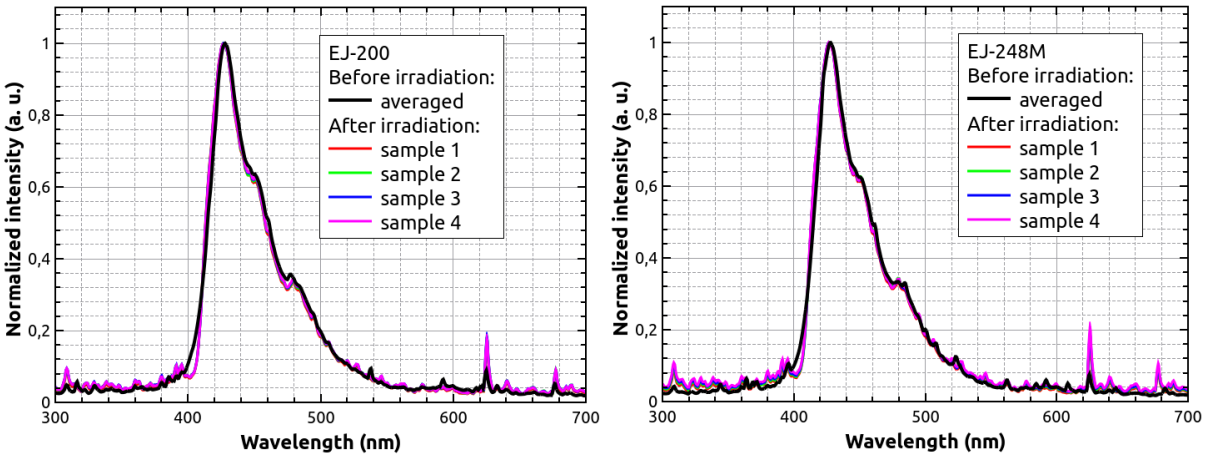

Figure 5.20: Emission spectrum measured through radioluminescence for both EJ-200 (**left**) and EJ-248M (**right**) scintillators before and after irradiation for doses ranging from 1.8 to 18.7 Gy (taken from [172], with permission).

The light yield of the scintillators has also been measured using a calibrated PhotoMultiplier Tube (PMT) and a ^{137}Cs γ-ray source. The position of the 476 keV Compton edge from this source is used to determine the light yield, which was measured both before and after the irradiation as a function of the height at which the source is placed, as plotted in Figure 5.21. No significant light yield degradation was observed for either of the plastics due to irradiation.

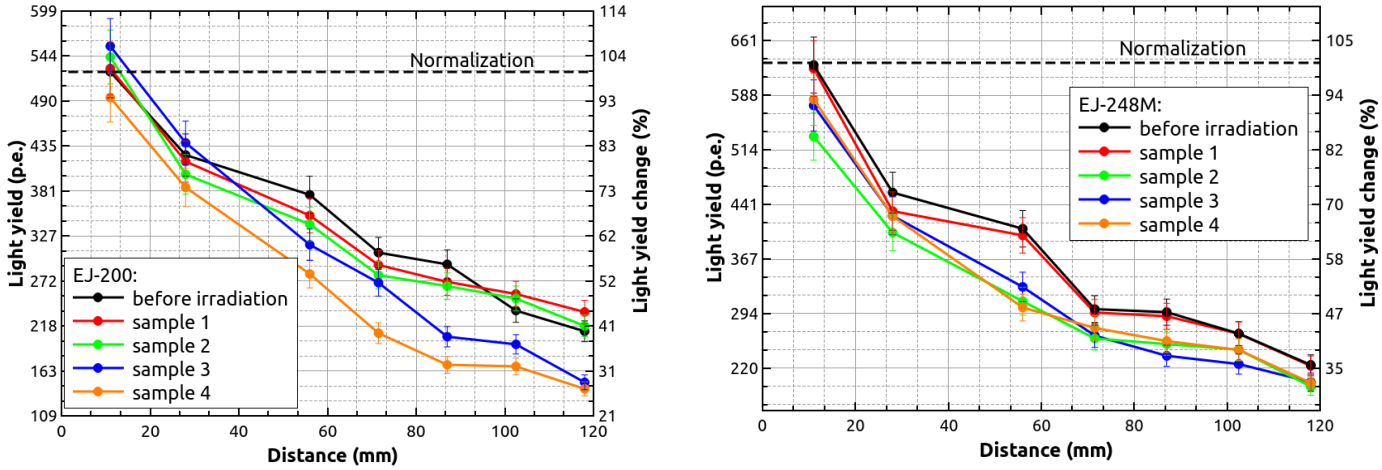

Figure 5.21: Light yield measured as a function of the scintillator height for EJ-200 (**left**) and EJ-248M (**right**) scintillators for different doses compared to the non-irradiated result (taken from [172], with permission).

Finally, an activation analysis was carried out on the samples irradiated with the highest dose of 18.7 Gy. The bars were placed on HPGe detectors about 15 minutes after the end of the irradiation (time needed to transport the samples from the irradiation room to the HPGe laboratory). The measured spectra for both plastics as well as the background are shown in Figure 5.22. The only significant activation peak observed during this analysis is at 511 keV for both plastics, corresponding to the ^{12}C(p,n) ^{11}C decay where the daughter nuclei

emits β^+. The 1022 keV line observed in the spectrum for one of the detectors corresponds to pile-up from the 511 keV line. The measured decay time of the 511 keV line for EJ-200 and EJ-248M, respectively 1275 ± 18 s and 1207 ± 9 s, are in good agreement with the ^{11}C β^+ decay [211].

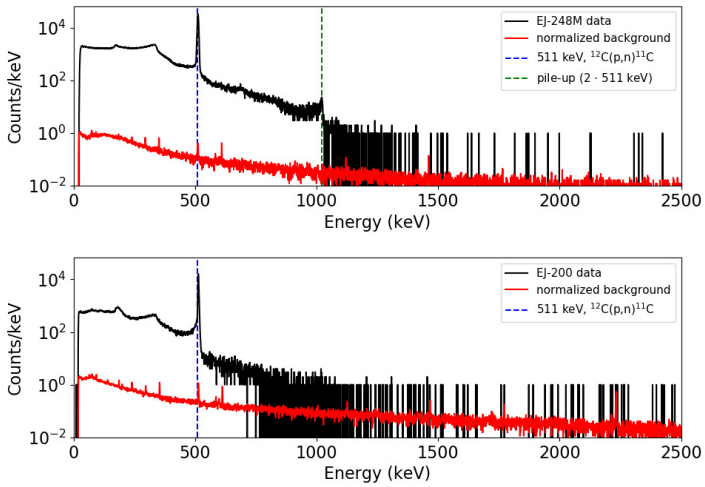

Figure 5.22: Activation spectrum measured for irradiated EJ-248M (**top**) and EJ-200 (**bottom**) scintillators (taken from [172], with permission).

5.6.2.2 *Electronics irradiation*

The last version of the FEE presented in Section 5.2.2 has not yet been used for qualification tests since its first production is taking place in late 2023. The first FEE version is very similar, only minor upgrades were brought to the new version.

The first version of the POLAR-2 FEE has been irradiated at IFJ using the 58 MeV proton beam. The 40 mm diameter beam has been shaped into a 25 mm square beam using brass collimators. Since SiPMs are irradiated separately for a dedicated study (se Chapter 6), the only sensitive parts are located in the central rigid part of the FEE (the rest just being connectors, resistors, and capacitors).

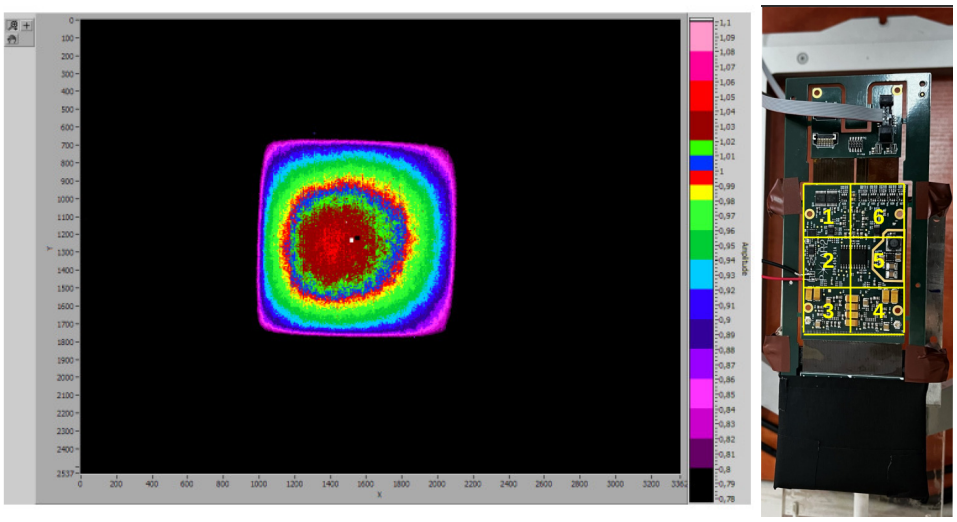

Figure 5.23: **Left:** Uniformity of the square beam used to irradiated the POLAR-2 FEE [107]. **Right:** Picture of the POLAR-2 FEE mounted on the beam line showing the 6 irradiation regions.

Because of the big surface of the FEE central part, it was irradiated in 6 steps as depicted in Figure 5.23. The FEE has been irradiated three times with 0.17 Gy and a fourth time with 0.25 Gy for a total equivalent dose of about 11 years in space. Data was acquired at each irradiation step to ensure that the FEE was fully functional. The FEE has shown to be radiation hard to levels above the expected dose during the POLAR-2 life time. The critical components of an LVPS Hub, as illustrated in Figure 5.24, was also irradiated to ensure its radiation hardness. A Kintex FPGA from Xilinx, planned to be used in the BEE, was irradiated as well. The irradiation campaign was very successful and did not show any malfunction or failure due to radiation for any of the components tested. The detailed results of the electronics irradiation will be given in a later work [109].

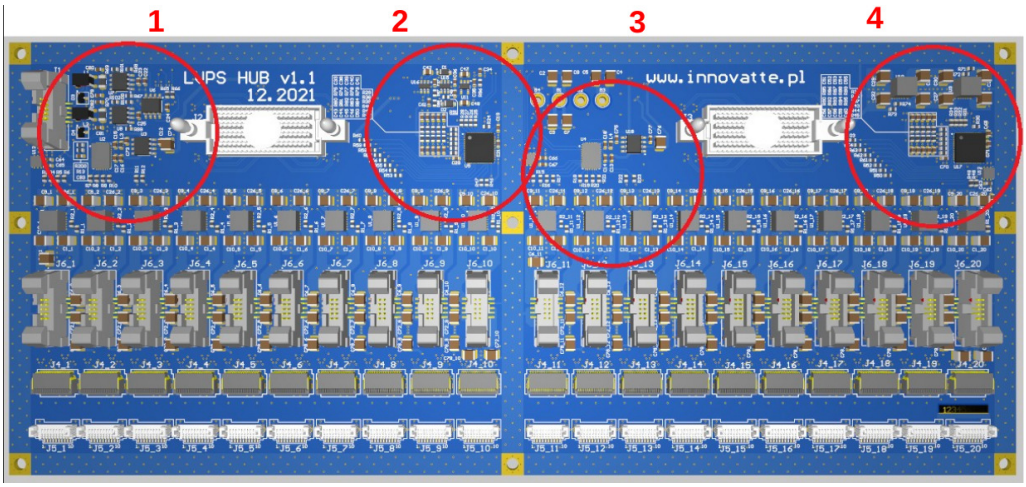

Figure 5.24: CAD model of the LVPS Hub showing the irradiated spots [107].

5.6.2.3 *Radiation sensitive Field Effective Transistor (RadFET)*

In order to monitor the radiation environment during the POLAR-2 operation in-orbit, several Radiation sensitive Field Effective Transistors (RadFET) will be placed on the instrument. As no space is left on the very compact FEE, several RadFETs will be placed on the BEE in order to be able to monitor the radiation dose in orbit and cross check the simulations. This is important to be certain about the amount of radiation that reaches the SiPMs to have a precise idea of the evolution of the instrument response due to radiation damage. Having RadFETs on board can also help to model the radiation background. The 1μm V-T03 RadFET with a plastic package from Varadis was selected for this purpose. It was irradiated with protons to characterize its behavior with radiation.

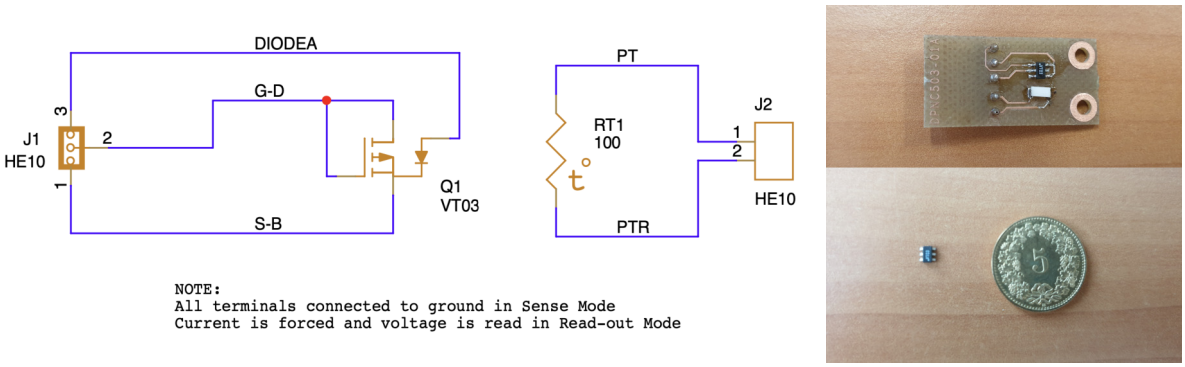

Figure 5.25: **Left:** Schematics of the RadFET testboard used during irradiation (from Stéphane Débieux). A PT100 thermistor is placed next to the RadFET to monitor the temperature. The pins are all manually connected to ground during irradiation. **Right:** Picture of the RadFET test board and RadFET chip.

The dose can be measured by forcing a current and measuring a voltage. The voltage increase is directly linked to the dose through the formula:

$$\Delta V = A \times dose^{B} \tag{5.1}$$

where the voltage increase is given in Volts and the dose in rad. The A and B calibrated parameters are provided by the manufacturer for each chip, and are given in Table 5.4.

Dose range	A	σ_A	B	σ_B
0–1 krad	$3.04 \cdot 10^{-3}$	$5.34201 \cdot 10^{-5}$	$8.0979 \cdot 10^{-1}$	$2.68 \cdot 10^{-3}$
0–125 rad	$1.45 \cdot 10^{-3}$	$2.73404 \cdot 10^{-5}$	$9.5127 \cdot 10^{-1}$	$4.13 \cdot 10^{-3}$

Table 5.4: Calibration parameters provided by the RadFET manufacturer to be used with formula (5.1)

The recommended measurement current is 11 μA for the chip that was irradiated, which corresponds to the current at which the I-V characteristics temperature dependence is minimal. Between each irradiation step, the voltage was measured using the recommended 11 μA current but also two other currents of 12.5 μA and 14 μA. The measured doses are compared to the simulated one in Table 5.5. The obtained doses for different injected currents are consistent to each other, while the simulated doses are deviating from the measured ones. This is likely due to a bad modelling of the chip package in the simulations, and should be corrected in the future in order to precisely monitor the radiation levels in orbit.

Irr. Time [s]	$\text{dose}_{11\mu A}$[rad]	$\text{dose}_{12.5\mu A}$ [rad]	$\text{dose}_{14\mu A}$[rad]	Sim. dose [rad]
0	-	-	-	-
10	19.95	19.95	19.11	16.6
20	39.60	40.47	41.34	33.3
30	64.20	62.42	59.77	50
45	91.98	93.79	93.79	74.6
225	560.15	558.79	547.99	375.7

Table 5.5: Measured and simulated RadFET dose. The temperature is monitored with a PT100 and was in average 23.53 ± 0.46°C during the irradiation and measurement session.

5.7 SPACE QUALIFICATION: VIBRATION AND SHOCK TESTS

Before being placed on the CSS, POLAR-2 has to survive extremely violent launch conditions. The payload has therefore to be tested with extreme vibration and shock conditions to ensure its mechanical robustness. This was a particularly challenging test for POLAR due to the fragility of the MA-PMTs entrance windows made of borosilicate glass, and the first vibration campaign was not very successful since all the PMTs broke. This was later solved by dividing the dampers at the top of the modules into several pads to give the material space to expand. Since POLAR-2 is based on more mechanically robust technology, i.e. SiPMs, a thinner layer of dampers is expected to be enough to sustain launch conditions. In order to qualify its mechanical design, a single POLAR-2 prototype module was tested using a vibration table at MPE, Garching, Germany [130]. The experimental setup is first presented, followed by a summary of the sinusoidal and random vibration tests and shock tests.

5.7.1 *Experimental Setup*

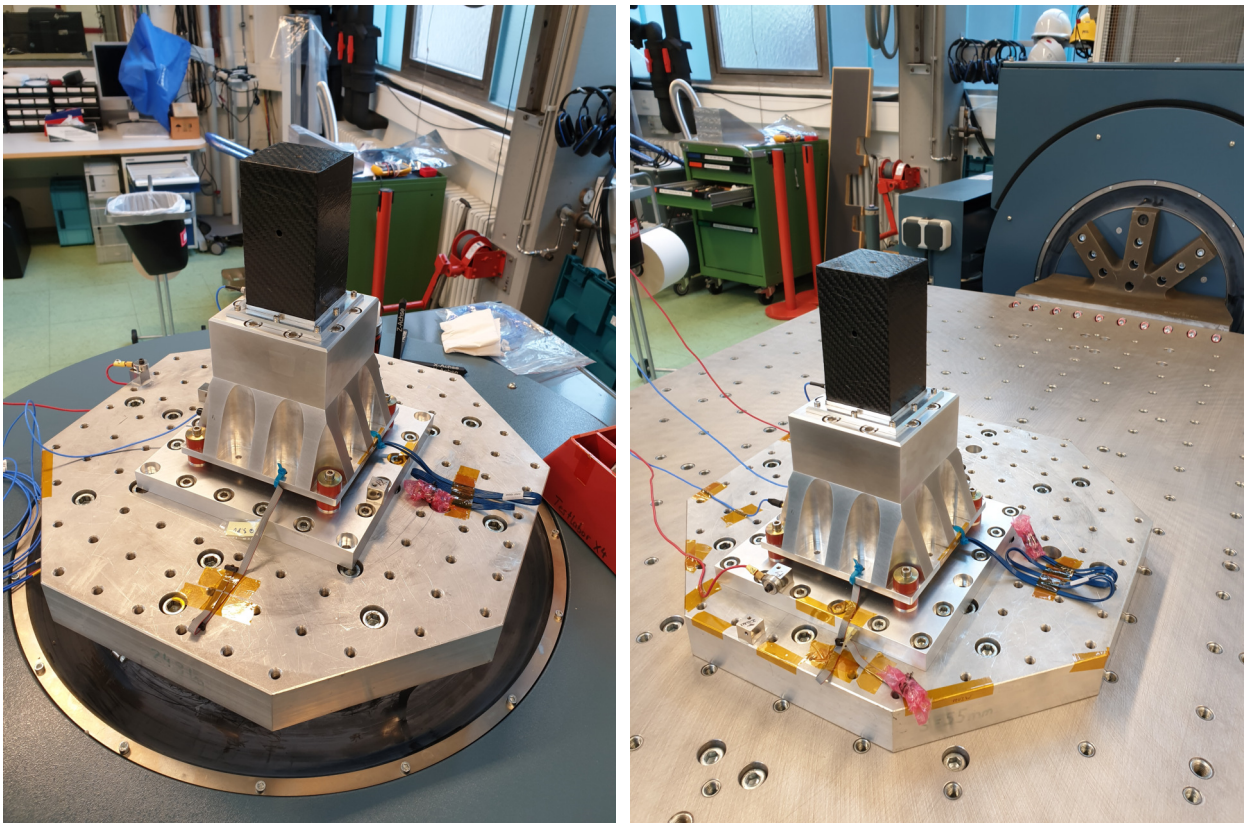

Figure 5.26: **Left:** Single module directly mounted on top of the electro-magnet, placed vertically in order to shake the module along the Z (vertical) axis. **Right:** Single module mounted on the sliding table in order to test the vibrations and shocks along the X and Y axes. The module is first shacked in one direction, the module is then unmounted from the table to be rotated by 90° and test the other direction. The electromagnet is turned horizontal compared to the previous picture in order to slide the table.

The vibration and shock setup is shown in Figure 5.26, for which a grid for a single prototype module was developed with 4 dampers on the base. The vibration and shock campaign took place in the test facilities of the Max Planck Institute for Extraterrestrial Physics in Garching, Germany. The vibration and shock conditions are specified as a requirement by the Technology and Engineering Center for Space Utilization (CSU) of the Chinese Academy of Sciences, and will be detailed in the next sections. These conditions have to be tested along the three X, Y, and Z axes. As shown on the first picture of Figure 5.26, the vertical Z axis is tested by mounting the module directly on the electromagnet, vertically oriented. The second picture shows the electromagnet oriented horizontally and connected to a sliding table, on which the module is mounted. This configuration is used for testing the vibrations and shocks along the X and Y directions. The module is first tested in one direction, and they unmounted from the table and rotated by 90° in the horizontal plane to test the other axis.

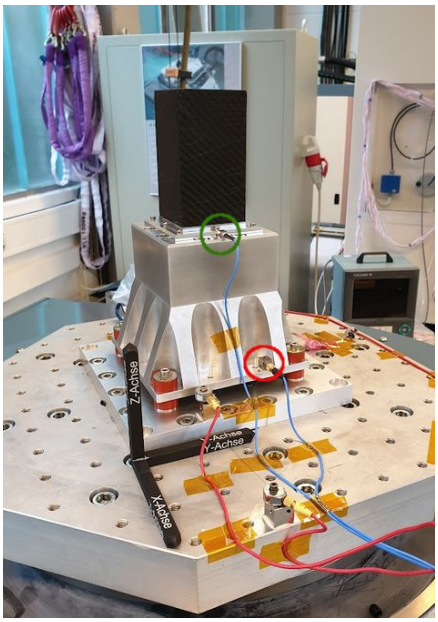

Figure 5.27: Definition of the X-Y-Z frame with respect to the polarimeter module. The Z axis is defined as the vertical direction (along the scintillator length), and the X and Y directions are defined in the horizontal plane along the scintillators rows and columns. Accelerometers are placed on the flange of the module (green) and near the dampers (red) in order to monitor the resonance spectrum during and between the different tests.

Two accelerometers are placed on the module in order to monitor the load at two different points of the module. The first accelerometer, circled in green in Figure 5.27, is placed on the flange at the base of the target. The other sensor, shown in red in Figure 5.27, is placed near the dampers at the base of the module. Figure 5.27 also shown the X-Y-Z frame convention with respect to the module.

A load sweep is taken as a reference at the beginning of the test, as shown along the z-axis in Figure 5.28 for both accelerometers, and is measured between each vibration or shock run to check that the resonance spectrum is stays the

same. A change in the resonance spectrum could indicate that the mechanical configuration of the module is no longer the same, which could potentially be explained by a component breaking. It is therefore a way, in addition to data acquisition, to check that the module survived each vibration and shock steps.

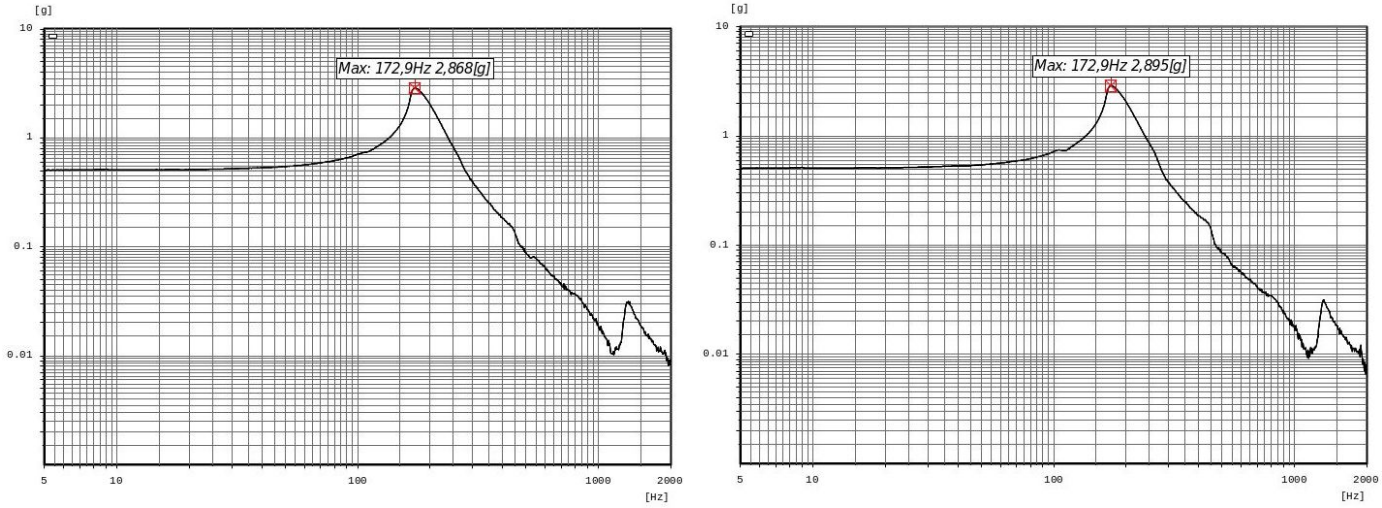

Figure 5.28: Load measured before the tests with the flange (**left**) and damper (**right**) accelerometers along the z-axis (from Kurt Dittrich).

The module is submitted to sinusoidal and random vibrations, as well as shocks of different strengths. The list of tests is summarized in Table 5.6. The detailed results of the test are provided in [130], while the next sections summarize the tests requirements and outcome.

Date	Time (CET)	Test Type	Test Axis
18 Oct 2021	14:03	Sinusoidal Vibration	Z
	15:37	Random Vibration	
	16:52	Shock	
19 Oct 2021	14:14	Sinusoidal Vibration	Y
	15:37	Random Vibration	
	16:47	Shock	
20 Oct 2021	12:10	Sinusoidal Vibration	X
	13:53	Random Vibration	
	14:49	Shock	

Table 5.6: Summary of the vibration and shock tests carried out at MPE on a single module.

5.7.2 *Sinusoidal Vibrations*

The first test consists of sinusoidal vibrations with frequency from 4 to 100 Hz. The specifications of test is given for different sub-ranges of frequency in Table 5.7.

Frequency range [Hz]	Qualification requirement
4-12	15 mm
12-17	8.8 g
17-75	14.5 g
75-100	11 g

Table 5.7: Requirements used for the sinusoidal vibrations qualification test performed on the 3 axis (x, y, and z), with an acceleration rate of 2 octave/minute.

The load measured during the test along the Y-axis is given for the two accelerometers in Figure 5.29. No major damage was observed in the prototype module during the sinusoidal tests for any of the axes. The only notable damage is a small mark on the external part of the aluminum mechanics due to the washer of the damper touching the grid during the Y vibration, as shown on the left picture of Figure 5.31.

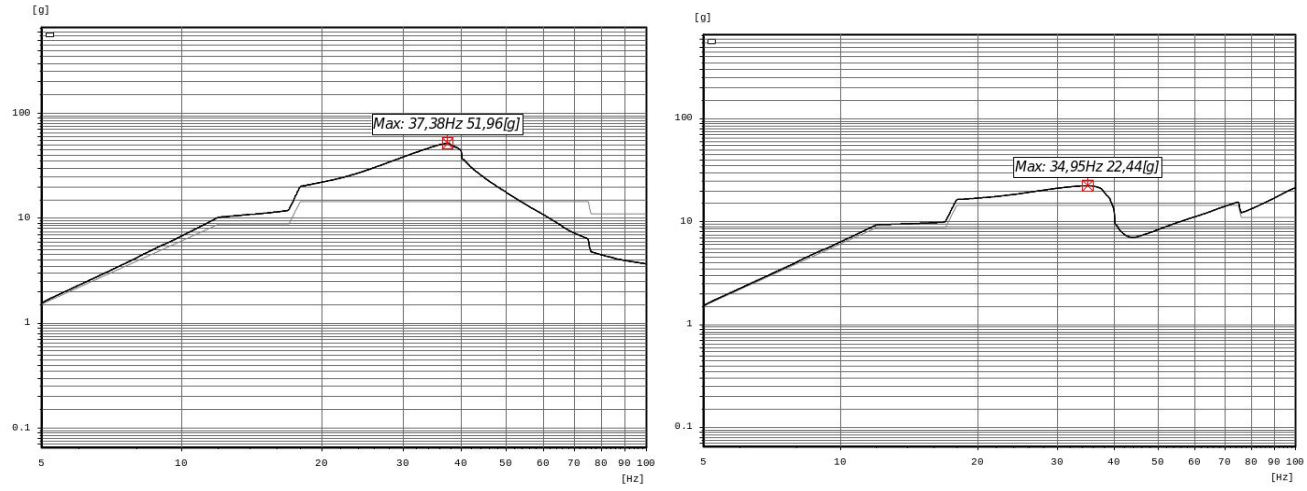

Figure 5.29: Load measured by the flange (**left**) and damper (**right**) sensors during the sinusoidal vibration test along the Y-axis (from Kurt Dittrich).

Two frames from the video taken during the sinusoidal vibration test along the Y-axis are shown in Figure 5.30. An impressive balancing effect of the module along its vertical axis can be observed. All the tests along the Z and Y axes were performed using the same dampers previously used in POLAR. The X axis was tested using another kind of damper, more rigid, developed by Centre National

d'Etudes Spatiales (CNES). Both types of dampers are shown in Figure 5.31. The material of the dampers used in POLAR are softer than the one developed at CNES. The temperature of the dampers during the tests was monitored with a thermal camera. The CNES damper heated up to 60°C while the Chinese damper from POLAR did not go above 40°C.

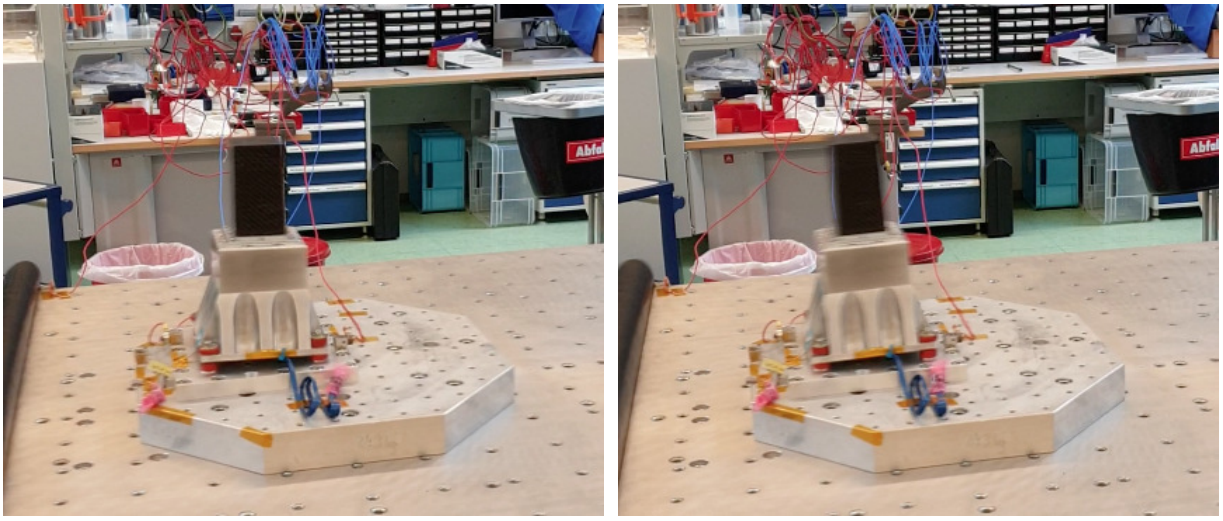

Figure 5.30: Screenshots of the video of the Y-axis sinusoidal vibration test showing the balancing effect on the prototype module.

Figure 5.31: Chinese (**left**) and CNES (**right**) dampers mounted on the prototype grid. It can be observed on the left picture that the aluminum grid has been slightly damaged by the washer touching the surface of the grid during the vibration.

5.7.3 *Random Vibrations*

After testing for sinusoidal vibrations, the module has to be exposed to random vibrations from 12 to 2000 Hz. The requirements of the random vibrations are given for three frequency domains in Table 5.8.

	Frequency range [Hz]		
	12-250	250-800	800-2000
Power spectral density	6 dB/octave	0.14 g^2/Hz	9 dB/octave
Total RMS acceleration		11.65 grms	
Test duration		180 s	
Acceleration directions		3 axis	

Table 5.8: Requirements used for the random vibrations qualification test.

Random vibrations were applied to the prototype module on the three axes. No problem was encountered either by inspecting the resonance spectre or by texting the full functionality of the FEE. The measured load spectra on the two accelerometers are provided in Figure 5.32 for the Y-axis test.

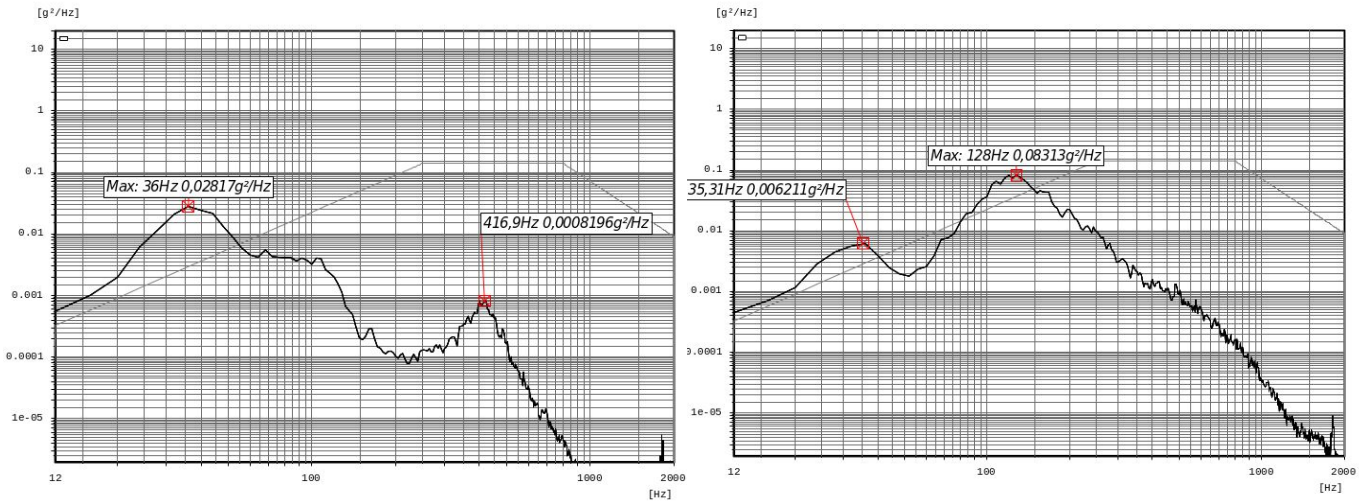

Figure 5.32: Load measured by the flange (**left**) and damper (**right**) sensors during the random vibration test along the Y-axis (from Kurt Dittrich). The injected load, which corresponds to the specifications in Table 5.8, is given as a reference by the gray curve.

5.7.4 *Shock*

The last tests after vibrations is injecting shocks into the system. The specified amplitude of the shocks are given in Table 5.9 in the 100-500 and 500-3000 Hz ranges.

	Frequency range [Hz]	
	100-500	500-3000
Shock response spectral acceleration	9 dB/octave	800 g
Test duration	3 times per axis	
Acceleration directions	3 axis	

Table 5.9: Requirements used for the shock qualification test.

The acceleration measured as a function of time during the Y shock test is given in Figure 5.33 for both the accelerometer placed on the flange of the module and the one placed directly on the sliding table. The very efficient dampening of the POLAR-2 module is clearly visible by comparing these two curves. While the amplitude in acceleration measured on the vibration table goes up to ±250 g, the accelerometer on the module does not measure accelerations higher than ±10 g during the shock injection. Figure 5.33 also gives the load measured after the shock test along the Y-axis. No mechanical or functional damage was observed after the shock test in any of the three axes.

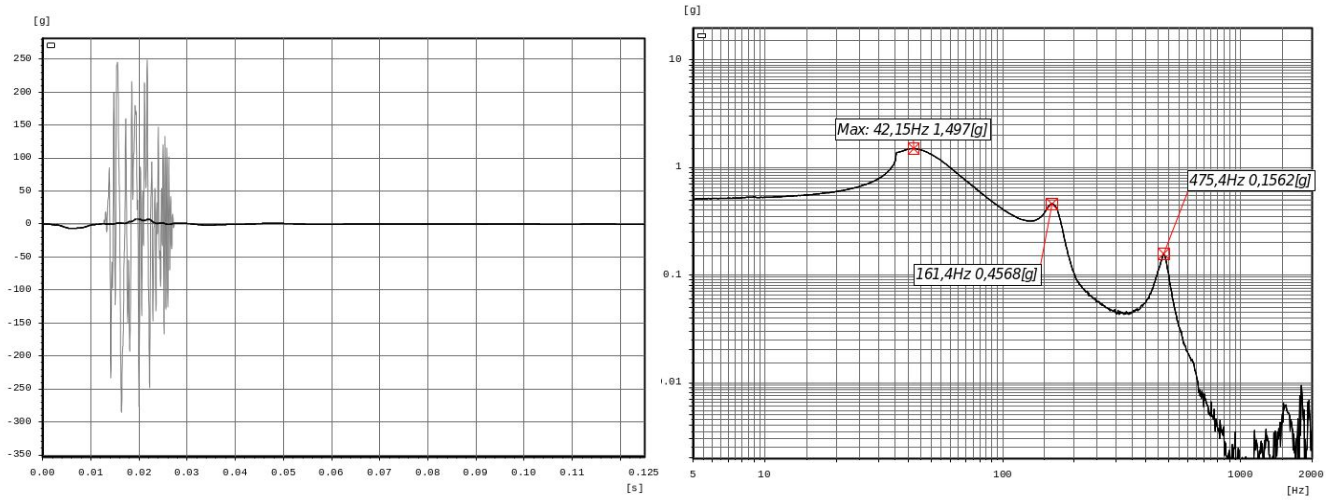

Figure 5.33: **Left:** Acceleration as a function of time during the Y-axis shock test measured on the table (gray curve) and on the flange of the module (black curve). **Right:** Load measured after the shock test along the Y-axis (from Kurt Dittrich).

5.7.5 *Overall test outcome*

A single POLAR-2 polarimeter module prototype was tested under specified rocket launch conditions. Sinusoidal and random vibrations as well as shocks were injected in all three axes. The functionality of the module was tested between each test, and the module was took apart at the end of the campaign for visual inspection (see Figure 5.34). The overall module design has been shown to be withstanding the launch conditions. Future vibration and shock tests could be performed on a higher scale prototype using a 3×3 polarimeter grid, shown in Figure 5.34.

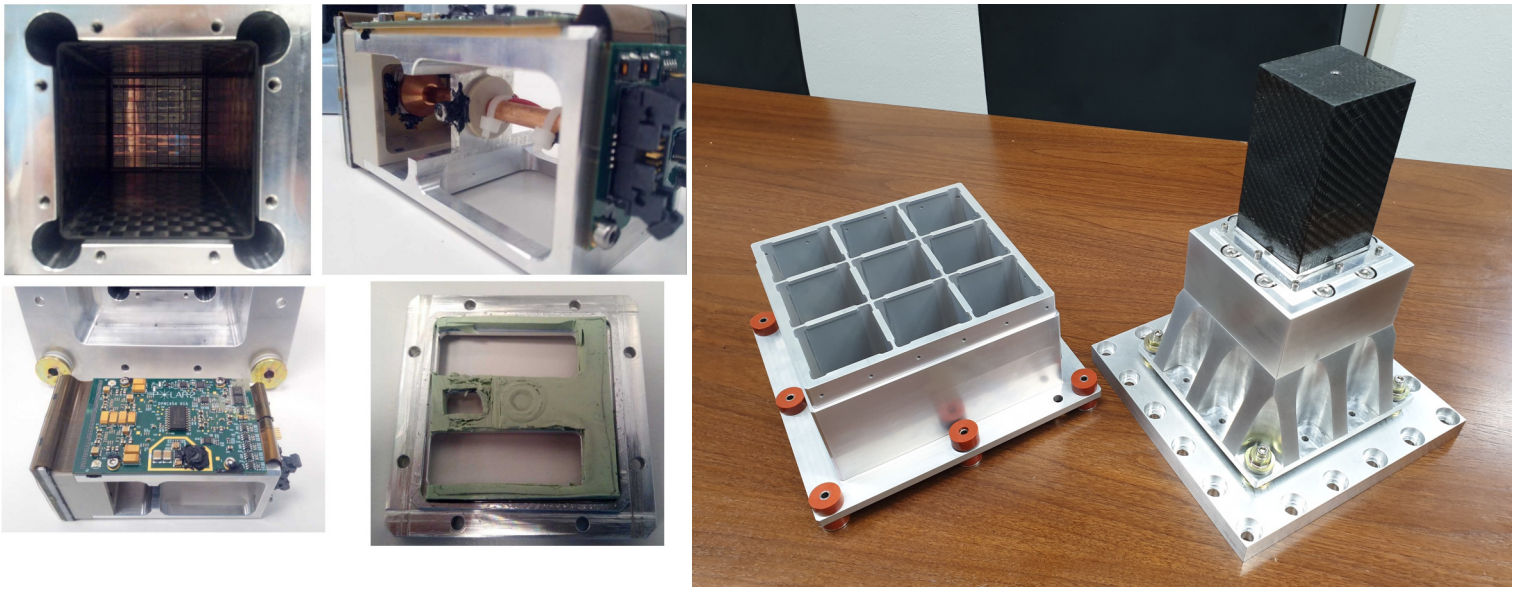

Figure 5.34: **Left:** Pictures of the different parts of the polarimeter modules after right after the vibration and shock test campaign [130]. After a careful visual inspection, no damage is observed. **Right:** Single module mechanics used for the vibration test next to the 3×3 grid built for testing a small case version of the final polarimeter with several modules. The grid is compatible with the dampers used for the single module vibration and shock tests, and could therefore be used for a future higher scale vibration-shock test.

5.8 SPACE QUALIFICATION: THERMAL VACUUM TEST

In order to validate the thermal design of the polarimeter modules, the 3×3 polarimeter grid was placed in a thermal vacuum chamber at MPE, Garching, in May 2022. Due to the limited number of available POLAR-2 FEEs, only 4 real modules were placed in the grid. The other 5 slots were taken by dummy modules designed to mimic the thermal behavior of the FEE. A dummy FEE as well as a functional one are shown in Figure 5.35. The modules underwent several thermal cycles from -32 to 40°C.

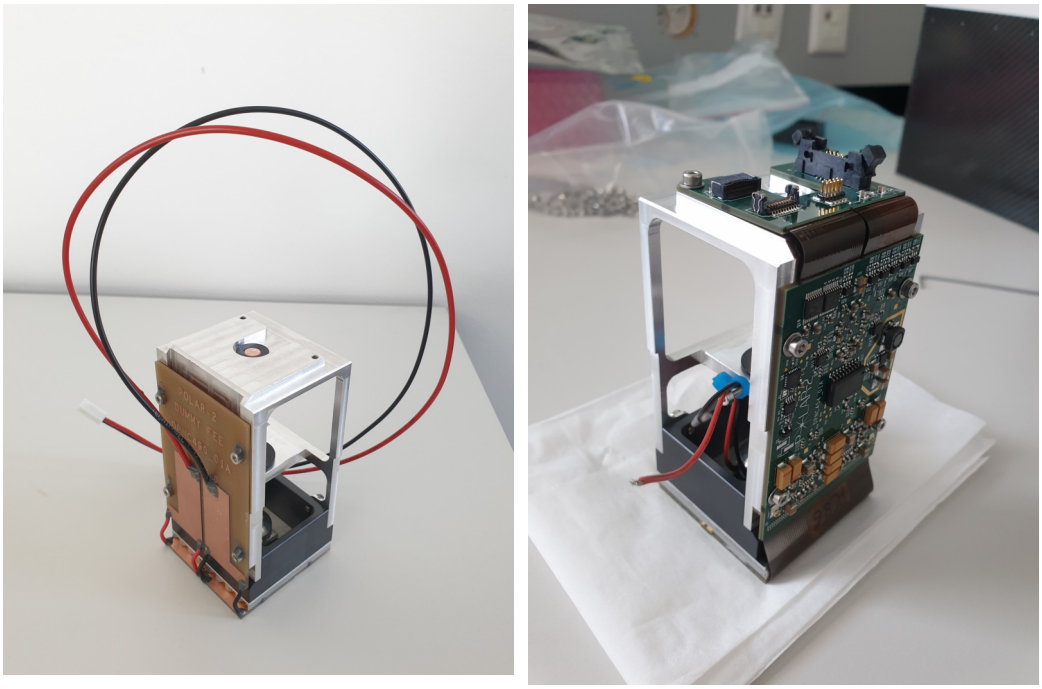

Figure 5.35: **Left:** Dummy FEE with power resistors to emulate the heat from the components that consume the most (FPGA, ASICs, Peltier). These fake electronics are used to mimic the thermal behavior of the real modules for 5 emplacements in the 3×3 grid, since only 4 actual FEE were available at the time of the test. **Right:** Real POLAR-2 FEE used for the four functional modules during the test.

Before the Thermal Vacuum Test (TVT), the mini polarimeter as well as all the cables and material to be used in vacuum were placed in a vacuum chamber, shown in Figure 5.36, for outgassing all the elements and not pollute the main chamber. After 10 days of outgassing the 3×3 polarimeter is moved to the thermal vacuum chamber. The 4 real modules are powered and read out using a General Purpose Input/Output (GPIO) board developed at DPNC used as a back-end electronics. The two NTCs of each real module can be monitored with time using this board, which also allows to check for normal operation of the FEEs. The 5 fake modules are powered through the GPIO adapter board, on which D-Sub connectors are mounted in order to communicate with the inside of the chamber through the patch panel. Figure 5.37 shows the acquisition system directly connected to the mini polarimeter for acquisition testing before

closing the chamber. The different parts of the readout system are depicted in the diagram of Figure 5.38.

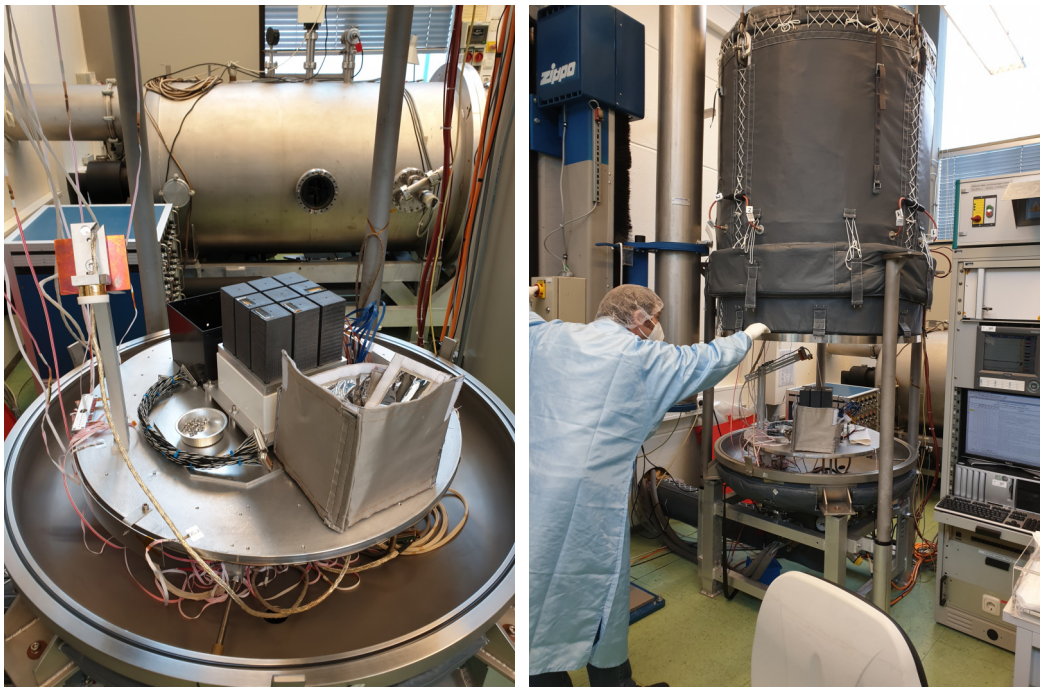

Figure 5.36: Vacuum chamber used to outgas all the material before placing it in the actual thermal chamber. The purpose of this outgassing procedure is to prevent pollution of the thermal chamber.

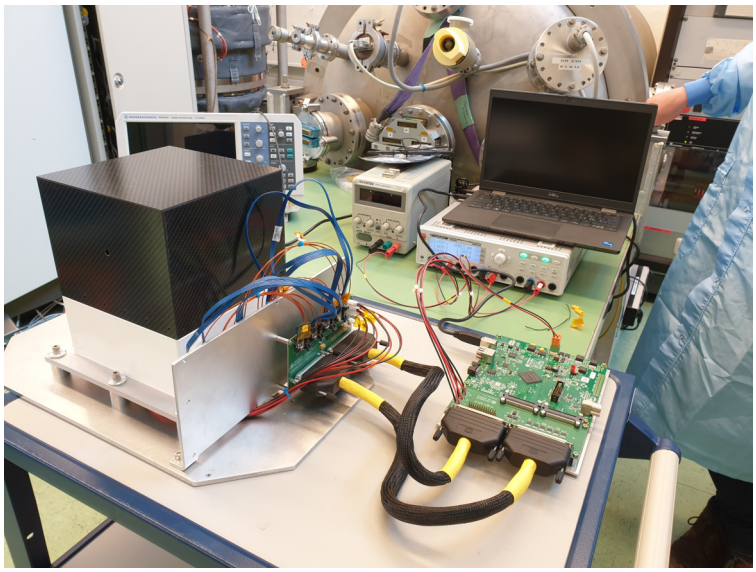

Figure 5.37: Testing of the data acquisition system outside the thermal chamber, based on a GPIO back-end developed by the DPNC for general use.

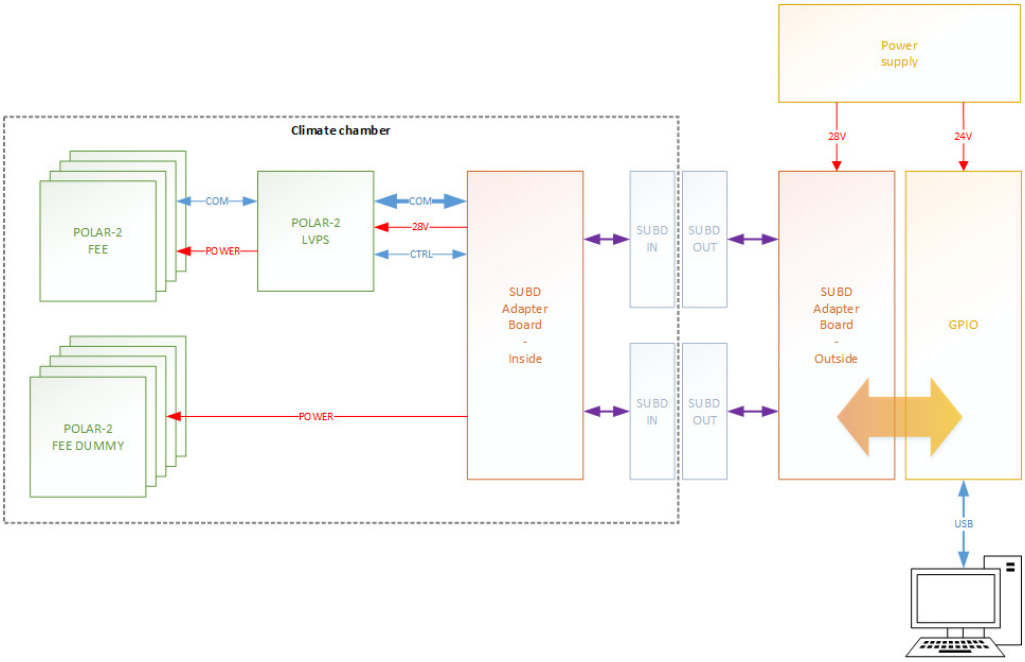

Figure 5.38: Block diagram of the experimental setup used for the Thermal Vacuum Test at MPE (from Jérôme Stauffer).

In addition to the 8 NTC thermistors of the 4 real modules, 19 PT1000 temperature sensors are placed at different locations on the grid and modules in order to monitor in detail the thermal behavior of the system and to have a precise input for the thermal simulations of the POLAR-2 instrument. The 3×3 grid is shown in Figure 5.39 while being assembled at DPNC before the test as well as during the installation of the PT1000 before closing the thermal vacuum chamber.

An MLI piece is covering the top part if the polarimeter down to the bottom of the scintillators. The MLI is covering all the way down to the bottom of the grid on two faces, while the two other sides of the polarimeter aluminum grid are painted with the CovaTherm white paint in order to mimic the final configuration on the CSS.

One of the four modules stopped working at the beginning of the test due to a wrong manipulation which connected the 3.8 V power connector of the module to a 28 V bias. The other 3 real modules as well as the 5 fake modules still worked properly for the test, and no damage or malfunction was observed due to the thermal cycling. The polarimeter was thermally cycled under vacuum with different configurations. The first cycles were ran with the Peltier element turned off, in order to asses the passive thermal behavior of the system. The Peltier were later powered for the last few cycles. Figure 5.40 shows the readout of the NTCs of the 3 functional modules during the cycling. A clear difference of 10°C is observed for each module between the SiPM arrays and the hottest part of the FEE. The modules were found to operate perfectly at all probed temperatures and the cycles provided a very useful input to thermal simulations.

Another thermal test was carried out in the frame of this thesis for the eXTP project. This work is described in Appendix C.

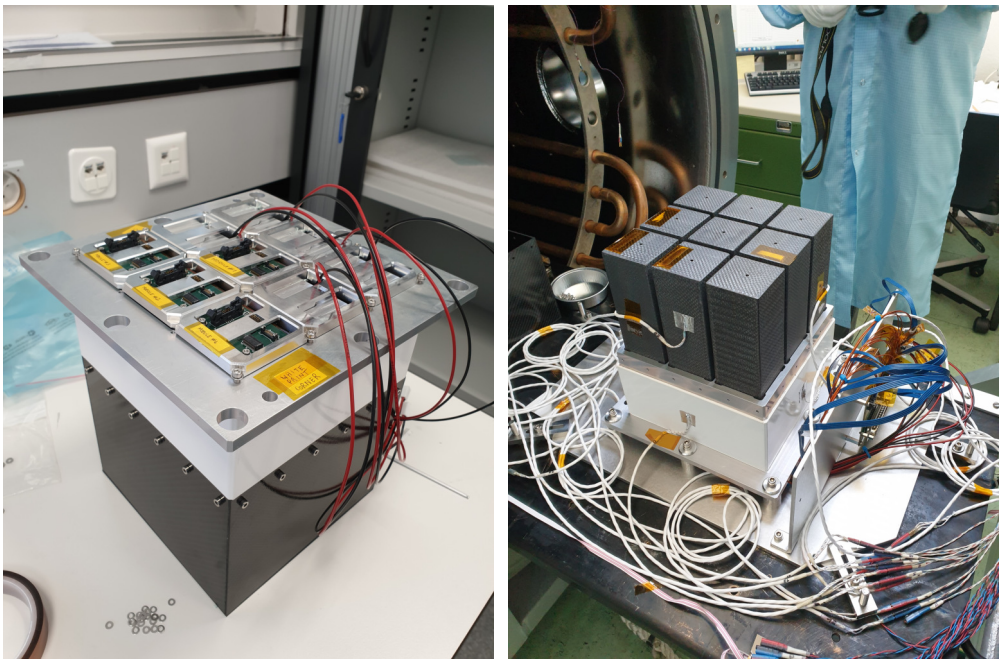

Figure 5.39: **Left:** Fully mounted 3×3 polarimeter grid in the DPNC clean room with 4 real modules and 5 dummies. **Right:** 3×3 grid placed in the thermal chamber at MPE. 19 PT1000 thermistors are placed on strategical emplacement on the polarimeter prototype in order to precisely monitor the thermal behavior of the system. This is a crucial input to perform reliable thermal simulations.

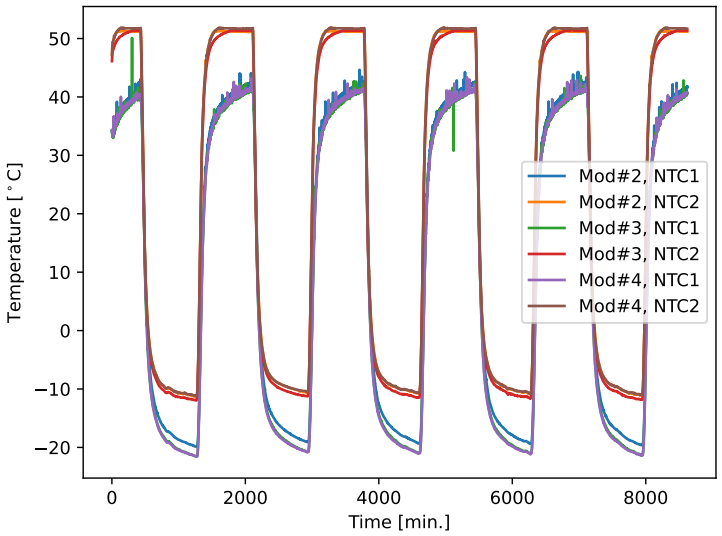

Figure 5.40: Temperature monitoring of the inside of 3 of the real polarimeter modules using the NTC sensors on the FEE. NTC1 is placed just at the back of the SiPM arrays, while NTC2 is placed near the FPGA and ASICs, which are the hottest components.

5.9 CONCLUSIONS AND OUTLOOK

Based on the legacy of the successful POLAR mission, which detected 55 GRBs and provided polarization results for 14 of them, the POLAR-2 detector is currently under development by a Swiss, Polish, Chinese, and German collaboration. With 4 times more polarimeter modules than its predecessor and thanks to technological upgrades, the POLAR-2 instrument will gain an order of magnitude in sensitivity. Shortening the scintillator bars to improve the signal-to-noise ratio and redesigning the module mechanics to optimize the contact surface between the scintillators and the sensors was part of this upgrade. The scintillators readout has also been upgraded, from multi-anode photomultiplier tubes to the twice more sensitive silicon photomultipliers. These improvements lead to a better collection of optical photons, significantly ameliorating the effective area of the polarimeter, especially at low energies. All qualification and calibration tests took place over the past years, and the module design is now ready for production as soon as the Phase D of the project is approved. The SiPMs and their behavior in radiation environments as well as the optical optimization and simulation of the polarimeter module are discussed in the following Chapters.

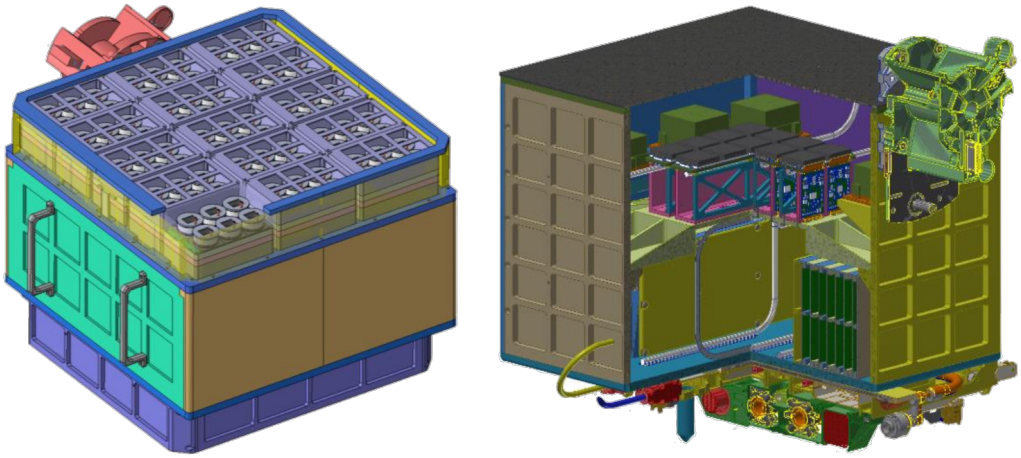

Figure 5.41: **Left:** CAD model of the Low energy Polarization Detector (LPD) payload being developed at GuangXi University (picture from Jianchao Sun). **Right:** CAD model of the Broad energy-band Spectrum Detector (BSD) payload being developed at IHEP (picture from Jianchao Sun).

In parallel to the development and construction of the POLAR-2 instrument, two other payloads that would greatly enhance the science capabilities of POLAR-2 are being proposed by our Chinese collaborators to be operated in parallel to POLAR-2 on the China Space Station. In the frame of this project, POLAR-2 is called the HPD for High-energy Polarization Detector. The other two payloads are the Broad energy-band Spectrum Detector (BSD), developed by IHEP in Beijing, and the Low-energy Polarization Detector (LPD) developed by GuangXi University in Nanning [68]. The BSD consists of a central array of segmented GaGG detectors read out by the POLAR-2 FEE and covered with a coded mask, with an outside ring of monolithic GaGG crystals also read out by SiPMs. The LPD employs Gas Pixel Detectors to measure the polarization in the keV band. The design of these two instruments are shown in Figure 5.41.

6

SIPM CHARACTERIZATION AND RADIATION DAMAGE ANNEALING STUDIES

In order to improve the Light Yield (LY) of the POLAR-2 modules, SiPMs were chosen over the PhotoMultiplier Tube (PMT) used in POLAR. Thanks to a Photo Detection Efficiency (PDE) twice larger than the PMTs' Quantum Efficiency (QE), and to some design optimization of the polarimeter modules, the SiPMs allow to greatly improve the light yield, as explained in Chapters 5 and 7. Increasing the light yield from 0.3 p.e./keV in POLAR (see Chapter 3) by more than a factor 5 allows to detect lower energy depositions into the plastic scintillators, and therefore leads to a better overall sensitivity at low energy, especially around a few tens of keV. Other than their higher sensitivity, SiPMs have many advantages compared to PMTs. They are indeed more compact, lighter, insensitive to magnetic fields, have a lower power consumption and require lower bias voltages. This is highly beneficial for space borne instruments due to the limited mass and volume available. The main significant drawbacks of using these silicon detectors in space are their high dark noise and their tendency to degrade with exposure to radiation.

The light yield corresponds to the amount of detected light per unit of incoming energy into the polarimeter, expressed in photoelectrons (p.e.) per keV. It is a crucial optical parameter to characterize the sensitivity of the detector.

When a SiPM is being operated in radiation fields, e.g. in low Earth orbit (LEO), its dark current and dark count rate (DCR) increase with the exposed dose due to radiation-induced damages in the silicon lattice [36, 78, 103, 179]. It is therefore important to characterize the sensors' behavior as a function of the absorbed dose, and especially the increase of dark noise, which will impact the long term performances of the overall instrument. After describing the characterization method used to pre-calibrate every SiPM channel, the behavior of the selected sensors for the POLAR-2 mission – the so called S13361-6075NE-04 array from Hamamatsu Photonics, and of the newer generation sensor – the S14161-6050HS-04, for different radiation doses will be presented.

A way to limit the dark noise, even before any radiation damage, is to operate the sensors as cold as possible. A thermo-electric cooling unit, a.k.a Peltier element, will be placed on the back of the SiPM arrays in each polarimeter module in order to cool them down (see Chapter 5). Operating at low temperature reduces the dark noise and allows the SiPM threshold to be lower, improving the sensitivity at low energy. But it does not prevent the radiation induced degradation of the instrument performances. An annealing strategy, which consists of heating up the sensors to recover part of the damages in the silicon lattice, has therefore been studied. For this purpose, numerous SiPMs from the S13 series from Hamamatsu with different microcell pitches (namely 25, 50, and 75 μm) were irradiated and stored at various temperatures. The performances recovery has then been studied as a function of the heating temperature used for annealing the lattice. As a figure of merit, the increase of dark current after a given dose with and without annealing have been compared for different

temperatures, giving a useful input to any experiment wanting to operate SiPMs in LEO or in the stratosphere.

e.g. GECAM [236, 237], Terzina [7], POEMMA [189], APT [104], GRID-01/02 [224, 242], SIRI [176–178], Glowbug [88], Daksha [11, 18]

6.1 SIPM CHARACTERIZATION

The S14161-6050HS-04 array, from hereon referred as S14, was first chosen due to its high PDE in order to maximize the LY of the instrument. Tests were also performed with the S13361-6075PE array, later called S13, which showed a much better photon counting ability at room temperature. Figure 6.1 shows a dark spectrum measured at room temperature with an S13 channel using the POLAR-2 Front-End Electronics (FEE). Due to the higher cell capacitance, S14 SiPMs did not show single photon counting ability at room temperature, preventing to convert accurately incoming energy into measured photo-electrons (p.e.).

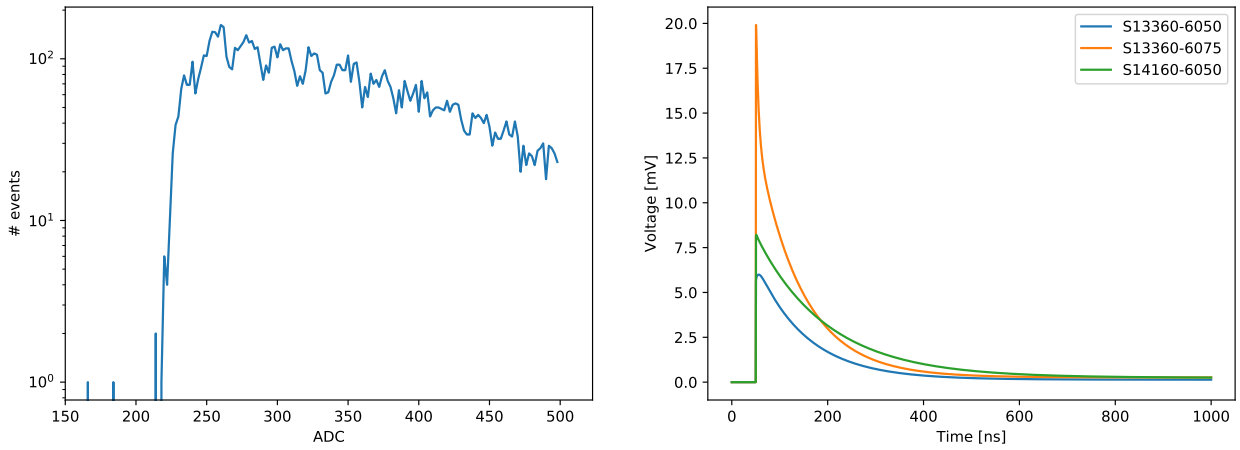

Figure 6.1: **Left:** Dark spectrum measured with the S13 SiPM. **Right:** S13 and S14. simulated pulse shapes for a light level of 50 p.e. using the Corsi model shown in the left part of Figure 6.2. The simulated pulse shape for the S13 SiPM with 50 μm microcell pitch is also shown for reference.

Simulated pulse shapes of the S13360-6075 and S14160-6050 arrays are also shown in Figure 6.1. The pulse shape simulated for the S13360-6050 is also shown for reference. Simulations have been performed using the PSpice cadence® software [31], modeling the SiPM using the Corsi model [44, 45] as shown in Figure 6.2. The S13360-6075 pulse is much sharper than the S14160-6050 one, because the latter SiPM type has a higher capacitance compared to the former. The higher amplitude for S13360-6075 is due to its higher gain, as specified in Table 6.1 which compares the specifications of S13 and S14 SiPMs. As shown in the right plot of Figure 6.3 for the S14 SiPM, there is a good match between the simulated and measured pulse shapes.

Note that the PSpice simulation in Figure 6.2 also shows the modeling of the pre-amplification and shaping stages of the CITIROC ASIC [29], not used for obtaining the pulse shapes presented here.

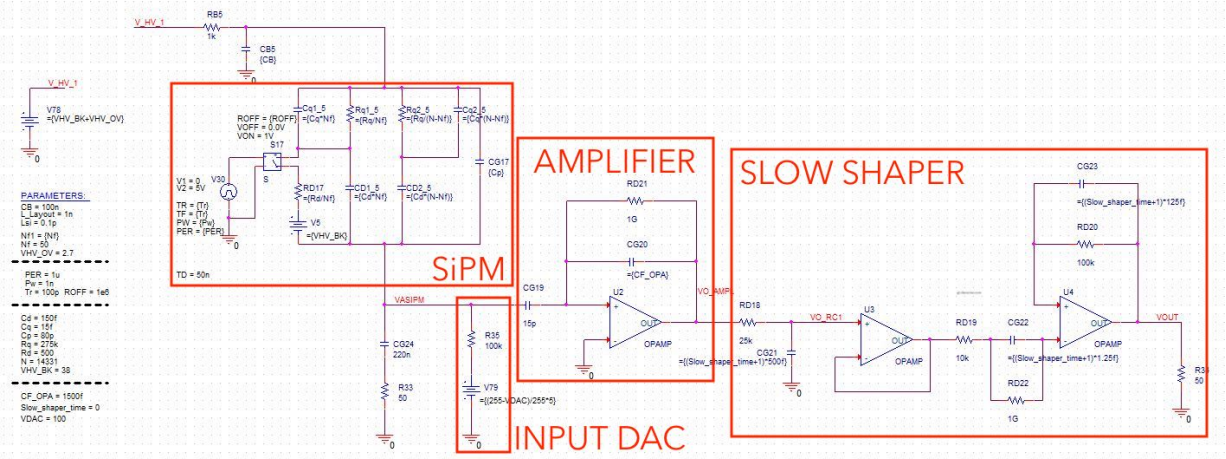

Figure 6.2: PSpice simulation in the Orcad Cadence software [31] used to simulate the S14 SiPM using the Corsi model [44, 45] and the first stages of the CITIROC ASIC ([29]).

Although the S13 series have a lower QE than the S14 generation, using the 75 μm microcell pitch S13 SiPMs allows to get a PDE approximately equal to that of the S14 (only available with 50 μm microcells) in the 400-500 nm range, thanks to a lower number of cells and therefore a smaller dead-space fraction. The S13360-6075, having a lower capacitance but a comparable PDE, was therefore selected for the final POLAR-2 FEEs for its photon counting ability leading to a better energy determination.

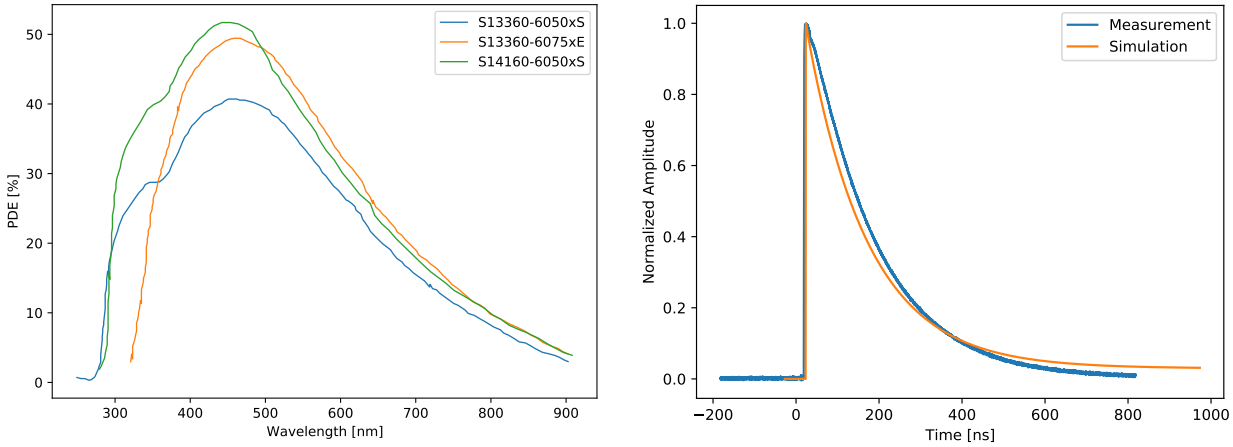

Figure 6.3: **Left:** Photo-detection efficiency of the S13360-60(50/75) and S14160-6050 SiPMs. Using the S13 generation with bigger microcells gives an efficiency comparable to that of the S14 in the 400-500 nm thanks to less dead space. The relevant wavelength interval for POLAR-2 is 400-500 nm, which corresponds the plastic scintillator emission range. **Right:** Shape comparison of the simulated normalized pulse shape to a measured pulse.

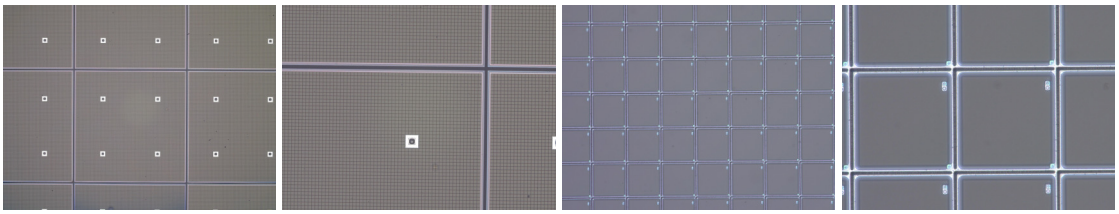

Figure 6.4: Microscope views of the S13 SiPM array taken with a Keyence VHX optical microscope. The left two images show the 6×6 mm^2 channels while the last two are zoomed in two show the microcells.

Figure 6.4 shows microcells pictures at different scales taken with a Keyence VHX digital optical microscope. In the first two pictures can be seen the 6×6 mm^2 channels, while the last two pictures show the microcells and their individual quenching resistors.

	S13361-6075PE	S14161-6050HS
Geometrical fill factor	82%	74%
Operating temperature	-40 to +60°C	-40 to +85°C
Spectral response range	320-900 nm	270-900 nm
PDE @450 nm (max)	50%	
Breakdown voltage	53±5 V	38 V
Recommended V_{OP}	V_{BD} + 3.0	V_{BD} + 2.7
V_{OP} variation across array	typ. ±0.1, max. ±0.3 V	typ. ±0.1, max. ±0.2 V
Cross talk probability	7%	
Dark count (thr. 0.5 p.e.)	typ. 2, max. 6 MHz	-
Dark current	-	typ. 2.5, max. 7.5 μA
Terminal capacitance	1280 pF	2000 pF
Gain	$4.0 \cdot 10^6$	$2.5 \cdot 10^6$
Temperature coefficient	54 mV/°C	34 mV/°C

Table 6.1: Important parameters of the S13361-6075PE-04 and S14161-6050HS-04 SiPMs from Hamamatsu (at recommended overvoltage and T=25°C) [93–95]

Table 6.1 shows the specifications of both S13360-6075 and S14160-6050 SiPMs. The only drawbacks of S13 over S14 are the higher temperature coefficients and the bigger breakdown voltage value and variations between batches. But these points are not really problematic when detailed pre-calibration is performed on every SiPM channel. Indeed, the current versus voltage, so called I-V characteristics, is measured around the breakdown region as a function of temperature for each SiPM channel. This allows not only to precisely characterize the voltages

non-uniformity among the SiPM arrays, but also to measure the temperature dependence of the breakdown, important to correct for temperature variations in the instrument and have an operating over-voltage as stable as possible.

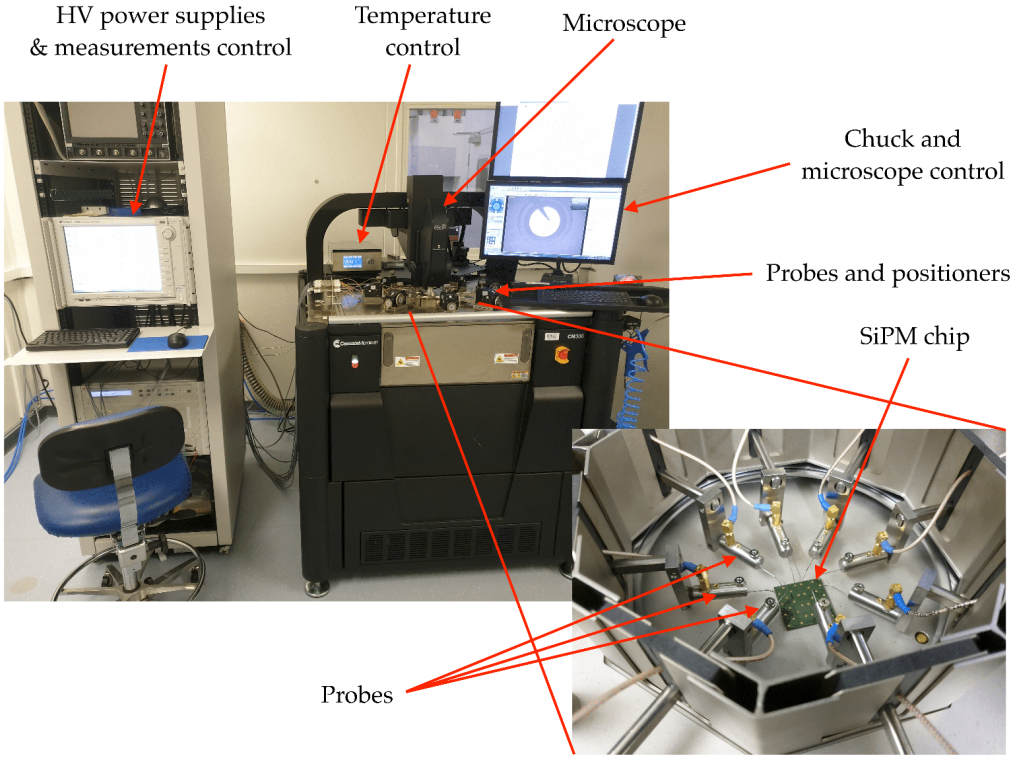

Figure 6.5: Cascade CM300 professional probe station setup used for measuring I-V curves at various temperatures [55]. The system is equipped with 8 probes, which allow to measure 4 channels in parallel, and macros can be written to automatically scan all the channels of a SiPM array.

In order to efficiently characterize the current versus voltage for an entire SiPM array at various temperatures, a semi-automatic probe station was used. I-V curves can be measured from -55°C up to 60°C using the Cascade CM300 with 8 probes in order to measure 4 channels in parallel, as shown in Figure 6.5. A macro is used to automatically scan the 16 channels of the SiPM array.

Measured I-V curves for an S14 channel are shown in the left of Figure 6.6 for temperatures ranging from -40 to +40°C. The linear dependency of the breakdown voltage on temperature can be observed, as well as the increase of dark current with temperature. The spread of the I-V characteristics among different channels can be observed in the right plot of Figure 6.6, showing the average and standard deviation of current versus voltage for 160 channels measured at room temperature.

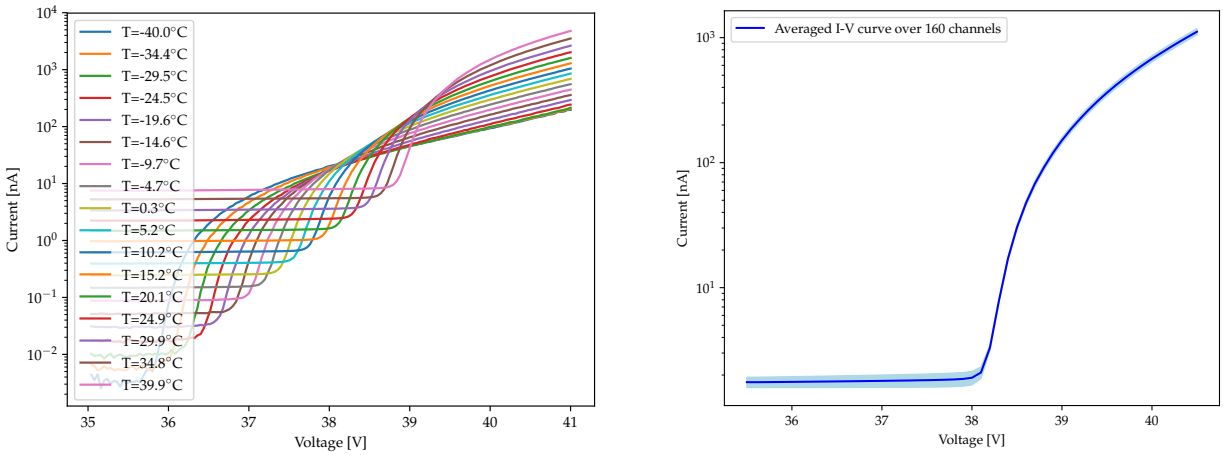

Figure 6.6: **Left:** I-V curves measured for an S14161-6050HS-04 channel for temperatures ranging from -40 to +40°C. A linear dependence of the breakdown voltage with temperature can clearly be observed. **Right:** I-V curve averaged over 160 SiPM channels measured at room temperature. As can be seen from the blue shaded area, which shows the standard deviation, the I-V characteristics is very reproducible from channel to channel. [55]

The breakdown voltage is extracted from the I-V measurement using two methods, shown in Figure 6.7. The first method consists of taking the maximum of the first voltage derivative of the current's logarithm. The other way used to compute the breakdown is to use the second voltage derivative of the current's logarithm, as depicted in the second plot of Figure 6.7. The breakdown values obtained with these two methods are very similar and the average is taken. The breakdown voltage measured over 160 S14 channels is V_{BD} = 38.206±0.023 V, corresponding to a relative deviation of $(1.102 \pm 0.696) \cdot 10^{-3}$ from the inspection data provided by the manufacturer.

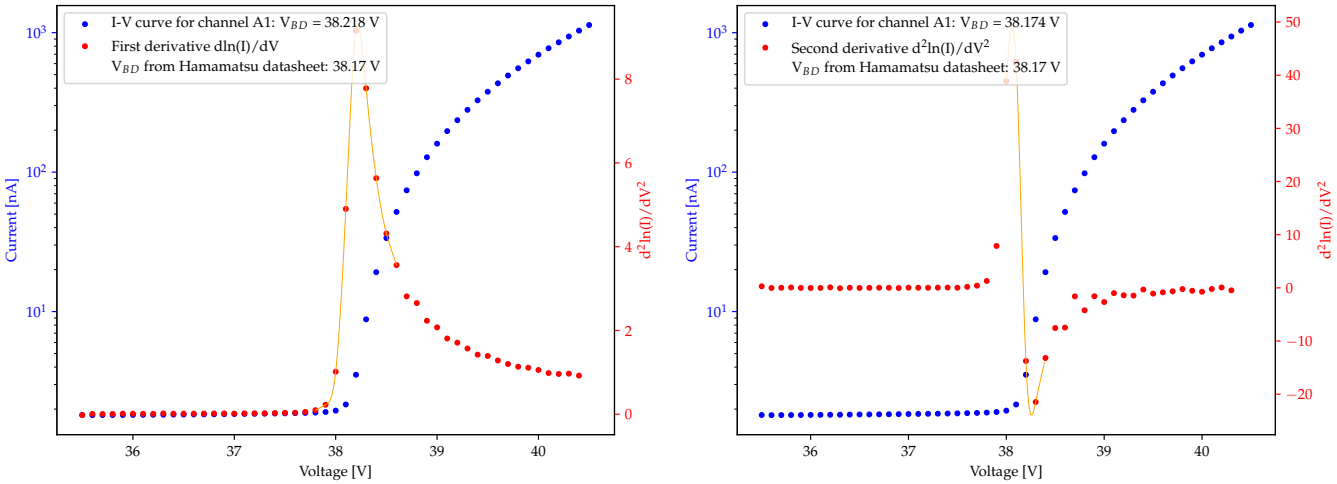

Figure 6.7: **Left:** Extraction of the breakdown voltage from a measured I-V curve by using the peak position of the first voltage derivative of the natural logarithm of the current. **Right:** Extraction of the breakdown voltage from a measured I-V curve by finding where the second voltage derivative of the natural logarithm of the current is null. [55]

The I-V curves and breakdown values shown here were obtained for the S14 generation, but similar results are obtained with the S13 type. Measuring the I-V curves for various temperatures for every single channels of the instrument allows to extract the linear relation between breakdown position and temperature. Negative Temperature Coefficient (NTC) thermistors placed on the back of the SiPM arrays are used to precisely monitor the temperature of the sensors. This is then used to correct the operating voltage for thermal variations in order to keep the operation point as stable as possible with time. The breakdown non-uniformities are also corrected within each individual module (64 channels, 4 S13 arrays) using an 8-bit DAC internal to the CITIROC ASIC [29] (see Chapter 5).

6.2 SIPM PERFORMANCE DEGRADATION IN SPACE-LIKE RADIATION CONDITIONS

The sensitive part of Silicon Photo-Multipliers consists of the depletion layer between a p-doped and an n-doped silicon lattice. When exposed to radiation, the silicon lattice can suffer from bulk damage [36, 78, 103, 179]. The absorbed radiation will cause point defects in the lattice, leading to a higher intrinsic current in the sensor caused by the higher resistivity due to impurities. The higher dark current and Dark Count Rate (DCR) will lead to a higher noise, degrading the Signal-to-Noise Ratio (SNR). This will oblige the instrument to be operated with a higher trigger threshold, causing a lower sensitivity to low energy photons in the case of POLAR-2.

SIMULATION SETUP	SiPM dose (Gy/yr)		
	at 340 km	at 383 km	at 450 km
Bare SiPM	1.29	2.79	8.86
Full Instrument	4.10×10^{-2}	8.24×10^{-2}	1.82×10^{-1}
Full Instrument + CSS	3.89×10^{-2}	7.89×10^{-2}	1.74×10^{-1}

Table 6.2: Annual expected dose in the SiPMs for different simulation scenarios and orbit altitudes. The 'Bare SiPM' case corresponds to the most pessimistic simulation setup, where bare sensors without any shielding are orbiting the Earth. The 'Full Instrument' scenario corresponds to the full POLAR-2 payload orbiting by itself, while the last case 'Full Instrument + CSS' is the most realistic case and contains a rough design of the neighbor payloads as well as the experimental module of the space station. The numbers are provided for different altitudes since the orbit of the space station might change during the lifetime of the mission, 383 km being the averaged altitude reported during the first year of the CSS's life. [171]

Since SiPMs are subject to radiation damage, it is crucial to simulate the space radiation environment and its impact on the sensors based on the instrument design. Simulating the polarimeter in Geant4 [6] and extracting the expected radiation environment from SPENVIS [48], the expected dose in each sensor can be computed [171]. Table 6.2 gives the expected yearly dose in Gray for the SiPMs (averaged over the 6400 POLAR-2 channels) for different simulation scenarios. The first and most pessimistic scenario is having bare SiPMs without any shielding. The other two scenarios are giving the expected dose accounting for the entire instrument design, which will shield the sensors, with and without the presence of the space station. The case including the space station is of course the most realistic one, but doses are also computed for the other two cases to cross check that the simulation results make sense. The doses are computed for an orbit with an inclination of 42°, and for 3 different altitudes since it impacts the amount of radiation, 383 km being the averaged altitude of the China Space Station (CSS) over its first year of operation. POLAR-2 is above all a victim of strong radiation fields when crossing the South Atlantic Anomaly (SAA). Named because of its location on the planisphere, the SAA is the intersection region of

the Earth's surface/lower orbit with the inner van Allen belt [60, 148], where charged particles are trapped because of the Earth's magnetosphere. This region corresponds to the fraction of the orbit at which most of the radiation will be absorbed into the instrument. Figure 6.8 shows the dose distribution in the 100 modules of POLAR-2. The outermost modules have higher doses since less material is shielding them from radiation. A small asymmetry in this map can be observed, with a smaller expected dose in the top right corner due to the presence of neighboring payloads.

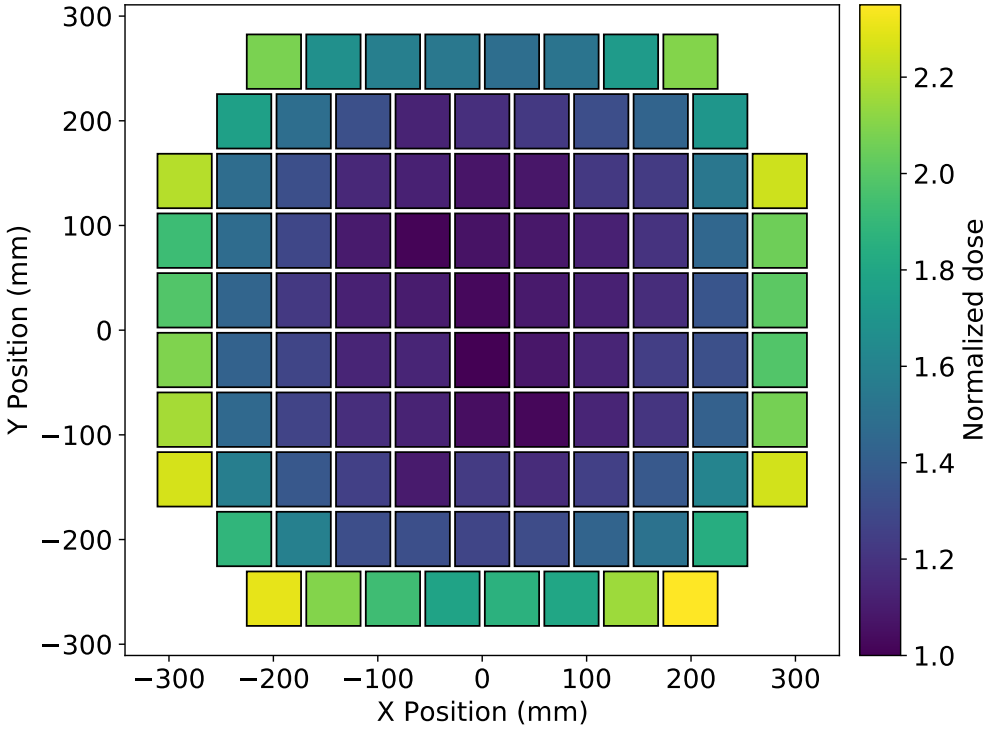

Figure 6.8: Normalized dose distribution per detector module in the POLAR-2 instrument (seen from the top) due to background radiation. The asymmetry is due to shielding from neighbor instruments on the payload platform and from the robotic arm adapter piece. The bottom right corner is not facing any neighbor payload, and the adapter is installed on the bottom side. It should be noted that the module configuration is not in a 10×10 configuration but in a more complex layout, which was the baseline design of the polarimeter at the time. (taken from [171], with permission)

SiPM arrays from both the S13 and the S14 generations were irradiated to several doses, ranging from a few years to a few tens of years equivalent in the POLAR-2 orbit. The irradiation setup is first presented, followed by the main results on irradiated SiPMs performance.

6.2.1 *SiPM irradiation setup*

The SiPMs were irradiated at the Institute of Nuclear Physics of the Polish Academy of Sciences, IFJ-PAN, in Krakow. The irradiation setup, described in [173], is shown in Figure 6.9.

Figure 6.9: **Left:** Irradiation setup ate IFJ-PAN, Krakow, Poland. **Right:** Four single channel SiPMs placed on the proton beam axis (taken from [51], with permission).

A 58 MeV proton beam, whose profile is shown in Figure 6.10, is used to irradiate the sensors up to the required dose. The needed irradiation time is also obtained through simulations.

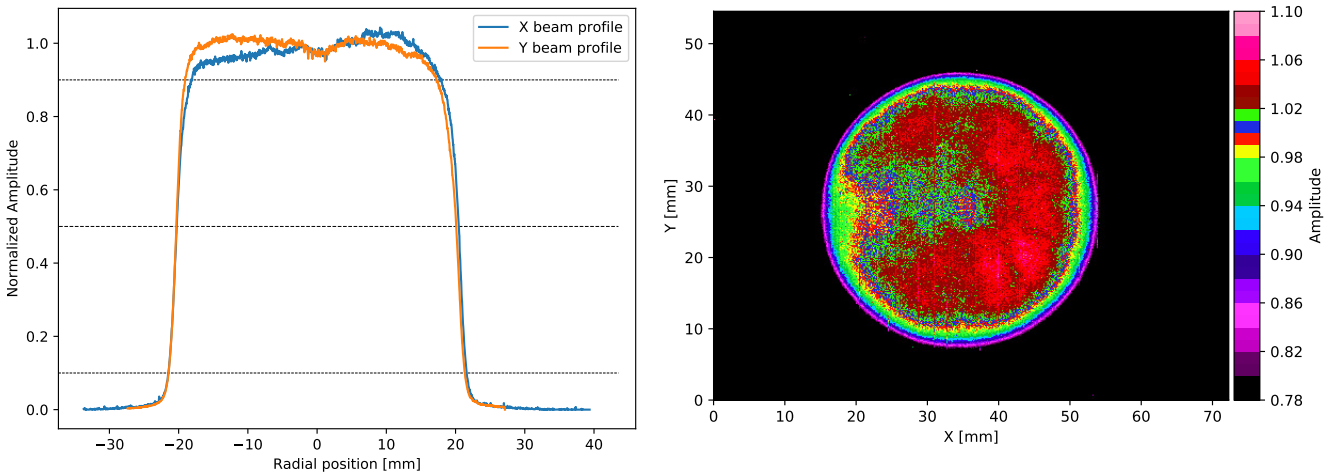

Figure 6.10: **Left:** Normalized intensity of the proton beam along the X and Y directions (taken from [51], with permission) **Right:** Two-dimensional image of the normalized beam profile (taken from [51], with permission)

The sensors are exposed to doses ranging from a quarter of a Gray to 2.31 and 4.96 Gy for the S14 and S13 types, respectively [171].

6.2.2 *Irradiated SiPM performances*

The channels of an S13 and S14 arrays were exposed to different doses using a lead shield to mask some of the channels, as described in [171]. Fluences from $1.90 \cdot 10^8$ to $3.73 \cdot 10^9$ protons/cm^2 have been used to expose the sensors to the needed dose. Figure 6.11 summarizes the important results obtained for the S13 SiPMs. The I-V has been characterized before irradiation for every channel as well as at different times after the irradiation took place. As observed in Figure 6.11 for a dose of 0.267 Gy, a dramatic increase of current is to be expected after several years of operation. The dark current then decreases with time when the sensors are stored at room temperature due to annealing effects.

Thanks to thermal energy from the ambient temperature, some point defects in the silicon lattice can be recovered.

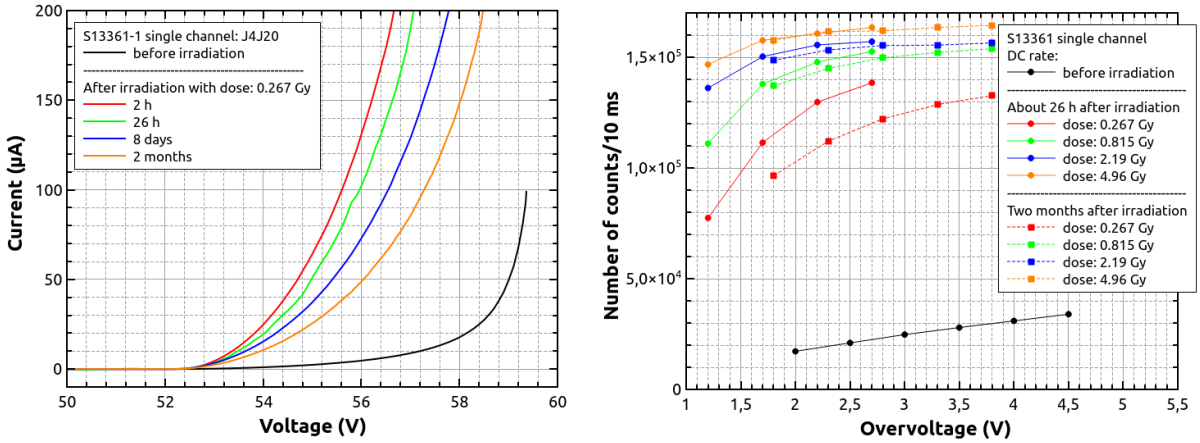

Figure 6.11: **Left:** I-V curves measured before and after irradiation for an S13 SiPM exposed to 0.267 Gy, equivalent to 3.38 years in space for POLAR-2. The SiPMs were stored at a non-stabilized room temperature of about 25°C. An annealing affect can be observed, as the post-irradiation current decreases with time. **Right:** Number of measured dark counts per interval of 10 ms with a 0.5 p.e. threshold. The measured rate clearly goes with the amount of radiation absorbed by the sensors. An annealing effect is observed as well in the form of a decrease of the rate with time after irradiation. (taken from [171], with permission)

The dark count rate has also been measured as a function of the overvoltage and for different doses and measurement temperatures. The results obtained at 25°C for the S13 type are shown in Figure 6.11. For a given temperature, the rate increases with the amount of radiation to which the silicon has been exposed to. An annealing effect is also seen here, where the rate decreases with time after irradiation with the sensors being stored at room temperature. Similar effects are observed for the S14 SiPMs [171].

An increase of dark count rate of about an order of magnitude is expected for POLAR-2 after two years of operation on the CSS. Considering an intrinsic SiPM crosstalk of about 10 %, this would correspond to an increase in threshold of 0.5 p.e. per year. Given a light yield of about 1.5 p.e./keV (see Chapter 7), the sensors' radiation damage implies a yearly energy threshold increase of 0.75 keV. This may not seem alarming compared to the wide energy range covered by

POLAR-2, but as for a typical GRB spectra most of the photons are emitted on the low energy end of the instrument sensitivity range, a small increase in energy threshold would have a large impact on the polarimeter's sensitivity.

The activation of the irradiated SiPMs mounted on FR4 PCBs has also been studied by placing the irradiated samples on High Purity Germanium detector (HPGe) directly after irradiation. The main contribution detected is a 511 keV coming from β^+ decay of copper, tin, carbon, and potassium [171]. The contribution of this activation to the total dose at which the sensors will be exposed in space has been judged to be negligible.

Except for precisely characterizing the deterioration of the SiPMs' performances with radiation, the other main outcome of this irradiation work is the need for studying in detail the behavior of the annealing effect for different temperatures for the expected doses that POLAR-2 will face in space. The annealing effect could be used to mitigate the effect of radiation on the sensors during the operation of the polarimeter. This would not only apply to POLAR-2, but to any space-based instrument wanting to operate SiPM-based instruments in similar environments (e.g. LEO). It was therefore decided to irradiate several sensors, to store them at various temperatures and monitor their performances with time. This work is described in the next section.

6.3 STUDYING THERMAL ANNEALING OF IRRADIATED SIPM

21 S13 single channel SiPMs with 3 different microcell sizes have been irradiated with the same proton beam previously described in Subsection 6.2.1. The sensors have been exposed to a dose of 0.134 Gy, equivalent to 1.7 years in space for POLAR-2. These SiPMs have then been stored at different temperatures and their I-V characteristics have been monitored over time. The dark spectra of these sensors after different levels of annealing have also been measured. We first describe here the setup used to measure and store the sensors, followed by the results obtained in this study, already published in [51]. We then conclude on how the annealing effect can be used to improve the performance of SiPM-based space missions.

6.3.1 *Storage and measurement setups [51]*

This section (6.3.1) is taken from [51], with a few small adaptations.

With the aim of studying the silicon lattice recovery through annealing effect, SiPMs have been stored in different thermal and electrical bias conditions. SiPMs of each of the 3 types were stored within 24 hours [1] after irradiation at 6 different temperatures ranging from -22.8±1.8 to 48.7±3.3°C. Several 50 μm SiPMs were also stored at room temperature[2] with different bias voltages (2 with 3 V overvoltage, 1 with 8 V and 1 with 12 V). The number of SiPMs stored at each condition is summarized in Table 6.3, while the setups for biasing the SiPMs and storing them at the highest temperatures are shown in Figure 6.12.

Chamber ID	1	2	3	4	5	6
Chamber type	Freezer	Fridge	Room temperature	Polystyrene + Power resistor		
Storage Temperature [°C]	-22.8±1.8	6.3±0.9	20.5±0.6	29.7±0.6	38.7±1.6	48.7±3.3
# of 25 μm SiPMs	1	1	1	1	1	1
# of 50 μm SiPMs	1	1	1+4 biased	1	0	1
# of 75 μm SiPMs	1	1	1	1	1	1

Table 6.3: List of storage conditions for the SiPMs used in this study. One SiPM of each cell size (25, 50, and 75 μm) is passively stored at each of the 6 temperatures. For the 50 μm, the effect of different over-voltages (3, 8, and 12V) is studied at room temperature. The SiPMs in chamber #6 were later placed in a climatic chamber in order to characterize the annealing at higher temperatures (75 and 100°C)

1 The irradiation took place in Krakow, Poland, while the storage and characterization of the SiPMs post-irradiation were performed in Geneva, Switzerland. The samples therefore spent about 24 h at ambient temperature before being stored in controlled conditions. This does not affect the results since we study the temperature dependence of the annealing effect relative to the first measurement point (after transportation) and all samples were stored under the same condition in this 24 h period.

2 All the setups where placed in a clean room, where the temperature is controlled at 20°C.

As illustrated in Table 6.3, the coldest storage temperatures were reached using a freezer and a fridge, while the hottest ones were reached using power resistors placed in purpose build polystyrene chambers (see Figure 6.12) and tuned to reach specific temperatures. The temperatures were monitored every few days to ensure their stability and calculate their uncertainties. At the end of the measurement campaign, the annealing effect on even higher temperatures have been studied by storing several SiPMs in a climatic chamber with temperatures of 75 and 100°C. The biased SiPMs were stored in a dark box and biased using an in house developed power supply board based on the LT3482 DC/DC converter from Linear Technology. For these biased SiPMs great care was taken in the design of the dark box in order for the SiPMs to remain in good thermal contact with the box. Thereby, the temperature of the SiPMs, despite the significant heat dissipation inside of the SiPM, was at 20.5 ± 0.6°C throughout the test.

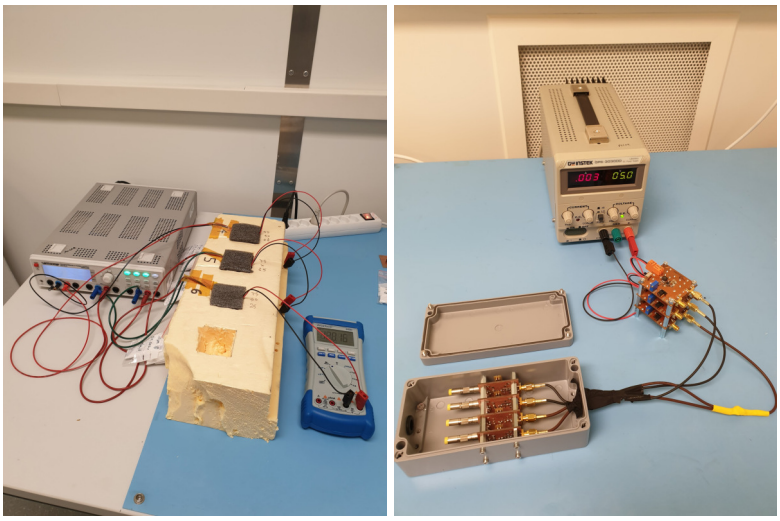

Figure 6.12: ***Left:*** SiPM storage setup for high temperatures. A block of polystyrene (yellow) is used in which cavities of $50 \times 50 \times 50\,\mathrm{mm}^3$ are cut. The SiPMs, along with a power resistor are stored in the various cavities. The power resistors are powered using the power supply which provides a current calibrated to reach the required stable temperature in the cavities. The cavities are closed off with a lid of foam while the temperature is occasionally monitored using a PT100. ***Right:*** The SiPMs stored at different bias voltages. The SiPMs are stored in a dark box, seen opened in the figure, which allows to run the SiPMs in dark conditions with good thermal conduction towards the aluminum box. As a result the SiPMs remain thermalized with the clean room, which has a controlled temperature. The bias voltages are provided through several in house developed power supply boards based on the LT3482 DC/DC converter from Linear Technology. (taken from [51], with permission)

The two main features measured to study the annealing effect are the dark current and the dark count rate (DCR) of the SiPMs with respect to the time after irradiation. The former is actually measured versus voltage through an I-V characterization at room temperature all along the 2 months of storage, while the latter is measured for a 5 V overvoltage at both 0 and 20°C at the end of the 2 months storage. Great care was taken to minimize the time for each SiPM to

be taken out of their thermal storage unit, while at the same time it was ensured that the SiPMs reached measurement temperature before measuring. It was found that removing the SiPMs from their storage for 10 minutes would allow for complete thermalization with the room. This way the total time outside of the thermal storage unit was negligible (15 minutes per measurement: 10 minutes for thermalizing and 5 for measuring the I-V characteristics) while ensuring that all I-V measurements are performed with the SiPM thermalized to 20°C.

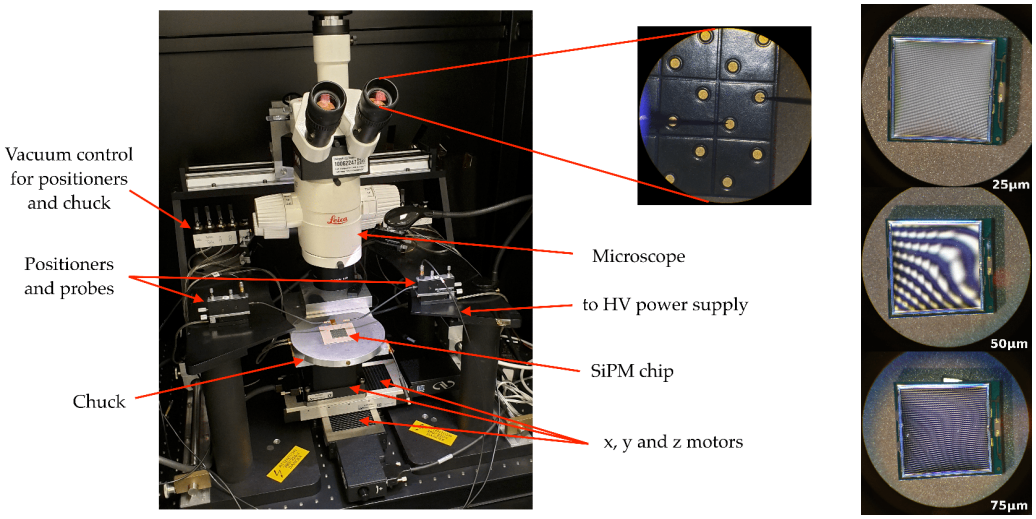

Figure 6.13: **Left:** Probe station setup used for I-V characterization. **Right:** Microscope view of the 25/50/75 μm SiPMs. (taken from [51], with permission)

The I-V characterization is made using an in-house designed probe station shown in Figure 6.13, based on Keithley electrometers and controlled through a LabView^{TM} program. The Cascade CM300 semi-automatic probe station mentioned in section 6.1 is not used here since the sensors are single channel, so one would have to switch sensor for each measurement in any case. The DCR is measured in a climatic chamber, shown in Figure 6.14, where the SiPM waveforms are readout with a Teledyne Lecroy Wavesurfer 510 oscilloscope through a transimpedance amplifier (TIA) board based on ADA4817 and AD8000 operational amplifiers. The use of a climatic chamber ensures a stable temperature all along the measurements, and allows to acquire dark spectra at different temperatures, namely 0 and 20°C.

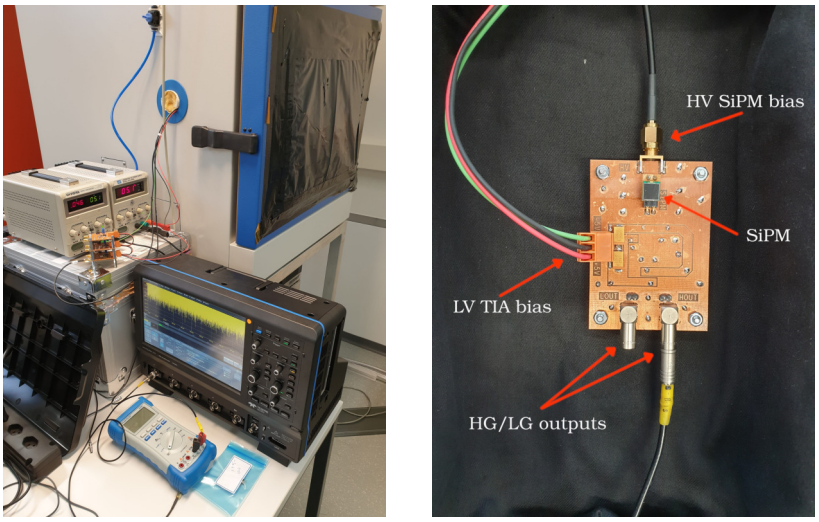

Figure 6.14: Climatic chamber setup and transimpedance amplifier board used to characterize the SiPMs dark spectra (taken from [51], with permission)

For each dark spectrum, 20 waveforms of 10 ms are acquired with a threshold of 0.5 photoelectron (p.e.). An analysis similar to that described in [171] is applied to the waveforms. A Savitzky-Golay algorithm [206] is applied twice to clean the data. The waveform is then subtracted to a time-delayed copy of itself in order to ease the peak finding process. Finally, an amplitude threshold of 20 mV for the 50 μm SiPM, 25 mV for the 75 μm SiPM, and a deadtime threshold[3] of 120 ns are applied (see Figure 6.23). Note that the SiPMs are operated at 5 V overvoltage to have a higher prompt crosstalk (compared to that at 3 V overvoltage, that is the Hamamatsu recommended operation point) and therefore more peaks to fit in the dark spectrum. This makes the analysis easier and does not affect its quality since we are interested in the relative comparison of the photoelectron resolution for different annealing conditions. Each dark spectra is fitted using a sum of Gaussians.

This section (6.3.2) is taken from [51], with a few small adaptations.

6.3.2 *Temperature dependence of the annealing effect on the SiPM current [51]*

The measured I-V characteristics for 75 μm SiPMs are shown in Figure 6.15 for both the SiPMs stored at the lowest and room temperatures. The curves for other microcell sizes and annealing temperatures are provided in appendix A. A zoomed-in version is also displayed as a corner plot in log-scale in order to highlight the evolution of the I-V shape around the breakdown region. From those plots it is clearly seen that there is almost no effect on the post-irradiation dark current on the SiPMs stored at -22.8$\pm$1.8°C, while for those stored at room temperature almost half of the dark current is recovered after about 2 months.

3 This inter-pulse time threshold is used to get rid of delayed crosstalk and afterpulsing.

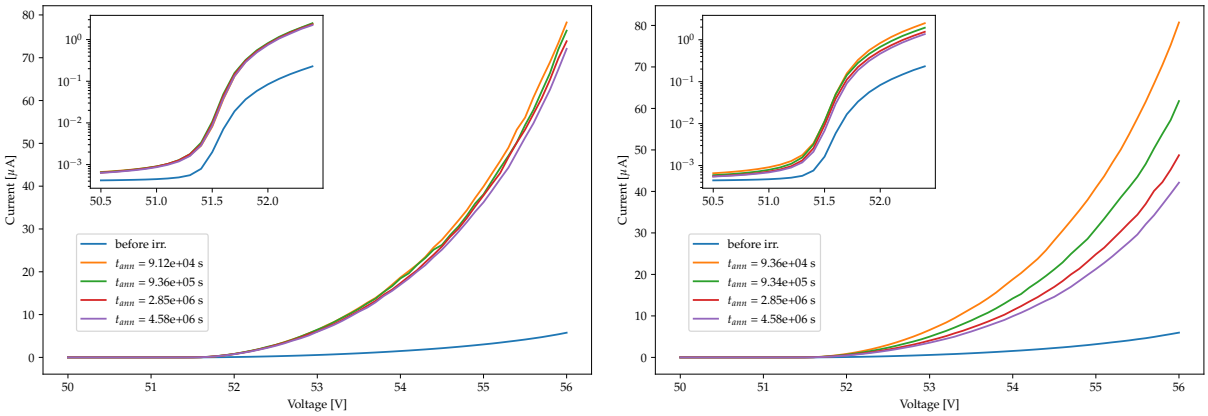

Figure 6.15: Post-irradiation time evolution of the I-V characteristics of 75 μm SiPMs at $-22.8 \pm 1.8°C$ (**left**) and at $20.5 \pm 0.6°C$ (**right**). We only show a few I-V curves here even though a lot more curves were measured for the convenience of the reader. All the curves are provided in appendix A. (taken from [51], with permission)

For a better representation of the temperature dependent improvement in dark current, it was decided to work with the current measured at 3 V overvoltage[4] (standard operating point recommended by the manufacturer). The time evolution of the 3 V overvoltage current for different storage temperatures are shown in Figure 6.16 for the three types of SiPMs. In this figure the y-axis shows the normalized current, meaning the dark current relative to that measured during the first measurement after irradiation.

4 The breakdown voltage is determined from the square root of the current versus the voltage. Two linear fits are performed, one for the region below the breakdown, and one for the region above. The breakdown is taken as the point of intersection of these two linear fits. This method has been compared to other methods (first and second derivative of the current's logarithm) that gave similar breakdown values.

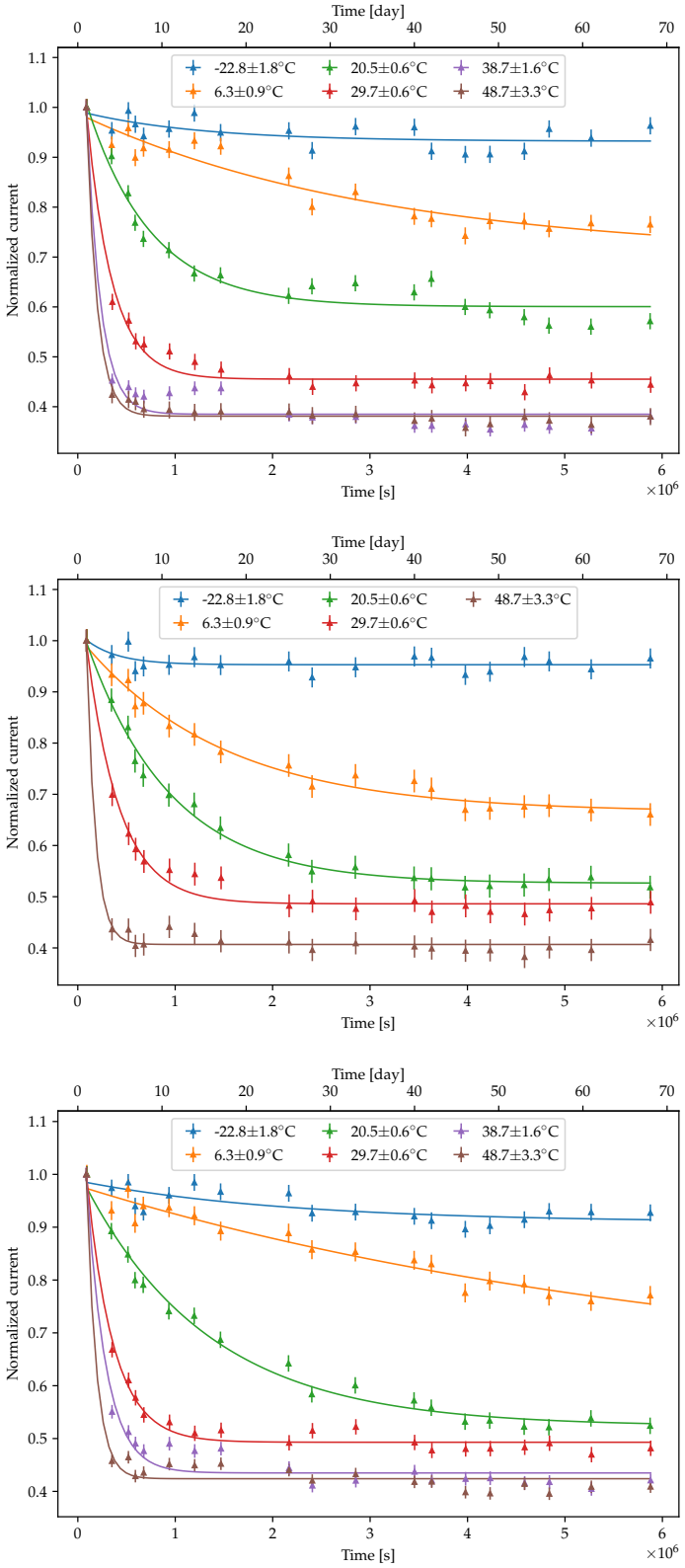

Figure 6.16: Normalized current (to the first data point in time) measured at 3V overvoltage vs. time after irradiation for SiPMs stored at different temperatures (as explained in the legend). The curves are fitted with an exponential function, for the 25 μm (**top**), 50 μm (**middle**), and 75 μm (**bottom**) SiPMs. (taken from [51], with permission)

It can be noticed that the current at this fixed operation point is following an exponential decay with time, whose amplitude, time constant, and offset vary with the storage temperature. The data points in Figure 6.16 are therefore fitted with an exponential function, whose fit parameters are plotted versus the storage temperature in Figure 6.17. The exponential offset is correlated to the fraction of the post-irradiation dark current that can be recovered after an infinite amount of time, while the exponential slope can be seen as a dark current recovery rate. It can clearly be seen that the annealing process is both faster and more efficient (meaning that the current is reduced by a significant fraction) at higher temperatures. Furthermore, almost no annealing effect is observed at $-22.8 \pm 1.8°C$.

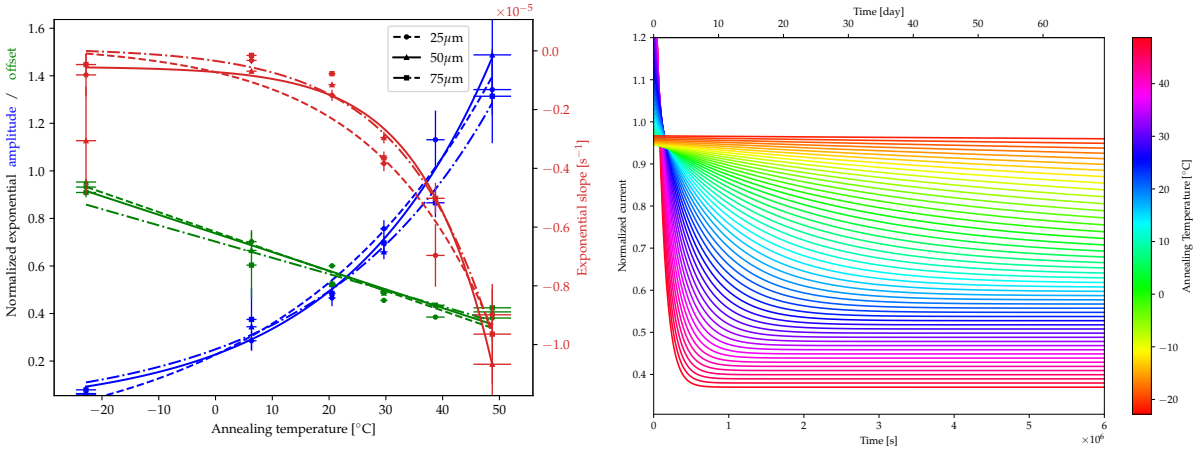

Figure 6.17: Normalized exponential fit parameters for current vs. time after irradiation (**left**) and the temperature dependency of the exponential annealing effect for the 75 μm SiPM as predicted based on the fit results (**right**) (taken from [51], with permission)

The exponential offset has a linear dependency in storage temperature, while the amplitude and exponential slope appear to have an exponential behavior. These exponential fit parameters are consequently fitted, and the fit results are shown in Table 6.4. Using these fit parameters one can get the exponential decay shape of the current versus time for a wide range of temperatures. The right plot of Figure 6.17 shows the evolution of this extrapolated exponential decay with temperature for the 75 μm SiPM.

Parameter	Pitch [μm]	Amplitude	Slope [$^{\circ}C^{-1}$]	Offset
Amplitude	25	$(4.12\pm2.06)\cdot10^{-1}$	$(2.76\pm0.81)\cdot10^{-2}$	$(-1.86\pm2.17)\cdot10^{-1}$
	50	$(2.33\pm0.82)\cdot10^{-1}$	$(3.79\pm0.62)\cdot10^{-2}$	$(-5.73\pm97.05)\cdot10^{-3}$
	75	$(2.66\pm0.98)\cdot10^{-1}$	$(3.26\pm0.64)\cdot10^{-2}$	$(-1.60\pm10.99)\cdot10^{-2}$
Slope	25	$(-9.59\pm8.83)\cdot10^{-7}\ s^{-1}$	$(4.75\pm1.74)\cdot10^{-2}$	$(2.32\pm12.77)\cdot10^{-7}\ s^{-1}$
	50	$(-1.84\pm1.17)\cdot10^{-7}\ s^{-1}$	$(8.22\pm1.26)\cdot10^{-2}$	$(-5.36\pm3.44)\cdot10^{-7}\ s^{-1}$
	75	$(-4.41\pm3.26)\cdot10^{-7}\ s^{-1}$	$(6.36\pm1.45)\cdot10^{-2}$	$(9.79\pm69.20)\cdot10^{-8}\ s^{-1}$
Offset	25	-*	$(-8.30\pm0.66)\cdot10^{-3}$	$(7.44\pm0.21)\cdot10^{-1}$
	50	-*	$(-7.84\pm0.93)\cdot10^{-3}$	$(7.37\pm0.27)\cdot10^{-1}$
	75	-*	$(-6.83\pm0.88)\cdot10^{-3}$	$(7.03\pm0.27)\cdot10^{-1}$

Table 6.4: Fit parameters of the normalized temperature-dependant exponential parameters shown in Figure 6.17. The amplitude and slope are fitted with exponential functions of the form $a\exp(bx)+c$, while a linear fit* of the form $ax+b$ is performed on the temperature dependency of the offset. [51]

Another way of analysing the impact of annealing on the dark current is to use the current related damage rate α, as defined in [179]:

$$\alpha = \frac{\Delta I}{\Phi_{eq} V} \tag{6.1}$$

where V is the sensitive volume in cm^3, Φ_{eq} the equivalent fluence in cm^{-2}, and ΔI the current increase due to irradiation[5].

The fluence with which the SiPMs have been irradiated is $10^8\ p/cm^2$, and the effective surface for each type of sensor is derived using the numbers summarized in table 6.5.

n_{cells}	cell pitch [μm]	Fill factor [%]	Effective channel surface [mm^2]
57600	25	47	16.92
14400	50	74	26.64
6400	75	82	29.52

Table 6.5: SiPM channel effective surface for S13360-6025/50/75 SiPMs [51]

5 As discussed in the following talk: "SiPMs in high radiation environment" by Erika Garutti, one should use an extended version of (6.1) for devices with gain like SiPMs: $\alpha_G = \frac{\Delta I}{\Phi_{eq}\cdot V\cdot G\cdot \mathrm{ECF}\cdot \mathrm{PDE}}$ where G is the gain, ECF the excess charge factor, and PDE the photo detection efficiency. Since a relatively low fluence was used in this study, the effect of radiation on the Gain can be neglected. Moreover, as the α parameter is extracted for a quite low overvoltage (3 V), the ECF can be expected to be quite low, so as its dependence on radiation damage for a small fluence. We therefore use the definition in (6.1) for the current related damage rate.

In order to get the sensitive volume of each type of sensor, the effective surfaces in table 6.5 need to be multiplied by the thickness of the Silicon depletion layer, which is about 2 μm for Hamamatsu SiPMs [78]. The depletion width can be estimated using its relation to the micro-cell capacitance: $C_{\mu\text{cell}} = \varepsilon_0 \cdot \varepsilon_{\text{Si}} \cdot \frac{A}{d}$, with $\varepsilon_0 = 9.95 \cdot 10^{-14} F/cm$ the vacuum permittivity, ε_{Si} the relative permittivity of Silicon, A the effective surface of the micro-cell, and d the depletion width. Having the sensitive volume and the fluence, the dark current data from Figure 6.16 can be converted into current related damage rate (see Figure 6.18).

The current related damage rate obeys the following relation with time [179]:

$$\alpha(t) = \alpha_I \exp\left(-\frac{t}{\tau}\right) + \alpha_0 - \beta \ln\left(\frac{t}{t_0}\right) \tag{6.2}$$

where α_I, α_0, and β are the amplitudes of each terms in A/cm, t_0 defines the time unit, and τ follows the Arrhenius relation [36]:

$$\frac{1}{\tau} \equiv k(T) = k_0 \exp\left(-\frac{E_a}{k_B T}\right) \tag{6.3}$$

where $k_B = 8.617 \cdot 10^{-5}$ eV/K is the Boltzmann constant, E_a is the activation energy of the defects, and T the annealing temperature.

The relation (6.2) is used to fit the current related damage rate for the three types of SiPMs at different annealing temperatures. The fits are shown in Figure 6.18, while the time dependent fit parameters are given in Table 6.6 for the different amplitudes and the Arrhenius plots for the exponential decay time are provided in Figure 6.19. Note that there is almost no recovery for the coldest annealing temperature (-22.8 ± 1.8°C), resulting into big errors on the fit parameters due to the flat nature of the curve.

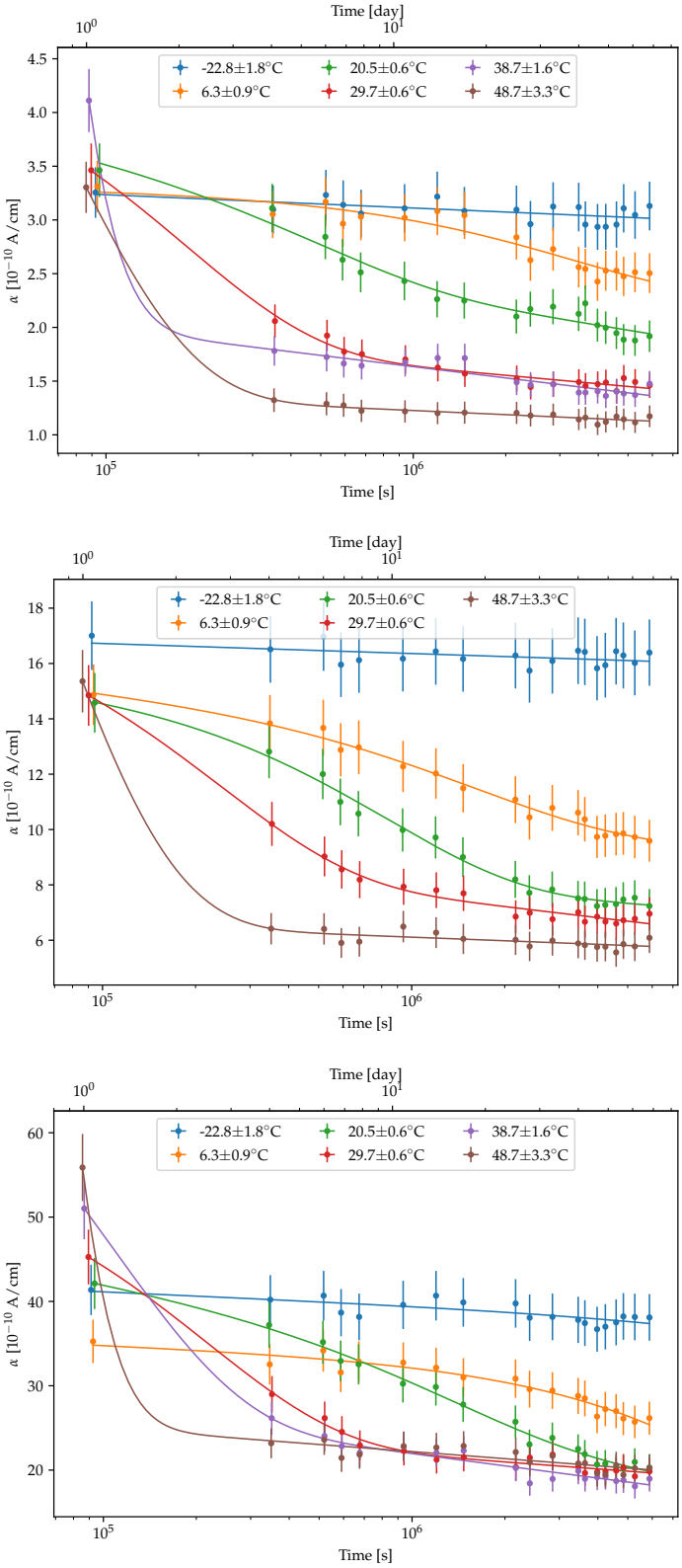

Figure 6.18: Current related damage rate vs. time after irradiation, fitted with the function (6.2), for the 25 μm (**top**), 50 μm (**middle**), and 75 μm (**bottom**) SiPMs. Systematic effects coming both from the measurement procedure and from variations among samples contributes to the error on α, whereas the error bars used in Figure 6.16 only contained a contribution from the former source systematic uncertainties, the latter being washed out by the current normalization. We do observe outlying curves due to a spread between samples, e.g. for the 75μm SiPM at 6.3°C, but the trend of these curves behave as expected. [51]

Pitch	Temperature [°C]	α_I [10^{-10}A/cm]	α_0 [10^{-10}A/cm]	β [10^{-10}A/cm]
25 μm	-22.8 ± 1.8	$(2.93 \pm 2204.00) \cdot 10^{-1}$	(3.57 ± 220.80)	$(5.46 \pm 4.26) \cdot 10^{-2}$
	6.3 ± 0.9	$(8.80 \pm 3.28) \cdot 10^{-1}$	(2.69 ± 1.57)	$(2.43 \pm 10.48) \cdot 10^{-2}$
	20.5 ± 0.6	$(8.37 \pm 3.01) \cdot 10^{-1}$	(5.56 ± 1.06)	$(2.33 \pm 0.70) \cdot 10^{-1}$
	29.7 ± 0.6	(2.50 ± 0.21)	(3.06 ± 0.35)	$(1.05 \pm 0.24) \cdot 10^{-1}$
	38.7 ± 1.6	$(1.30 \pm 4018.00) \cdot 10^{2}$	(3.73 ± 0.28)	$(1.52 \pm 0.19) \cdot 10^{-1}$
	48.7 ± 3.3	(6.65 ± 1.66)	(1.99 ± 0.13)	$(5.55 \pm 0.85) \cdot 10^{-2}$
50 μm	-22.8 ± 1.8	(1.57 ± 1566.00)	$(1.69 \pm 156.80) \cdot 10^{1}$	$(1.57 \pm 1.59) \cdot 10^{-1}$
	6.3 ± 0.9	(3.32 ± 1.19)	$(1.81 \pm 0.50) \cdot 10^{1}$	$(5.52 \pm 3.26) \cdot 10^{-1}$
	20.5 ± 0.6	(6.79 ± 1.05)	$(1.19 \pm 0.43) \cdot 10^{1}$	$(2.95 \pm 2.80) \cdot 10^{-1}$
	29.7 ± 0.6	(8.53 ± 0.71)	$(1.53 \pm 0.18) \cdot 10^{1}$	$(5.56 \pm 1.17) \cdot 10^{-1}$
	48.7 ± 3.3	$(3.48 \pm 2.12) \cdot 10^{1}$	(8.63 ± 0.92)	$(1.83 \pm 0.62) \cdot 10^{-1}$
75 μm	-22.8 ± 1.8	(3.67 ± 169.20)	$(4.61 \pm 16.27) \cdot 10^{1}$	$(7.47 \pm 7.61) \cdot 10^{-1}$
	6.3 ± 0.9	$(2.16 \pm 4.03) \cdot 10^{1}$	$(1.97 \pm 3.51) \cdot 10^{1}$	$(5.69 \pm 6.88) \cdot 10^{-1}$
	20.5 ± 0.6	$(1.32 \pm 0.40) \cdot 10^{1}$	$(5.72 \pm 1.71) \cdot 10^{1}$	(2.40 ± 1.10)
	29.7 ± 0.6	$(3.11 \pm 0.22) \cdot 10^{1}$	$(3.82 \pm 0.45) \cdot 10^{1}$	(1.19 ± 0.30)
	38.7 ± 1.6	$(5.38 \pm 0.94) \cdot 10^{1}$	$(5.04 \pm 0.41) \cdot 10^{1}$	(2.06 ± 0.28)
	48.7 ± 3.3	$(1.94 \pm 7203.00) \cdot 10^{3}$	$(3.91 \pm 0.35) \cdot 10^{1}$	(1.22 ± 0.24)

Table 6.6: Fit parameters vs. annealing temperature obtained using the expression (6.2) for the 3 microcell pitches. The fit for -22.8 ± 1.8°C gives very big error due to the fact that α versus time is flat since there is almost not annealing at this temperature. [51]

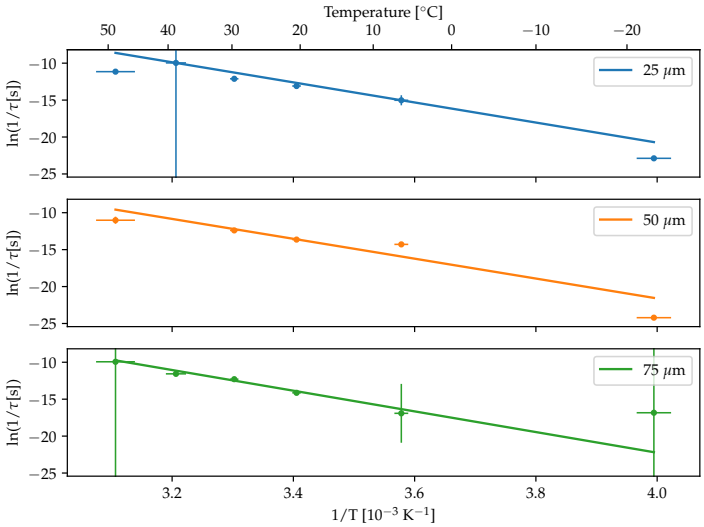

Figure 6.19: Arrhenius plot for the decay time τ for the 25 μm (**top**), 50 μm (**middle**), and 75 μm (**bottom**) SiPMs (taken from [51], with permission)

The Arrhenius plots in Figure 6.19, which show the fit values for τ as a function of temperature, are fitted using the relation (6.3). The fit parameters and their corresponding physical quantities are provided in Table 6.7. k_0 corresponds to the frequency at which the defects try to escape [103]. A rate of the order $10^{12} - 10^{13}$ Hz is expected from a dissociative process [42, 175, 179]. This is compatible with the values obtained from the offset of the fit. It is therefore likely that the exponential decay part in (6.2) is caused by a dissociation of the defects.

Pitch	$\ln(k_0\ [s^{-1}])$	$k_0\ [s^{-1}]$	Slope [K]	E_a [eV]
25 μm	$(3.36\pm0.37)\cdot10^1$	$4.05 \cdot 10^{14}\ ^{+1.78\cdot10^{15}}_{-4.05\cdot10^{14}}$	$(-1.36\pm0.11)\cdot10^4$	1.17 ± 0.09
50 μm	$(3.22\pm1.08)\cdot10^1$	$9.82 \cdot 10^{13}\ ^{+1.89\cdot10^{16}}_{-9.82\cdot10^{13}}$	$(-1.35\pm0.32)\cdot10^4$	1.16 ± 0.28
75 μm	$(3.37\pm0.75)\cdot10^1$	$4.51 \cdot 10^{14}\ ^{+1.49\cdot10^{16}}_{-4.51\cdot10^{14}}$	$(-1.40\pm0.23)\cdot10^4$	1.21 ± 0.20

Table 6.7: Linear fit parameters obtained for the Arrhenius plots in Figure 6.19. The activation energy E_a for defect migration or dissociation is computed from the slope ($E = k_B T$), while k_0 obtained from the offset of the fit corresponds to the frequency at which defects will try to escape [103]. [51]

The annealing effect has also been studied at higher temperatures, by storing at the end of the measurement campaign the SiPMs previously stored at 48.7±3.3°C for a few days in a climatic chamber. The SiPMs were first annealed at a temperature of 75°C, and then at 100°C. Figure 6.20 shows the I-V curve taken

for a 25 μm SiPM after stabilization[6] for each measured annealing temperature as well as the current at 3 V overvoltage extracted from each of these I-V curves for all three types of SiPMs.

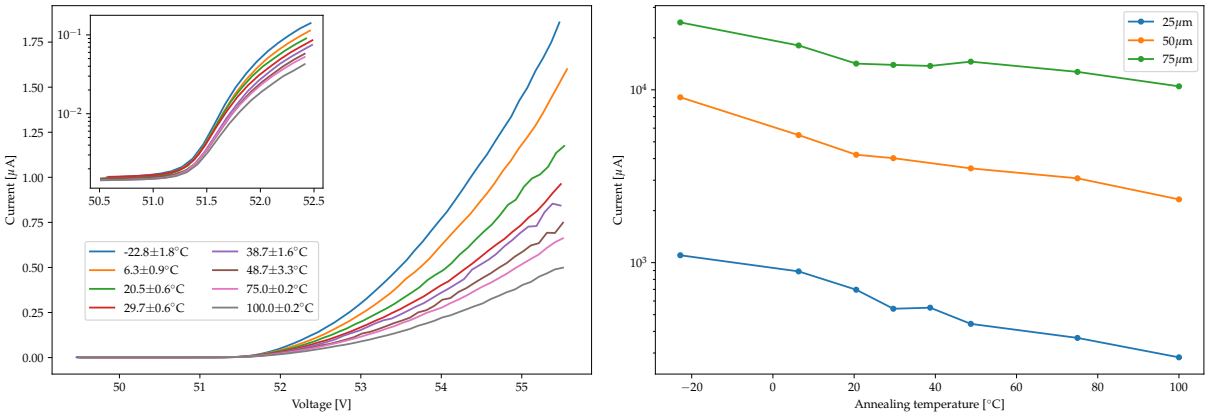

Figure 6.20: I-V curve measured after stabilization for annealing temperatures up to 100°C for the 25 μm SiPM (**left**) and current at 3 V overvoltage for 25, 50, and 75 μm SiPMs after stabilization including high annealing temperatures (**right**). (taken from [51], with permission)

Figure 6.21 shows the current at 3 V overvoltage of Figure 6.20 normalized by the current measured right after the irradiation. The curves therefore provides the recovery fraction for the 25, 50, and 75 μm SiPMs as a function of the annealing temperature. The solid lines given for all three kinds of SiPM are the normalized current values after an infinite time, calculated using the exponential fit parameters in Table 6.4. Even though there is a quite good match up to 50°C between the current measured after about 2 months and the value at infinity computed from the fit, the measured current at 75 and 100°C are higher than the values from the extrapolation of the fit. As previously explained, the SiPMs were only stored for a couple of days in a climatic chambers at both 75 and 100°C, but this is sufficient for the annealing to stabilize since the effect is significantly faster at high temperatures. The non-linearity observed in Figure 6.21 is therefore due to a saturation effect of the annealing process at high temperatures, which is not accounted for in the solid lines derived from the fits since those fits were performed in the range -22.8±1.8 to 48.7±3.3°C.

6 The I-V curve shown in the figure were taken after a few days for the 75 and 100°C annealing temperatures, where the annealing goes very fast. The I-V curves for the other annealing temperatures correspond to the last ones shown in Figure A.1, taken after about 2 months of annealing.

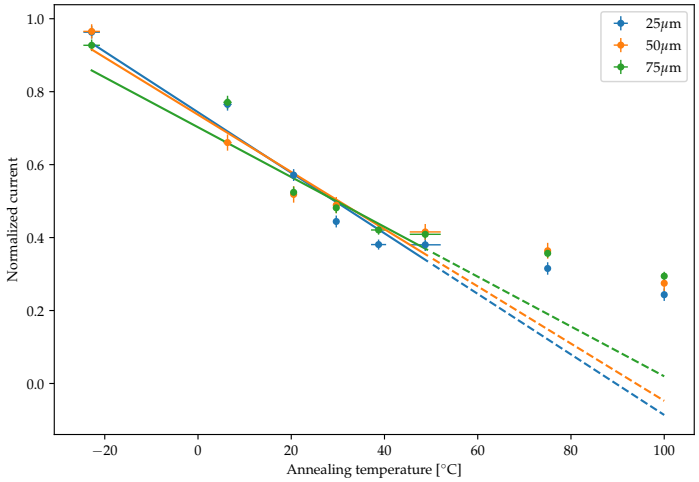

Figure 6.21: Normalized current at 3 V overvoltage for 25, 50, and 75 μm SiPMs after stabilization including high annealing temperatures. A linear fit is performed on the data points below 50°C. A saturation of the annealing effect is observed at higher temperatures. (taken from [51], with permission)

Although the above annealing studies were performed with breakdown correction to ensure the same overvoltage was used when comparing the current between different SiPMs, the breakdown stability has also been checked, as shown for the 50 μm SiPM in Figure 6.22. It can be seen from this plot that the breakdown voltage[7] variations for the different annealing temperature are all within 0.1 V. A correlation between the breakdown variations of the different SiPMs can clearly be observed from these curves, implying the variation is a result of local temperature variations in the laboratory[8]. A similar behavior is observed for the 25 and 75 μm SiPMs.

7 One should note that the breakdown voltages in this analysis are computed by performing linear fits on the regions below and above breakdown of the $\sqrt{I}$ vs. V curve, and by taking the intersection point between the two lines. Other methods using first and second voltage derivative of the current logarithm were found to give similar breakdown values

8 The breakdown voltages are corrected for the temperature measured in the clean room where the I-V characterizations are made. The observed fluctuations with time are therefore likely due to local temperature variations in the laboratory, but they do not affect the analysis since the breakdown is computed for every measurement to ensure that the current is always extracted for the same overvoltage.

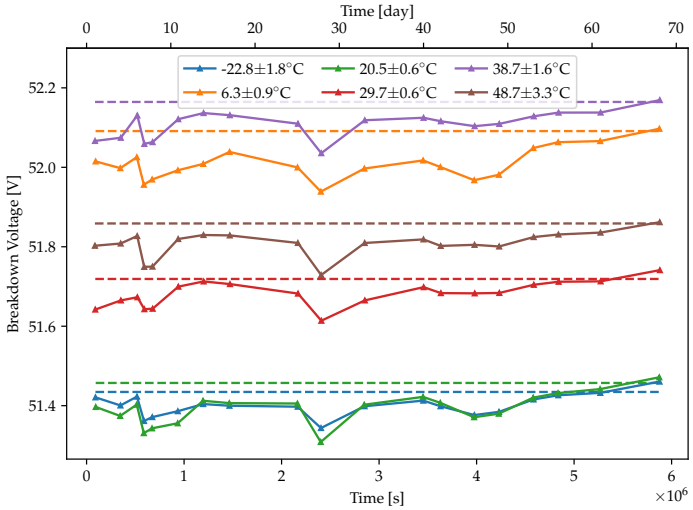

Figure 6.22: Temperature corrected breakdown voltage vs. time after irradiation for the 75 μm SiPMs. A similar behavior is observed for the 25 and 50 μm SiPMs. The common variations of the breakdowns is due to local temperature variations in the measurement room. Horizontal dashed lines corresponds to the breakdowns measured before irradiation. (taken from [51], with permission)

6.3.3 *Temperature dependence of the annealing effect on the SiPM dark spectrum [51]*

This section (6.3.3) is taken from [51], with a few small adaptations.

Analysing the effect of radiation damage and the related recovery on the SiPM's dark current and breakdown voltage does not give a complete picture of the evolution of the performances of the sensor. In order to get an idea of the photon resolution degradation after irradiation and behavior with annealing, the dark spectra of the detectors should also be studied. An example of fitted spectra for a non-irradiated 50 μm SiPM measured at 0°C is shown in Figure 6.23, where the applied thresholds mentioned in section 6.3.1 are indicated with the red lines on the top plot.

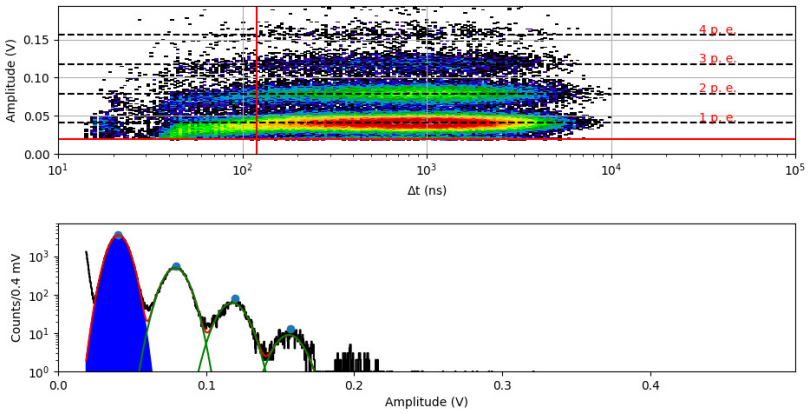

Figure 6.23: Trigger count map in the amplitude-time space, where an amplitude threshold of 20 mV and an inter-pulse time threshold of 120 ns are applied (top) and corresponding dark spectra fitted with a sum of Gaussians (bottom) for a non-irradiated 50μm SiPM as measured at 0°C (taken from [51], with permission)

As can be seen in Figure 6.24, the performance recovery associated with the annealing effect does not only apply to dark current, but also to the photon resolution. Indeed, the peaks in the dark spectra gets narrower and more recognizable at higher annealing temperatures both at 0 and 20°C measurement temperatures. We only show here the spectra for 50 μm SiPMs, since similar behaviors are observed for the 75 μm ones. The dark spectrum for a non irradiated SiPM is also given as a reference.

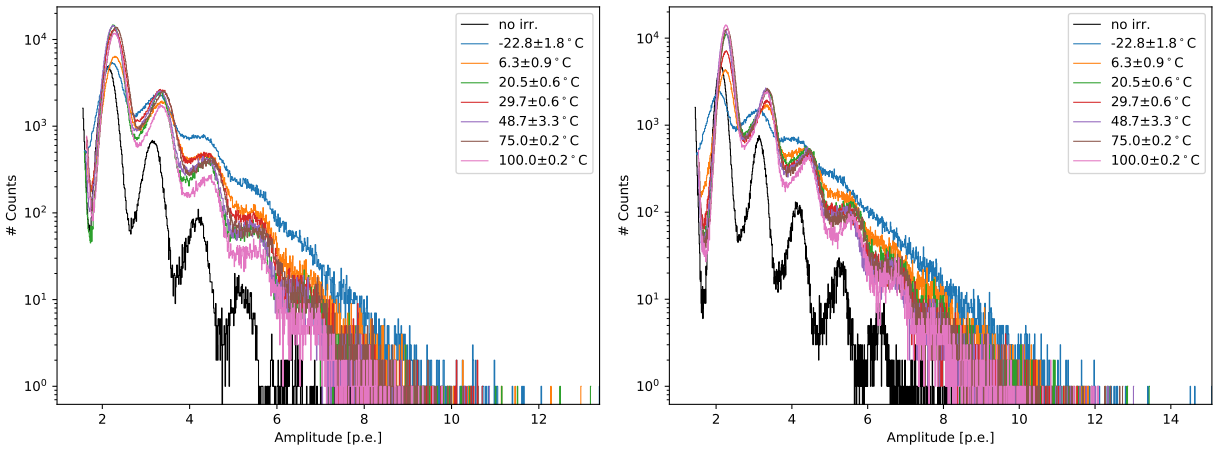

Figure 6.24: Dark spectrum for a 50 μm SiPM as measured at 0 (**left**) and 20°C (**right**) for different annealing temperatures (taken from [51], with permission)

Another interesting feature to analyse is the effect of annealing on the DCR as a function of the applied threshold. From these curves, provided in Figure 6.25 for the 50 μm, we first see the improvement of resolution with annealing, but also a change in slope, implying that the main contribution to the rate is shifting towards low amplitudes.

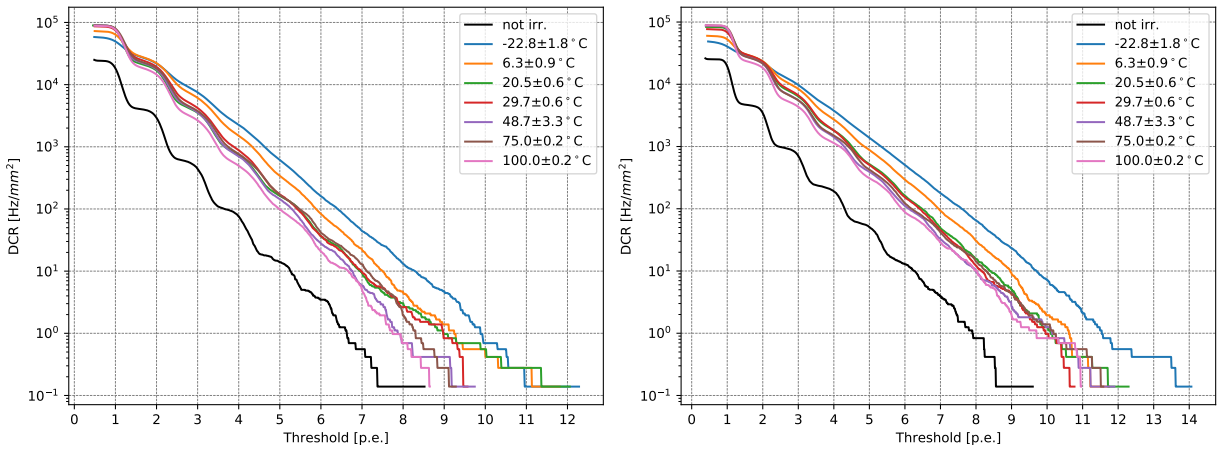

Figure 6.25: DCR as a function of the threshold for a 50 μm SiPM as measured at 0 (**left**) and 20°C (**right**) for different annealing temperatures (taken from [51], with permission)

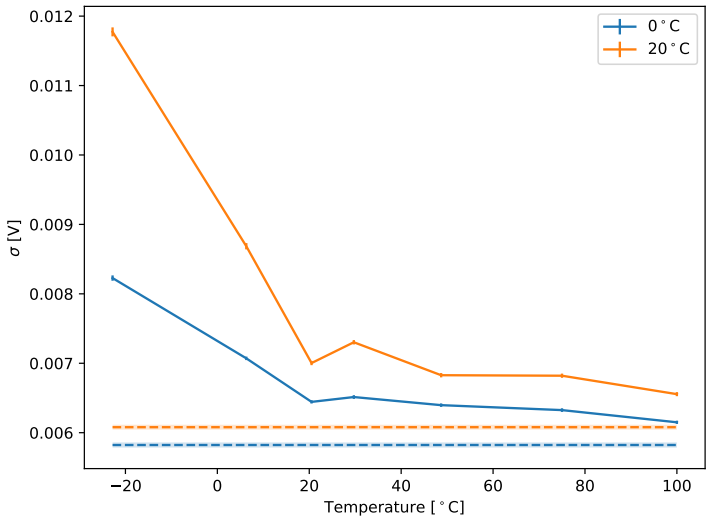

Figure 6.26: First photo-electron peak width vs. annealing temperature for the 50 μm SiPMs as measured at 0 and 20°C. The horizontal dashed lines correspond to the values before the irradiation. (taken from [51], with permission)

The width of the first peak in the dark spectra, corresponding to single photoelectron events, is shown as a function of annealing temperature in Figure 6.26, where we clearly see the improvement at high temperatures. A linear fit of the peak width versus peak number in each spectrum has been performed, the offset of the linear function corresponding to the first peak width, and the slope to the increase in the width from a peak n to a peak $n+1$. While the former has shown a degradation with irradiation, and as discussed above an improvement with annealing, the latter was not affected by the irradiation.

This section (6.3.4) is taken from [51], with a few small adaptations.

6.3.4 *Bias voltage dependence of the annealing effect [51]*

All the above results were obtained for SiPMs passively stored at different annealing temperatures. When used in an experiment, the sensors will be biased, which implies the need of a comparison of the annealing effect between biased and unbiased SiPMs. Figure 6.27 shows the 3 V overvoltage current and breakdown voltage time evolution for different 50 μm SiPMs stored at 20.5 ± 0.6°C with different bias voltage. Two sensors were stored with a 3 V overvoltage, which corresponds to the recommended operation point by the manufacturer, and two other chips were stored with higher overvoltages of 8 and 12 V. The data for an unbiased SiPM stored at the same temperature, which corresponds to the one already presented in section 6.3.2, is also plotted for comparison.

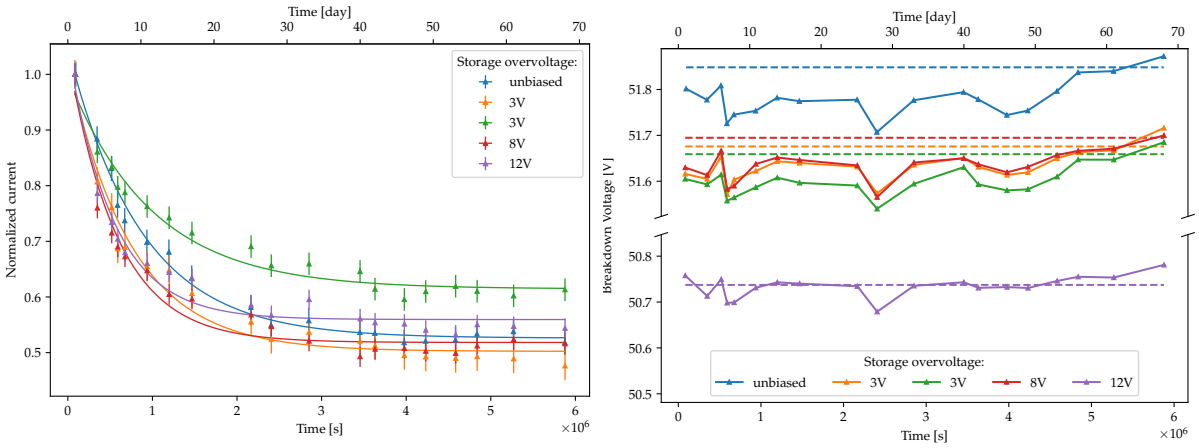

Figure 6.27: Normalized current measured at 3V over-voltage (**left**) and breakdown voltage (**right**) vs. time after irradiation for the 50μm SiPM stored at room temperature (20.5 ± 0.6°C) (taken from [51], with permission)

Both the dark current and the breakdown voltage show a similar behavior for unbiased and biased detectors. One of the current versus voltage curves is outlying for one of the chips stored at 3 V (the green one in Figure 6.27). This might be due to a spread among SiPM chips. The trends for the different biased SiPMs are compatible with the unbiased one, making the results presented in the previous sections still valid for experiments operating at a normal overvoltage. The exponential fit parameters of the normalized current provided in Table 6.8.

Overvoltage [V]	Normalized amplitude	Slope [s^{-1}]	Normalized offset
Unbiased	$(5.22 \pm 0.16) \cdot 10^{-1}$	$(-1.15 \pm 0.07) \cdot 10^{-6}$	$(5.26 \pm 0.05) \cdot 10^{-1}$
3	$(5.20 \pm 0.28) \cdot 10^{-1}$	$(-1.34 \pm 0.13) \cdot 10^{-6}$	$(5.02 \pm 0.09) \cdot 10^{-1}$
3	$(3.80 \pm 0.19) \cdot 10^{-1}$	$(-1.00 \pm 0.11) \cdot 10^{-6}$	$(6.15 \pm 0.08) \cdot 10^{-1}$
8	$(5.21 \pm 0.30) \cdot 10^{-1}$	$(-1.73 \pm 0.16) \cdot 10^{-6}$	$(5.18 \pm 0.08) \cdot 10^{-1}$
12	$(4.90 \pm 0.29) \cdot 10^{-1}$	$(-1.88 \pm 0.18) \cdot 10^{-6}$	$(5.60 \pm 0.07) \cdot 10^{-1}$

Table 6.8: Exponential fit parameters for the normalized 3 V overvoltage current versus time shown on the left plot of Figure 6.27 for 50μm SiPMs stored at an annealing temperature of 20°C with different bias voltages. [51]

The dark spectra and DCR versus threshold were also measured for different annealing bias voltages (see Figure 6.28). The unbiased (blue curve) and first 3 V biased (orange curve) SiPMs show a similar photoelectron resolution, but the biased SiPM has a higher dark count rate. Furthermore, no significant difference in photoelectron resolution is observed for different bias voltages. Therefore, if a good thermal contact to the sensor is ensured, no electrical annealing effects [43] due to local self-heating are observed, which makes the passive study performed in the previous sections still relevant.

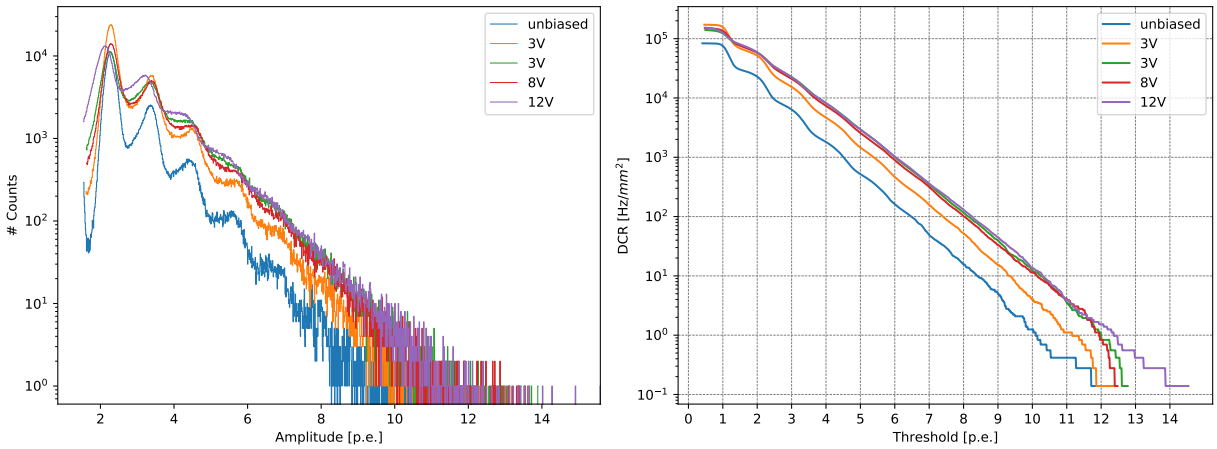

Figure 6.28: Dark spectrum (**left**) and DCR versus threshold (**right**) for 50μm SiPMs with different annealing bias voltage, measured at 20°C (taken from [51], with permission)

6.3.5 *Implications for the POLAR-2 experiment and other SiPM-based space instruments [51]*

This section (6.3.5) is taken from [51], with a few small adaptations.

We discuss in this section the application of the annealing effect characterized in the previous sections to the POLAR-2 experiment, and to some extends to other space-borne experiments. POLAR-2's 6400 scintillators will be read out by S13361-6075PE-04 arrays, which consist of 16 channels of the 6 mm S13360-6075PE SiPM type studied in the previous section. Arrays have also been

irradiated with different doses to study the radiation damage, as described in section 6.2. The annealing of the array is compared to the one of the single channel SiPM, which consist of the same technology, in Figure 6.29. This figure shows the I-V curve at different time after proton irradiation with a dose of 0.267 Gy, as well as the I-V before irradiation. The arrays were stored at an approximate temperature of 25°C (not controlled like in the case of the single channel sensors used to study the annealing).

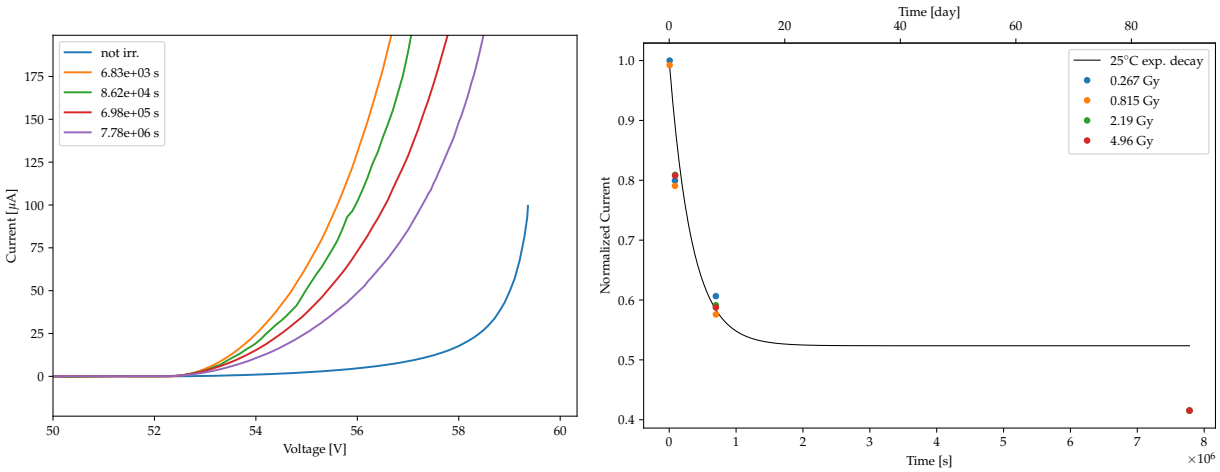

Figure 6.29: I-V curve time evolution for the S13361-6075PE SiPM stored at 25°C and irradiated with 0.267 Gy (**left**) and time evolution of the normalized current at 2 V overvoltage for an S13361-6075PE SiPM exposed to 0.267, 0.815, 2.19, and 4.96 Gy (**right**). The black curve corresponds to the exponential decay at an annealing temperature of 25°C interpolated from the study on single channel SiPMs (see Figure 6.17). (taken from [51], with permission)

The 3 V overvoltage current is also plotted as a function of time in Figure 6.29 for 4 different doses. A black line gives the exponential decay expected for a 25°C annealing temperature extracted from the fits of Figure 6.17. It can be noticed that the first data points match well the curve extracted from the single channel SiPM study, while the last data point for each dose is lower than expected for the array. This can easily be explained by the fact that the arrays were not stored in a controlled temperature environment (since the purpose of those sensor were to study their radiation damage right after the irradiation campaign, not for annealing studies). The arrays were therefore annealed more than when being stored continuously at 25°C, probably because of an increase of temperature in the storage room sometimes during the 2 months due to the weather. Based on this and the fact that the first 3 points match our expectations, we will assume that the arrays, as used in POLAR-2, have the same behavior than the single channel SiPMs regarding annealing. This is to be expected since the technology is the same and the SiPMs only differ in the mechanics which couples them to the neighboring channels.

As already mentioned in chapter 5, POLAR-2 will be equipped with an active cooling system based on Peltier elements directly placed on the back of the SiPMs to reduce their operating temperature. An option could therefore be to invert the current polarity of the Peltier elements after some operating time in

order to heat up the SiPMs and partially recover their original performances. However, the implementation of such an option in the design of the front-end electronics is quite complex. The retained solution has thus been to place power resistors on the back of the PCB holding the SiPMs. These resistors will be powered only during the annealing phase, while the Peltier will be turned off.

Bake it until you make it.

Operating temperature [°C]		-10	0	20
Scenario 1 "No Annealing"	25μm		15.7 ± 0.8	
	50μm		15.4 ± 2.2	
	75μm		7.2 ± 0.9	
Scenario 2 "Continuous annealing"	25μm	13.15 ± 0.73	11.93 ± 0.67	9.49 ± 0.59
	50μm	12.74 ± 1.84	11.61 ± 1.67	9.35 ± 1.36
	75μm	5.80 ± 0.72	5.36 ± 0.65	4.51 ± 0.55
Scenario 3a (1 day) "Continuous + Stimulated annealing"	25μm	8.02 ± 0.45	7.27 ± 0.41	5.79 ± 0.36
	50μm	7.40 ± 1.07	6.75 ± 0.97	5.43 ± 0.79
	75μm	3.59 ± 0.45	3.31 ± 0.40	2.79 ± 0.34
Scenario 3b (2 days) "Continuous + Stimulated annealing"	25μm	5.87 ± 0.33	5.32 ± 0.30	4.24 ± 0.26
	50μm	5.48 ± 0.79	4.99 ± 0.72	4.02 ± 0.58
	75μm	2.69 ± 0.34	2.49 ± 0.30	2.10 ± 0.25
Scenario 3c (10 days) "Continuous + Stimulated annealing"	25μm	4.32 ± 0.24	3.92 ± 0.22	3.12 ± 0.19
	50μm	4.39 ± 0.63	4.00 ± 0.57	3.22 ± 0.47
	75μm	2.09 ± 0.26	1.93 ± 0.24	1.63 ± 0.20

Table 6.9: Increase of the dark current at 3 V overvoltage after 1 year of operation for different annealing scenarios. The numbers are also provided for the 25 and 50μm SiPMs for other experiments using these sensors. The different annealing scenarios are defined as follow: **Scenario 1.** Increase of dark current after 1 year of operation in LEO neglecting the annealing effect during the operation. No annealing is considered here and the radiation damage is assumed to be independent of the temperature. **Scenario 2.** Increase of dark current after 1 year of operation in LEO considering the continuous annealing happening all along the operation, given the operating temperature. **Scenario 3.** Same as *Scenario 2* but followed by a 1 (**a**), 2 (**b**) or 10 (**c**) days stimulated annealing at 50°C after 1 year of operation in order to recover part of the original performances. The annealing is stimulated via an active heating of the sensors. [51]

An increase of the dark current at 3 V overvoltage by a factor 7.2±0.9 is expected every year for the orbit and shielding conditions of POLAR-2 if operating at low enough temperatures where the annealing effect is not significant. This

yearly dark current increase, also provided in Table 6.9 for the three types of sensors studied in this paper, is an upper value for an instrument exposed to a dose rate of 0.0789 Gy/yr. The current increase of SiPMs can be considered as proportional to the dose rate for LEO experiments receiving relatively low levels of radiation. The factor provided for *Scenario 1* can therefore be scaled up or down for other instruments with different amounts of shielding. Depending on the operating temperature of the instrument, some continuous annealing effect could dampen this current increase. We therefore provide the factor corrected for the annealing effect for the three types of SiPMs and for three different operating temperatures, namely -10, 0 and 20°C. This is shown in Table 6.9 as *Scenario 2*. The effect of continuous annealing at operating temperature on the linearly increasing current is described by the following expression:

$$F_I(t) = 1 + (K-1) \cdot t[yr] \cdot [A(T) \exp(B(T) \cdot \tilde{t}[s]) + C(T)] \tag{6.4}$$

where K is the yearly increase in current without annealing (Scenario 1) and A(T), B(T) and C(T) are the exponential amplitude, slope and offset obtained from the exponential fits of Figure 6.16 and reported as a function of temperature in Figure 6.17. $\tilde{t}$ is the time corrected for the duration of the SiPMs transportation from Krakow to Geneva after the irradiation session, and is calculated as $\tilde{t} = t + t_0 = t + \frac{1}{B(T)} \ln\left(\frac{1-C(T)}{A(T)}\right)$ where t_0 is the time of the first post-irradiation measurement. The values for t_0 are 76616 s, 72935 s and 70432 s, respectively for the 25, 50, and 75 μm SiPMs. This time correction allows to use the amplitude and offset obtained from the fits in Figure 6.16 without having to renormalize them.

Finally, *Scenario 3* of Table 6.9 provides the increase in current for the case of *Scenario 2* followed by an active heating of the instrument performed after 1 year of operations at 50°C in order to partially recover the dark current. The numbers are provided for a stimulated annealing of 1, 2 and 10 days. Assuming an operating point of 0°C for POLAR-2, an annual increase of dark current by a factor 5.36 ± 0.65 can be expected. The effect of radiation on the polarimeter performances can be mitigated by heating up the sensors to a temperature of 50°C for 1 (or 2) days after a year of operation. After this procedure, the 1 year increase of current would be reduced to 3.31 ± 0.40 (or 2.49 ± 0.30). Table 6.9 can be used to estimate dark current increase of S13360-6025/50/75 SiPMs related to radiation damage. It can also be used for estimating the required thermal conditions for any space borne experiment using SiPMs as photosensors, and planning an annealing strategy to extend the life time of the mission.

6.4 CONCLUSIONS

Together with the plastic scintillators, Silicon Photo-Multipliers form the central organ of the POLAR-2 instrument. While the scintillators are responsible for converting the incoming gamma radiation into optical photons, the SiPMs permit to convert this light into a measurable signal that can be processed by the readout electronics. It is therefore of high importance to characterize these sensors on a channel-by-channel basis to get a precise idea of the behavior of each individual channel of the polarimeter. This characterization has to be performed as a function of temperature as the thermal conditions might vary within the instrument and with time. A characterization procedure, scalable at bigger scale for producing the entire instrument with 6400 channels, has therefore been developed in order to measure the temperature dependence of the breakdown voltages of every SiPM channels. This not only allows to correct for non-uniformity of the operating point within the polarimeter modules in order to get a more uniform instrumental response, but it is also crucial to keep the operation point stable with time when the instrument is subject to temperature variations.

Due to its space-based nature, the POLAR-2 instrument is not only subject to varying thermal conditions, but it is also exposed to a harsh radiation environment. Orbiting the Earth at an averaged altitude of 383 km and an inclination of 42°, the instrument is exposed to most of the radiation when crossing the SAA. Simulations based on the instrument design and the knowledge of the radiation environment were carried out to estimate the yearly expected dose in the sensors, allowing to reproduce the same conditions at an irradiation facility. POLAR-2 will be able to monitor the absorbed dose during the mission thanks to the use of Radiation sensitive Field Effective Transistors (RadFET), as described in Chapter 5. The degradation of the SiPMs' performances in term of dark current and dark count rate were studied as a function of the exposed dose and measurement temperature, allowing to precisely characterize the evolution of the instrument sensitivity with time in orbit. An annealing effect was also observed. That is, an improvement of the SiPMs' performance after the degradation due to irradiation. This effect, explained by silicon lattice point defects being fixed by the ambient thermal energy, could be taken to our advantage to limit the impact of radiation on the sensors once in space.

The effect of annealing has been studied as a function of temperature by irradiating 21 single channel SiPMs and storing them at various temperatures for a couple of months. The current versus voltage was measured every few days in order to monitor the evolution of the dark current of the irradiated SiPMs under different thermal conditions. The storage temperatures ranged from -20°C, where no annealing effect was observed, to +50°C, where post-irradiation the dark current was reduced by 60% in less than a week. The dark spectra was also measured in order to study the recovery of single photon resolution with annealing. Finally, the yearly increase of dark current for different proposed annealing strategies were provided. Useful numbers can be extrapolated from

this for any space-based instruments that wants to operate SiPMs and make use of annealing to improve their life time.

7

OPTICAL CHARACTERIZATION, SIMULATION, AND CALIBRATION OF THE POLAR-2 MODULES

The primary particles of interest for the POLAR-2 science case are photons of energy ranging from a few keV up to several hundred of keV. However, when a γ-ray enters the polarimeter, it deposits energy in the detector that is converted into optical photons through scintillation. The optical photons produced in the scintillator bars have then to be transported to the optical sensors to be converted into an electrical signal with the highest possible efficiency. In consequence, even though the polarimeter modules are γ-ray detectors, they are an optical system in which optimizing the photon collection is crucial.

The polarimeter modules were designed based on the POLAR modules, with several technological improvements and optimization. The upgrade of the sensors from MA-PMTs to SiPMs, greatly improving the light detection efficiency, is one of them. The scintillators have also been shortened to improve the SNR, and have been made wider to limit the dead space between scintillator bars. During the polarimeter module development process, optical elements were therefore characterized and tested with module prototypes in order to improve the light collection of the system. An optical simulation of the module was implemented in Geant4 in order to model the optical behavior of the system. Improving the light collection not only increases the effective area of the detector, but is also crucial for lowering the energy threshold down to a few keV, where γ-rays only produce a few optical photons in the scintillators.

In this chapter, we start by discussing the development and characterization work of the different optical compounds of the POLAR-2 polarimeter modules is described. The Geant4 optical simulation of the target is then presented together with comparisons to measured data.

7.1 OPTICAL DESIGN AND CHARACTERIZATION OF THE POLARIMETER MODULE

The focus is here on the optical part of the POLAR-2 polarimeter module, whose design is described in Section 5.2. The optical part makes the bridge between the primary γ-ray and the measured electronic signal. It is therefore composed of an array of 64 plastic scintillator bars, individually wrapped with different reflective foils as described in Section 5.2.4. The scintillators are held together by a plastic mechanical grid. A reflective foil is placed on one end of the scintillator array to reflect back the optical photons into the target, while the SiPM arrays are coupled to the other side through a Room Temperature Vulcanizing (RTV) silicone optical pad.

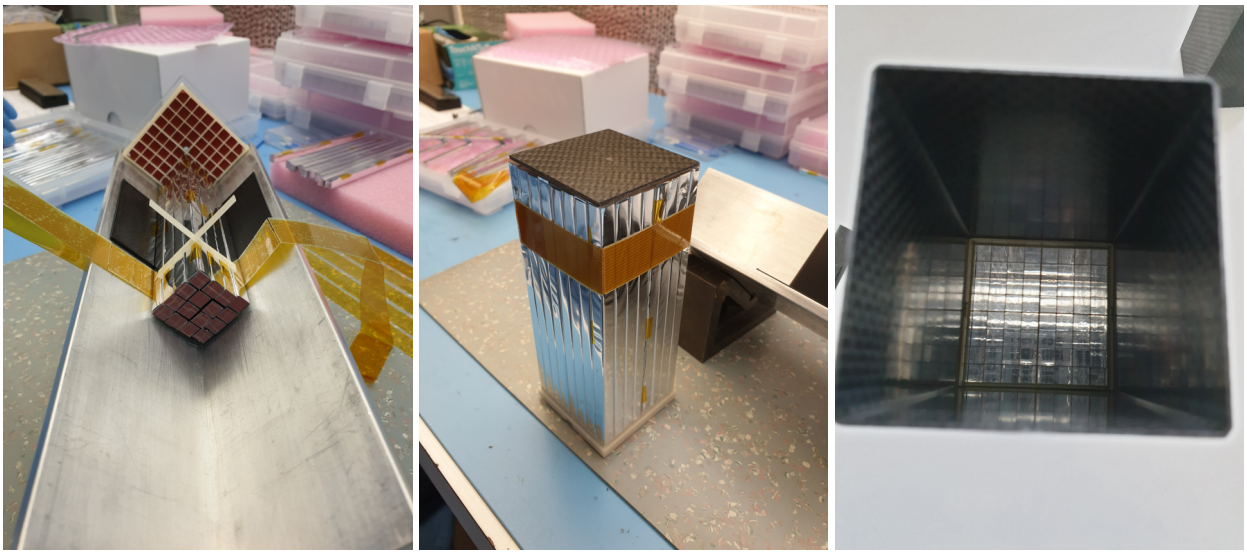

Figure 7.1: **Left:** A quarter of a target being assembled in the plastic alignment grid. **Middle:** A fully assembled target ready to be integrated into a polarimeter module. **Right:** Target inserted in a carbon fiber socket seen from the FEE side.

Figure 7.1 shows several pictures of a polarimeter target during assembly. When the incoming γ-ray is depositing energy in a scintillator bar, this produces scintillating light in the 400-500 nm (see Figure 7.13) which will travel in the bar. As detailed in Chapter 5, the four long sides of the bars and one extremity are covered with highly reflective foil, while the sixth side of the bar is coupled to the SiPM channel through a soft silicone based optical pad. The scintillating photons are therefore propagating along the bar, undergoing multiple internal reflections and reflections on the foils, whose goal is to bounce back the photons in the scintillator. The reflectivity of the foils is a key parameter for an optimal light collection. The photons finally reach the extremity of the bar coupled to the SiPM and are being converted into an electronic signal. We now describe the optical characterization of the reflective foils, plastic grid, scintillator bars, and optical pad. Another crucial optical element of the chain, the SiPMs, were discussed in the previous Chapter.

7.1.1 *Reflective foils*

The role of the reflective foils is to keep as many optical photons as possible inside the scintillators until they reach the SiPMs where they get absorbed through the photo-electric effect. Maximizing the reflectivity in the 400-500 nm wavelength interval, corresponding to emission wavelengths of the plastic scintillators, is therefore decisive on the overall optical efficiency of the module. As a consequence, the reflectivity and transmissivity of several kinds of reflecting films were measured [54] at the Optical Quality Control Lab of the CERN Thin Film & Glass service using a Perkin Elmer Lambda650 spectrometer [99]. Such a spectrometer is shown in Figure 7.2 equipped with the so-called Universal Reflectance Accessory (URA) used to measure the specular component of reflectivity.

Figure 7.2: Perkin Elmer Lambda650 Spectrometer equipped with the Universal Reflectance Accessory used to measure the specular reflectance

The URA module can be replaced in order for the spectrometer to be used with a 150 mm diameter integration sphere, which can be used to measure the total reflectance of the sample, the diffuse component of its reflectivity, or its transmittance. A schematic view of the integration sphere in the total reflectivity measurement mode is shown in Figure 7.3. The sample is placed at the bottom of the integration sphere, while a small aperture is present for the light source to illuminate the inside of the sphere. The inside of the sphere is coated with highly reflective Teflon, and a calibration measurement is taken without sample as a reference. The light is first reflected on the sample, then on the inside of the sphere until it reaches the central detector.

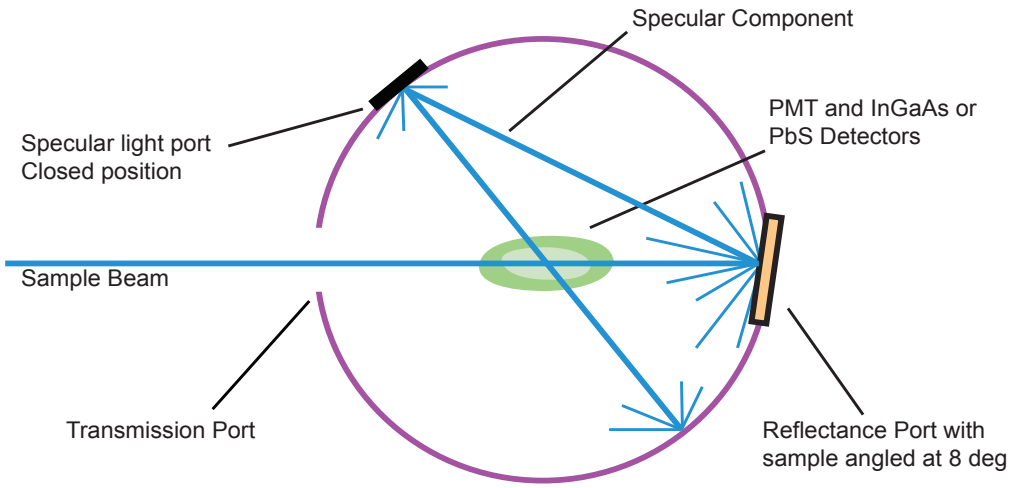

Figure 7.3: Drawing of the 150 mm integration sphere used to measure the total reflectance of the sample placed at the bottom of the closed sphere.

Several samples of highly reflective foils are being investigated as candidate for the wrapping of scintillators. The first tested foil is the Vikuiti from 3M, a 65 μm thick Enhanced Specular Reflector (ESR) which was previously used in POLAR. The Claryl film from Toray , an aluminized PET layer available in several thicknesses from 8 to 36 μm, was also tested as a reflector. Finally, the Astrosolar® foil from Baader Planetarium, used for optical Solar observations, was also considered. The total reflectance of all of these reflective foil was measured in the 300-600 nm range and is plotted in Figure 7.4.

www.3m.com

www.toray.eu/eu/

www.baader-planetarium.fr

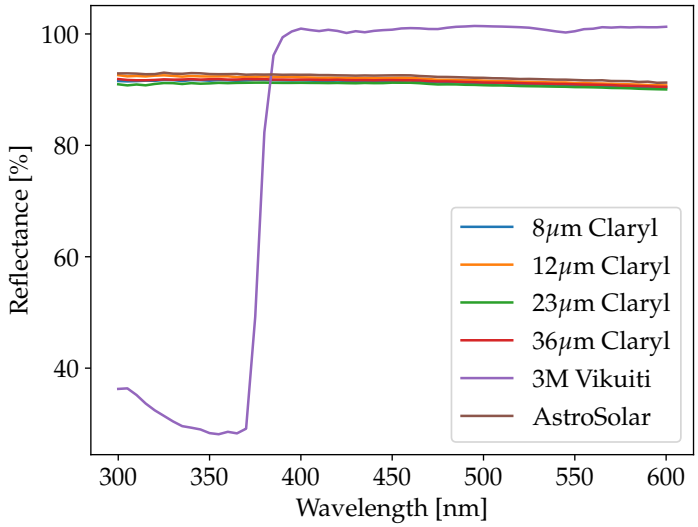

Figure 7.4: Total reflectance spectrum of all the Claryl foils compared to that of Vikuiti and AstroSolar

Both the Astrosolar and Claryl samples, for different thicknesses of PET substrate for the latter, show a similar total reflectance. The reflectance is between 90 and 94% with a very small decrease with increasing wavelength, typical of Aluminum reflectors. The PET layer thickness does not have a significant effect on the reflectance, since it is the Aluminum coating on top of the substrate that

gives its reflectivity to the sample. The measured Claryl reflectance matches the expected reflectance from Aluminum [97]. For the Vikuiti sample, the behavior is completely different: above 380 nm, the total reflectance is compatible with 100%, and the precision of the spectrometer does not actually allow to disentangle the sample reflectance with a perfect reflection. This difference is due to the fact that the Vikuiti foils are not coated with Aluminum as the other samples, but are instead entirely composed of plastic. This cutoff being below 400 nm it is not relevant for POLAR-2 as the emission range of the plastic scintillators used for the polarimeter is 400-500 nm (see Figure 7.13). The Vikuiti reflectance being clearly higher than all of the other characterized samples, it makes a perfect candidate as the reflective foil for POLAR-2.

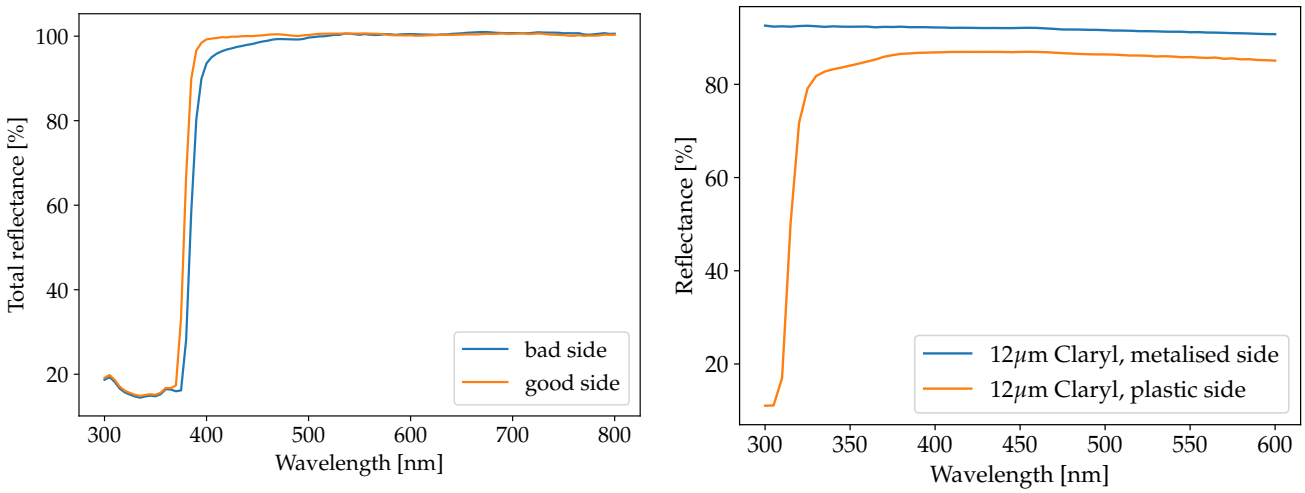

Figure 7.5: **Left:** Total reflectance of a 3M Vikuiti foil measured on both sides. The reflectance is slightly higher in the 400-500 nm range of interest on one side of the reflective foil. This side should therefore be placed facing the scintillators, to minimize the loss of optical photons. **Right:** Total reflectance measured for both sides of a Claryl sample. The reflectivity is higher on the metalized side, which is meant to be the reflecting side, while the other side is not as efficient since the photons have to cross the transparent PET layer before being reflected on the Aluminum layer.

Both sides of the Vikuiti and Claryl samples are also compared through a total reflectance measurement, as depicted in Figure 7.5. For the Vikuiti, the total reflectance is slightly lower on one side in the 350-450 nm interval where the reflectance is up to 5% lower. This implies that one has to take care of which side of the Vikuiti is facing the scintillator when wrapping a bar. To maximize light collection, the more reflective side should be placed facing the scintillator. In the case of the Claryl sample, the reflectivity is almost 10% higher on the metalized side at the relevant wavelengths, while a cutoff due to the plastic composition of the substrate is observed on the other side.

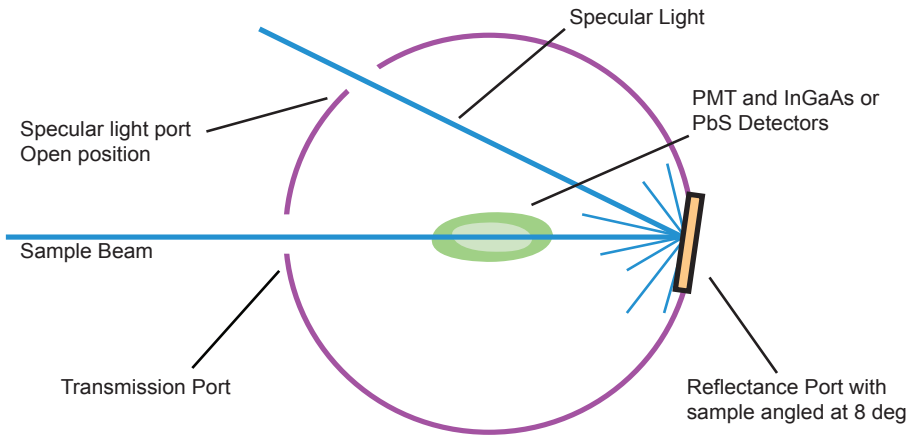

Figure 7.6: Drawing of the integration sphere being used for diffuse reflectance measurement. The configuration is very similar to the one used for the total reflectance measurement, except that an aperture is made at a precise location on the sphere in order to get rid of the specular component of the reflection.

The diffuse component of the reflectivity of the different foils has been measured using the same integration sphere, but in a different configuration. As depicted in Figure 7.6, an aperture is made on the sphere at the location where the specular component is reflected, in order to get rid of it. Only the diffuse component of the reflectivity is therefore collected by the integration sphere. The diffuse reflectance measurements results are shown in the left plot of Figure 7.7, where it can be observed that the Vikuiti is a specular reflector with a diffuse component of the sub-percent level in the visible range, while the Claryl has a bigger diffuse contribution of the order of 3 to 5%. It can also be noticed that the diffuse component becomes significant for Vikuiti below the 380 nm cutoff, where the specular reflectance contribution to the total reflectance is going down to about 50%, as shown in the right plot of Figure 7.7.

The bigger contribution of th diffuse reflectance for Claryl compared to Vikuiti can also be observed by eye. Indeed, by looking at your own reflection on a piece of Vikuiti, the image is clear, while it becomes blurry with Claryl due to the diffuse component.

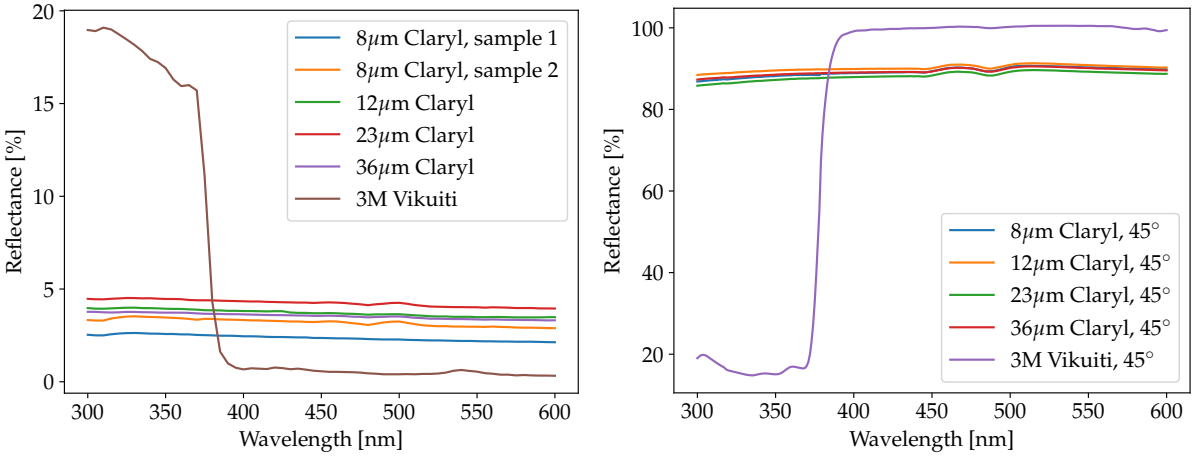

Figure 7.7: **Left:** Measured diffuse reflectance spectrum for Vikuiti and Claryl samples with the integration sphere. **Right:** Measured specular reflectance for Vikuiti and Claryl samples with the URA for a 45° incident angle.

In addition to keeping the light inside the scintillators to maximize light collection, the role of the reflective foils is also to prevent photons from going to the neighbor channels, causing optical crosstalk. The transmittance of the considered reflectors is in consequence a key parameter to be characterized as well. The transmittance of the samples can be measured by using the same integration sphere but placing the foil at the entrance. The reflectance port previously used to place the sample at the bottom of the sphere is now covered with a highly reflective Teflon end-cap, and the light going through the foil is collected, as depicted in Figure 7.8.

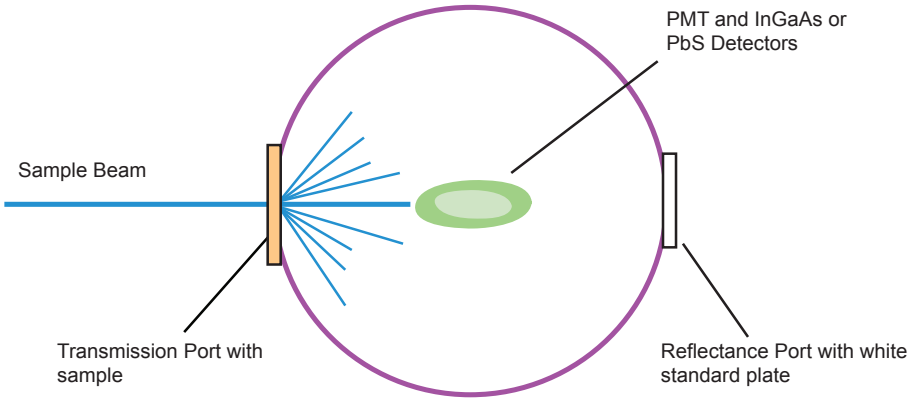

Figure 7.8: Drawing of the integration sphere configuration for a transmittance measurement. The sample is placed at the entrance of the integration sphere while the reflectance port used for the previous measurements is closed with a Teflon-coated cap.

The measured spectral transmittance for different foils are plotted in Figure 7.9. The averaged transmittance in the 400-500 nm range is around 1-2% for both Claryl and Vikuiti, while the Astrosolar foil has a transmittance smaller than the resolution of the spectrometer and seems therefore consistent with no transmission. The result for the Astrosolar foil was to be expected since it has been design as a filter with optical density of 5 to observe the Sun, meaning that only 10^{-5} of the photons will be transmitted though the foil.

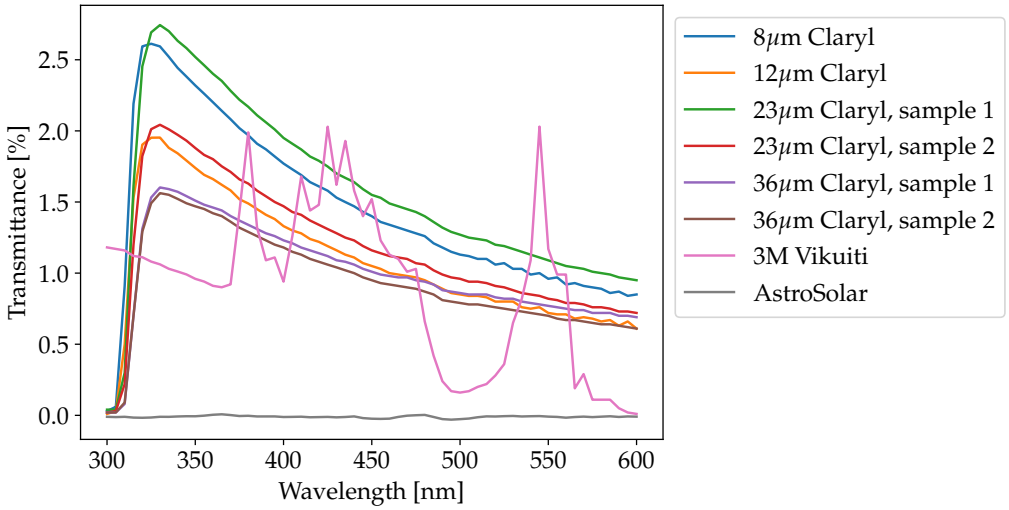

Figure 7.9: Transmittance spectrum measured for Vikuiti, Claryl, and Astrosolar samples.

Even though the transmittances for the Claryl and Vikuiti are in the same order of magnitude, we can observe a more complex structure in the Vikuiti curve. This is due to the higher complexity of the Vikuiti foil, which is made of numerous layers of plastics playing with interferences to reflect back almost all the photons. No complex structure is observed for the Claryl since it just consists of a PET transparent layer coated on one side with Aluminum.

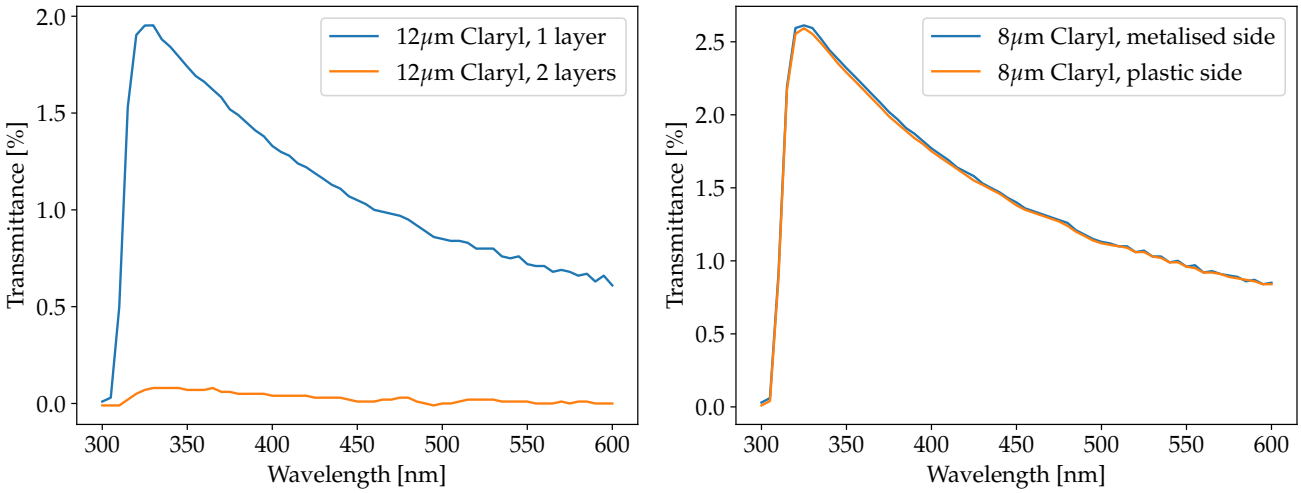

Figure 7.10: **Left:** Measured transmittance for one and two layers of 12 μm thick Claryl. **Right:** Claryl sample transmittance measured for both sides. The transmittance being obviously not direction dependent, the spectra are the same.

The transmittance of two layers of Claryl is compared to that of a single layer in Figure 7.10. Adding a second layer reduces the transmittance by almost two orders of magnitude. The transmittance measured on both the plastic and metalized sides of the Claryl are shown in the right plot of the same figure. As one could expect, the transmittance is the same in both directions, while the reflectance is better on the metalized side (see Figure 7.5). Since the Vikuiti has

the best reflectivity performances of all the tested reflective foils, it has been selected as the primary reflector for wrapping the POLAR-2 scintillator bars. Nevertheless, because of its mechanical rigidity, it cannot be folded around the bar to cover the 4 sides. Four 5.9×122 mm strips of the 65 μm thick Vikuiti are therefore used to cover the long sides of the bar. A single 25×122 mm foil of 8 μm thick Claryl is then used to wrap the scintillator and the 4 Vikuiti strips and hold them together. Each bar can thus be wrapped individually, with the Claryl preventing photons to escape from small gaps between Vikuiti strips in the corners of the bar. Since two layers of Vikuiti and two layers of Claryl are separating each bars, almost no crosstalk[†] is expected from the 122 mm (out of the total 125 mm of the bar length) covered by reflective foils. The remaining 3 mm are covered by the plastic alignment grid used to assemble all the bars together. The optical properties of the grid material were therefore studied.

[†] *Assuming a transmittance of 1% for both foils, the expected crosstalk over the wrapped fraction of the bar with 4 layers separating neighbor bars is* $0.01^4 = 10^{-8}$.

7.1.2 *Plastic alignment grids*

As it covers 2.4% of the height of the scintillators, characterizing the transmittance of the plastic composing the alignment plastic grids is important for understanding all the contributions to the inter-channels optical crosstalk. 20×20 mm^2 plastic plates of different thicknesses made with the same material as the alignment grid were therefore printed at the CERN Polymer Lab in order to measure the transmittance of the material. The accuracy on the sample thickness achieved with the 3D printer is better than 50 μm. The same setup as used in the previous section to characterize the reflectors is used to measure the transmittance of the plastic samples.

The grid is 3 mm thick, and the scintillator bars are 125 mm long. The details of the alignment grid design are provided in Section 5.2

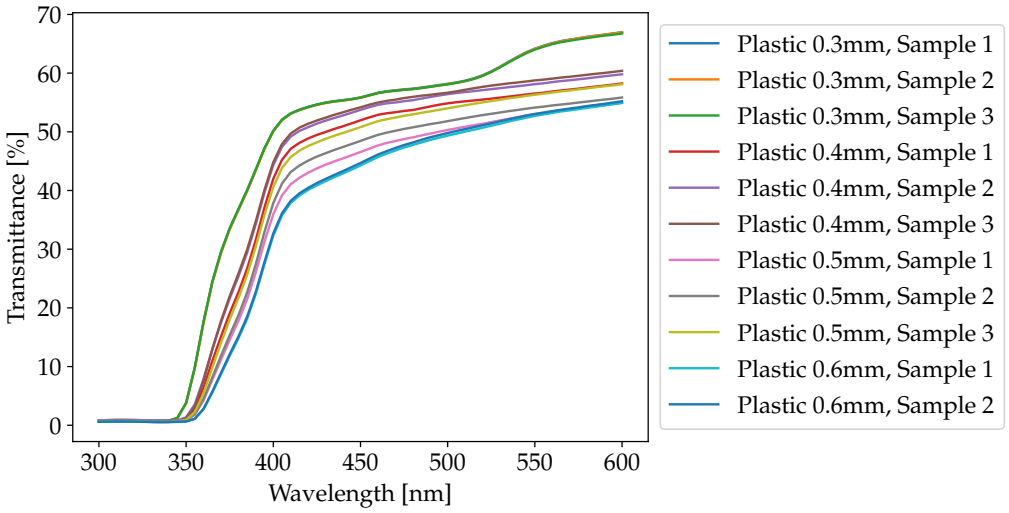

Figure 7.11: Spectral transmittance measurement of the plastic grid material for different thicknesses.

The measured transmittance spectra for different samples and thicknesses are plotted in Figure 7.11. As could be expected, the transmittance is getting lower with the increasing thickness of the sample. An average transmittance between 40 and 60% is measured in the 400-500 nm range. The transmittance in this interval

is fitted as a function of the sample thickness to extrapolate the transmittance at the desired thickness. The grid having very thin segments, the transmittance over the 3 mm of grid height between two scintillators can be as high as 60%. Furthermore, the grid is placed at the extremity of the scintillators on the SiPM side. The grid transparency will therefore have a significant contribution to the optical crosstalk and has to be accounted for in the optical simulations.

As mentioned in Chapter 5, the thickness of the grid between scintillators is 0.2 mm for most of the channels, and 0.5 mm for the central middle cross separating the 4 quarters of the module.

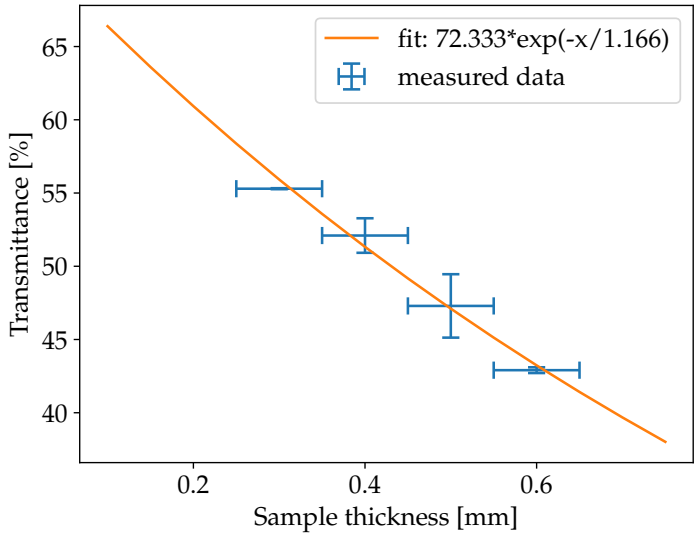

Figure 7.12: Transmittance of the epoxy resin used to print the plastic alignment grid as a function of the sample thickness, fitted with an exponential function. An attenuation length of 1.166 mm is found.

Because of the complex shape and mechanical fragility of the plastic grids, no reflective or absorbing coating can be uniformly applied to the pieces to reduce the crosstalk from the grid. A last point that should be mentioned is the effect of "yellowing" of the resin that has been observed on the printed plastic grids after some times. This yellowing effect, caused by thermo-oxidation, appears to be quite common for epoxy based resins [137], and has not shown any impact on the mechanical properties of the alignment grid. It is therefore not leading to any issue for the polarimeter module since it does not have a significant effect on the transmittance properties of the material either.

7.1.3 *Scintillator bars*

The dimensions and mechanical integration of the scintillator bars in the polarimeter module has already been described in the Section 5.2. Hence, we describe here the features of the scintillators important for the optical simulation of the module. Two types of scintillators were considered as candidate for POLAR-2: the EJ-248M plastic scintillator from Eljen Technology [64], already used in POLAR, and the EJ-200 scintillator [63] from the same company, which is reported to have higher scintillation efficiency.

The optical simulations of a POLAR-2 module will be describe in details in Section 7.2

First, the emission spectrum of the scintillator has to properly be implemented in the Geant4 optical simulations of the polarimeter. The theoretical optical

emission spectrum provided in the data sheet is used as an input since it is consistent with the one measured in the lab [172]. It should be noted that while the emission of the scintillator is given as a function of the photon wavelength in the scintillator data sheets [63, 64], it has to be implemented versus energy in the optical simulations. As the energy is inversely proportional to the wavelength of a photon ($E = hc/\lambda$), a Jacobian transformation [180] has to be applied for correctly implementing the emission spectrum. The x-axis of the spectrum has therefore to be transformed as follows:

$$\mathrm{d}\lambda \rightarrow \mathrm{d}E = -\frac{hc}{\lambda^2}\mathrm{d}\lambda, \tag{7.1}$$

while the y-axis of the spectrum becomes:

$$f(\lambda)\mathrm{d}\lambda = f(E)\mathrm{d}E \implies f(E) = f(\lambda)\frac{\mathrm{d}\lambda}{\mathrm{d}E} = -f(\lambda)\frac{\lambda^2}{hc}. \tag{7.2}$$

where $f(\lambda)$ is the spectrum as a function of the wavelength, provided in the data sheet, and f(E) the spectrum versus energy as implemented in the optical simulations. The negative sign just represents the opposite direction of integration between λ and E. This transformation also applies to other optical spectra implemented in the simulations, like the PDE of the SiPM. The importance of correctly dealing with input spectra is depicted in Figure 7.13.

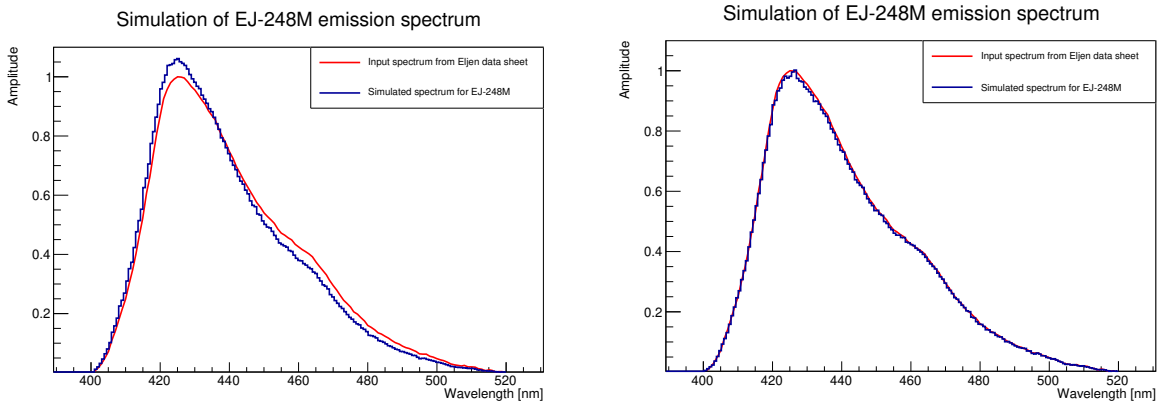

Figure 7.13: **Left:** Incorrect way of converting the emission spectrum simply using the formula $E = hc/\lambda$. The red curve shows the reference spectrum from the data sheet while the blue line its implementation in the simulations. A clear difference can be observed **Right:** When applying the proper Jacobian transformation to convert the wavelength spectrum into an energy spectrum, a very good match is observed between the simulated scintillator emission spectrum and the original one.

The EJ-200 scintillator type has been studied as a potential replacement for the previously used EJ-248M in POLAR since it is reported to have a higher scintillation efficiency: 10'000 photons/MeV versus 9'200 photons/MeV for EJ-248M. EJ-200 has therefore been used for the first prototype modules of POLAR-2, but showed a lower efficiency than EJ-248M when testing both modules with radioactive sources. This observation is contrary to what we could expect from

the EJ-200 higher scintillation efficiency. Discussions with the manufacturer lead to the idea that the EJ-200 material being softer, its surface quality might be lower when diamond milling the scintillators, degrading the final optical efficiency. In order to confirm the theory that a rougher surface for EJ-200 could imply more photons lost at the scintillator interface, the surface quality of both types of scintillators had to be characterized. For this purpose, we used an Interference Optical Microscope (IOM) developed at the Geneva High School of Landscape, Engineering and Architecture (HEPIA) [117, 118].

The IOM setup, shown in Figure 7.14, is composed of an optical objective read out by a CCD camera, and a support for placing the sample controlled via piezo-electric elements for very fine moving step. The sample surface plane is slightly tilted compared to the microscope focal plane in order to vertically scan the slope of the sample [118].

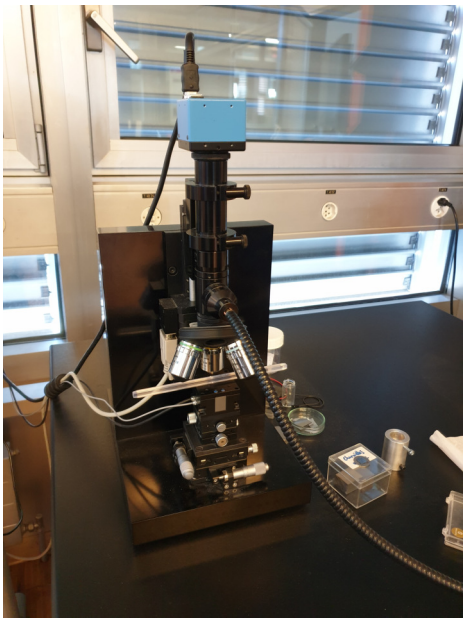

Figure 7.14: Interference Optical Microscope setup at HEPIA in Geneva used to characterize the roughness of the scintillator surface [117].

Examples of a 266×355 μm area measured with the IOM for both EJ-248M and EJ-200 diamond-polished scintillators are displayed in Figure 7.15. Clear lines due to the diamond polishing process can be observed on the samples. The arithmetic average height R_a and the root mean square roughness R_q [74] are computed for both scintillators and given at the top of each map. Values of $R_a = 46$ nm and $R_q = 63$ nm are computed for the EJ-248M scan presented in Figure 7.15, while the EJ-200 scan gives $R_a = 129$ nm and $R_q = 168$ nm. The EJ-200 scanned surface, whose 3D version is shown in Figure 7.16, is clearly rougher than the EJ-248M one. Several samples of both types have been measured similarly in order to gather statistics on the surface quality of both plastics.

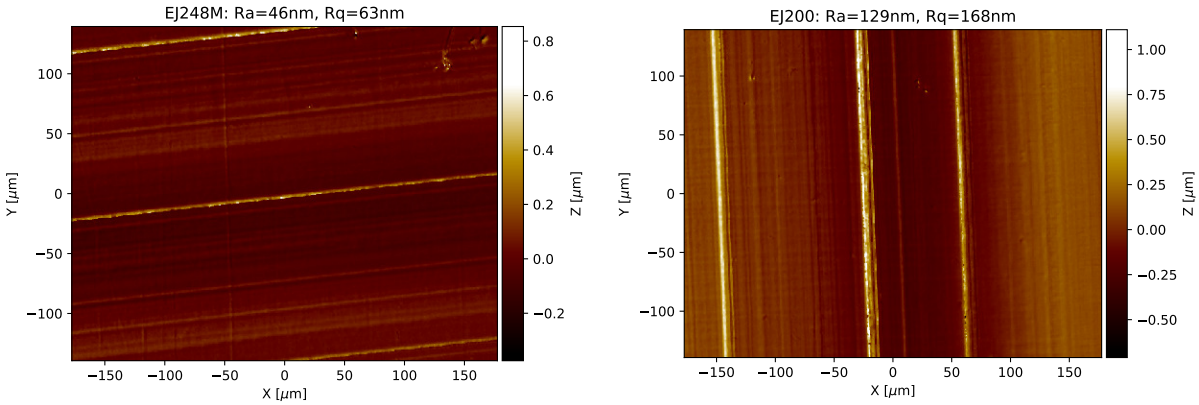

Figure 7.15: Surface scan measured on a EJ-248M (**left**) and EJ-200 (**right**) scintillator bar with the IOM.

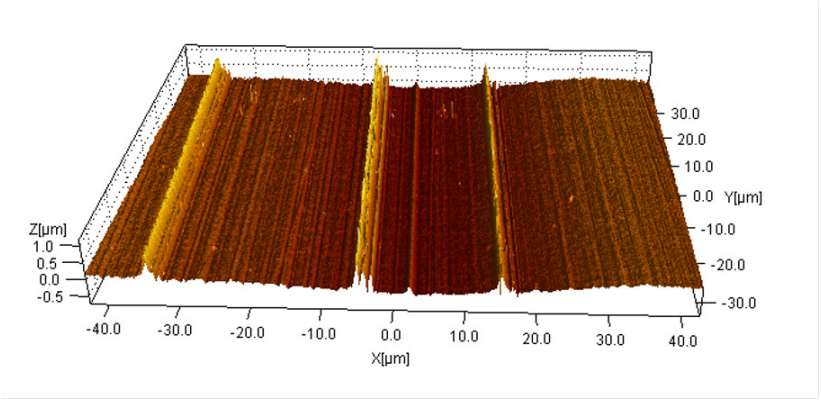

Figure 7.16: 3D version of the EJ-200 surface scan presented in Figure 7.15.

The implication of roughness on the optical efficiency of the system will be discussed in section 7.2.2, where the implementation of the measured roughnesses for different scintillator types in the optical simulations will be discussed. Other types of plastic scintillators, not considered for POLAR-2, have also been measured with the IOM setup as it can serve as a useful input for other experiments.

7.1.4 *Optical coupling pad*

To optically couple the SiPM arrays to the scintillator bars, a silicone based pad has been developed at DPNC. Made of MAPSIL QS1123 RTV silicone [89, 157], the pad was first developed with thicknesses of 500 and 350 μm. The technique has later been refined to mold the optical pad directly on the SiPM arrays, as displayed in Figure 7.17, and to reduce the pad thickness down to 150^{+0}_{-20} μm.

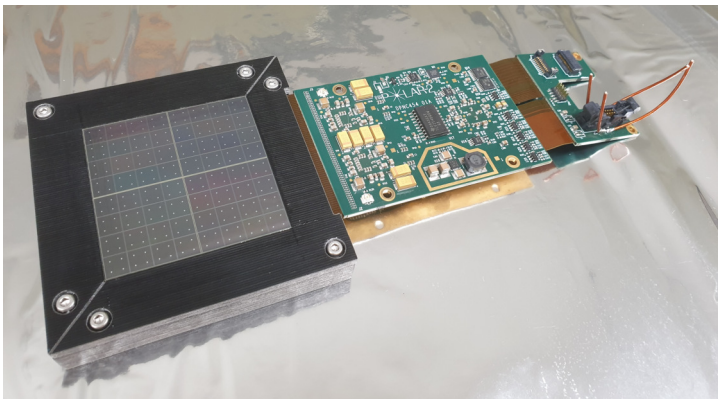

Figure 7.17: MAPSIL QS1123 optical pad molded on the POLAR-2 FEE [53]

The importance of having an optical coupling pad to get a smoother contact between the sensors and scintillators compared to directly pressing these two against each other has been shown via optical simulations. A module has been simulated with a 0.3 mm thick optical pad and with an air gap of the same thickness. Injecting 10'000 50 keV electrons in one of the central channels (#36) of the module, the case with an air gap (872'736±934 events) gives only 80.06±0.11% of the photons detected in the case where an optical pad was used (1'090'087±1'044 events). This 0.3 mm thick air gap might seem dramatic, but it is actually representative of the fact that not all the bars' extremities are in the same plane. The main role of the optical pad is therefore also to correct for misalignment of the scintillator bars in the Z direction (axis along the length of the scintillator). The pad is also protecting the SiPM surface against vibration induced mechanical damages during the launch. The silicon material for the optical pad was chosen to have a refractive index comprised between that of the plastic scintillator and the epoxy resin of the SiPM ($n_{scint} = 1.58 > n_{optpad} = 1.5324 > n_{SiPMresin} = 1.51$) in order to optimize the light transmission. An abrupt drop in refractive index from the plastic directly to air/vacuum would increase internal reflections, which we want on the vikuiti sides but not at the interface with the SiPMs where the light should go out of the scintillator bar.

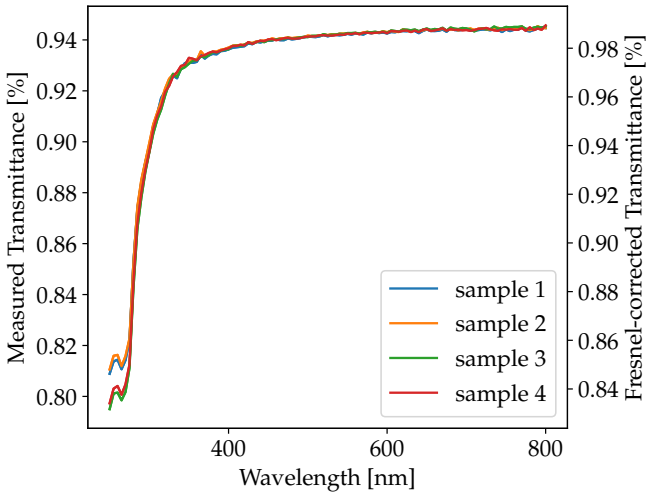

Figure 7.18: Optical pad spectral transmittance measured with several 350 μm thick samples. The right y-axis shows the actual transmittance of the material itself once correcting for Fresnel losses.

As all the optical photons being collected by the SiPMs will first go through the optical pad, it is imperative to characterize its transmittance. Such measurement was performed with the same setup used for the reflective foils and alignment grid, and is shown in Figure 7.18 for several samples of the same thickness. The transmittance measured in the 400-500 nm interval is consistent between samples and its averaged value $93.95 \pm 0.14\%$. A cutoff is observed below 300 nm, which is a typical feature of Phenyl based silicone [114]. The actual optical pad in the final design being 150 μm thick, the photon loss could be even smaller that what was measured for the 350 μm thick sample, leading to a higher transmittance. However, most of the photon loss in this transmittance measurement is caused by Fresnel losses at the interface of the sample due to difference in refractive index between the sample and the surrounding air. The measured transmittance can be corrected for Fresnel losses by applying a normalization defined as:

$$T = 1 - \left(\frac{n_{air} - n_{optpad}}{n_{air} + n_{optpad}} \right)^2 \tag{7.3}$$

where $n_{optpad} = 1.5324$ and $n_{air} = 1.000293$ are the refractive index of the optical pad and of the surrounding air, respectively. We here use the fact that the optical beam used to measure the transmittance is orthogonal to the sample plane. The corrected transmittance in the 400-500 nm interval is $98.29 \pm 0.14\%$, which matches the value reported by CNES [89] for this material. One can note that the Fresnel losses in the actual polarimeter module are not so large since the refractive index of the optical pad and that of the surrounding materials (scintillator bars and SiPM's resin) are relatively comparable.

7.2 MODULE'S OPTICAL SIMULATIONS WITH GEANT4 AND CALIBRATION

The optical simulation of the polarimeter module, whose Geant4 visualization rendering is displayed in Figure 7.19, contains all the key optical components to fully simulate the optical behavior of the system. It is composed of 64 scintillator bars, individually wrapped with 4 strips of Vikuiti surrounded by a foil of Claryl. A 50×50 mm^2 Vikuiti foil is placed at the top of the target. The alignment plastic grid is built at the other extremity of the module, where the optical pad and SiPM arrays are also placed. Environmental volumes, whose material can either be assigned to *Vacuum* to reproduce the behavior in space or *Air* to reproduce the behavior of tests performed on ground, are built between each elements which are not physically in contact. This is for instance the case of the Vikuiti strips and scintillator bars, which are separated by such volumes to properly implement the properties of the optical interfaces of each compounds. An air/vacuum gap is needed between the scintillators and the vikuiti foils in order to have a big difference in refractive index between the bar and its surrounding material to maximize internal reflections. Gluing the reflective foils directly on the scintillators would deteriorate the light yield as it would decrease the amount of internal reflections in the bar. More details on the module design were discussed in Section 5.2. General peculiarities of implementing optical simulations in Geant4 are discussed in [61].

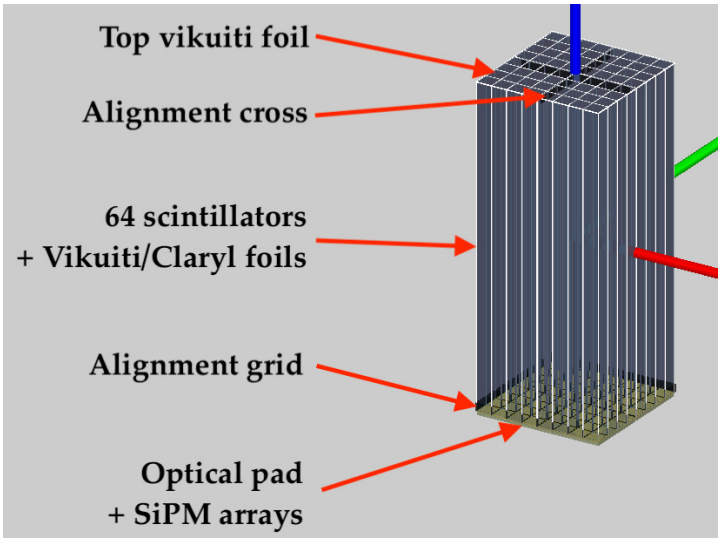

Figure 7.19: Implementation of the polarimeter module in the optical simulations.

7.2.1 *Energy dependent scintillation: the Birks effect*

The scintillation efficiency, that is the amount of light produced per unit of deposited energy, is a crucial parameter to fully understand the optical response of the module. The scintillation efficiency of both EJ-248M and EJ-200 scintillators is given in the data sheet for 10 MeV electrons [63, 64], but its value is energy and

particle dependent. Indeed, the efficiency drops at lower energy, as described by the Birks' law [19]:

$$\frac{\mathrm{d}L}{\mathrm{d}x} = \frac{S\frac{\mathrm{d}E}{\mathrm{d}x}}{1 + kB\frac{\mathrm{d}E}{\mathrm{d}x}} \tag{7.4}$$

where L is the light yield of the scintillator, S is its scintillation efficiency, $\frac{\mathrm{d}E}{\mathrm{d}x}$ the energy loss per track length, and kB is the Birks' constant in units of distance over energy. For our scintillator candidates this constant is $kB = 0.143$ mm/MeV [241] (with a density of 1.023 g/cm^3) and is given as an input to the optical simulations. This is typical of polyvinyl toluene (PVT) materials, for which the Birks' constant is around $1.5 \cdot 10^{-2}$ g MeV^{-1}cm^{-2} [20, 127, 215]. Interesting limits of this law can be noticed:

The Birks constant was measured for EJ-248M in [241] for POLAR, the same value is assumed for EJ-200 as the material composition is very similar.

$$\lim_{\frac{\mathrm{d}E}{\mathrm{d}x}\to 0} \frac{\mathrm{d}L}{\mathrm{d}x} = S\frac{\mathrm{d}E}{\mathrm{d}x}\ ; \qquad \lim_{\frac{\mathrm{d}E}{\mathrm{d}x}\to \infty} \frac{\mathrm{d}L}{\mathrm{d}x} = \frac{S}{kB} = cst. \tag{7.5}$$

The luminescence yield can also be expressed per unit of energy as follows:

$$\frac{\mathrm{d}L}{\mathrm{d}E} = \frac{S}{1 + kB\frac{\mathrm{d}E}{\mathrm{d}x}} \tag{7.6}$$

The scintillation efficiency in optical photons per keV is plotted in red in Figure 7.20 as a function of energy for incoming electrons both from the theoretical Birks formula (7.4) and from the optical simulation results. The simulations slightly over-estimates the scintillation efficiency in the 10-300 keV range compared to the theoretical value. The simulated curve not accounting for Birks' effect is also shown in black and matches with the constant 9.2 optical photons per keV provided in the data sheet. Figure 7.20 also shows the comparison of two methods used to compute the theoretical behavior of Birks' effect on the scintillation efficiency.

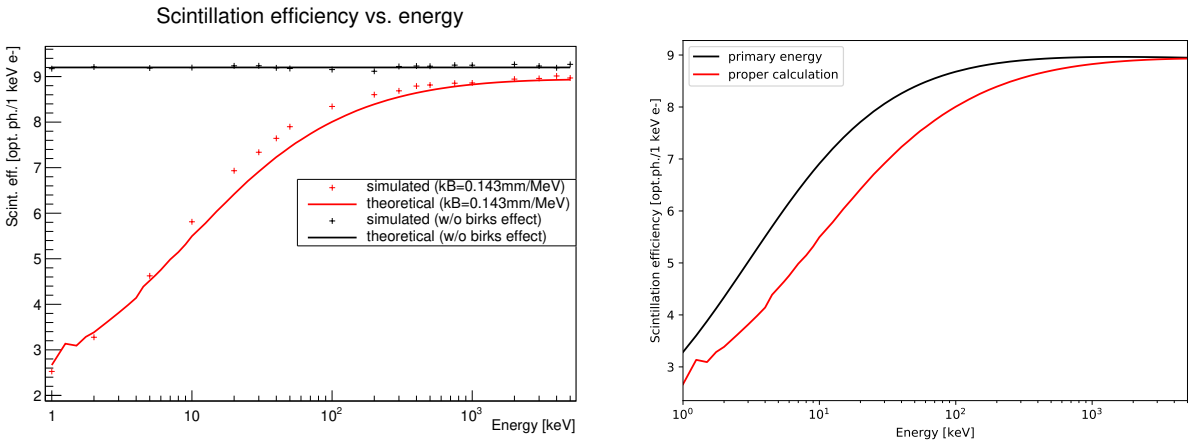

Figure 7.20: **Left:** Simulated scintillation efficiency as a function of energy compared to the theoretical behavior based on Birks' law, with and without Birks effect. In the case with no Birks effect (kB is set to zero), no energy dependence of the nominal 9.2 photons/keV scintillation efficiency is observed. **Right:** Comparison of the theoretical Birks effect scintillation efficiency as a function of energy when accounting only the primary energy of the electron versus properly calculating the electron's energy as it looses energy in the scintillator.

The simplest but incorrect way of making the computation is to only account for the primary energy of the electron, read the stopping power $\frac{\mathrm{d}E}{\mathrm{d}x}$ in PVT in Figure 7.21 for the given energy, and use the expression (7.4) to simply compute the scintillation efficiency for each energy. The correct way of computing the scintillation efficiency for each energy is to start from the primary energy, read the electron energy loss in Figure 7.21, apply this energy loss on an infinitesimal track length to compute a new energy, and repeat the process until the electron has deposited all its energy. Looping down over the energy of the electron as it deposits part of it in the scintillator is the proper way of calculating the scintillation efficiency, and is compared to the over-estimated scintillation efficiency got from using the primary energy only in the right plot of Figure 7.20.

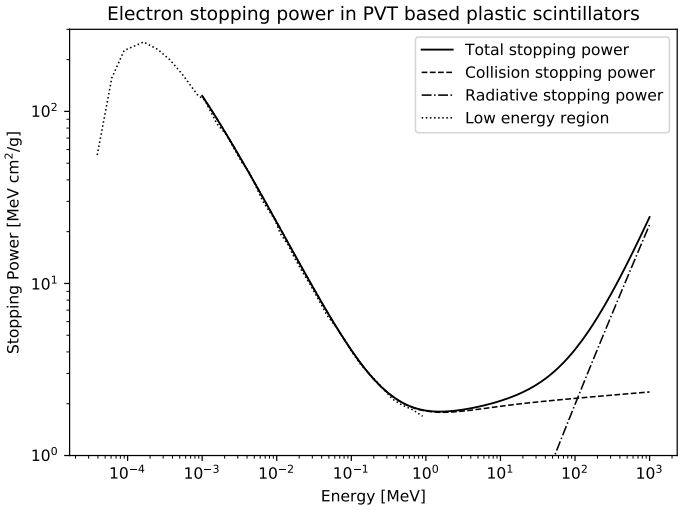

Figure 7.21: Electron stopping power in polyvinyl toluene. The sub-keV part is taken from [72], and the high energy part from [158].

7.2.2 *Influence of the scintillator surface quality on the light output*

After having measured the surface quality of both EJ-200 and EJ-248M scintillators (see Section 7.1.3), it has to be implemented in the Geant4 optical simulations. The way Geant4 deals with the roughness of a given transparent surface is by deviating each incoming photon when it crosses the surface by an angle α added on top of the refracting angle. This angle is picked from a Gaussian distribution. The input given to the simulations is the width of this Gaussian distribution, σ_α. The wider the distribution, the rougher the surface. A rougher surface will therefore cause a bigger spread of the photons' deviation. The surfaces can also be seen as composed of many micro-facets [184], whose orientations are tilted by an angle α compared to the average surface.

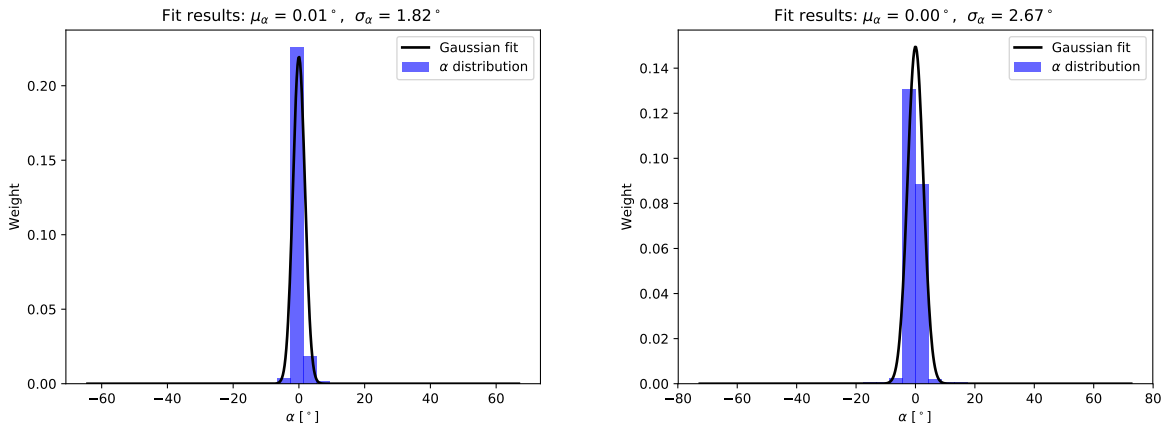

Figure 7.22: Extraction of the σ_α parameter for the samples measured in Figure 7.15. **Left:** EJ-248M **Right:** EJ-200

The maps measured were analyzed on order to extract a σ_α value for each type of plastic (see Section 7.1.3). A distribution of the angle between two points of the measured map and the average surface plane is filled for every point on the map. Examples of obtained Gaussian distributions for both types of plastics are shown in Figure 7.22. Several maps were measured for each plastic giving the averaged values of $\sigma_\alpha^{EJ-248M} = 1.82 \pm 0.09^\circ$ and $\sigma_\alpha^{EJ-200} = 3.45 \pm 0.14^\circ$, the latter being bigger since EJ-200 is rougher than EJ-248M.

We now define the light output fraction as being the fraction of the injected optical photons reaching the SiPMs. This fraction does not include the PDE of the SiPM and is used as a figure of merit of the optical efficiency of the target. Two attenuation lengths can be defined in order to disentangle the intrinsic scintillator material attenuation from the photons lost because of the surface roughness of the scintillator. We therefore define the Bulk Attenuation Length (BAL) and Technical Attenuation Length (TAL) [120, 121] as follows:

$$BAL: \ I(x) = A_1 e^{-\frac{x}{\lambda_1}} \ ; \qquad TAL: \ I(x) = A_1 e^{-\frac{x}{\lambda_1}} + A_2 e^{-\frac{x}{\lambda_2}} \tag{7.7}$$

The BAL represent the intrinsic material property that is given in the manufacturer data sheets [63, 64] as being 380 cm for EJ-200 and 250 cm for EJ-248M. The light output fraction was simulated for the BAL injecting optical photons along the bar direction at different height in the scintillator and for different roughnesses. The corresponding Gun Particle Source (GPS) file used in Geant4 to inject optical photons is:

```
/gps/particle opticalphoton
/gps/pos/type Plane
/gps/pos/shape Rectangle
/gps/pos/centre 0.0 0.0 1.0 cm
/gps/pos/halfx 0.1 cm
/gps/pos/halfy 0.1 cm
/gps/direction 0 0 -1
/gps/ene/type Arb
/gps/ene/diffspec 0
/gps/hist/type arb
/gps/hist/point 2.5e-06 0.06295
...
/gps/hist/point 3.09e-06 0.00883
/gps/hist/inter Lin
```

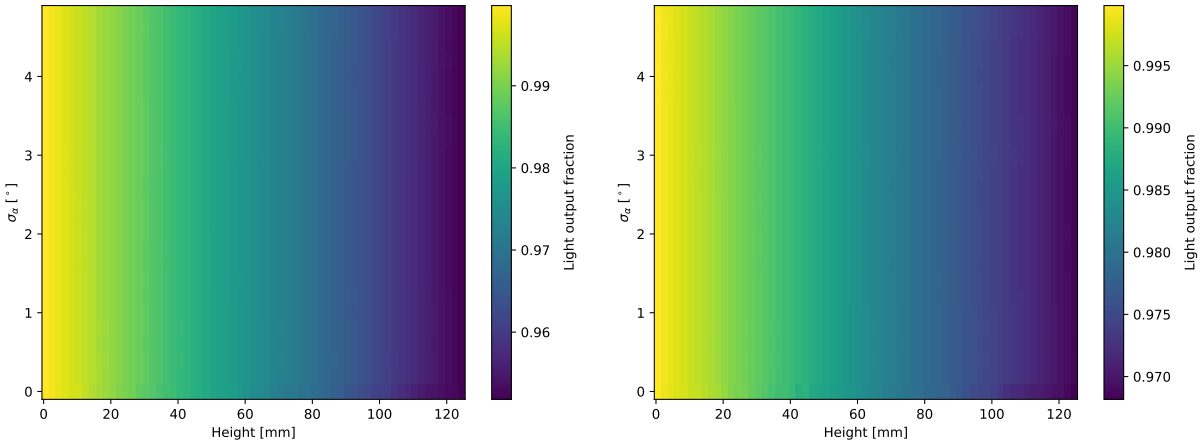

Figure 7.23: Simulated light output fraction for the EJ-248M (**left**) and EJ-200 (**right**) scintillators injecting light parallel to the scintillator length direction. The simulations are performed with perfect reflectors and 100% sensitive SiPMs so that the light output only reflects the optical light loss at the scintillator surface due to the roughness. It is shown as a function of the roughness of the scintillator surface and the height at which the light is injected along the scintillator bar, 0 mm being the extremity of the bar on the SiPM side, and 125 mm the extremity of the bar facing the deep space. As the optical light is injected along the scintillator length, the photons are not crossing the 4 long faces of the scintillator bar and are directly going to the sensor. No roughness dependence is therefore observed while the light output decreases when the light is injected further away from the SiPM channel, due to the bulk attenuation length of the scintillating material.

The resulting light output map from these simulations is shown in Figure 7.23, where we clearly see a decreasing light output with the height for both plastics. This is explained by the bulk attenuation length of the material: when the photons are injected near the SiPMs (small height), more will reach the sensor than when they are injected on the other side of the bar. No significant dependence of the light output on σ_α is observed, since the photon are propagating along the bar direction and are therefore not crossing the scintillators surfaces except once when they reach the optical pad and sensor. The same simulations can be ran injecting photons from a given height but in isotropic directions from a sphere. This is done by using the following GPS:

We would expect a small dependency in σ_α as some photons can bounce back and travel more than once along the bar, but this is not observed here.

```
/gps/particle opticalphoton
/gps/energy 3 eV
/gps/pos/type Surface
/gps/pos/shape Sphere
/gps/pos/radius 1 mm
/gps/pos/centre 0.325 0.325 0.0 cm
/gps/ang/type cos
```

The resulting light output fraction maps for EJ-248M and EJ-200 are shown in Figure 7.24. As in the previous case, the light output is decreasing with height. However, this decrease is much more dramatic and is also σ_α dependent. As one could expect, the rougher the surface, the lower the light output since more photons are lost when crossing the scintillator surface and being reflected back by the ESR. This reflects the technical attenuation length, described in

equation (7.7), which accounts not only for the intrinsic light attenuation from the material but also for the scintillator shape and surface quality, as well as for the performances of the reflectors. This case is therefore more representative of the actual module.

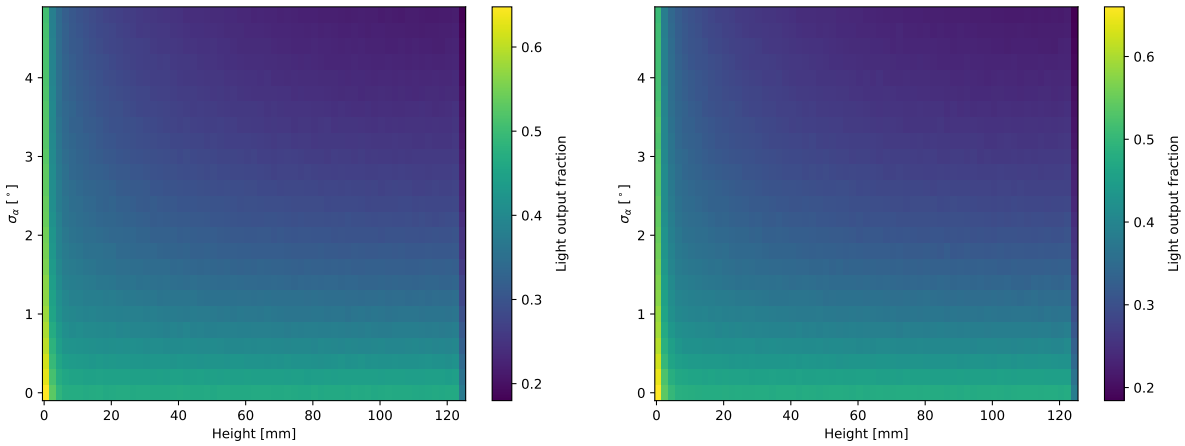

Figure 7.24: Simulated light output fraction for the EJ-248M (**left**) and EJ-200 (**right**) scintillators injecting light with an isotropic symmetry. The simulations are performed with perfect reflectors and 100% sensitive SiPMs so that the light output only reflects the optical light loss at the scintillator surface due to the roughness. It is shown as a function of the roughness of the scintillator surface and the height at which the light is injected along the scintillator bar, 0 mm being the extremity of the bar on the SiPM side, and 125 mm the extremity of the bar facing the deep space. As the optical light is injected with a radial symmetry, photons are crossing the scintillator surface and reflected back many times before reaching the sensors. The light output is in consequence highly dependent on the surface roughness, as the loss of photons decreases with a higher surface quality. The light output fraction is also dependent on the injection position, this time not only because of the optical attenuation intrinsic to the material, but also because photons injected further away from the sensors will have crossed the surfaces many more times before reaching it. This reflects the technical attenuation length describe by the second expression in equation (7.7).

The light yield of the polarimeter module is measured using the ^{137}Cs Compton Edge (CE) at 476 keV (see later in this section). The light output maps in Figure 7.24 can be therefore convolved along the height dimension with the simulated penetration profile of 476 keV photons in the scintillators plotted in Figure 7.25.

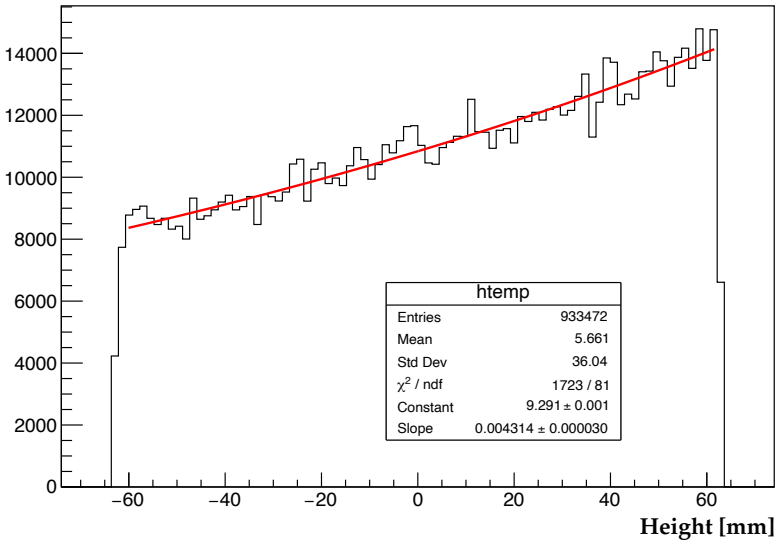

Figure 7.25: Penetration profile of 476 keV photons in the plastic scintillator fitted with an exponential. The 476 keV energy corresponds to the ^{137}Cs Compton edge used to determine the module light yield (see section 7.2.3).

Through this convolution, we obtain the light output fraction profile as a function of the surface roughness for both scintillator types. The light output fractions can then simply be read from these curves by using the roughness parameters computed from the measurements, $\sigma_\alpha^{EJ-248M} = 1.82 \pm 0.09°$ and $\sigma_\alpha^{EJ-200} = 3.45 \pm 0.14°$. The corresponding light output fractions for the EJ-248M and EJ-200 scintillators are respectively 0.323±0.004 and 0.273±0.004. The impact of the rougher EJ-200 surface is therefore visible on the light output fraction and is countering the higher scintillation efficiency of Ej-200 compared to EJ-248M.

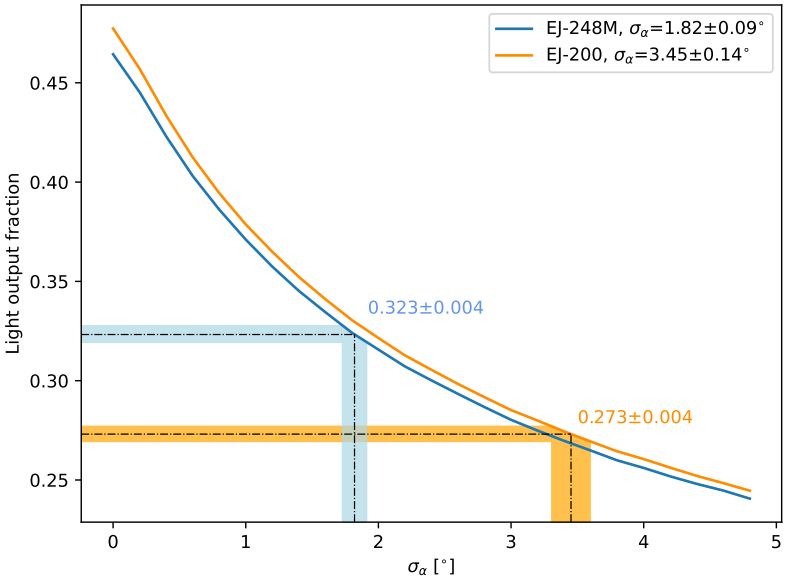

Figure 7.26: Simulated light output fraction for 476 keV photons for both EJ-248M and EJ-200 plastics as a function of the surface roughness. The light output fractions corresponding to the measured surface roughness are displayed for both scintillator types.

Furthermore, knowing the σ_α values for both types of material from measurements, the height profile of the light output fraction can be extracted from the maps of Figure 7.24. The resulting curves can be fitted with a sum of two exponentials, as in the TAL expression of equation (7.7).

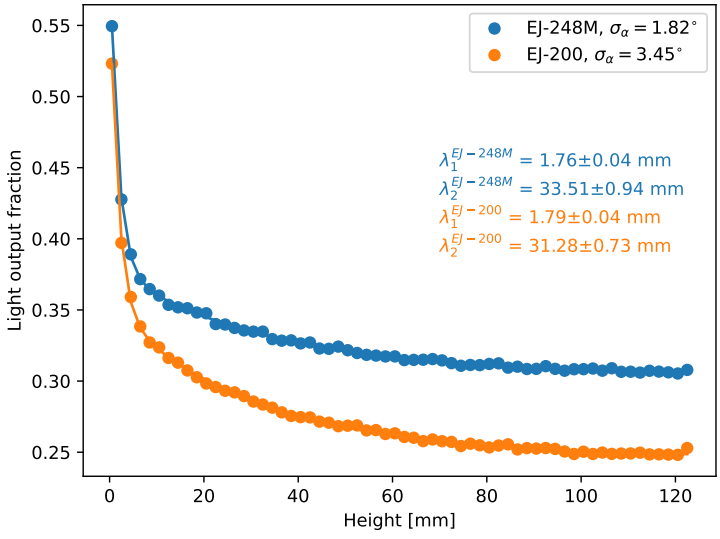

Figure 7.27: Light output fraction as a function of the injection height for the measured roughness of both EJ-248M and EJ-200 plastics fitted with the TAL expression in equation (7.7).

The effect of scintillator roughness on the light output can further be observed by measuring the light yield of difference scintillator shapes. This was done using cylindrically shaped scintillators of 12.7 mm diameter and 25.4 mm height. The light output was in this case larger for EJ-200 than for EJ-248M because of the different volume to surface ratio [172]. Indeed, the cylinders having a bigger volume to surface ratio, the contribution of the surface roughness to the overall light output was less pro-eminent than for the scintillator bars and was therefore not important enough to counter balance the bigger scintillation efficiency of EJ-200.

7.2.3 *Optical light yield*

The light output fraction is a good figure of merit to assess the optical efficiency of the target itself. However, to completely represent the efficiency of the polarimeter module, a more physical quantity is used: the Light Yield. The LY is the number of detected photons, also known as photo-electrons, per unit of incoming energy in the detector. The bigger the LY, the better the sensitivity of the polarimeter, especially at low energies where having a good LY is crucial since only a few photons are produced through the scintillation process.

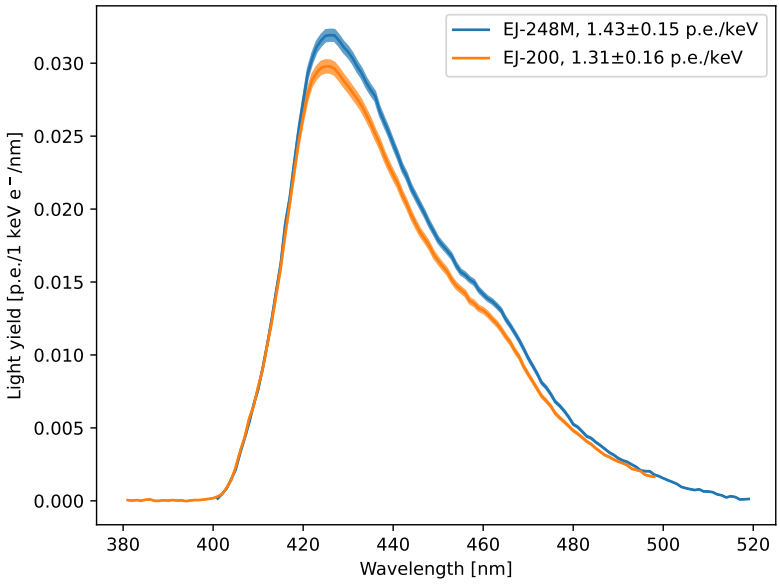

Figure 7.28: Computed light yield in photoelectrons per keV per unit of wavelength as a function of the photon wavelength for both EJ-248M and EJ-200 scintillators. This light yield spectrum is obtained by convolving the scintillator emission spectrum with the SiPM PDE and the light output fraction for the measured roughness from Figure 7.26. The integration of these curves leads to the module light yields of $LY_{EJ-248M} = 1.43 \pm 0.15$ p.e./keV and $LY_{EJ-200} = 1.31 \pm 0.16$ p.e./keV.

Based on the light output fractions obtained for both scintillators from simulations, the expected light yield can be computed. This is done in Figure 7.28, where the light output fraction is convolved with the efficiency of the sensors (PDE) and the scintillator emission spectrum. The light yield per unit of wave-

length is plotted as a function of the photon wavelength for both plastics. By integrating the curves, the light yield in number of photo-electrons per keV is obtained. The resulting values are $LY_{EJ-248M} = 1.43 \pm 0.15$ p.e./keV and $LY_{EJ-200} = 1.31 \pm 0.16$ p.e./keV. The light yield for EJ-248M is indeed higher than that of EJ-200 although the latter has a larger scintillation efficiency, as observed in the laboratory.

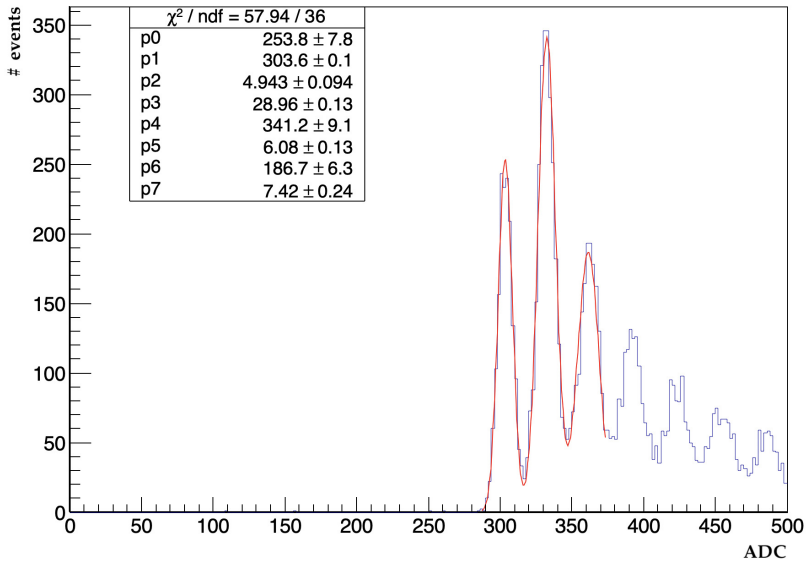

Figure 7.29: Dark spectrum of the SiPMs measured with a POLAR-2 prototype module. The first peaks of the finger-like structure are fitted using a sum of Gaussians, as expressed in equation (7.8). The position of each peak is extracted in order to determine the distance between peaks, which gives the conversion from HG ADC to photo-electrons.

As mentioned in Section 5.2.5, the prototype POLAR-2 modules are being calibrated either with radioactive sources in the POLAR-2 laboratory at CERN, or with an X-ray beam like the one at the European Synchrotron Radiation Facility (ESRF) in Grenoble, France. In the first case, ^{241}Am and ^{137}Cs sources are employed in order to determine the light yield of the polarimeter module. As discussed in Section 5.2.2, the data is read out using two different gains, the high (HG) and low (LG) gains. A dark spectrum, with no radioactive source, is first taken in order to measure the single photo-electron spectrum, also know as *finger plot*. The finger structure, of which a measured example is shown in Figure 7.29 is fitted using a sum of Gaussian distributions:

$$p_0 \exp\left(-\frac{1}{2}\left(\frac{x-p_1}{p_2}\right)^2\right) + p_4 \exp\left(-\frac{1}{2}\left(\frac{x-(p_1+p_3)}{p_5}\right)^2\right) + p_6 \exp\left(-\frac{1}{2}\left(\frac{x-(p_1+2p_3)}{p_7}\right)^2\right) \tag{7.8}$$

The fit allows to extract the position of the peaks corresponding to a integer number of photo-electrons. This can be used to convert the ADC values in the

high gain channel (ADC_{HG}) into a number of photo-electrons. A ^{137}Cs source is then placed on top of the polarimeter module and the spectrum is measured, this time in the low gain channel. An example of measured spectrum is plotted in Figure 7.30. A particular feature of the Cesium spectrum can be measured with the polarimeter plastic scintillators: the Compton Edge (CE). The CE position can be fitted using an error function:

$$C(x) = p_0 \,\mathrm{erf}(\frac{x - p_2}{p_1}) \tag{7.9}$$

The CE energy being known (476 keV), its position in low gain ADC is used to determine the conversion factor from ADC_{LG} to energy.

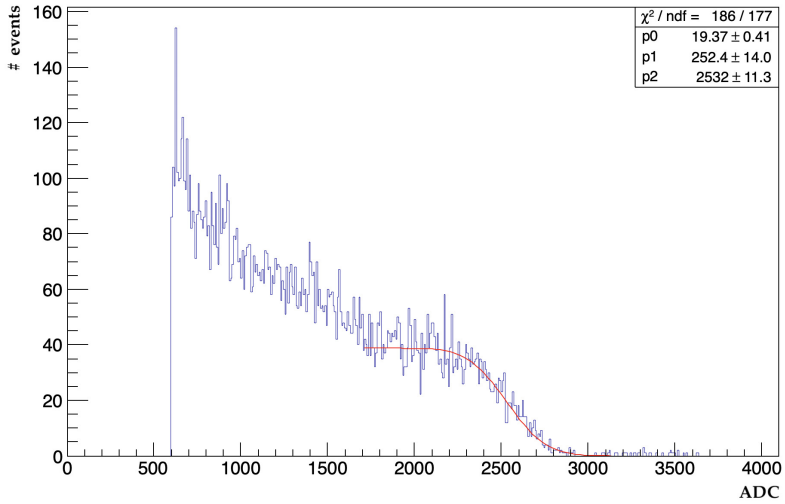

Figure 7.30: ^{137}Cs spectrum measured with a POLAR-2 prototype module using the LG channel. The Compton Edge position is fitted with an error function expressed in equation (7.9) to determine the LG ADC to keV conversion.

The final step in order to determine the conversion between energy and detected photons is to measure the ratio between HG and LG values. This is done by placing an Americium source on top of the module. The HG to LG ratio is computed on an event-by-event basis. The histogram of the ratio is fitted with a Gaussian to determine the conversion factor between LG and HG. The final light yield can be computed as follows:

$$LY = \frac{r_{ADC}}{d_{finger}} \times \frac{CE}{476keV} \tag{7.10}$$

where

d_{finger}	finger separation distance in ADC_{HG}/p.e.
r_{ADC}	HG to LG ratio in ADC_{HG}/ADC_{LG}
CE	Cesium Compton edge position in ADC_{LG}

It should be noted that the ADC to energy conversion could be determined directly using the ^{241}Am source, whose 59.5 keV photo-peak is visible in the

HG channel. This method would not require to compute the HG to LG ratio. However, since the photons will be more prompt to scattering due to their lower energy, the photo peak position will not be exactly at 59.5 keV but rather lower due to initial scattering interactions, therefore including an uncertainty on the measurement. This uncertainty is reduced when using the Cesium CE, for which the energy is higher.

A more accurate way of measuring the LY is using an X-ray beam, like the one provided at ESRF. A calibration campaign with several prototype modules took place in April 2023 [10], the setup is discussed in Section 5.2.5. In this case the position of the beam is precisely known and the 64 channels of the module can be scanned. A 60 keV beam shooting from the module's Zenith direction, whose photo-peak is visible in both HG (see Figure 7.31) and LG channels, can be used to determine the LY of every channel.

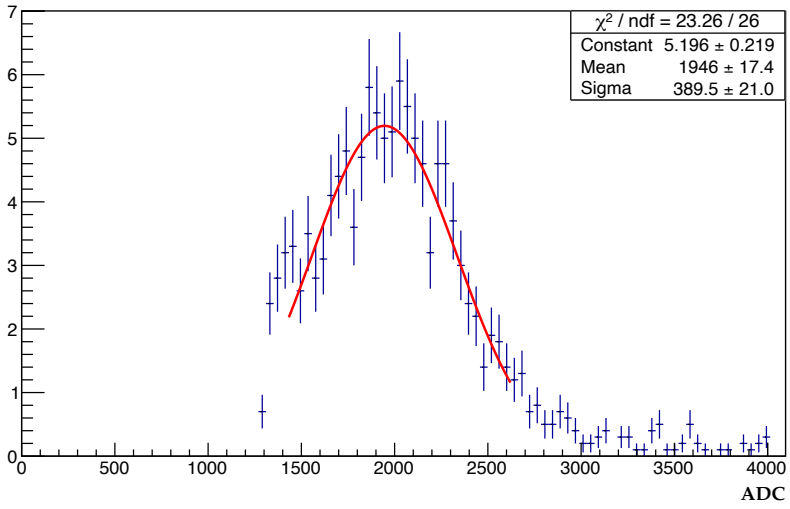

Figure 7.31: 60 keV photo-peak measured with the HG channel at the ESRF facility using an EJ-200 target.

The resulting LY distributions measured for all the channels of EJ-200 and EJ-248M modules are shown in Figure 7.31. The measured averaged light yields are respectively 1.23 ± 0.20 p.e./keV and 1.37 ± 0.32 p.e./keV. Table 7.1 compares the measured light yield values to the simulated ones. Measurements agree with simulations for both types of plastic. For comparison, the light yield of POLAR modules was around 0.3 p.e./keV. The optical efficiency of the polarimeter module has therefore improved considerably, greatly increasing the overall instrument sensitivity.

	LY_{EJ-200} [p.e./keV]	$LY_{EJ-248M}$ [p.e./keV]
Measurement	1.23 ± 0.20	1.37 ± 0.32
Simulation	1.31 ± 0.16	1.43 ± 0.15

Table 7.1: Measured and simulated light yield for EJ-200 and EJ-248M POLAR-2 modules.

However, a big spread can be observed for the light yield of the EJ-248M, with two out-sanding groups of scintillator bars. The first group of scintillators has a light yield centered around 1.21 p.e./keV with a standard deviation of 0.31 p.e./keV, while the averaged light yield of the second group is 1.61±0.19 p.e./keV. The lower light yield group is likely due to a non-uniform optical coupling between the scintillators and the SiPM arrays caused by the repeated assembly-disassembly of the modules during the calibration campaign. Furthermore, light yield of around 1.6 p.e./keV has already been measured for an entire EJ-248M module during preliminary prototypes testing at CERN. Considering this higher light yield for EJ-248M in the case of a good optical contact for the entire module, we notice a deviation from the simulated value.

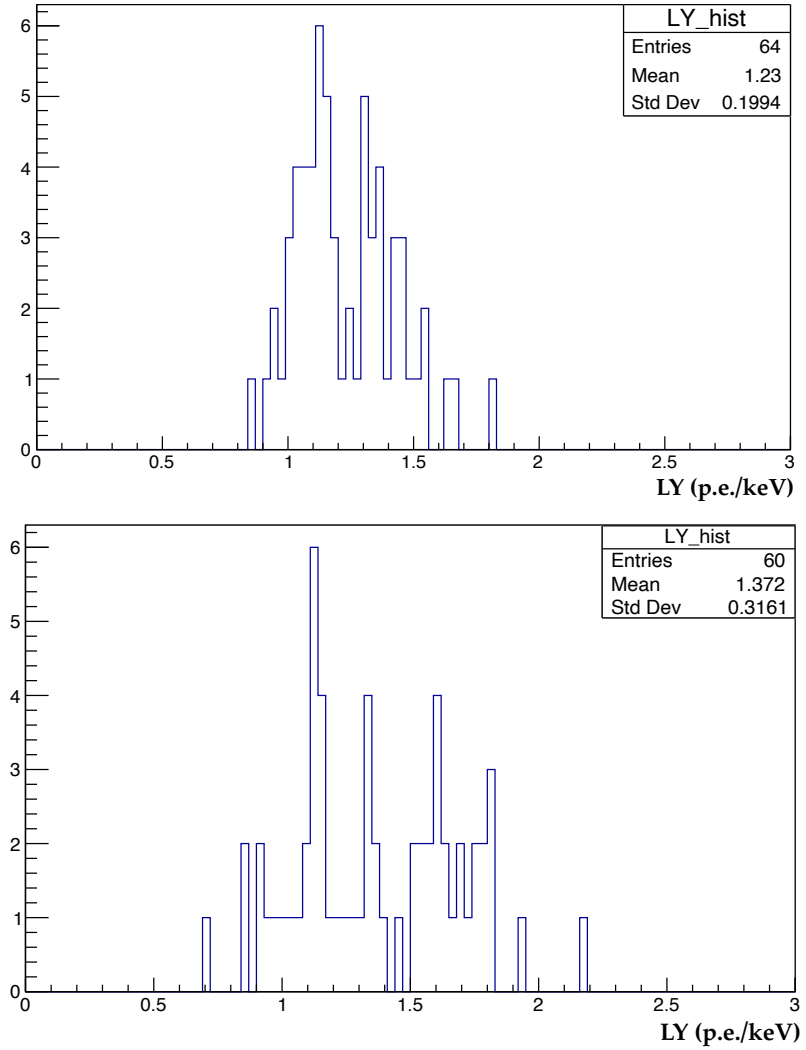

Figure 7.32: Measured light yield distribution for every channel of an EJ-200 (**top**) and EJ-248M (**bottom**) module. Respective light yields of $LY_{EJ-200} = 1.23 \pm 0.20$ p.e./keV and $LY_{EJ-248M} = 1.37 \pm 0.32$ p.e./keV are obtained. It can be noticed in the histograms that only 60 channels are used for the EJ-248M measurement because of malfunctioning channels in the FEE used for this measurement. A big spread can also be observed for the EJ-248M light yield with two groups of channels. This is likely due to bad optical coupling of the group of channels with low light yield, since around 1.6 p.e./keV light yield has been achieved with previous measurements of EJ-248M targets.

The under estimation of the light yield for EJ-248M simulations is likely to be caused by an over estimation of the scintillator roughness for this material. This might be due to the fact that less samples were measured for EJ-248M compared to EJ-200, and that because of samples availability, the EJ-248M bars that were measured on the IOM had already been used in a prototype module. They could therefore have some scratches on the surfaces, leading to a higher measured roughness than for a brand new scintillator.

7.2.4 *Optical cross talk*

Optical photons can escape from a given scintillator to reach one of the neighbor channels, this is called optical crosstalk and has to properly be measured and simulated in order to fully understand the response of the polarimeter. The optical crosstalk for POLAR was of the order of 10-15%. Photons going to the wrong readout channel can happen either via propagation through the optical coupling pad, the SiPM resin, the not completely opaque plastic alignment grid, or gaps between the reflective foils used to wrap the major part of the scintillator bars. A feature of the polarimeter module design important for the crosstalk is the fact that the target is divided in four quadrants due to the use of four 16 channels SiPM arrays for the readout. The pitch between channels is therefore 6.2 mm inside a quarter of the module, and 6.5 mm between two neighbour channels that do not belong to the same quarter due to the middle cross spacing between the four SiPM arrays. We expect less crosstalk between the channels separated by the middle cross due to the higher distance separating them.

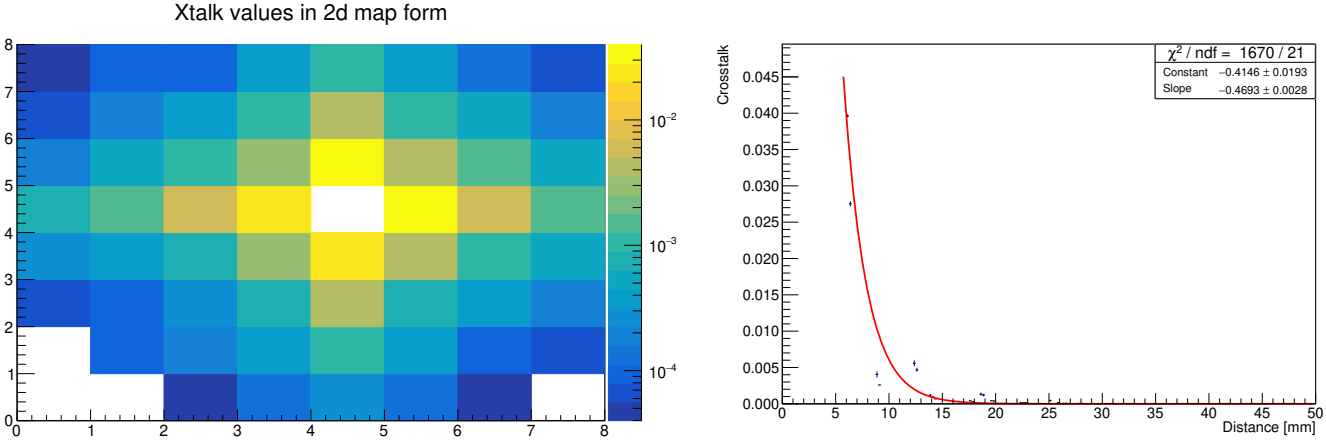

Figure 7.33: Crosstalk map (**left**) and crosstalk as a function of the neighbor bar distance (**right**) for a 150 μm thick optical coupling pad.

Optical light is injected in channel #36 in the simulations, which is located near the center of the module, at the corner of one of the quarters. This way the optical crosstalk to both direct neighbours and neighbours through the middle cross can be studied. A 8×8 map of the simulated crosstalk in each channels of the module for an injection in channel #36 is plotted in Figure 7.33. This figure also shows the crosstalk extracted versus the physical distance to the primary channel, fitted with an exponential. As expected, a slightly lower crosstalk is observed in the map to the neighbour through the middle cross than to the direct neighbour. The map is shown as a one dimensional plot in Figure 7.34, where the number of optical photons reaching the SiPM is plotted as a function of the channel number. A periodical behavior is observed with a peak every 8 channels due to the geometry of the module, with the peaks going lower and lower as we go away from channel #36. The crosstalk was simulated here for a 150 μm thick optical pad, which is used for coupling the scintillator target with the SiPM arrays in the final design. As the crosstalk is dependent on the thickness of the optical pad, the simulations were repeated as a function of this

thickness in order to characterize the increase of crosstalk for both direct and "middle cross" neighbour. The result is plotted in Figure 7.34, with a crosstalk of 2.40% for a 150 μm thick pad.

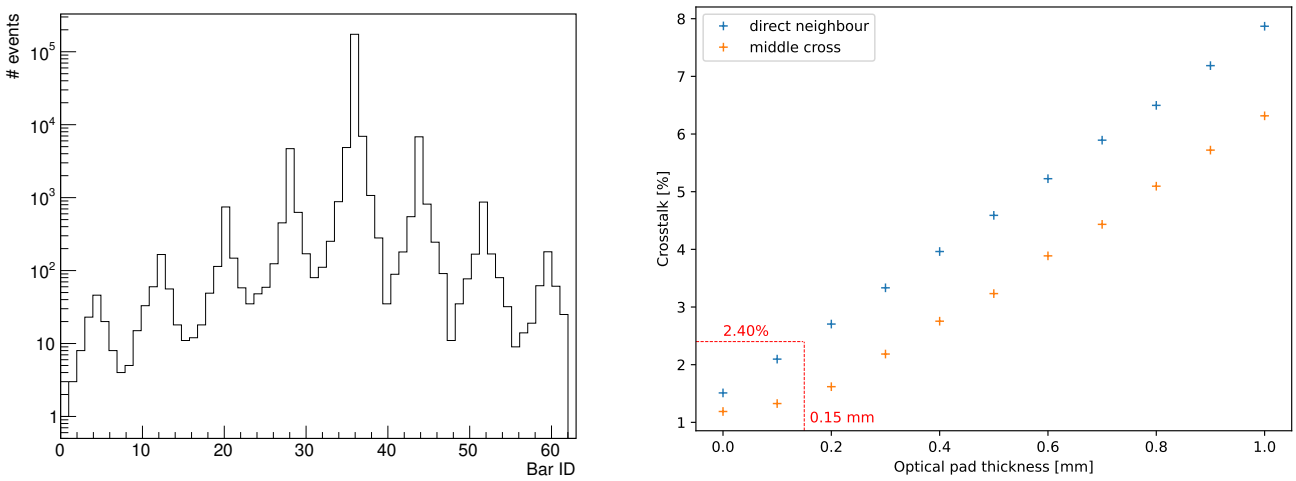

Figure 7.34: **Left**: Event distribution in the 8×8 bars array. A clear 8 bar modulation due to the module geometry is observed, with most of the events in the injected channel (#36). **Right:** Optical crosstalk as a function of the optical coupling pad thickness for both 0.2 mm and 0.5 mm pitches (within a SiPM array, and between two arrays where the pitch is bigger to due the middle cross).

The optical crosstalk can be estimated with a simple calculation to ensure that the simulated crosstalk is reasonable. As the reflecting foil are almost perfectly reflecting all the photons (see Section 7.1.1), the main crosstalk contributions come from the optical pad and the alignment grid. The contribution of the alignment grid can be calculated by multiplying the fraction of scintillator height that it covers, 3 mm/125 mm=2.4%, by the grid transmittance of 60.9% for a 0.2 mm thickness (see Section 7.1.2), which leads to a crosstalk of 1.46%. Doing the same calculation for a "middle cross" neighbour, where the grid is 0.5 mm thick and the transmittance is 47.1%, one obtains a crosstalk of 1.13%. Both crosstalk contributions from the grid are compatible with the value obtained for a null optical pad thickness in Figure 7.34, showing the great accuracy of the optical simulations.

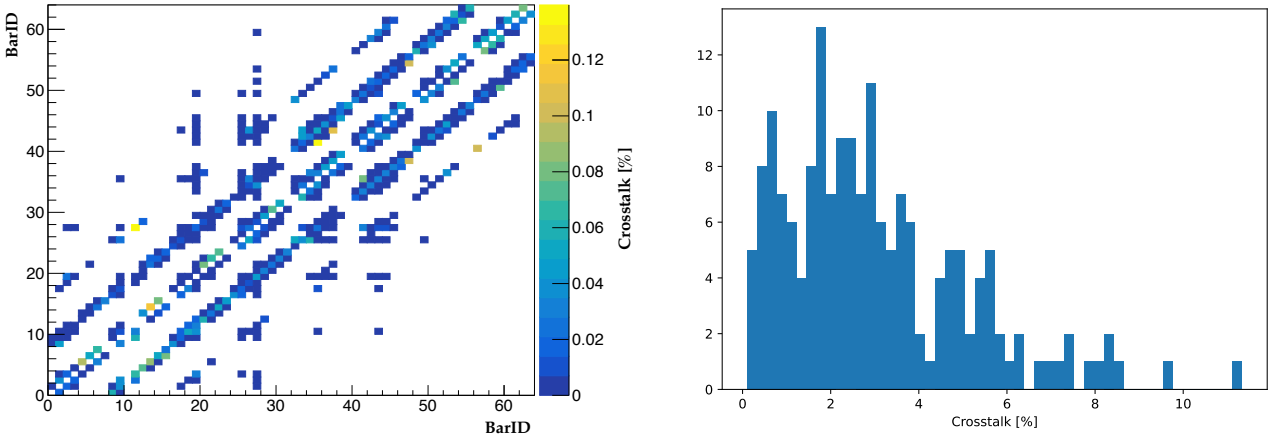

Figure 7.35: **Left:** Measured 64×64 crosstalk map showing for each channel the measured crosstalk to the other 63 channels. **Right:** Distribution of the measured crosstalk extracted from the map for the first neighbours of every of the 64 channels.

The optical crosstalk for every channel is measured by scanning the module with a ^{137}Cs source. The measured crosstalk is shown in Figure 7.35 for each channel versus each other 63 channels in the form of a 64×64 map. The central diagonal correspond to the crosstalk in one direction (row), while the two diagonals on each side shifted by 8 channels correspond to the neighbour in the other direction (column) as well as the diagonal neighbour (that do not share an edge but only a corner with the main channel). The other two diagonals on the outside, shifted by 16 channels are crosstalk to the second order neighbour in the column direction. The crosstalk to the second neighbour in the row direction can be seen around the main diagonal.

The crosstalk values to the first neighbour are also filled in a histogram plotted in Figure 7.35. The great improvement compared to POLAR can be observed. As mentioned earlier, the optical crosstalk in POLAR was about 10 to 15% because of the thick optical pad (1 mm versus 150 μm for POLAR-2) and of the thick MA-PMT entrance window. An average crosstalk of $2.63 \pm 2.10\%$ is measured from this histogram, compatible with the 2.40% simulated value reported in Figure 7.34.

7.3 CONCLUSIONS

The role of the POLAR-2 polarimeter modules is to convert the energy deposited by the incoming γ-rays into optical photons, which will later be collected by photo-sensors. The conversion of the deposited energy into optical light has to be done with the highest possible efficiency. The polarimeter module is therefore not only a γ-ray detector, but is an optical system whose optical components have to be optimized, characterized, and simulated.

The POLAR-2 polarimeter module consists of a target of 8×8 elongated plastic scintillators, individually wrapped in highly reflective foils. The individual wrapped bars are held together with a specially developed mechanical grid, and dampers are placed at the top of the target for vibration dampening. Once inserted into its carbon fiber socket, the target is coupled to the SiPM arrays and their front-end electronics thanks to a thin and soft optical pad.

The reflectance and transmittance of several reflective foils have been characterized, as well as the transmissivity of the optical pad and of the mechanical grid used to align the scintillators. Two scintillating materials were investigated for the module: EJ-248M, previously used in POLAR, and EJ-200, which has a 9% higher scintillation efficiency. The surfaces of several scintillators of both types were scanned with an interference optical microscope in order to characterize the surface quality of both plastics.

Based on the characterization of the different optical components composing the module, a complete optical simulation of a polarimeter module was implemented in Geant4. Among other things, the surface quality of both plastic scintillator candidates was included in the simulation using the σ_α roughness parameter in Geant4. Simulations shown that although the EJ-200 material has a higher scintillation efficiency, a higher overall optical efficiency is to be expected from EJ-248M, whose surface roughness is lower. Indeed, because the EJ-248M material is harder than the EJ-200, it has a smoother surface and therefore less light is lost at the interfaces, counter balancing the difference in scintillation efficiency. This was confirmed through lab measurements by measuring the light yield of a module based on EJ-248M and comparing it to that measured for an EJ-200 target. Defined as the number of detected optical photon per amount of deposited energy, the light yield is a good figure of merit to assess the optical efficiency of the module. As expected from simulations, a better light yield was measured with EJ-248M, which was selected as the scintillating material for the final design of the polarimeter. Finally, the optical crosstalk, corresponding to the fraction of optical light escaping from a given channel to one of its neighbour channels, was also simulated. The crosstalk measured in the lab matched the simulated values, with an improvement of almost an order of magnitude compared to POLAR.

Finally, it should be noted that the optical simulations developed for POLAR-2 are also useful for other similar instruments. Simulation work for determining the optimal design configuration were conducted for another GRB dedicated

polarimeter, the LEAP experiment. The simulation work performed for LEAP is described in Appendix D.

CONCLUSION & OUTLOOK

CONCLUSION & OUTLOOK

After introducing the gamma-ray burst paradigm and what we can learn on these astrophysical sources using polarization measurements, the state of the art of high energy polarimetry was presented. The work performed in the frame of this thesis was separated in two parts: data analysis on the POLAR experiment and instrumentation work on its successor mission, POLAR-2.

As the second dedicated GRB γ-ray polarimeter, POLAR measured the polarization of 14 bursts. Although all being compatible with a low degree of polarization, some of the GRBs shown an interesting hint for a time evolving polarization angle washing out the time integrated polarization degree. Another useful input for theoretical models is the energy dependence of polarization. In the frame of this thesis, the existing POLAR analysis framework was therefore modified to perform energy resolved polarization analysis. No significant energy dependence on either the polarization degree or angle was found. However, due to limited statistics, the results were not very constraining and are not ruling out any existing photospheric or synchrotron energy dependent polarization model. The next step in this work is to simulate fake bursts in order to compare the sensitivity to the energy dependence of polarization between POLAR and POLAR-2. The energy dependent fitting can also be implemented in a more generic way in order to directly compare the data against any theoretical energy resolved model.

As limited statistics with POLAR prevented for detailed energy and time resolved analyses, the need for a bigger and more sensitive polarimeter dedicated to the prompt emission of GRBs emerged. Creatively named POLAR-2, the successor mission to POLAR is currently under development and accepted for a launch to the China space station. Lead by university of Geneva (departments of high energy physics and of astronomy), the collaboration is also composed of the institute of high energy physics of Beijing (IHEP), the national polish center for nuclear research (NCBJ), and the Max Planck institute for extraterrestrial physics in Garching (MPE). The design and development of the instrument was first presented. It consisted of improving the scientific performances of the polarimeter as well as developing characterization and assembly techniques. Many space qualification tests, namely component irradiation, vibration and shock tests, or thermal vacuum cycling, were conducted in the frame of this thesis. As the main drawback of the sensors employed in POLAR-2, the silicon photomultipliers' radiation damage and its effect on the instruments performances were studied. Thermal annealing, consisting of heating up irradiated sensors to recover part of their original performances, was therefore characterized as a function of temperature for different sensor types. Annealing strategies which can be applied to any space-based mission employing SiPMs were presented. Finally, the optical characterization, optimization, and simulation work for the POLAR-2 polarimeter modules was discussed. Many optical tests were conducted on reflective foils, optical coupling material, scintillator surface quality

et cetera in order to optimize the light collection of the polarimeter module. The module was implemented in Geant4 to carry out optical simulations of the system and understand its optical behavior. The simulated optical performances have shown a good agreement with the outcome of the calibration campaigns, indicating a good understanding of the module.

After 4 years of effort, not only with the work described in this thesis but also thanks to the work carried out by the rest of the collaboration, the POLAR-2 polarimeter design is now ready to be frozen. The mass production phase of the polarimeter module should therefore be imminent. While the entire assembly of the overall instrument should take about a year, verification tests as well as additional preparations for the launch will be required. The current time frame is in consequence to send the POLAR-2 high energy polarimeter to the China Space Station late 2026. In parallel, two other payloads are under preparation to enhance the science outcome of POLAR-2. One payload will consist of a low energy polarimeter (LPD) based on gas pixel detectors and developed at GuangXi University, while the other payload developed by the institute of high energy physics of Beijing will employ GaGG crystals to perform high energy spectrometry.

Part IV

APPENDIX

A

I-V TEMPORAL EVOLUTION FOR DIFFERENT ANNEALING TEMPERATURES

In this chapter are provided all the I-V curves measured for the 25, 50, and 75μm SiPMs at each storage temperatures.

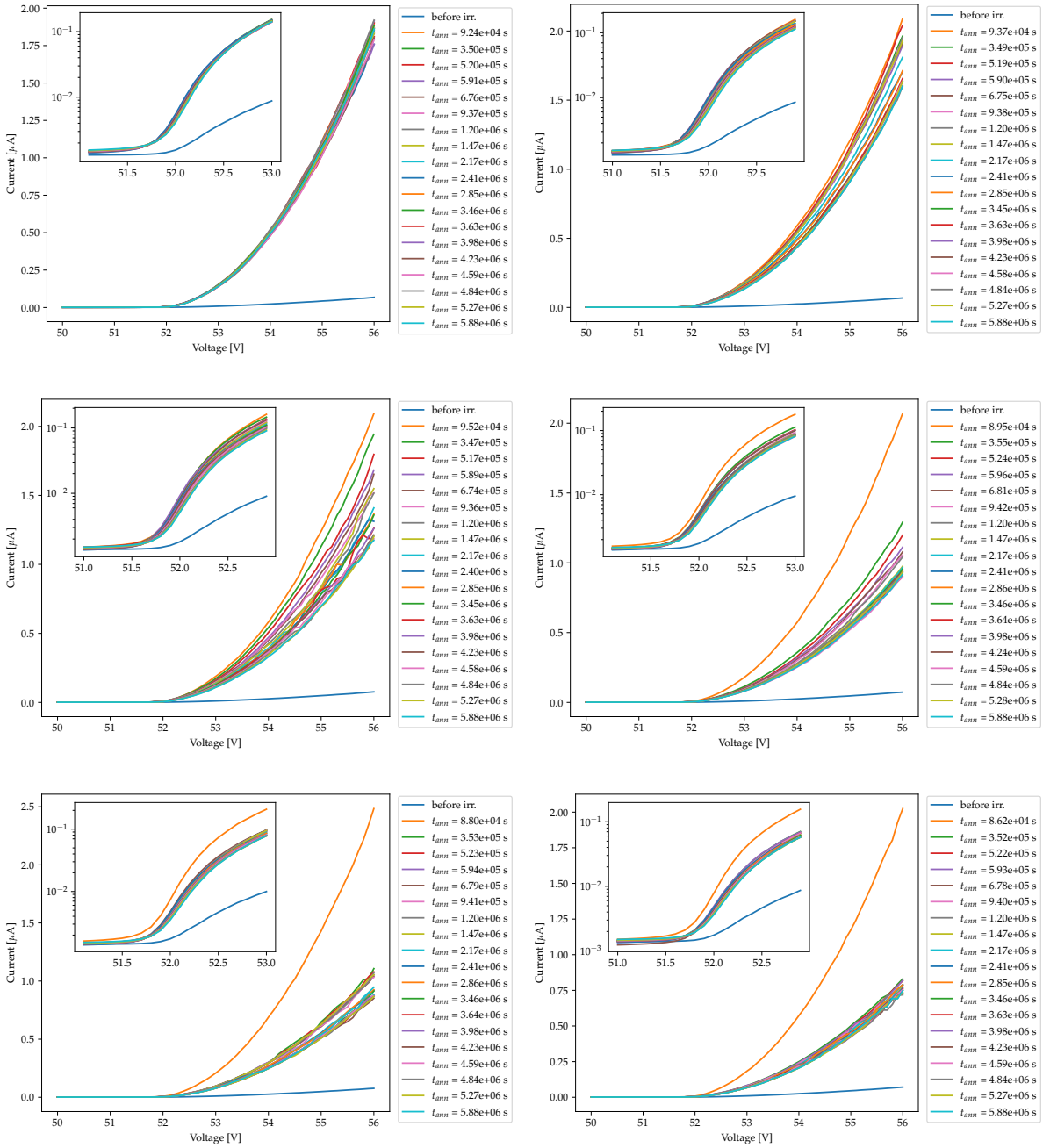

Figure A.1: Post-irradiation time evolution of the I-V characteristics of 25μm at -22.8 ± 1.8°C, 6.3 ± 0.9°C, 20.5 ± 0.6°C, 29.7 ± 0.6°C, 38.7 ± 1.6°C and 48.7 ± 3.3°C (from left to right, top to bottom) (taken from [51], with permission)

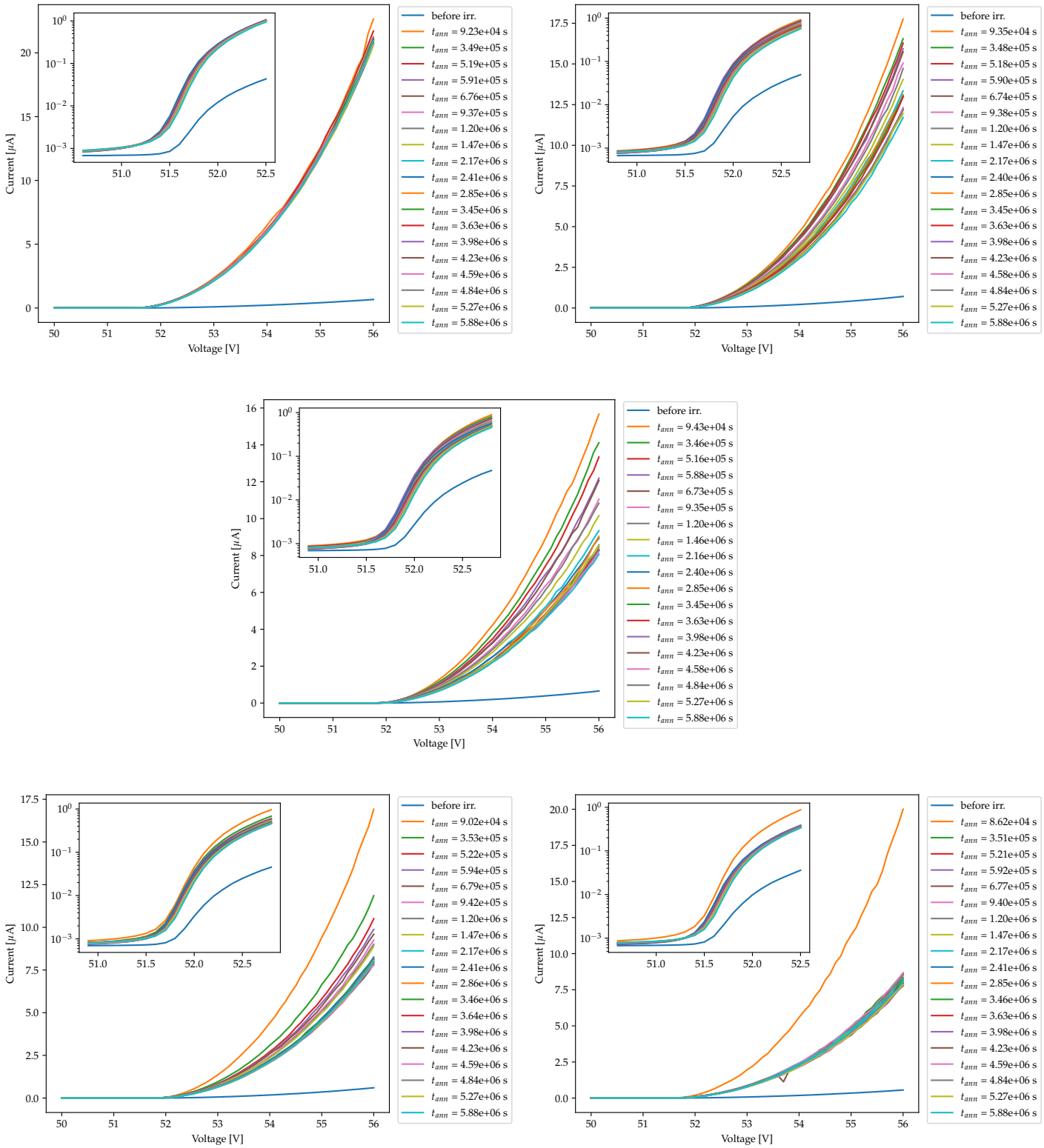

Figure A.2: Post-irradiation time evolution of the I-V characteristics of $50\mu m$ at $-22.8 \pm 1.8°C$, $6.3 \pm 0.9°C$, $20.5 \pm 0.6°C$, $29.7 \pm 0.6°C$ and $48.7 \pm 3.3°C$ (from left to right, top to bottom) (taken from [51], with permission)

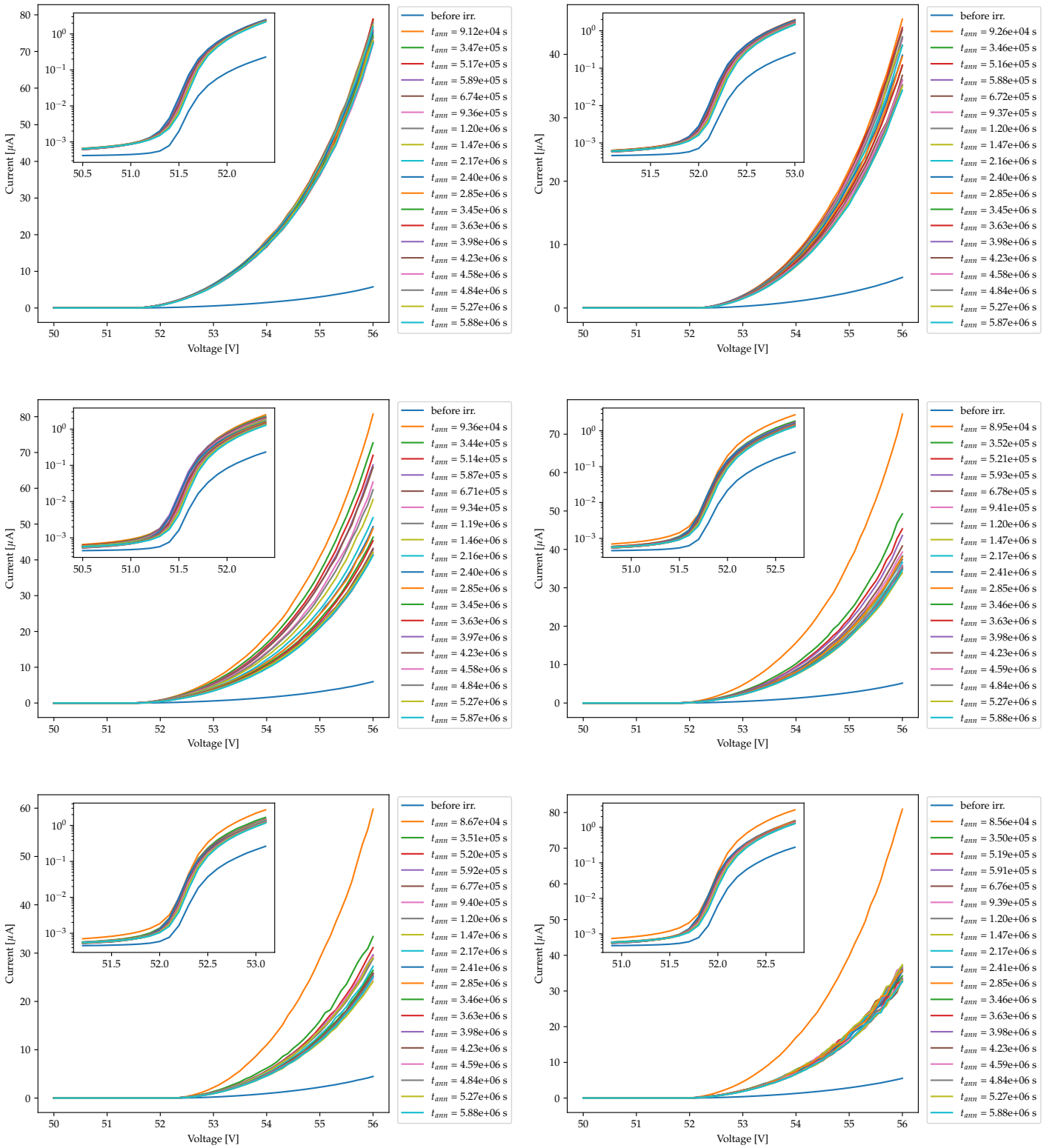

Figure A.3: Post-irradiation time evolution of the I-V characteristics of $75\mu m$ at $-22.8 \pm 1.8°C$, $6.3 \pm 0.9°C$, $20.5 \pm 0.6°C$, $29.7 \pm 0.6°C$, $38.7 \pm 1.6°C$ and $48.7 \pm 3.3°C$ (from left to right, top to bottom) (taken from [51], with permission)

B

DESIGN OF THE POLAR-2 LOGO

The logo of the POLAR-2 mission is shown in Figure B.1. The logo consists of the China Space Station (CSS) orbiting the Earth, circled by the flags of the 4 countries member of the collaboration. "POLAR-2" is written on the top right corner, with an "O" representing a GRB explosion from which a polarized wave is emitted.

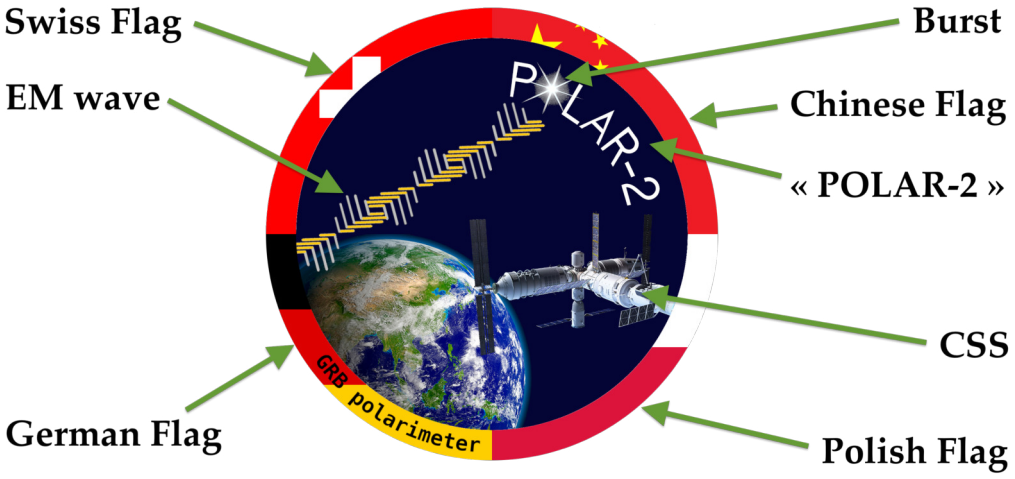

Figure B.1: Logo of the POLAR-2 mission

In order to be printed on the PCB, a simplified version of the logo has also been created. This logo as well as its rendering on a sample PCB are shown in Figure B.2.

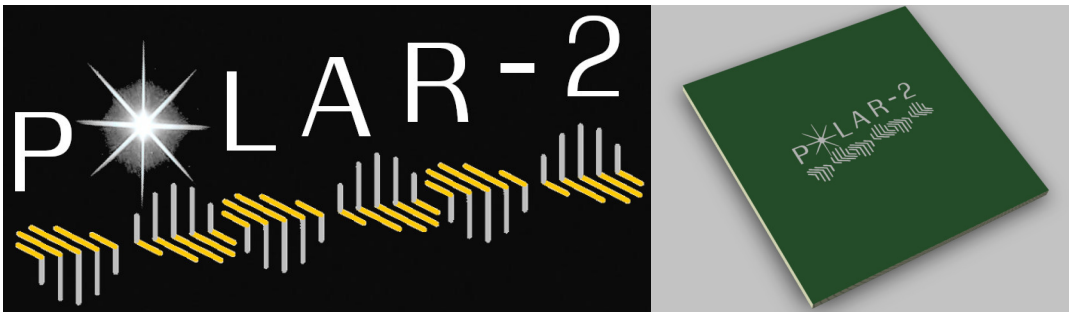

Figure B.2: Simplified POLAR-2 logo to be printed on the electronics and its rendering on a piece of PCB

C

EXTP DEVELOPMENT WORK

C.1 THE ENHANCED X-RAY TIMING AND POLARIMETRY MISSION (EXTP)

The enhanced X-ray Timing and Polarimetry mission (eXTP) mission [239] was born from the European mission concept Large Observatory For X-ray Timing (LOFT) and the Chinese mission concept X-ray Timing and Polarimetry mission (XTP). The scientific goal of eXTP is to simultaneously study the spectral, temporal, and polarization properties of extreme cosmic sources in the 0.5-30 keV range.

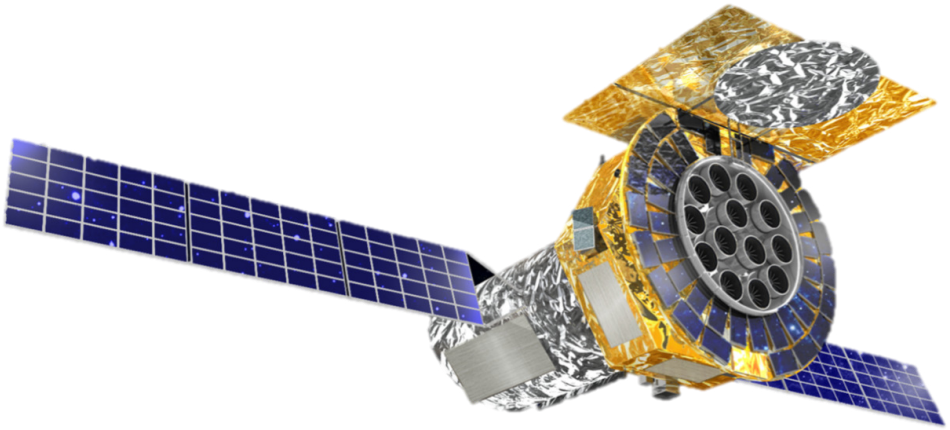

Figure C.1: Model of the eXTP satellite [244].

The satellite, whose design is shown in Figure C.1, is composed of four instruments:

- the Large Area Detector of the eXTP mission (LAD) [69]. Composed of 640 Silicon Drift Detectors (SDDs), the LAD will have an effective area of 3.4 m^2 in the 6-10 keV range. It will be sensitive from 2 to 30 keV with a FoV narrower than 1° and a spectral resolution reaching 250 eV at 6 keV.
- the Spectroscopic Focusing Array of the eXTP mission (SFA). With an operating range of 0.5-10 keV, the SFA will be composed of 9 X-ray optics each with a 12′ FoV. It will have a total effective area of 0.8 m^2 at 2 keV and 0.5 m^2 at 6 keV, and a time resolution of 10 μs. The energy resolution at 5.9 keV will be better than 180 eV.
- the Polarimetry Focusing Array of the eXTP mission (PFA). The PFA will employ 4 telescopes based on imaging GPDs. It will provide polarimetric measurements in the 2-10 keV range with a FoV similar to that of the SFA.
- the Wide Field Monitor of the eXTP mission (WFM) [98]. Composed of 6 coded mask cameras based on similar SDD than the one employed in the

LAD, the WFM will cover 3.7 sr in the 2-50 keV range. It will have the capability of sending alerts for transient events.

Our group in DPNC is responsible for the Detector Assembly of the LAD (DA), described in the next section.

C.2 LARGE AREA DETECTOR (LAD) ASSEMBLY AND QUALIFICATION

The LAD is composed of 640 SDDs divided into 40 modules of 4×4 detectors. Each of the 16 detectors in a module has its own readout electronics, whose design and layout are shown in Figures C.2 and C.3. The detector is composed of three main parts: the SDD (sensitive part), the readout electronics (FEE), and the so-called back-bone which serves as a mechanical adapter to the main frame of the module.

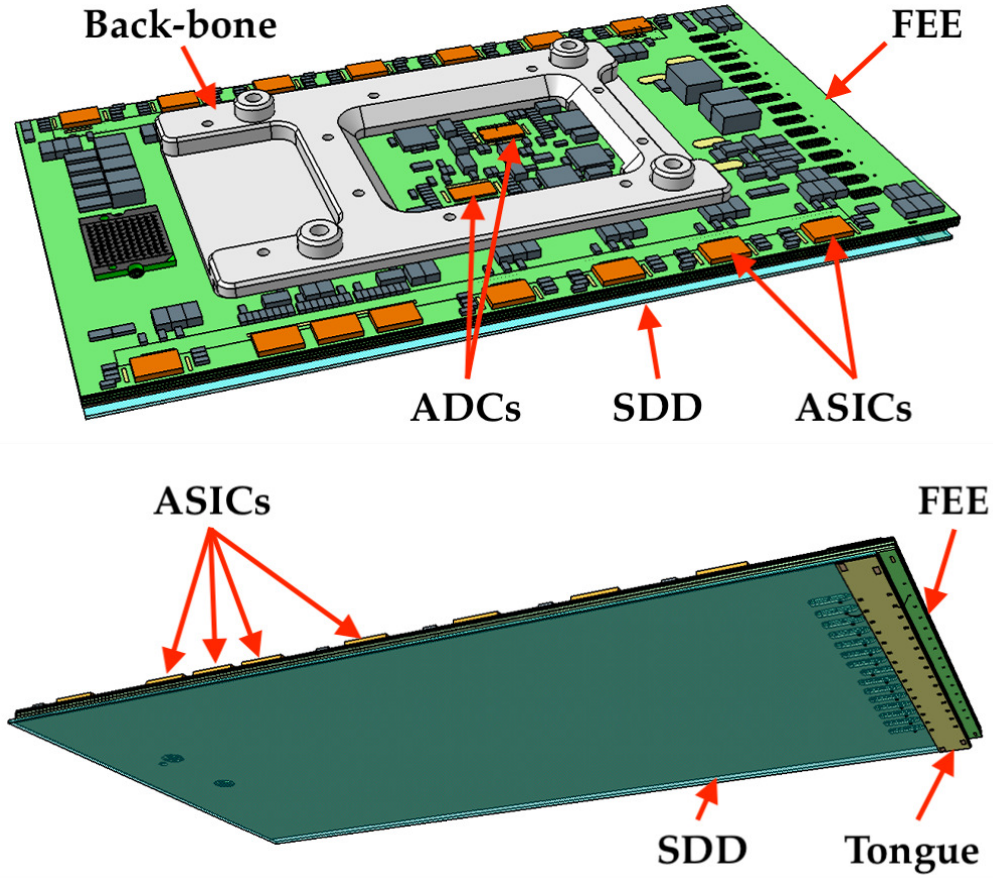

Figure C.2: LAD module seen from the FEE (**top**) and SDD (**bottom**) sides

The LAD project is led by INAF-IAPS (Istituto di Astrofisica e Planetologia Spaziali) in Rome, Italy. The SDD is developed by the INFN (Istituto Nazionale di Fisica Nucleare) of Trieste and FBK (Fondazione Bruno Kessler) in Italy. The Back-End electronics (BEE) is developed both for the LAD and WFM by the University of Tübingen, Germany. The ASICs and ADCs used on the FEE are developed by CEA (Comissariat de l'Energie Atomique) in France. As mentioned earlier, DPNC is responsible for the FEE and assembly of the LAD modules. The

detector development and assembly work performed at DPNC is also useful for the STROBE-X mission [203], which plans to use the same SDDs.

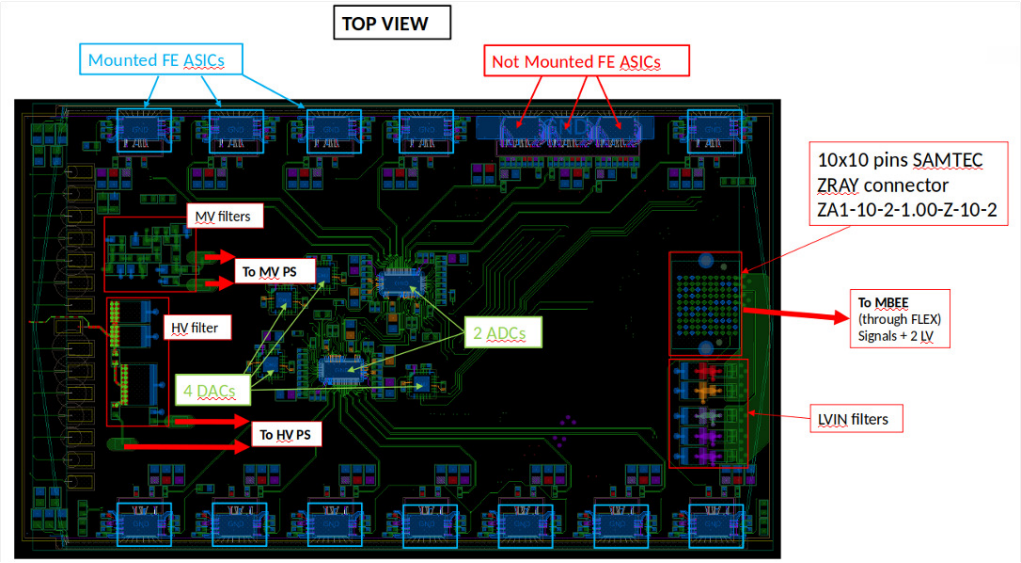

Figure C.3: Layout of the LAD FEE (from Yannick Favre).

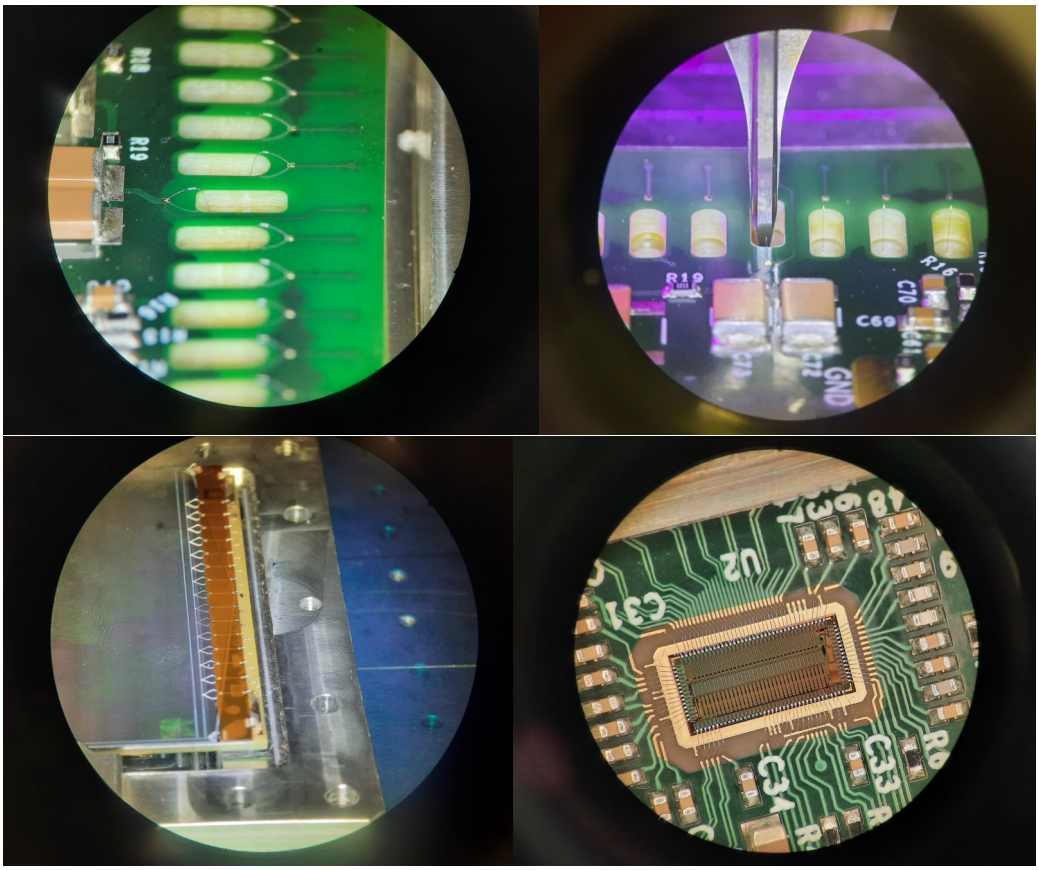

Figure C.4: Microscope pictures of the bonding process for a LAD FEE (by Gabriel Pelleriti).

The current development FEE is composed of 14 IDeF-X ASICs and 2 OWB-1 ADCs from CEA. The final flight model design will use a new generation of IDeF-X ASIC, allowing a more compact design to read out all the lines from the SDD using 28 ASICs. The current FEE already has a spot to host the final design of the ASIC as soon as its development is over (see top right corner of Figure C.3). The Medium and High Voltages (MV/HV) are provided through cables soldered on the FEE, while the signals and Low Voltage (LV) go through a Z-Ray connector from Samtec. The assembly of the LAD modules is highly complex, and a dedicated procedure was developed at DPNC [112, 195]. The details of the procedure are shown in Figure C.5. Challenging parts of the assembly are the very precise mechanical alignment of the pieces and the necessity of bonding many components on different sides of the detector. Pictures from the preliminary bonding tests are shown in Figure C.4.

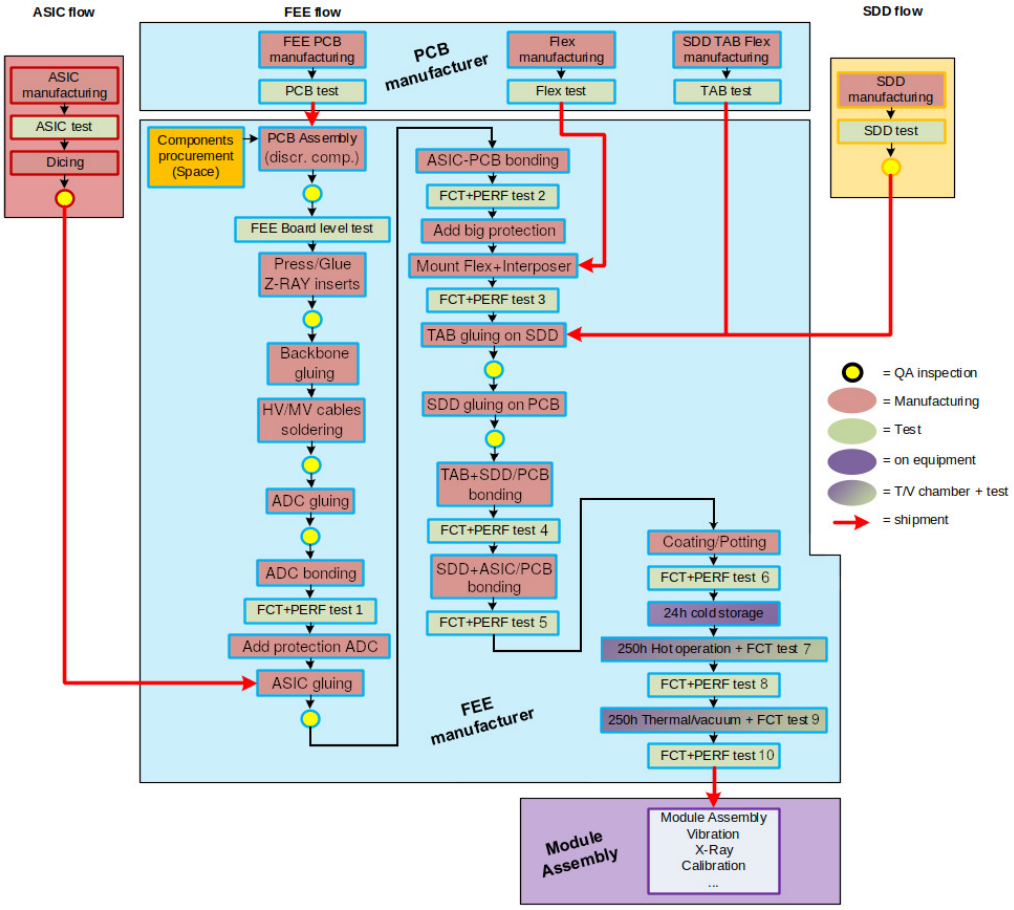

Figure C.5: Chart showing the detailed step for the LAD detector assembly.

Because of the wide temperature range at which the LAD should operate, the CTE (Coefficient of Thermal Expansion) mismatch between different parts of the detector, e.g. the FR4 PCB and SDD, could cause mechanical damages to the detector or could impact its scientific performances. An assembled dummy module was thermal cycled at the CERN Quality Assurance and Reliability Testing (QART) Lab in order to qualify its mechanical properties at extreme temperatures required for eXTP. The module is shown in the thermal chamber

in Figure C.6 together with thermo-mechanical simulations of the deformation caused by a temperature variation of 100°C.

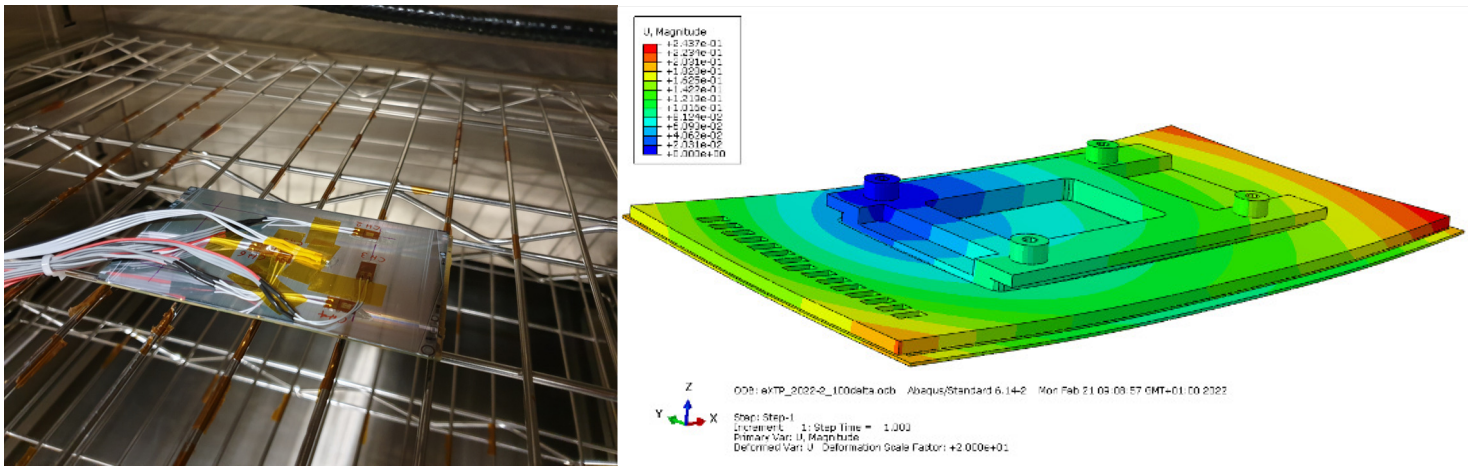

Figure C.6: **Left:** A LAD prototype module equipped with strain gauges in a thermal chamber at the CERN Qart lab. **Right:** Finite Element Analysis of the mechanical constraints applied on the LAD module for $\Delta T = -100°C$ (from Franck Cadoux).

Strain gauges were placed at different locations on the prototype in order to monitor the mechanical deformation as a function of temperature. The module was exposed to a total of 11 cycles between 50 and -70°C, with two PT1000 sensors to monitor the temperature. The strain and temperature measured during a cycle are plotted in Figure C.7. The design of the module was qualified for the required temperature range and the data from the test were used to validate the finite element analysis.

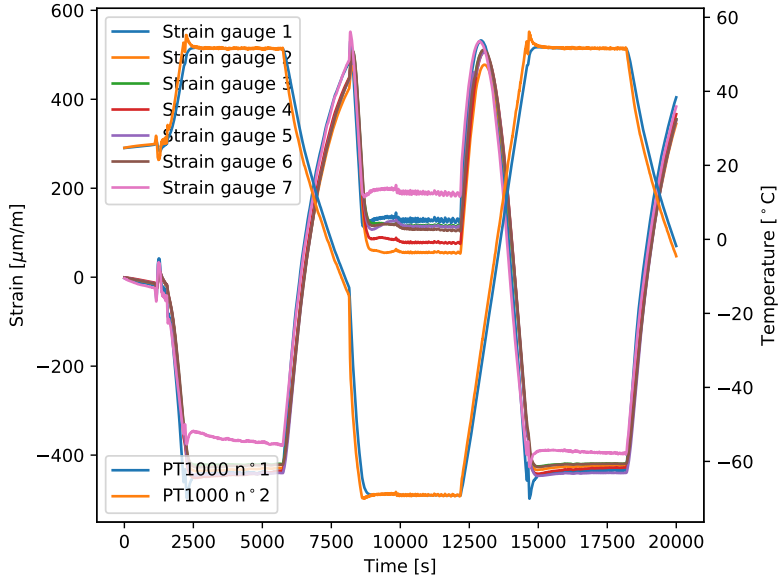

Figure C.7: Deformation and temperature measured by the strain gauges and PT1000 placed on the module for a single cycle.

D

OPTICAL SIMULATION APPLICATION TO OTHER INSTRUMENTS: THE LEAP DETECTOR MODULE

D.1 THE LARGE AREA BURST POLARIMETER

Based on the legacy of the Gamma RAy Polarimeter Experiment (GRAPE) experiment [23, 24], who successfully flew in 2011 and 2014 on balloon flights, the LargE Area Burst Polarimeter (LEAP) mission is under development [162, 164, 169]. Lead by the University of New Hampshire (US), the LEAP mission is proposed for a launch to the International Space Station (ISS) in 2027. The overall detector design and proposed location on the ISS are pictured in Figure D.1. As its predecessor mission, it is a dual-phase Compton polarimeter.

Unlike POLAR and POLAR-2, which are single-phase polarimeters, LEAP uses two different materials for scattering and absorption

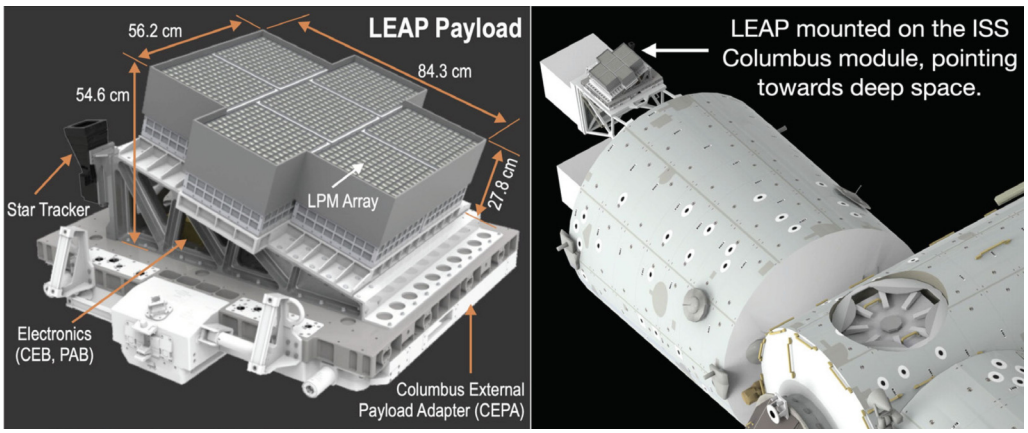

Figure D.1: **Left:** LEAP payload design. [169] **Right:** Location of the LEAP instrument on the Columbus module of the ISS. [169]

The instrument is divided into 7 modules each consisting of a 12×12 array of scintillators. Each segment of this array, called a Polarimeter Detector Element (PDE), is composed of a 17×17×100 mm^3 scintillator bar read out by an R9880U PhotoMultiplier Tube (PMT) from Hamamatsu, wrapped with Vikuiti, and individually encapsulated in a mechanical housing. A highly reflective Teflon mechanical piece is responsible for adapting the scintillator to the PMT, the optical coupling between the latter two is achieved using a 1 mm thick DC93-500 optical pad. The scintillator material can either be plastic or Cesium Iodide (CsI). A picture of a plastic based PDE as well as the distribution of plastic and CsI bars within a module are presented in Figure D.2. The detection principle is that a photon Compton scatters in a plastic bar, in which Compton scattering cross section is optimum down to a few keV due to the low-Z nature of the material, and is then ideally entirely absorbed in a CsI scintillator, leading to a smaller energy spread in the spectral response of the instrument than for a single phase polarimeter.

To not be mixed with Photo Detection Efficiency, not used in this Chapter.

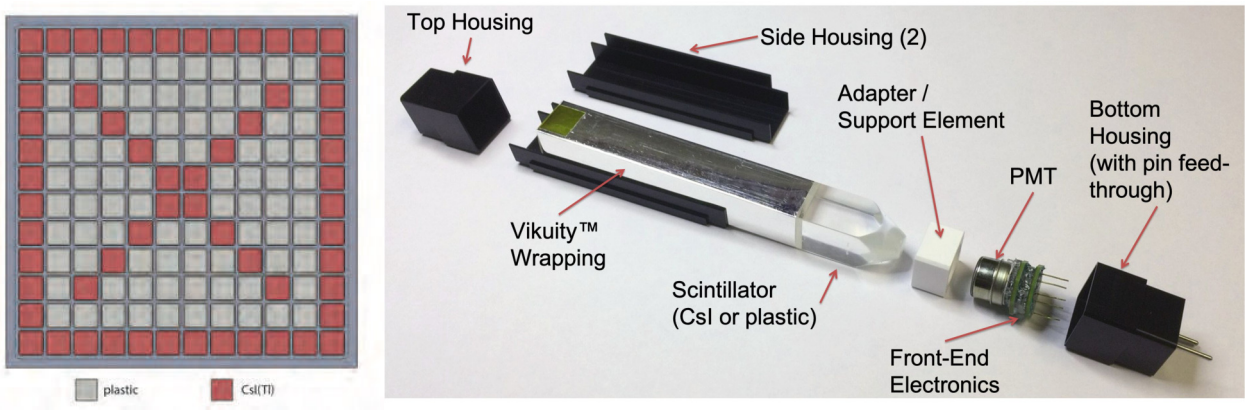

Figure D.2: **Left:** Layout of a 12×12 LEAP module showing the distribution of plastic and CsI scintillators. [164] **Right:** Picture of an exploded Polarimeter Detector Element prototype. [169]

D.2 OPTICAL SIMULATIONS OF THE LEAP POLARIMETER DETECTOR ELEMENT

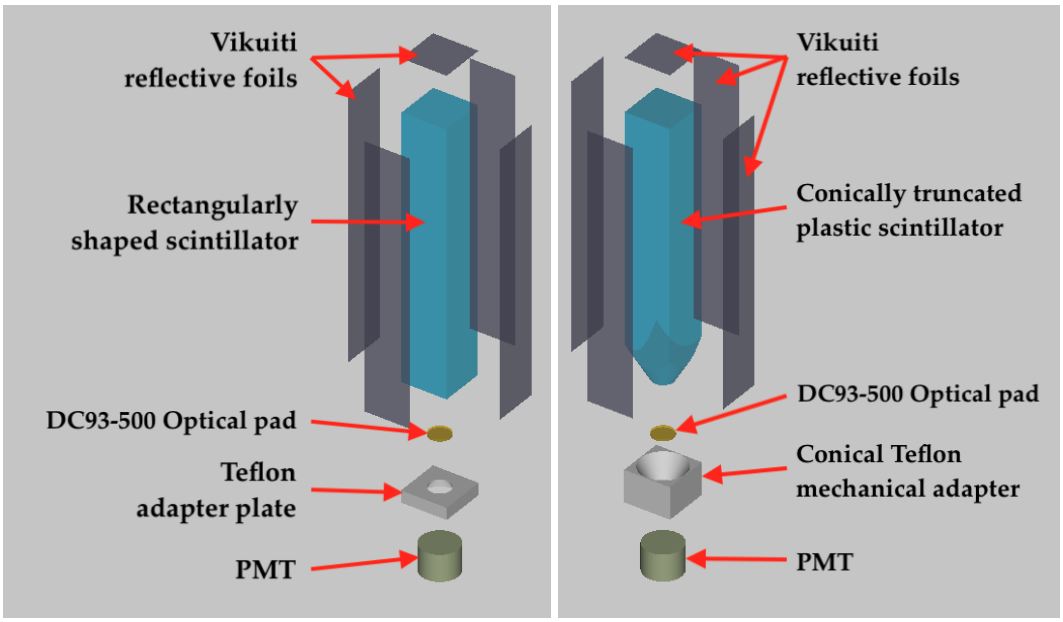

Figure D.3: **Left:** Geometry of the modified PDE removing the conical truncation in the scintillator design. **Right:** Implementation of the original LEAP PDE design in the Geant4 optical simulations.

As depicted in Figure D.2, the original LEAP PDE design a truncated scintillator, with one end of the bar going from the square 17×17 mm^2 down to the circular 8 mm diameter shape of the PMT entrance. As this truncation cannot increase the light output based on phase space conservation (application of the Liouville theorem), the POLAR-2 optical simulations described in Chapter 7 are applied to the LEAP design in order to compare the optical efficiency of the original design with a non-tapered bar. A non-tapered bar would simplify the mechanical design of the PDE and greatly reduce the cost of the scintillators.

Both EJ-200 and EJ-248M materials are investigated as the shape and roughness of the scintillator has shown to have a significant impact on the light output (see Chapter 7). Both PDE designs are shown in Figure D.3.

The simulated light output maps for the technical attenuation length (that accounts for the scintillator shape and surface quality, see Chapter 7 and Figure 7.24 for details) are given in the height-roughness space in Figure D.4 for both designs and with both types of plastic. It can be noticed that the light output is dropping faster near the PMT for a conically tapered bar.

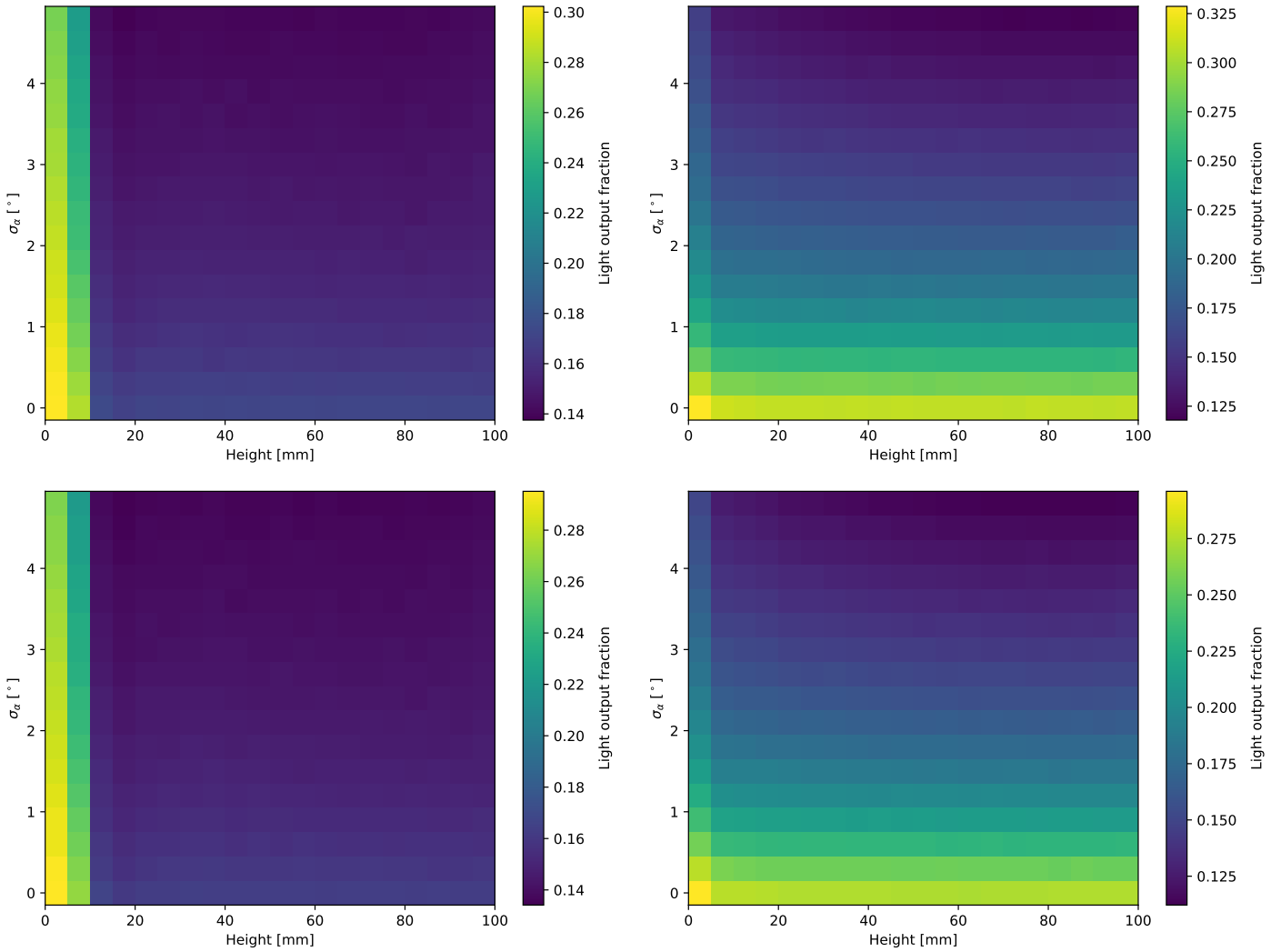

Figure D.4: Light output map in the height-roughness space simulated for a conically truncated scintillator (**left**) and a simplified rectangular scintillator (**right**) for both EJ-200 (**top**) and EJ-248M (**bottom**) plastic.

The light yield measurements with PDE prototypes take place at University of New Hampshire, USA. A ^{109}Cd is placed at the top of the scintillator bar. The decay of Cadmium into Silver leads to an emission line at 22 keV, corresponding to the K-level of ^{109}Ag. This 22 keV peak is used in order to measure the light yield of the PDE. The penetration profile of 22 keV photons into the plastic

scintillator was therefore simulated and fitted with an exponential, as shown in Figure D.5.

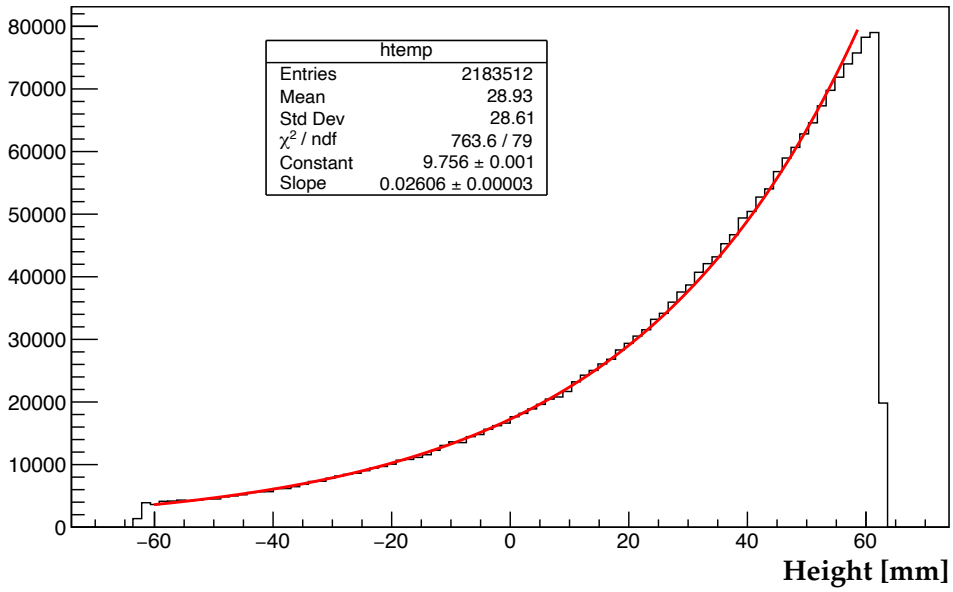

Figure D.5: Simulated penetration profile of 22 keV photons in the plastic scintillator.

The maps in Figure D.4 can be convoluted with the profile of Figure D.5 in order to get the light output as a function of the roughness of the scintillator surface. As the σ_α value is known for both EJ-200 and EJ-248M (see Chapter 7), the light output value for both types of plastics can be extracted for both geometries. The resulting light output fractions from the optical simulations are summarized in Table D.1. As for POLAR-2, the light output is lower with EJ-200 because of its rougher surface which counter-balances the higher scintillation efficiency. The conical tapering slightly improves the light output for EJ-200, but removing the tapering gives much better performances for EJ-248M. The light output is 24.6 % higher for a non-tapered EJ-248M bar than for a tapered EJ-200 bar. Even though the scintillation efficiency for EJ-200 is 8.7 % higher than for EJ-248M, the non-tapered EJ-248M design will therefore lead to the best light yield. These simulations result still have to be verified through lab measurements, which will lead the decision on whether to use the tapering and on the choice of the scintillating material. Removing the tapering is not only a way of improving the optical performances of the system, but will also significantly reduce the cost of the scintillators.

	EJ-200	EJ-248M
Conically tapered bar	14.21±0.04%	14.40±0.04%
Square bar	13.85±0.04%	17.71±0.04%

Table D.1: Light output fraction obtained with the LEAP design for a 22 keV source for both EJ-200 and EJ-248M with both scintillator designs.

BIBLIOGRAPHY

[1] "3ML online documentation." Last consulted in May 2023. URL: https://threeml.readthedocs.io/en/stable/index.html.

[2] Q. Abarr et al. "Performance of the X-Calibur hard X-ray polarimetry mission during its 2018/19 long-duration balloon flight." In: *Astroparticle Physics* 143 (2022), p. 102749. DOI: 10.1016/j.astropartphys.2022.102749.

[3] B. P. Abbott et al. "GW170817: Observation of Gravitational Waves from a Binary Neutron Star Inspiral." In: *Phys. Rev. Lett.* 119 (16 2017), p. 161101. DOI: 10.1103/PhysRevLett.119.161101.

[4] B. P. Abbott et al. "Gravitational Waves and Gamma-Rays from a Binary Neutron Star Merger: GW170817 and GRB 170817A." In: *The Astrophysical Journal Letters* 848.2 (2017), p. L13. DOI: 10.3847/2041-8213/aa920c.

[5] V. A. Acciari et al. "Observation of inverse Compton emission from a long γ-ray burst." In: *Nature* 575.7783 (2019), pp. 459–463. DOI: 10.1038/s41586-019-1754-6.

[6] S. Agostinelli et al. "Geant4—a simulation toolkit." In: *Nuclear Instruments and Methods in Physics Research Section A: Accelerators, Spectrometers, Detectors and Associated Equipment* 506.3 (2003), pp. 250–303. DOI: 10.1016/S0168-9002(03)01368-8.

[7] R. Aloisio et al. "The Terzina instrument on board the NUSES space mission." In: *PoS* ICRC2023 (2023), p. 391. DOI: 10.22323/1.444.0391.

[8] Nicolas De Angelis et al. "Energy-resolved polarization analysis of Gamma-Ray Bursts' prompt emission with the POLAR and POLAR-2 instruments." *In preparation*. 2023.

[9] Pierre Auger. "Sur les rayons β secondaires produits dans un gaz par des rayons X." In: *CR Acad. Sci.(F)* 177 (1923), p. 169.

[10] A. Bacelj, N. De Angelis, A. Elwertowska, M. Kole, T. Kowalski, G. Koziol, H. Li, N. Produit, J. Sun, and K. Zezulinski. *Final Calibration Measurements of the Space Based Gamma-Ray Detector POLAR-2 using Synchrotron Radiation [Data set]. European Synchrotron Radiation Facility.* 2026. DOI: 10.15151/ESRF-ES-1092783487.

[11] Suman Bala et al. *Prospects of measuring Gamma-ray Burst Polarisation with the Daksha mission*. 2023. arXiv: 2306.16781 [astro-ph.IM].

[12] Cosimo Bambi and Andrea Santangelo. *Handbook of X-ray and Gamma-ray Astrophysics*. Springer Singapore, 2022. DOI: 10.1007/978-981-16-4544-0.

[13] D. Band et al. "BATSE Observations of Gamma-Ray Burst Spectra. I. Spectral Diversity." In: *The Astrophysical Journal* 413 (1993), p. 281. DOI: 10.1086/172995.

[14] S. D. Barthelmy et al. "An origin for short γ-ray bursts unassociated with current star formation." In: *Nature* 438.7070 (2005), pp. 994–996. DOI: 10.1038/nature04392.

[15] D. Bernard. "HARPO, a gas TPC active target for high-performance γ-ray astronomy; demonstration of the polarimetry of MeV γ-rays converting to e+e- pair." In: *Nuclear Instruments and Methods in Physics Research Section A: Accelerators, Spectrometers, Detectors and Associated Equipment* 936 (2019), pp. 405–407. DOI: 10.1016/j.nima.2018.10.016.

[16] D. Bernard. "MeV-GeV polarimetry with $\gamma \rightarrow$e+e-: Asserting the performance of silicon strip detectors-based telescopes." In: *Nuclear Instruments and Methods in Physics Research Section A: Accelerators, Spectrometers, Detectors and Associated Equipment* 1042 (2022), p. 167462. ISSN: 0168-9002. DOI: 10.1016/j.nima.2022.167462.

[17] V. Bhalerao et al. "The Cadmium Zinc Telluride Imager on AstroSat." In: *Journal of Astrophysics and Astronomy* 38.2 (2017), p. 31.

[18] Varun Bhalerao et al. "Science with the Daksha High Energy Transients Mission." 2022. URL: https://arxiv.org/abs/2211.12052.

[19] J. B. Birks. "Scintillations from Organic Crystals: Specific Fluorescence and Relative Response to Different Radiations." In: 64.10 (1951), pp. 874–877. DOI: 10.1088/0370-1298/64/10/303.

[20] J. B. Birks. *The Theory and Practice of Scintillation Counting*. Pergamon, 1964. DOI: 10.1016/C2013-0-01791-4.

[21] J K Black. "TPCs in high-energy astronomical polarimetry." In: *Journal of Physics: Conference Series* 65.1 (2007), p. 012005. DOI: 10.1088/1742-6596/65/1/012005.

[22] J. S. Bloom et al. "Closing in on a Short-Hard Burst Progenitor: Constraints from Early-Time Optical Imaging and Spectroscopy of a Possible Host Galaxy of GRB 050509b." In: *The Astrophysical Journal* 638.1 (2006), p. 354. DOI: 10.1086/498107.

[23] P. F. Bloser, J. S. Legere, J. R. Macri, M. L. McConnell, T. Narita, and J. M. Ryan. "GRAPE - A Balloon-Borne Gamma-Ray Polarimeter Experiment." In: *Chinese Journal of Astronomy and Astrophysics* 6.S1 (2006), p. 393. DOI: 10.1088/1009-9271/6/S1/54.

[24] P.F. Bloser, J.S. Legere, M.L. McConnell, J.R. Macri, C.M. Bancroft, T.P. Connor, and J.M. Ryan. "Calibration of the Gamma-RAy Polarimeter Experiment (GRAPE) at a polarized hard X-ray beam." In: *Nuclear Instruments and Methods in Physics Research Section A: Accelerators, Spectrometers, Detectors and Associated Equipment* 600.2 (2009), pp. 424–433. DOI: 10.1016/j.nima.2008.11.118.

[25] Bosnjak, Z., Götz, D., Bouchet, L., Schanne, S., and Cordier, B. "The spectral catalogue of INTEGRAL gamma-ray bursts - results of the joint IBIS/SPI spectral analysis." In: *A&A* 561 (2014), A25. DOI: 10.1051/0004-6361/201322256.

[26] Burgess, J. M., Kole, M., Berlato, F., Greiner, J., Vianello, G., Produit, N., Li, Z. H., and Sun, J. C. "Time-resolved GRB polarization with POLAR and GBM - Simultaneous spectral and polarization analysis with synchrotron emission." In: *A&A* 627 (2019), A105. DOI: 10.1051/0004-6361/201935056.

[27] J. Michael Burgess, Damien Bégué, Jochen Greiner, Dimitrios Giannios, Ana Bacelj, and Francesco Berlato. "Gamma-ray bursts as cool synchrotron sources." In: *Nature Astronomy* 4.2 (2020), pp. 174–179. DOI: 10.1038/s41550-019-0911-z.

[28] Burlon, D., Ghirlanda, G., Ghisellini, G., Greiner, J., and Celotti, A. "Time resolved spectral behavior of bright BATSE precursors*." In: *A&A* 505.2 (2009), pp. 569–575. DOI: 10.1051/0004-6361/200912662.

[29] "CITIROC-1A ASIC datasheet." December 2019. URL: https://www.weeroc.com/products/sipm-read-out/citiroc-1a.

[30] J. Tomsick on behalf of the COSI collaboration. "The Compton Spectrometer and Imager Project for MeV Astronomy." In: *PoS* ICRC2021 (2021), p. 652. DOI: 10.22323/1.395.0652.

[31] "Cadence OrCAD PSpice website." Last consulted in July 2023. URL: https://www.orcad.com/pspice.

[32] Regina Caputo et al. "All-sky Medium Energy Gamma-ray Observatory eXplorer mission concept." In: *Journal of Astronomical Telescopes, Instruments, and Systems* 8.4 (2022), p. 044003. DOI: 10.1117/1.JATIS.8.4.044003.

[33] Tanmoy Chattopadhyay et al. "Hard X-Ray Polarization Catalog for a Five-year Sample of Gamma-Ray Bursts Using AstroSat CZT Imager." In: *The Astrophysical Journal* 936.1 (2022), p. 12. DOI: 10.3847/1538-4357/ac82ef.

[34] Tanmoy Chattopadhyay et al. "Prompt Emission Polarimetry of Gamma-Ray Bursts with the AstroSat CZT Imager." In: *The Astrophysical Journal* 884.2 (2019), p. 123. DOI: 10.3847/1538-4357/ab40b7.

[35] M. Chauvin, M. Jackson, T. Kawano, M. Kiss, M. Kole, V. Mikhalev, E. Moretti, H. Takahashi, and M. Pearce. "Optimising a balloon-borne polarimeter in the hard X-ray domain: From the PoGOLite Pathfinder to PoGO+." In: *Astroparticle Physics* 82 (2016), pp. 99–107. DOI: 10.1016/j.astropartphys.2016.06.005.

[36] A Chilingarov, H Feick, E Fretwurst, G Lindström, S Roe, and T Schulz. "Radiation studies and operational projections for silicon in the ATLAS inner detector." In: *Nuclear Instruments and Methods in Physics Research Section A: Accelerators, Spectrometers, Detectors and Associated Equipment* 360.1 (1995). Proceedings of the Sixth Pisa Meeting on Advanced Detectors, pp. 432–437. DOI: 10.1016/0168-9002(95)00110-7.

[37] T. L. Cline, U. D. Desai, R. W. Klebesadel, and I. B. Strong. "Energy Spectra of Cosmic Gamma-Ray Bursts." In: *Astrophysical Journal* 185 (1973), p. L1. DOI: 10.1086/181309.

[38] Wayne Coburn and Steven E. Boggs. "Polarization of the prompt γ-ray emission from the γ-ray burst of 6 December 2002." In: *Nature* 423.6938 (2003), pp. 415–417. DOI: 10.1038/nature01612.

[39] Edward Collett. "Field guide to polarization." In: Spie Bellingham, WA. 2005. DOI: 10.1117/3.626141.

[40] Arthur Holly Compton and Samuel King Allison. *X-rays in theory and experiment*. New York: D. Van Nostrand Company, Inc New York, 1935. Chap. xiv, 828 pages illustrations 24 cm.

[41] Paul Coppin, Krijn D. de Vries, and Nick van Eijndhoven. "Identification of gamma-ray burst precursors in Fermi-GBM bursts." In: *Phys. Rev. D* 102 (10 2020), p. 103014. DOI: 10.1103/PhysRevD.102.103014.

[42] J. W. Corbett. "Electron-Radiation Damage in Semiconductors and Metals." In: *Academic, New York (edited by F. Seitz and D. Turnbull)* (1966), p. 39.

[43] M. Cordelli, E. Diociaiuti, A. Ferrari, S. Miscetti, S. Müller, G. Pezzullo, and I. Sarra. "An induced annealing technique for SiPMs neutron radiation damage." In: *Journal of Instrumentation* 16.12 (2021), T12012. DOI: 10.1088/1748-0221/16/12/T12012.

[44] F. Corsi, A. Dragone, C. Marzocca, A. Del Guerra, P. Delizia, N. Dinu, C. Piemonte, M. Boscardin, and G.F. Dalla Betta. "Modelling a silicon photomultiplier (SiPM) as a signal source for optimum front-end design." In: *Nuclear Instruments and Methods in Physics Research Section A: Accelerators, Spectrometers, Detectors and Associated Equipment* 572.1 (2007), pp. 416–418. DOI: 10.1016/j.nima.2006.10.219.

[45] F. Corsi et al. "Electrical Characterization of Silicon Photo-Multiplier Detectors for Optimal Front-End Design." In: *2006 IEEE Nuclear Science Symposium Conference Record*. Vol. 2. 2006, pp. 1276–1280. DOI: 10.1109/NSSMIC.2006.356076.

[46] E. Costa et al. "Discovery of an X-ray afterglow associated with the γ-ray burst of 28 February 1997." In: *Nature* 387.6635 (1997), pp. 783–785. DOI: 10.1038/42885.

[47] Enrico Costa, Paolo Soffitta, Ronaldo Bellazzini, Alessandro Brez, Nicholas Lumb, and Gloria Spandre. "An efficient photoelectric X-ray polarimeter for the study of black holes and neutron stars." In: *Nature* 411.6838 (2001), pp. 662–665. DOI: 10.1038/35079508.

[48] E. J. Daly. "Radiation environment evaluation for ESA projects." In: *AIP Conference Proceedings* 186.1 (May 1989), pp. 483–499. ISSN: 0094-243X. DOI: 10.1063/1.38166.

[49] A. De Angelis et al. "Science with e-ASTROGAM: A space mission for MeV–GeV gamma-ray astrophysics." In: *Journal of High Energy Astrophysics* 19 (2018), pp. 1–106. DOI: 10.1016/j.jheap.2018.07.001.

[50] A. De Angelis et al. "The e-ASTROGAM mission." In: *Experimental Astronomy* 44.1 (2017), pp. 25–82. DOI: 10.1007/s10686-017-9533-6.

[51] N. De Angelis et al. "Temperature dependence of radiation damage annealing of Silicon Photomultipliers." In: *Nuclear Instruments and Methods in Physics Research Section A: Accelerators, Spectrometers, Detectors and Associated Equipment* 1048 (2023), p. 167934. DOI: 10.1016/j.nima.2022.167934.

[52] Nicolas De Angelis. "High Voltage Power Supply Chip Irradiation - POLAR-2 Technical Note." *Internal document, available upon request*. December 2020.

[53] Nicolas De Angelis. "Polarimeter module assembly procedure - POLAR-2 Technical Note." *Internal document, available upon request*. March 2023.

[54] Nicolas De Angelis. "Reflective Foils Characterisation for Scintillators Wrapping - POLAR-2 Technical Note." *Internal document, available upon request*. March 2020.

[55] Nicolas De Angelis. "Study of the Hamamatsu S14161 SiPM I-V characteristic for POLAR-2 - POLAR-2 Technical Note." *Internal document, available upon request*. December 2019.

[56] Nicolas De Angelis et al. "Development and science perspectives of the POLAR-2 instrument: a large scale GRB polarimeter." In: *PoS* ICRC2021 (2021), p. 580. DOI: 10.22323/1.395.0580.

[57] Nicolas De Angelis et al. "Energy-dependent polarization of Gamma-Ray Bursts' prompt emission with the POLAR and POLAR-2 instruments." In: *PoS* ICRC2023 (2023), p. 619. DOI: 10.22323/1.444.0619.

[58] De Broglie, Louis. "Recherches sur la théorie des Quanta." In: *Ann. Phys.* 10.3 (1925), pp. 22–128. DOI: 10.1051/anphys/192510030022.

[59] Wei Den, Haocheng Zhang, Bing Zhang, and Hui Li. "COLLISION-INDUCED MAGNETIC RECONNECTION AND A UNIFIED INTERPRETATION OF POLARIZATION PROPERTIES OF GRBs AND BLAZARS." In: *The Astrophysical Journal Letters* 821.1 (2016), p. L12. DOI: 10.3847/2041-8205/821/1/L12.

[60] A. J. Dessler. "The Vernov Radiation Belt (Almost)." In: *Science* 226.4677 (1984), pp. 915–915. DOI: 10.1126/science.226.4677.915.

[61] E. Dietz-Laursonn. *Peculiarities in the simulation of optical physics with GEANT4*. 2016. arXiv: 1612.05162 [physics.ins-det].

[62] Einstein, Albert. "Über einen die Erzeugung und Verwandlung des Lichtes betreffenden heuristischen Gesichtspunkt." In: *Annalen der Physik* 17 (1905), pp. 132–148. URL: 10.1002/andp.19053220607.

[63] "Eljen EJ-200 datasheet." Last consulted in August 2023. URL: https://eljentechnology.com/products/plastic-scintillators/ej-200-ej-204-ej-208-ej-212.

[64] "Eljen EJ-248M datasheet." Last consulted in August 2023. URL: https://eljentechnology.com/products/plastic-scintillators/ej-244-ej-248-ej-244m-ej-248m.

[65] Teruaki Enoto et al. "Performance verification of the Gravity and Extreme Magnetism Small explorer (GEMS) x-ray polarimeter." In: *Space Telescopes and Instrumentation 2014: Ultraviolet to Gamma Ray*. Ed. by Tadayuki Takahashi, Jan-Willem A. den Herder, and Mark Bautz. Vol. 9144. International Society for Optics and Photonics. SPIE, 2014, p. 91444M. DOI: 10.1117/12.2056841.

[66] Sergio Fabiani et al. "CUSP: a two CubeSats constellation for space weather and solar flares x-ray polarimetry." In: *Space Telescopes and Instrumentation 2022: Ultraviolet to Gamma Ray*. Ed. by Jan-Willem A. den Herder, Shouleh Nikzad, and Kazuhiro Nakazawa. Vol. 12181. International Society for Optics and Photonics. SPIE, 2022, 121810J. DOI: 10.1117/12.2629233.

[67] Hua Feng et al. "PolarLight: a CubeSat X-ray polarimeter based on the gas pixel detector." In: *Experimental Astronomy* 47.1 (2019), pp. 225–243. DOI: 10.1007/s10686-019-09625-z.

[68] Huan-Bo Feng, Hong-Bang Liu, Yan-Jun Xie, Zong-Wang Fan, Dong Wang, Shu-Lin Liu, Qian Liu, Hang-Zhou Li, Fei Xie, and En-Wei Liang. "Spectral and polarimetric characterization of the Gas Microchannel plate Pixel Detector." In: *Journal of Instrumentation* 18.08 (2023), P08012. DOI: 10.1088/1748-0221/18/08/P08012.

[69] Marco Feroci et al. "The large area detector onboard the eXTP mission." In: *Space Telescopes and Instrumentation 2022: Ultraviolet to Gamma Ray*. Ed. by Jan-Willem A. den Herder, Shouleh Nikzad, and Kazuhiro Nakazawa. Vol. 12181. International Society for Optics and Photonics. SPIE, 2022, p. 121811X. DOI: 10.1117/12.2628814.

[70] Henrike Fleischhack. *AMEGO-X: MeV gamma-ray Astronomy in the Multi-messenger Era*. 2021. arXiv: 2108.02860 [astro-ph.IM].

[71] D. A. Frail, S. R. Kulkarni, L. Nicastro, M. Feroci, and G. B. Taylor. "The radio afterglow from the γ-ray burst of 8 May 1997." In: *Nature* 389.6648 (1997), pp. 261–263. DOI: 10.1038/38451.

[72] Z. Francis, S. Incerti, M. Karamitros, H.N. Tran, and C. Villagrasa. "Stopping power and ranges of electrons, protons and alpha particles in liquid water using the Geant4-DNA package." In: *Nuclear Instruments and Methods in Physics Research Section B: Beam Interactions with Materials and Atoms* 269.20 (2011). 12th International Conference on Nuclear Microprobe Technology and Applications, pp. 2307–2311. DOI: 10.1016/j.nimb.2011.02.031.

[73] A. S. Fruchter et al. "Long γ-ray bursts and core-collapse supernovae have different environments." In: *Nature* 441.7092 (2006), pp. 463–468. DOI: 10.1038/nature04787.

[74] E.S. Gadelmawla, M.M. Koura, T.M.A. Maksoud, I.M. Elewa, and H.H. Soliman. "Roughness parameters." In: *Journal of Materials Processing Technology* 123.1 (2002), pp. 133–145. DOI: 10.1016/S0924-0136(02)00060-2.

[75] T. J. Galama et al. "An unusual supernova in the error box of the γ-ray burst of 25 April 1998." In: *Nature* 395.6703 (1998), pp. 670–672. DOI: 10.1038/27150.

[76] "Gamma-Ray Bursts - Talk by Daisuke Yonetoku." January 2018. URL: https://www.lowbg.org/ugnd/workshop/groupC/sn20180108/files/0804_Yonetoku.pdf.

[77] He Gao and Peter Mészáros. "Reverse Shock Emission in Gamma-Ray Bursts Revisited." In: *Advances in Astronomy* (2015), p. 192383. DOI: 10.1155/2015/192383.

[78] E. Garutti and Yu. Musienko. "Radiation damage of SiPMs." In: *Nuclear Instruments and Methods in Physics Research Section A: Accelerators, Spectrometers, Detectors and Associated Equipment* 926 (2019). Silicon Photomultipliers: Technology, Characterisation and Applications, pp. 69–84. ISSN: 0168-9002. DOI: 10.1016/j.nima.2018.10.191.

[79] N. Gehrels et al. "A new γ-ray burst classification scheme from GRB 060614." In: *Nature* 444.7122 (2006), pp. 1044–1046. DOI: 10.1038/nature05376.

[80] N. Gehrels et al. "A short γ-ray burst apparently associated with an elliptical galaxy at redshift z = 0.225." In: *Nature* 437.7060 (2005), pp. 851–854. DOI: 10.1038/nature04142.

[81] Ramandeep Gill and Jonathan Granot. *Prompt GRB Polarization from Non-Axisymmetric Jets*. 2023. arXiv: 2310.01357 [astro-ph.HE].

[82] Ramandeep Gill and Jonathan Granot. "Temporal evolution of prompt GRB polarization." In: *Monthly Notices of the Royal Astronomical Society* 504.2 (Apr. 2021), pp. 1939–1958. ISSN: 0035-8711. DOI: 10.1093/mnras/stab1013.

[83] Ramandeep Gill, Jonathan Granot, and Pawan Kumar. "Linear polarization in gamma-ray burst prompt emission." In: *Monthly Notices of the Royal Astronomical Society* 491.3 (Oct. 2019), pp. 3343–3373. DOI: 10.1093/mnras/stz2976.

[84] Ramandeep Gill, Merlin Kole, and Jonathan Granot. "GRB Polarization: A Unique Probe of GRB Physics." In: *Galaxies* 9.4 (2021). DOI: 10.3390/galaxies9040082.

[85] S. V. Golenetskii, E. P. Mazets, R. L. Aptekar, and V. N. Ilyinskii. "Correlation between luminosity and temperature in γ-ray burst sources." In: *Nature* 306.5942 (1983), pp. 451–453. DOI: 10.1038/306451a0.

[86] J. Goodman. "Are gamma-ray bursts optically thick?" In: *The Astrophysical Journal* 308 (Sept. 1986), p. L47. DOI: 10.1086/184741.

[87] J. Greiner et al. "GRB 080913 AT REDSHIFT 6.7." In: *The Astrophysical Journal* 693.2 (2009), p. 1610. DOI: 10.1088/0004-637X/693/2/1610.

[88] J.E. Grove et al. *Glowbug, a Low-Cost, High-Sensitivity Gamma-Ray Burst Telescope*. 2020. arXiv: 2009.11959 [astro-ph.iM].

[89] O. Guillaumon, S. Remaury, P. Nabarra, P. Guigue-Joguet, and H. Combes. "DEVELOPMENT OF A NEW SILICONE ADHESIVE FOR SPACE USE: MAPSIL®QS 1123." URL: http://esmat.esa.int/materials_news/isme09/pdf/4-New/S7%20-%20Guillaumon.pdf.

[90] D. Götz, S. Covino, A. Fernández-Soto, P. Laurent, and Ž. Bošnjak. "The polarized gamma-ray burst GRB 061122." In: *Monthly Notices of the Royal Astronomical Society* 431.4 (Apr. 2013), pp. 3550–3556. DOI: 10.1093/mnras/stt439.

[91] D. Götz, P. Laurent, S. Antier, S. Covino, P. D'Avanzo, V. D'Elia, and A. Melandri. "GRB 140206A: the most distant polarized gamma-ray burst." In: *Monthly Notices of the Royal Astronomical Society* 444.3 (Sept. 2014), pp. 2776–2782. DOI: 10.1093/mnras/stu1634.

[92] Diego Götz, Philippe Laurent, François Lebrun, Frédéric Daigne, and Željka Bošnjak. "VARIABLE POLARIZATION MEASURED IN THE PROMPT EMISSION OF GRB 041219A USING IBIS ON BOARD INTEGRAL." In: *The Astrophysical Journal* 695.2 (2009), p. L208. DOI: 10.1088/0004-637X/695/2/L208.

[93] "Hamamatsu datasheet - S13360 series." October 2022. URL: https://www.hamamatsu.com/jp/en/product/optical-sensors/mppc/mppc_mppc-array.html.

[94] "Hamamatsu datasheet - S13361-6050." May 2022. URL: https://www.hamamatsu.com/jp/en/product/optical-sensors/mppc/mppc_mppc-array.html.

[95] "Hamamatsu datasheet - S14160/S14161 series." June 2020. URL: https://www.hamamatsu.com/jp/en/product/optical-sensors/mppc/mppc_mppc-array.html.

[96] Zachary Harvey. "Neutron flux and energy characterization of a plutonium-beryllium isotopic neutron source by monte carlo simulation with verification by neutron activation analysis." In: (Jan. 2010).

[97] G. Hass and J. E. Waylonis. "Optical Constants and Reflectance and Transmittance of Evaporated Aluminum in the Visible and Ultraviolet*." In: *J. Opt. Soc. Am.* 51.7 (1961), pp. 719–722. DOI: 10.1364/JOSA.51.000719.

[98] M. Hernanz et al. *The Wide Field Monitor onboard the eXTP mission*. 2018. arXiv: 1807.09330 [astro-ph.IM].

[99] "High Performance LAMBDA Spectrometer Accessories - datasheet." Last consulted in January 2021. URL: http://perkinelmer.com.

[100] Jens Hjorth and Joshua S. Bloom. *The Gamma-Ray Burst - Supernova Connection*. 2011. arXiv: 1104.2274 [astro-ph.HE].

[101] Jens Hjorth et al. "A very energetic supernova associated with the γ-ray burst of 29 March 2003." In: *Nature* 423.6942 (2003), pp. 847–850. DOI: 10.1038/nature01750.

[102] Jens Hjorth et al. "The optical afterglow of the short γ-ray burst GRB 050709." In: *Nature* 437.7060 (2005), pp. 859–861. DOI: 10.1038/nature04174.

[103] Frank Hönniger. "Radiation Damage in Silicon - Defect Analysis and Detector Properties." PhD thesis. Department Physik der Universität Hamburg, 2007. URL: https://inspirehep.net/files/f1ccf3f290d0ec203961dbdcd962701a.

[104] Y. Htet et al. "Prompt and Accurate GRB Source Localization Aboard the Advanced Particle Astrophysics Telescope (APT) and its Antarctic Demonstrator (ADAPT)." In: *PoS* ICRC2023 (2023), p. 956. DOI: 10.22323/1.444.0956.

[105] Yong Huang, Shicong Hu, Songzhan Chen, Min Zha, Cheng Liu, Zhiguo Yao, Zhen Cao, et al. "LHAASO observed GRB 221009A with more than 5000 VHE photons up to around 18 TeV." In: *GRB Coordinates Network* 32677 (2022), p. 1. URL: https://gcn.nasa.gov/circulars/32677.txt.

[106] Johannes Hulsman. "GOWIN Radiation Dose for POLAR-2 - POLAR-2 Technical Note." *Internal document, available upon request*. May 2020.

[107] Johannes Hulsman. "Proton Irradiation of FEE, LVPS and FPGA - POLAR-2 Technical Note." *Internal document, available upon request*. March 2023.

[108] Johannes Hulsman. "Simulations on the Energy Deposit in a GW1N-LV4 Chip - POLAR-2 Technical Note." *Internal document, available upon request*. March 2020.

[109] Johannes Hulsman, Nicolas De Angelis, Slawmoir Mianowski, et al. "Space Radiation Qualification of POLAR-2 Electronics." *In preparation*. 2024.

[110] Johannes Hulsman and Nicolas De Angelis. "Simulation and measurement of Peltier elements activation - POLAR-2 Technical Note." *Internal document, available upon request*. March 2021.

[111] Stanley D. Hunter. "The advanced energetic pair telescope for gamma-ray polarimetry." In: *Space Telescopes and Instrumentation 2018: Ultraviolet to Gamma Ray*. Ed. by Jan-Willem A. den Herder, Shouleh Nikzad, and Kazuhiro Nakazawa. Vol. 10699. International Society for Optics and Photonics. SPIE, 2018, p. 106992M. DOI: 10.1117/12.2312732.

[112] Coralie Husi. "LAD Assembly report." *Internal document*.

[113] Coralie Husi. "Tests de fabrication de joint optique avec MAPSIL QS1123 THIXO-B." October 2021.

[114] "INNOVATION IN WATER PURIFICATION SYSTEMS WITH UV-C LEDS AND SILICONE OPTICS - François De Buyl." September 2017. URL: https://www.dow.com/documents/en-us/mark-prod-info/11/11-38/11-3860-01-innovation-in-water-purification-systems.pdf?iframe=true.

[115] Hirotaka Ito, Shigehiro Nagataki, Jin Matsumoto, Shiu-Hang Lee, Alexey Tolstov, Jirong Mao, Maria Dainotti, and Akira Mizuta. "SPECTRAL AND POLARIZATION PROPERTIES OF PHOTOSPHERIC EMISSION FROM STRATIFIED JETS." In: *The Astrophysical Journal* 789.2 (2014), p. 159. DOI: 10.1088/0004-637X/789/2/159.

[116] N.K. Iyer et al. "The design and performance of the XL-Calibur anticoincidence shield." In: *Nuclear Instruments and Methods in Physics Research Section A: Accelerators, Spectrometers, Detectors and Associated Equipment* 1048 (2023), p. 167975. DOI: 10.1016/j.nima.2022.167975.

[117] M. Jobin and R. Foschia. "Improving the resolution of interference microscopes." In: *Measurement* 41.8 (2008), pp. 896–903. DOI: 10.1016/j.measurement.2007.12.006.

[118] Marc Jobin, Philippe Passeraub, and Raphael Foschia. "Nanometrology for MEMS: combination of optical interference, atomic force microscopy, and nanoindentor-based actuator." In: *Optical Micro- and Nanometrology in Microsystems Technology*. Vol. 6188. International Society for Optics and Photonics. SPIE, 2006, 61880T. DOI: 0.1117/12.662868.

[119] E. Kalemci, S. E. Boggs, C. Kouveliotou, M. Finger, and M. G. Baring. "Search for Polarization from the Prompt Gamma-Ray Emission of GRB 041219a with SPI on INTEGRAL." In: *The Astrophysical Journal Supplement Series* 169.1 (2007), p. 75. DOI: 10.1086/510676.

[120] Ł. Kapłon. "Technical Attenuation Length Measurement of Plastic Scintillator Strips for the Total-Body J-PET Scanner." In: *IEEE TRANSACTIONS ON NUCLEAR SCIENCE* 67 (2020), pp. 2286–2289. DOI: 10.1109/TNS.2020.3012043.

[121] Ł. Kapłon et al. "Comparative studies of plastic scintillator strips with high technical attenuation length for the total-body J-PET scanner." In: *Nuclear Instruments and Methods in Physics Research Section A: Accelerators, Spectrometers, Detectors and Associated Equipment* 1051 (2023), p. 168186. DOI: 10.1016/j.nima.2023.168186.

[122] Arnas Kazakevičius. "Building of XY table and paint analysis to prove it to be space qualified." *CERN Summer Student Report*. September 2022.

[123] C. Kierans et al. "The 2016 Super Pressure Balloon flight of the Compton Spectrometer and Imager." In: *PoS* ICRC2017 (2017), p. 075. DOI: 10.22323/1.285.0075.

[124] Kitaguchi, Takao, Hayato, Asami, Iwakiri, Wataru, Takeuchi, Yoko, Kubota, Megu, Nishida, Kazuki, Enoto, Teruaki, and Tamagawa, Toru. "Development of the GEM-TPC X-ray Polarimeter with the Scalable Readout System." In: *EPJ Web Conf.* 174 (2018), p. 01015. DOI: 10.1051/epjconf/201817401015.

[125] Ray W. Klebesadel, Ian B. Strong, and Roy A. Olson. "Observations of Gamma-Ray Bursts of Cosmic Origin." In: *Astrophysical Journal* 182 (1973), p. L85. DOI: 10.1086/181225.

[126] O. Klein and Y. Nishina. "Über die Streuung von Strahlung durch freie Elektronen nach der neuen relativistischen Quantendynamik von Dirac." In: *Zeitschrift für Physik* 52.11 (1929), pp. 853–868. DOI: 10.1007/BF01366453.

[127] Glenn F. Knoll. *Radiation Detection and Measurement, 4th Edition*. Wiley, 2015. ISBN: 978-1-119-11299-0.

[128] Kole, M. et al. "The POLAR gamma-ray burst polarization catalog." In: *A&A* 644 (2020), A124. DOI: 10.1051/0004-6361/202037915.

[129] M. Kole et al. "Instrument performance and simulation verification of the POLAR detector." In: *Nuclear Instruments and Methods in Physics Research Section A: Accelerators, Spectrometers, Detectors and Associated Equipment* 872 (2017), pp. 28–40. DOI: 10.1016/j.nima.2017.07.070.

[130] Merlin Kole. "Module level vibration and shock tests MPE - POLAR-2 Technical Note." *Internal document, available upon request*. November 2021.

[131] Merlin Kole. "Scintillator Length Optimization Studies - POLAR-2 Technical Note." *Internal document, available upon request*. January 2020.

[132] Merlin Kole, Nicolas Produit, Dominik Rybka, Nicolas De Angelis, and Johannes Hulsman. "POLAR-2 Technical Design Report." *Last update* December 2022.

[133] Merlin Kole et al. "POLAR-2 module calibration and performances with the ESRF polarized X-ray beam." *Future work*. 2024.

[134] Thomas M. Koshut, Chryssa Kouveliotou, William S. Paciesas, Jan van Paradijs, Geoffrey N. Pendleton, Michael S. Briggs, Gerald J. Fishman, and Charles A. Meegan. "Gamma-Ray Burst Precursor Activity as Observed with BATSE." In: *Astrophysical Journal* 452 (Oct. 1995), p. 145. DOI: 10.1086/176286.

[135] Chryssa Kouveliotou, Charles A. Meegan, Gerald J. Fishman, Narayana P. Bhat, Michael S. Briggs, Thomas M. Koshut, William S. Paciesas, and Geoffrey N. Pendleton. "Identification of Two Classes of Gamma-Ray Bursts." In: *The Astrophysical Journal Letters* 413 (Aug. 1993), p. L101. DOI: 10.1086/186969.

[136] G. Koziol et al. "GCN Circ. 30728." August 2021. URL: https://gcn.gsfc.nasa.gov/gcn3/30728.gcn3.

[137] Andrey Krauklis and Andreas Echtermeyer. "Mechanism of Yellowing: Carbonyl Formation during Hygrothermal Aging in a Common Amine Epoxy." In: *Polymers* 10.9 (2018), p. 1017. ISSN: 2073-4360. DOI: 10.3390/polym10091017.

[138] S. R. Kulkarni, D. A. Frail, M. H. Wieringa, R. D. Ekers, E. M. Sadler, R. M. Wark, J. L. Higdon, E. S. Phinney, and J. S. Bloom. "Radio emission from the unusual supernova 1998bw and its association with the γ-ray burst of 25 April 1998." In: *Nature* 395.6703 (1998), pp. 663–669. DOI: 10.1038/27139.

[139] Shin Kurita et al. *Development of a micro-satellite TSUBAME for X-ray polarimetry of GRBs*. 2015. arXiv: 1503.01975 [astro-ph.IM].

[140] Davide Lazzati, Elena Rossi, Gabriele Ghisellini, and Martin J. Rees. "Compton drag as a mechanism for very high linear polarization in gamma-ray bursts." In: *Monthly Notices of the Royal Astronomical Society* 347.1 (Jan. 2004), pp. L1–L5. ISSN: 0035-8711. DOI: 10.1111/j.1365-2966.2004.07387.x.

[141] Emily M. Levesque et al. "GRB 090426: the environment of a rest-frame 0.35-s gamma-ray burst at a redshift of 2.609." In: *Monthly Notices of the Royal Astronomical Society* 401.2 (2010), pp. 963–972. DOI: 10.1111/j.1365-2966.2009.15733.x.

[142] Hancheng Li et al. "Gamma-ray polarimetry of the Crab pulsar observed by POLAR." In: *Monthly Notices of the Royal Astronomical Society* 512.2 (Feb. 2022), pp. 2827–2840. DOI: 10.1093/mnras/stac522.

[143] Hancheng Li et al. "POLAR measurements of the Crab pulsar." In: *PoS* ICRC2017 (2017), p. 820. DOI: 10.22323/1.301.0820.

[144] Hancheng Li et al. "Phase-resolved gamma-ray spectroscopy of the Crab pulsar observed by POLAR." In: *Journal of High Energy Astrophysics* 24 (2019), pp. 15–22. DOI: 10.1016/j.jheap.2019.10.001.

[145] Hancheng Li et al. "Polarization measurements of the Crab Pulsar with POLAR." In: *PoS* ICRC2021 (2021), p. 585. DOI: 10.22323/1.395.0585.

[146] Hao Li and Bo-Qiang Ma. "Lorentz invariance violation induced threshold anomaly versus very-high energy cosmic photon emission from GRB 221009A." In: *Astroparticle Physics* 148 (2023), p. 102831. ISSN: 0927-6505. DOI: 10.1016/j.astropartphys.2023.102831.

[147] Hui Li and Edward E. Fenimore. "Log-normal Distributions in Gamma-Ray Burst Time Histories." In: *The Astrophysical Journal* 469.2 (1996), p. L115. DOI: 10.1086/310275.

[148] W. Li and M.K. Hudson. "Earth's Van Allen Radiation Belts: From Discovery to the Van Allen Probes Era." In: *Journal of Geophysical Research: Space Physics* 124.11 (2019), pp. 8319–8351. DOI: 10.1029/2018JA025940.

[149] Zhengheng Li. "In-Orbit Calibration and Polarization Analysis for Gamma-Ray Bursts using POLAR Data." PhD thesis. Institute of High Energy Physics, Chinese Academy of Sciences, Beijing, June 2019. URL: http://ir.ihep.ac.cn/handle/311005/284111.

[150] Zhengheng Li et al. "In-orbit instrument performance study and calibration for POLAR polarization measurements." In: *Nuclear Instruments and Methods in Physics Research Section A: Accelerators, Spectrometers, Detectors and Associated Equipment* 900 (2018), pp. 8–24. DOI: 10.1016/j.nima.2018.05.041.

[151] Zhi-Yun Li, Tzihong Chiueh, and Mitchell C. Begelman. "Electromagnetically Driven Relativistic Jets: A Class of Self-similar Solutions." In: *The Astrophyscial Journaé* 394 (Aug. 1992), p. 459. DOI: 10.1086/171597.

[152] A. W. Lowell et al. "Polarimetric Analysis of the Long Duration Gamma-Ray Burst GRB 160530A With the Balloon Borne Compton Spectrometer and Imager." In: *The Astrophysical Journal* 848.2 (2017), p. 119. DOI: 10.3847/1538-4357/aa8ccb.

[153] A. Lowell et al. "Positional calibrations of the germanium double-sided strip detectors for the Compton spectrometer and imager." In: *High Energy, Optical, and Infrared Detectors for Astronomy VII*. Ed. by Andrew D. Holland and James Beletic. Vol. 9915. International Society for Optics and Photonics. SPIE, 2016, 99152H. DOI: 10.1117/12.2233145.

[154] C. Lundman, A. Pe'er, and F. Ryde. "Polarization properties of photospheric emission from relativistic, collimated outflows." In: *Monthly Notices of the Royal Astronomical Society* 440.4 (Apr. 2014), pp. 3292–3308. ISSN: 0035-8711. DOI: 10.1093/mnras/stu457.

[155] Christoffer Lundman, Indrek Vurm, and Andrei M. Beloborodov. "Polarization of Gamma-Ray Bursts in the Dissipative Photosphere Model." In: *The Astrophysical Journal* 856.2 (2018), p. 145. DOI: 10.3847/1538-4357/aab3e8.

[156] Y. E. Lyubarsky. "Transformation of the Poynting flux into kinetic energy in relativistic jets." In: *Monthly Notices of the Royal Astronomical Society* 402.1 (Feb. 2010), pp. 353–361. ISSN: 0035-8711. DOI: 10.1111/j.1365-2966.2009.15877.x.

[157] "MAP space coating website - MAPSIL-QS1132 manufacturer." Last consulted in August 2023. URL: https://www.map-coatings.com.

[158] M.A. Zucker M.J. Berger J.S. Coursey and J. Chang. *ESTAR, PSTAR, and ASTAR: Computer Programs for Calculating Stopping-Power and Range Tables for Electrons, Protons, and Helium Ions*. Version 2.0.1. 2017. DOI: 10.18434/T4NC7P.

[159] E. P. Mazets, S. V. Golenetskii, V. N. Il'inskii, V. N. Panov, R. L. Aptekar, Yu. A. Gur'yan, M. P. Proskura, I. A. Sokolov, Z. Ya. Sokolova, and T. V. Kharitonova. "Catalog of cosmic gamma-ray bursts from the KONUS experiment Pt 3." In: *Astrophysics and Space Science* 80.1 (1981), pp. 85–117. URL: https://adsabs.harvard.edu/full/1981Ap%26SS..80...85M.

[160] EP Mazets, SV Golenetskij, and VN Il'Inskij. "Burst of cosmic gamma-emission from observations on Cosmos 461." In: *Pisma v Zhurnal Eksperimentalnoi i Teoreticheskoi Fiziki* 19 (1974), pp. 126–128.

[161] B. McBreen, K. J. Hurley, R. Long, and L. Metcalfe. "Lognormal distributions in gamma-ray bursts and cosmic lightning." In: *Monthly Notices of the Royal Astronomical Society* 271.3 (Dec. 1994), pp. 662–666. ISSN: 0035-8711. DOI: 10.1093/mnras/271.3.662.

[162] M. McConnell et al. "LEAP — A Large Area Gamma-Ray Burst Polarimeter for the ISS." January 2020. URL: https://ui.adsabs.harvard.edu/abs/2020AAS...23537308M/abstract.

[163] Mark L. McConnell. "High energy polarimetry of prompt GRB emission." In: *New Astronomy Reviews* 76 (2017), pp. 1–21. DOI: 10.1016/j.newar.2016.11.001.

[164] Mark L. McConnell et al. "The LargE Area burst Polarimeter (LEAP) a NASA mission of opportunity for the ISS." In: *UV, X-Ray, and Gamma-Ray Space Instrumentation for Astronomy XXII*. Ed. by Oswald H. Siegmund. Vol. 11821. International Society for Optics and Photonics. SPIE, 2021, 118210P. DOI: 10.1117/12.2594737.

[165] Julie McEnery et al. *All-sky Medium Energy Gamma-ray Observatory: Exploring the Extreme Multimessenger Universe*. 2019. arXiv: 1907.07558 [astro-ph.IM].

[166] McGlynn, S., Clark, D. J., Dean, A. J., Hanlon, L., McBreen, S., Willis, D. R., McBreen, B., Bird, A. J., and Foley, S. "Polarisation studies of the prompt gamma-ray emission from GRB 041219a using the spectrometer aboard INTEGRAL*." In: *A&A* 466.3 (2007), pp. 895–904. DOI: 10.1051/0004-6361:20066179.

[167] McGlynn, S., Foley, S., McBreen, B., Hanlon, L., McBreen, S., Clark, D. J., Dean, A. J., Martin-Carrillo, A., and O'Connor, R. "High energy emission and polarisation limits for the INTEGRAL burst GRB122 *." In: *A&A* 499.2 (2009), pp. 465–472. DOI: 10.1051/0004-6361/200810920.

[168] Lise Meitner. "Über die β-Strahl-Spektra und ihren Zusammenhang mit der γ-Strahlung." In: *Zeitschrift für Physik* 11.1 (1922), pp. 35–54. DOI: 10.1007/BF01328399.

[169] Karla Oñate Melecio et al. "Evaluation of a prototype detector for the LargE Area burst Polarimeter (LEAP)." In: *UV, X-Ray, and Gamma-Ray Space Instrumentation for Astronomy XXII*. Ed. by Oswald H. Siegmund. Vol. 11821. International Society for Optics and Photonics. SPIE, 2021, 118210Q. DOI: 10.1117/12.2594568.

[170] M. R. Metzger, S. G. Djorgovski, S. R. Kulkarni, C. C. Steidel, K. L. Adelberger, D. A. Frail, E. Costa, and F. Frontera. "Spectral constraints on the redshift of the optical counterpart to the γ-ray burst of 8 May 1997." In: *Nature* 387.6636 (1997), pp. 878–880. DOI: 10.1038/43132.

[171] Slawomir Mianowski et al. "Proton irradiation of SiPM arrays for POLAR-2." In: *Experimental Astronomy* 55.2 (2023), pp. 343–371. DOI: 10.1007/s10686-022-09873-6.

[172] Slawomir Mianowski et al. "Proton irradiation of plastic scintillator bars for POLAR-2." In: *Experimental Astronomy* (2023). DOI: 10.1007/s10686-023-09906-8.

[173] Barbara Michalec, Jan Swakoń, Urszula Sowa, Marta Ptaszkiewicz, Teresa Cywicka-Jakiel, and Paweł Olko. "Proton radiotherapy facility for ocular tumors at the IFJ PAN in Kraków Poland." In: *Applied Radiation and Isotopes* 68.4 (2010). The 7th International Topical Meeting on Industrial Radiation and Radio isotope Measurement Application(IRRMA-7), pp. 738–742. DOI: 10.1016/j.apradiso.2009.11.001.

[174] Roberto Mignani, Andrew Shearer, Agnieszka Słowikowska, and Silvia Zane. *Astronomical Polarisation from the Infrared to Gamma Rays*. Springer, 2019.

[175] M. Mikelsen, J. H. Bleka, J. S. Christensen, E. V. Monakhov, B. G. Svensson, J. Härkönen, and B. S. Avset. "Annealing of the divacancy-oxygen and vacancy-oxygen complexes in silicon." In: *Phys. Rev. B* 75 (15 2007), p. 155202. DOI: 10.1103/PhysRevB.75.155202.

[176] L. J. Mitchell, B. F. Phlips, J. E. Grove, T. Finne, M. Johnson-Rambert, and W. N. Johnson. "Strontium Iodide Radiation Instrument (SIRI) – Early On-Orbit Results." 2019. URL: https://arxiv.org/abs/1907.11364.

[177] Lee J. Mitchell, Bernard F. Phlips, Richard S. Woolf, Theodore T. Finne, and W. Neil Johnson. "Strontium iodide radiation instrumentation II (SIRI-2)." In: *UV, X-Ray, and Gamma-Ray Space Instrumentation for Astronomy XXI*. Ed. by Oswald H. Siegmund. Vol. 11118. International Society for Optics and Photonics. SPIE, 2019, p. 111180I. DOI: 10.1117/12.2528073.

[178] Lee J. Mitchell, Bernard F. Phlips, Richard S. Woolf, Theodore T. Finne, W. Neil Johnson, and Emily G. Jackson. "Strontium Iodide Radiation Instrumentation (SIRI)." In: *UV, X-Ray, and Gamma-Ray Space Instrumentation for Astronomy XX*. Ed. by Oswald H. Siegmund. Vol. 10397. International Society for Optics and Photonics. SPIE, 2017, 103970B. DOI: 10.1117/12.2272606.

[179] Michael Moll. "Radiation Damage in Silicon Particle Detectors - microscopic defects and macroscopic properties." PhD thesis. Fachbereich Physik der Universität Hamburg, 1999. URL: https://mmoll.web.cern.ch/thesis/pdf/moll-thesis.pdf.

[180] J. Mooney and P. Kambhampati. "Get the Basics Right: Jacobian Conversion of Wavelength and Energy Scales for Quantitative Analysis of Emission Spectra." In: *The Journal of Physical Chemistry Letters* 4.19 (2013), pp. 3316–3318. DOI: 10.1021/jz401508t.

[181] Yuya Nakamura et al. "Performance of an emulsion telescope for gamma-ray observations in the GRAINE2018 balloon-borne experiment." In: *Progress of Theoretical and Experimental Physics* 2021.12 (Nov. 2021), 123H02. ISSN: 2050-3911. DOI: 10.1093/ptep/ptab148.

[182] Ehud Nakar and Tsvi Piran. "Time-scales in long gamma-ray bursts." In: *Monthly Notices of the Royal Astronomical Society* 331.1 (Mar. 2002), pp. 40–44. ISSN: 0035-8711. DOI: 10.1046/j.1365-8711.2002.05158.x.

[183] Nava, L., Ghirlanda, G., Ghisellini, G., and Celotti, A. "Spectral properties of 438 GRBs detected by Fermi/GBM." In: *A&A* 530 (2011), A21. DOI: 10.1051/0004-6361/201016270.

[184] J. Nilsson, V. Cuplov, and M. Isaksson. "Identifying key surface parameters for optical photon transport in GEANT4/GATE simulations." In: *Applied Radiation and Isotopes* 103 (2015), pp. 15–24. DOI: 10.1016/j.apradiso.2015.04.017.

[185] Etam Noah et al. "The Baby MIND spectrometer for the J-PARC T59(WAGASCI) experiment." In: *PoS* EPS-HEP2017 (2017), p. 508. DOI: 10.22323/1.314.0508.

[186] J. P. Norris, J. T. Bonnell, D. Kazanas, J. D. Scargle, J. Hakkila, and T. W. Giblin. "Long-Lag, Wide-Pulse Gamma-Ray Bursts." In: *The Astrophysical Journal* 627.1 (2005), p. 324. DOI: 10.1086/430294.

[187] J. P. Norris, R. J. Nemiroff, J. T. Bonnell, J. D. Scargle, C. Kouveliotou, W. S. Paciesas, C. A. Meegan, and G. J. Fishman. "Attributes of Pulses in Long Bright Gamma-Ray Bursts." In: *Astrophysical Journal* 459 (1996), p. 393. DOI: 10.1086/176902.

[188] JP Norris, GH Share, DC Messina, BR Dennis, UD Desai, TL Cline, SM Matz, and EL Chupp. "Spectral evolution of pulse structures in gamma-ray bursts." In: *Astrophysical Journal* 301 (1986), pp. 213–219.

[189] A. V. Olinto. "POEMMA (Probe Of Extreme Multi-Messenger Astrophysics) Roadmap Update." In: *PoS* ICRC2023 (2023), p. 1159. DOI: 10.22323/1.444.1159.

[190] Keita Ozaki, Satoru Takahashi, Shigeki Aoki, Keiki Kamada, Taichi Kaneyama, Ryo Nakagawa, and Hiroki Rokujo. "Demonstration of polarization sensitivity of emulsion-based pair conversion telescope for cosmic gamma-ray polarimetry." In: *Nuclear Instruments and Methods in Physics Research Section A: Accelerators, Spectrometers, Detectors and Associated Equipment* 833 (2016), pp. 165–168. DOI: 10.1016/j.nima.2016.07.033.

[191] Veres P. et al. "GCN Circ. 20461." 2017. URL: https://gcn.gsfc.nasa.gov/other/170114A.gcn3.

[192] B. Paczynski. "Gamma-ray bursters at cosmological distances." In: *The Astrophysical Journal* 308 (Sept. 1986), pp. L43–L46. DOI: 10.1086/184740.

[193] J. van Paradijs et al. "Transient optical emission from the error box of the γ-ray burst of 28 February 1997." In: *Nature* 386.6626 (1997), pp. 686–689. DOI: 10.1038/386686a0.

[194] Tyler Parsotan, Diego López-Cámara, and Davide Lazzati. "Photospheric Polarization Signatures from Long Gamma-Ray Burst Simulations." In: *The Astrophysical Journal* 896.2 (2020), p. 139. DOI: 10.3847/1538-4357/ab910f.

[195] Gabriel Pelleriti. "LAD Bonding reports." *Internal document*. 2022-2023.

[196] Patrick Petitjean, F. Y. Wang, X. F. Wu, and J. J. Wei. "GRBs and Fundamental Physics." In: *Space Science Reviews* 202.1 (2016), pp. 195–234. DOI: 10.1007/s11214-016-0235-6.

[197] Tsvi Piran. "The physics of gamma-ray bursts." In: *Rev. Mod. Phys.* 76 (4 2005), pp. 1143–1210. DOI: 10.1103/RevModPhys.76.1143.

[198] R. D. Preece, M. S. Briggs, R. S. Mallozzi, G. N. Pendleton, W. S. Paciesas, and D. L. Band. "The BATSE Gamma-Ray Burst Spectral Catalog. I. High Time Resolution Spectroscopy of Bright Bursts Using High Energy Resolution Data." In: *The Astrophysical Journal Supplement Series* 126.1 (2000), p. 19. DOI: 10.1086/313289.

[199] N. Produit et al. "Design and construction of the POLAR detector." In: *Nuclear Instruments and Methods in Physics Research Section A: Accelerators, Spectrometers, Detectors and Associated Equipment* 877 (2018), pp. 259–268. DOI: 10.1016/j.nima.2017.09.053.

[200] Nicolas Produit et al. "POLAR-2, the next generation of GRB polarization detector." In: *PoS* ICRC2023 (2023), p. 550. DOI: 10.22323/1.444.0550.

[201] F.G.A. Quarati, P. Dorenbos, J. van der Biezen, Alan Owens, M. Selle, L. Parthier, and P. Schotanus. "Scintillation and detection characteristics of high-sensitivity CeBr3 gamma-ray spectrometers." In: *Nuclear Instruments and Methods in Physics Research Section A: Accelerators, Spectrometers, Detectors and Associated Equipment* 729 (2013), pp. 596–604. ISSN: 0168-9002. DOI: 10.1016/j.nima.2013.08.005.

[202] A. R. Rao et al. "ASTROSAT CZT IMAGER OBSERVATIONS OF GRB 151006A: TIMING, SPECTROSCOPY, AND POLARIZATION STUDY." In: *The Astrophysical Journal* 833.1 (2016), p. 86. DOI: 10.3847/1538-4357/833/1/86.

[203] Paul S. Ray et al. *STROBE-X: X-ray Timing and Spectroscopy on Dynamical Timescales from Microseconds to Years*. 2019. arXiv: 1903.03035 [astro-ph.IM].

[204] Robert E. Rutledge and Derek B. Fox. "Re-analysis of polarization in the γ-ray flux of GRB 021206." In: *Monthly Notices of the Royal Astronomical Society* 350.4 (June 2004), pp. 1288–1300. DOI: 10.1111/j.1365-2966.2004.07665.x.

[205] Jeffrey D. Scargle. "Studies in Astronomical Time Series Analysis. V. Bayesian Blocks, a New Method to Analyze Structure in Photon Counting Data*." In: *The Astrophysical Journal* 504.1 (1998), p. 405. DOI: 10.1086/306064.

[206] Ronald W. Schafer. "What Is a Savitzky-Golay Filter? [Lecture Notes]." In: *IEEE Signal Processing Magazine* 28.4 (2011), pp. 111–117. DOI: 10.1109/MSP.2011.941097.

[207] David J. Spiegelhalter, Nicola G. Best, Bradley P. Carlin, and Angelika Van Der Linde. "Bayesian Measures of Model Complexity and Fit." In: *Journal of the Royal Statistical Society Series B: Statistical Methodology* 64.4 (Oct. 2002), pp. 583–639. ISSN: 1369-7412. DOI: 10.1111/1467-9868.00353.

[208] K. Z. Stanek et al. "Spectroscopic Discovery of the Supernova 2003dh Associated with GRB 030329*." In: *The Astrophysical Journal* 591.1 (2003), p. L17. DOI: 10.1086/376976.

[209] "On the Composition and Resolution of Streams of Polarized Light from different Sources." In: ed. by George Gabriel Stokes. Vol. 3. Cambridge Library Collection - Mathematics. Cambridge: Cambridge University Press, 2009, pp. 233–258. DOI: 10.1017/CBO9780511702266.010.

[210] Satoru Takahashi, Shigeki Aoki, Keiki Kamada, Saki Mizutani, Ryo Nakagawa, Keita Ozaki, and Hiroki Rokujo. "GRAINE project: The first balloon-borne, emulsion gamma-ray telescope experiment." In: *Progress of Theoretical and Experimental Physics* 2015.4 (Apr. 2015), 043H01. ISSN: 2050-3911. DOI: 10.1093/ptep/ptv046.

[211] "The National Nuclear Data Center at Brookhaven National Laboratory." URL: https://www.nndc.bnl.gov/nudat3/.

[212] Kenji Toma. *Polarization of GRB Prompt Emission*. 2013. arXiv: 1308.5733 [astro-ph.HE].

[213] J. Tomsick et al. "The Compton Spectrometer and Imager." In: *PoS* ICRC2023 (2023), p. 745. DOI: 10.22323/1.444.0745.

[214] John A. Tomsick et al. *The Compton Spectrometer and Imager*. 2019. arXiv: 1908.04334 [astro-ph.IM].

[215] L. Torrisi. "Plastic scintillator investigations for relative dosimetry in proton-therapy." In: *Nuclear Instruments and Methods in Physics Research Section B: Beam Interactions with Materials and Atoms* 170.3 (2000), pp. 523–530. DOI: 10.1016/S0168-583X(00)00237-8.

[216] Sascha Trippe. "POLARIZATION AND POLARIMETRY: A REVIEW." In: *Journal of The Korean Astronomical Society* 47.1 (Feb. 2014), pp. 15–39. DOI: 10.5303/JKAS.2014.47.1.15.

[217] Vadawale, S. V., Chattopadhyay, T., Rao, A. R., Bhattacharya, D., Bhalerao, V. B., Vagshette, N., Pawar, P., and Sreekumar, S. "Hard X-ray polarimetry with Astrosat-CZTI." In: *A&A* 578 (2015), A73. DOI: 10.1051/0004-6361/201525686.

[218] P. Veres et al. "Extreme Variability in a Long-duration Gamma-Ray Burst Associated with a Kilonova." In: *The Astrophysical Journal Letters* 954.1 (2023), p. L5. DOI: 10.3847/2041-8213/ace82d.

[219] Giacomo Vianello, Robert J. Lauer, Patrick Younk, Luigi Tibaldo, James M. Burgess, Hugo Ayala, Patrick Harding, Michelle Hui, Nicola Omodei, and Hao Zhou. *The Multi-Mission Maximum Likelihood framework (3ML)*. 2015. arXiv: 1507.08343 [astro-ph.HE].

[220] Nektarios Vlahakis and Arieh Königl. "Relativistic Magnetohydrodynamics with Application to Gamma-Ray Burst Outflows. I. Theory and Semianalytic Trans-Alfvénic Solutions." In: *The Astrophysical Journal* 596.2 (2003), p. 1080. DOI: 10.1086/378226.

[221] Yuan-Hao Wang et al. "Localization of Gamma-ray Bursts using the Compton polarimeter POLAR." In: *Nuclear Instruments and Methods in Physics Research Section A: Accelerators, Spectrometers, Detectors and Associated Equipment* 988 (2021), p. 164866. DOI: 10.1016/j.nima.2020.164866.

[222] Martin C. Weisskopf, Ronald F. Elsner, and Stephen L. O'Dell. "On understanding the figures of merit for detection and measurement of x-ray polarization." In: *Space Telescopes and Instrumentation 2010: Ultraviolet to Gamma Ray*. Ed. by Monique Arnaud, Stephen S. Murray, and Tadayuki Takahashi. Vol. 7732. International Society for Optics and Photonics. SPIE, 2010, 77320E. DOI: 10.1117/12.857357. URL: https://doi.org/10.1117/12.857357.

[223] Martin C. Weisskopf et al. "The Imaging X-ray Polarimetry Explorer (IXPE)." In: *Results in Physics* 6 (2016), pp. 1179–1180. DOI: 10.1016/j.rinp.2016.10.021.

[224] Jiaxing Wen et al. "GRID: a student project to monitor the transient gamma-ray sky in the multi-messenger astronomy era." In: *Experimental Astronomy* 48 (2019), pp. 77–95. DOI: 10.1007/s10686-019-09636-w.

[225] C. Wigger, W. Hajdas, K. Arzner, M. Güdel, and A. Zehnder. "Gamma-Ray Burst Polarization: Limits from RHESSI Measurements." In: *The Astrophysical Journal* 613.2 (2004), p. 1088. DOI: 10.1086/423163.

[226] Willis, D. R., Barlow, E. J., Bird, A. J., Clark, D. J., Dean, A. J., McConnell, M. L., Moran, L., Shaw, S. E., and Sguera, V. "Evidence of polarisation in the prompt gamma-ray emission from GRB131 and GRB924." In: *A&A* 439.1 (2005), pp. 245–253. DOI: 10.1051/0004-6361:20052693.

[227] Hualin Xiao et al. "In-flight energy calibration of the space-borne Compton polarimeter POLAR." In: *Astroparticle Physics* 103 (2018), pp. 74–86. DOI: 10.1016/j.astropartphys.2018.07.009.

[228] Shaolin Xiong et al. "Overview of the GRB observation by POLAR." In: *PoS* ICRC2017 (2017), p. 640. DOI: 10.22323/1.301.0640.

[229] Daisuke Yonetoku et al. "DETECTION OF GAMMA-RAY POLARIZATION IN PROMPT EMISSION OF GRB 100826A." In: *The Astrophysical Journal Letters* 743.2 (2011), p. L30. DOI: 10.1088/2041-8205/743/2/L30.

[230] Daisuke Yonetoku et al. "Gamma-Ray Burst Polarimeter (GAP) aboard the Small Solar Power Sail Demonstrator IKAROS." In: *Publications of the Astronomical Society of Japan* 63.3 (June 2011), pp. 625–638. DOI: 10.1093/pasj/63.3.625.

[231] Daisuke Yonetoku et al. "MAGNETIC STRUCTURES IN GAMMA-RAY BURST JETS PROBED BY GAMMA-RAY POLARIZATION." In: *The Astrophysical Journal Letters* 758.1 (2012), p. L1. DOI: 10.1088/2041-8205/758/1/L1.

[232] Bin-Bin Zhang, Bing Zhang, En-Wei Liang, Yi-Zhong Fan, Xue-Feng Wu, Asaf Pe'er, Amanda Maxham, He Gao, and Yun-Ming Dong. "A COMPREHENSIVE ANALYSIS OF FERMI GAMMA-RAY BURST DATA. I. SPECTRAL COMPONENTS AND THE POSSIBLE PHYSICAL ORIGINS OF LAT/GBM GRBs." In: *The Astrophysical Journal* 730.2 (2011), p. 141. DOI: 10.1088/0004-637X/730/2/141.

[233] Bing Zhang. *The Physics of Gamma-Ray Bursts*. Cambridge University Press, 2018. DOI: 10.1017/9781139226530.

[234] Bing Zhang and Huirong Yan. "THE INTERNAL-COLLISION-INDUCED MAGNETIC RECONNECTION AND TURBULENCE (ICMART) MODEL OF GAMMA-RAY BURSTS." In: *The Astrophysical Journal* 726.2 (2010), p. 90. DOI: 10.1088/0004-637X/726/2/90.

[235] Bing Zhang, Bin-Bin Zhang, En-Wei Liang, Neil Gehrels, David N. Burrows, and Peter Mészáros. "Making a Short Gamma-Ray Burst from a Long One: Implications for the Nature of GRB 060614." In: *The Astrophysical Journal* 655.1 (2007), p. L25. DOI: 10.1086/511781.

[236] D.L. Zhang et al. "Dedicated SiPM array for GRD of GECAM." 2021. URL: https://arxiv.org/abs/2112.04770.

[237] Dali Zhang et al. "The performance of SiPM-based gamma-ray detector (GRD) of GECAM-C." 2023. URL: https://arxiv.org/abs/2303.00537.

[238] Ping Zhang, Wojtek Hajdas, Si-ming Liu, Yang Su, You-ping Li, and Wei Chen. "In-flight Low Energy X-ray Calibration of POLAR Detector on TianGong2." In: *Acta Astronomica Sinica* 61.1 (January 2020). DOI: 10.15940/j.cnki.0001-5245.2020.01.003.

[239] S. N. Zhang et al. "eXTP: Enhanced X-ray Timing and Polarization mission." In: *Space Telescopes and Instrumentation 2016: Ultraviolet to Gamma Ray*. Ed. by Jan-Willem A. den Herder, Tadayuki Takahashi, and Marshall Bautz. Vol. 9905. International Society for Optics and Photonics. SPIE, 2017, 99051Q. DOI: 10.1117/12.2232034.

[240] Shuang-Nan Zhang et al. "Detailed polarization measurements of the prompt emission of five gamma-ray bursts." In: *Nature Astronomy* 3.3 (2019), pp. 258–264. DOI: 10.1038/s41550-018-0664-0.

[241] Xiaofeng Zhang, Hualin Xiao, Boxiang Yu, Silvio Orsi, Bobing Wu, Wei Hu, and Xuan Zhang. "Study of non-linear energy response of POLAR plastic scintillators to electrons." In: *Nuclear Instruments and Methods in Physics Research Section A: Accelerators, Spectrometers, Detectors and Associated Equipment* 797 (2015), pp. 94–100. DOI: 10.1016/j.nima.2015.06.031.

[242] Xutao Zheng et al. "In-orbit radiation damage characterization of SiPMs in GRID-02 CubeSat detector." 2022. URL: https://arxiv.org/abs/2205.10506.

[243] Yao Zhu, Sen Qian, Zhigang Wang, Hao Guo, Lishuang Ma, Zhile Wang, and Qi Wu. "Scintillation properties of GAGG:Ce ceramic and single crystal." In: *Optical Materials* 105 (2020), p. 109964. DOI: 10.1016/j.optmat.2020.109964.

[244] LAD eXTP collaboration. *LAD INSTRUMENT DESIGN DESCRIPTION AND JUSTIFICATION. internal document, draftv2.0* 2022-11-14.

[245] "polarpy plugin GitHub page." Last consulted in June 2022. URL: https://github.com/grburgess/polarpy.

[246] "`astromodels` online documentation." Last consulted in May 2023. URL: https://astromodels.readthedocs.io/en/latest/.

COLOPHON

This document was typeset using the typographical look-and-feel `classicthesis` developed by André Miede and Ivo Pletikosić. The style was inspired by Robert Bringhurst's seminal book on typography *"The Elements of Typographic Style"*. `classicthesis` is available for both LaTeX and LyX:

https://bitbucket.org/amiede/classicthesis/

Happy users of `classicthesis` usually send a real postcard to the author, a collection of postcards received so far is featured here:

http://postcards.miede.de/

Thank you very much for your feedback and contribution.